Dissertation Submitted to
Graduate School of Science of Osaka University
for a Doctorate of Science

Observation of baryon resonance in the $\gamma p \to \pi^0 \eta p$ reaction at LEPS/SPring-8

(LEPS/SPring-8 における $\gamma p \to \pi^0 \eta p$ 反応を用いたバリオン共鳴状態の観測)

Toru Matsumura

- 2004 January -

Research Center for Nuclear Physics (RCNP), Osaka University

Abstract

Understanding the mechanism of the baryon excitation is one of the important topics in hadron physics since it gives us new insight into non-perturbative QCD. The prediction of the baryon mass-spectra with a constituent quark-model, showing more baryon resonances than the experimental observation (missing resonance problem), is related with two possible scenarios: (i) the dynamical quark degrees of freedom used in the model are not physically realized, or (ii) the missing resonances couple weakly to the formation channel, where most of the experimental observations are based on the partial-wave analysis in the πN channel. Experimental evidence for the "missing" resonances would give information that allows one to distinguish these two scenarios. Such experimental work is being carried out at many nuclear physics laboratories, especially at high-energy photon beam facility.

In this thesis, the $\gamma p \to \pi^0 \eta p$ reaction has been studied for E_γ=1.62-2.40 GeV and $\cos(\theta^{\rm c.m.}_{\pi^0\eta}) < 0$ with an electro-magnetic (EM) calorimeter at the Laser-Electron-Photon facility of SPring-8 (LEPS), where the backward Compton γ-rays are generated by interaction between ultra-violet laser-light and 8 GeV storage electrons. Four final-state photons coming from $\pi^0\eta$ decay were detected by the EM calorimeter. The energy resolution σ_E of the calorimeter is estimated to be $(\sigma_E/E)^2 = (0.052/\sqrt{E})^2 + 0.044^2$, where E is the photon energy in GeV; The angular resolutions are almost same for both polar and azimuthal angles and are $\sigma = 2.1^\circ$ (1.2°) for a 100 MeV (1 GeV) photon.

Totally 469 events for the carbon target and 380 events for the CH_2 target were obtained as $\gamma p \to \pi^0 \eta p$ event samples from a systematic analysis; The proton-target data were extracted by subtracting the carbon contribution from CH_2 spectra. The $\sqrt{s}$ distribution clearly shows a resonance structure for the $\gamma p \to \pi^0 \eta p$ event samples. The mass and the width of the baryon resonance are estimated to be $M = 2080 \pm 20$ MeV/c^2 and $\Gamma = 100^{+60}_{-20}$ MeV/c^2, respectively. The mass distribution of the $\pi^0\eta$ system of the resonance concentrates around 0.9-1.0 GeV/c^2. The result indicates that the observed baryon resonance strongly couples to the scalar-isovector $a_0(980)$ meson. This is the first observation of the baryon resonance that couples strongly to the scalar meson. Although the spin-parity states of the baryon resonance is not identified quantitatively due to the low statistics, only s- and p-wave could be dominant contributions to the reaction since the mass of the resonance is approximately 160 MeV/c^2 larger than the $a_0(980)p$ production threshold ($\sim$1920 MeV/c^2).

Contents

Chapter 1

Introduction

1.1 Baryons and their internal structure

At present, we know that there are many ground-state baryons (such as $N, \Delta, \Lambda, \Sigma, \Xi, \Omega, ...$) and its excited states ($N^*, \Delta^*, \Lambda^*, \Sigma^*, \Xi^*, \Omega^*, ...$), which have been experimentally observed. However, either the mechanism of baryon excitations or the internal structure of the baryons have not been fully understood.

Historically, the first success in interpreting of the internal structure of the ground-state baryons was made by introducing the quark model which has been proposed by Gell-Mann and Zweig in 1964 [1, 2]. They introduced hypothetical elementary-particles, so-called "quarks", in order to classify the ground-state baryons into the pattern based on the $SU(3)_{\rm flavor} \times SU(2)_{\rm spin}$ symmetry. In the quark model, the baryons consist of three quarks (qqq); on the other hand, mesons (such as $\pi, K, \eta, ...$) are composed of a quark and an anti-quark ($q\bar{q}$). The mass difference of each baryon can be interpreted naively as the mass difference among the constituent u, d and s quarks although the mass splitting such as N-Δ or Λ-Σ cannot be explained in terms of symmetry, and some dynamics like spin-spin hyperfine interactions are needed to obtain the mass splitting. The mass relation between ground-state baryons is given with the well-known Gell-Mann-Okubo mass formula. The experimental evidence for the quark has been presented in the analysis of deep-inelastic electron scattering off a nucleon at SLAC, showing the presence of point-like particles inside a nucleon. Experimental failure in search for isolated quarks gave us a very important insight into the hadron property: the quark confinement, which means that quarks are confined inside a hadron with some confinement potentials. New meson states, such as the J/ψ [3, 4] and Υ states [5, 6], which consist of heavier quarks, c and b quarks, have been discovered in 1970s. The mass spectra of their excited states, which are called as charmonium ($c\bar{c}$) and bottomonium ($b\bar{b}$) states, is perfectly explained by assuming that such states have a wave function with two elementary quarlks bound in a Coulomb plus linear effective potential. Nowadays people believe that all hadrons (baryons and mesons) consist of the quarks. However, the internal structure of baryons is still unknown. For instance, we do not know how the quarks are confined in the baryons (see Fig. 1.1). The study of the baryon excitation mechanism would provide us precious information to answer such questions.

A theoretical framework is needed for an conceptual and quantitative understanding of the baryon

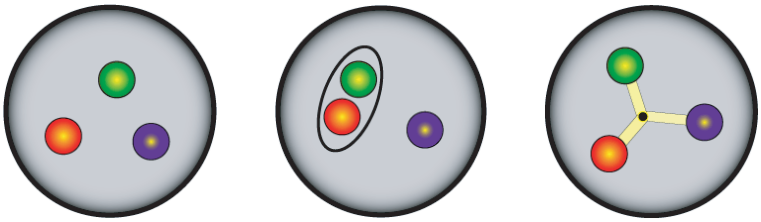

Figure 1.1: Effective degrees of freedom in quark models [7]: three equivalent constituent quarks, quark-diquark structure, quarks and flux tube.

excitation. Quantum chromodynamics (QCD) is the theory that governs strong interactions among quarks and gluons with color charge. Since the gluons themselves have a color charge, they directly interact with other gluons. This non-Abelian nature of the QCD results in the opposite screening effect compared to the quantum electrodynamics (QED) that is the theory describing the electro magnetic interaction: the coupling constant of the QCD becomes small as the energy scale increases (equivalently at short distances). For this reason, although the perturbative approach to the QCD at high energy is extremely successful, the perturbative QCD is meaningless at the typical energy scale of nucleons and their excited states (~ 1 GeV). Therefore, various QCD-based dynamical-models have been developed to describe the properties of baryon resonances, such as mass and width, magnetic moment, decay branching-ratio. For example, DeGrand et al have calculated the baryon masses with a bag model, in which the quarks are confined to the interior of hadrons by bag pressure [8, 9]. In this model quarks and gluons inside the bag interact each other based on one-gluon exchange (OGE) dynamics derived from QCD. Among such QCD-based dynamical-models, we will briefly introduce two models describing baryon excitations: a constituent quark model (CQM) and a deformed oscillator quark (DOQ) model.

Constituent quark model (CQM)

The detailed study for the excited baryon within a non-relativistic CQM has been performed by Isgur and Karl, and by their collaborators [13, 14]. In their model, the baryon wave-functions are described with three constituent valence quarks, where the quarks are not point-like but have the electric and the strong form factor. The confinement potential includes both a Coulomb-type potential given by short distance OGE (V) and a spin-dependent potential ($H_{\rm hyp}$). The Hamiltonian for the non-relativistic CQM is given as

$$H_{\rm NR} = \sum_i \left(m_i + \frac{\boldsymbol{p}_i^2}{2m_i} \right) + \sum_{i<j} \left(V^{ij} + H_{\rm hyp}^{ij} \right), \tag{1.1}$$

where m_i denotes the ith constituent quark mass, $\boldsymbol{p}_i$ is the ith quark momentum. Here, the mass of the light (u, d) quarks are 200-350 MeV and that of s quark is heavier about 150-200 MeV. Although the non-relativistic CQM reproduced successfully the mass spectrum of the low-lying baryon resonances, there were some criticisms because the kinematic energy of light quarks inside the baryon ($p/m \sim 1$) is not negligibly small; non-relativistic approximation would be inaccurate. Extension to a relativistic

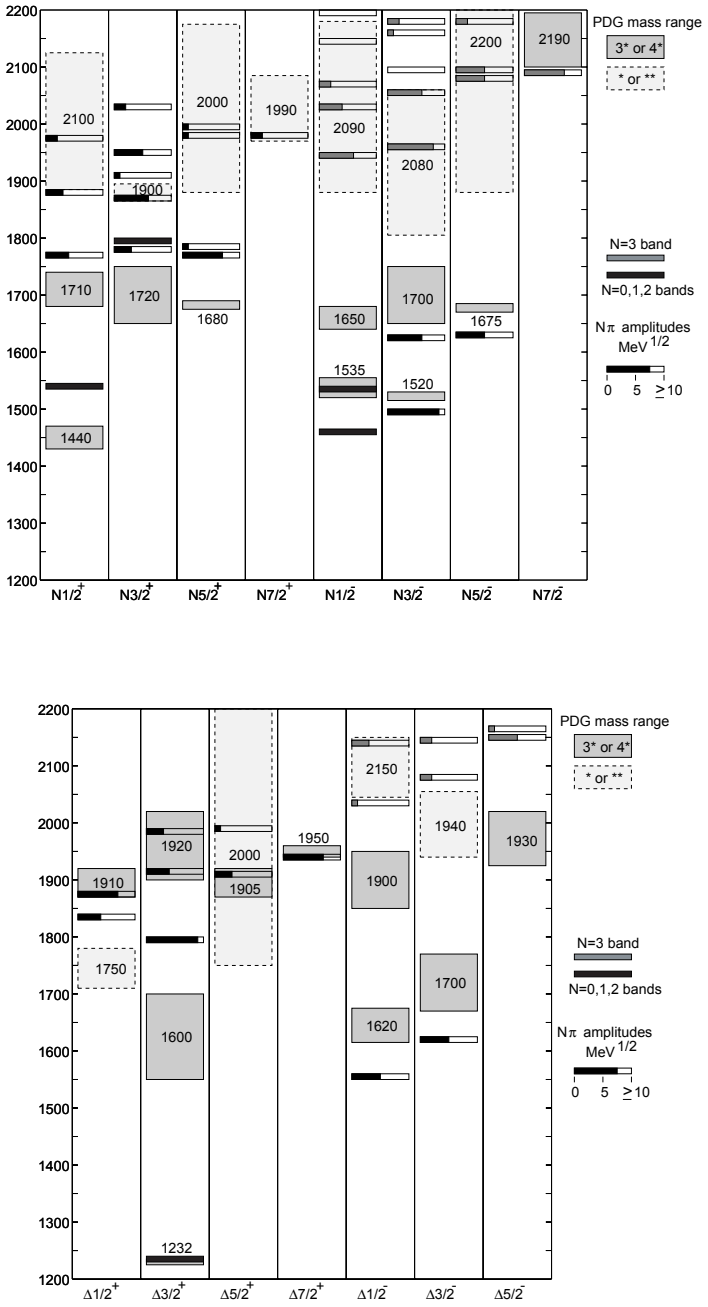

Figure 1.2: Calculated masses and $N\pi$ amplitudes for N^* (top figure) and Δ^* resonances (bottom figure) below 2200 MeV/c^2, which are based on the relativistic CQM in Ref. [10, 11]. The boxes in these figures show the range of central values for resonances masses from PDG [12].

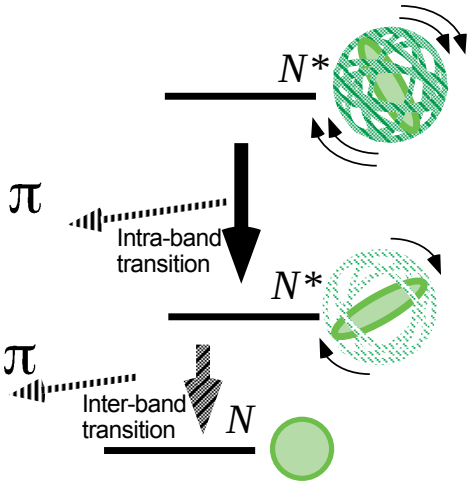

Figure 1.3: Schematic image of the intra-band transition ($N^* \rightarrow N^*$) and the inter-band transition ($N^* \rightarrow N$) in DOQ model [16].

CQM has been achieved by Capstick and Isgur [10]. In this model, the Schrödinger equation $H\Psi = E\Psi$ is solved in a Hilbert space for valence quarks with a finite spatial size [15]. The Hamiltonian is

$$H_{\rm R} = \sum_i \sqrt{\boldsymbol{p}_i^2 + m_i^2} + V, \tag{1.2}$$

where V is a relative-position and -momentum dependent potential (detail discussion is found in Ref.[10]). Figure 1.2 shows the non-strange baryon mass spectra obtained from the relativistic CQM compared with those from the PDG database. Although there are systematic deviations between the model and the experiment (+50 MeV for the positive parity states, and −50 MeV for the negative parity states), the pattern of the spectra is reproduced well. The theoretical predictions from CQM are, nowadays, referred from experimentalists who study baryon excitations.

Deformed oscillator quark (DOQ) model

The DOQ model, originally proposed in the early 80's [17, 18, 19, 20], is an effective non-relativistic quark model with a deformed harmonic-oscillator potential [21, 22, 23, 24, 25, 16]. The DOQ Hamiltonian is described as

$$H_{\rm DOQ} = \sum_{i=1}^{3} \left(\frac{p_i^2}{2m} + \frac{1}{2} m(\omega_x^2 x_i^2 + \omega_y^2 y_i^2 + \omega_z^2 z_i^2) \right) - H_{c.m.} \tag{1.3}$$

where $\omega_x, \omega_y, \omega_z$ are oscillator parameter which are related with deformation of the system, m is the mass of the constituent quark ($m \sim 300$ MeV/c^2) and $H_{c.m}$ is the Hamiltonian for the center of mass motion [25]. In the DOQ model excited states of baryons are strongly deformed while the ground states are spherical. For this reason, the excited baryons are interpreted as rotational bands due to the baryon deformation. Figure 1.4 shows the mass spectra of the excited baryons in terms of excitation energies

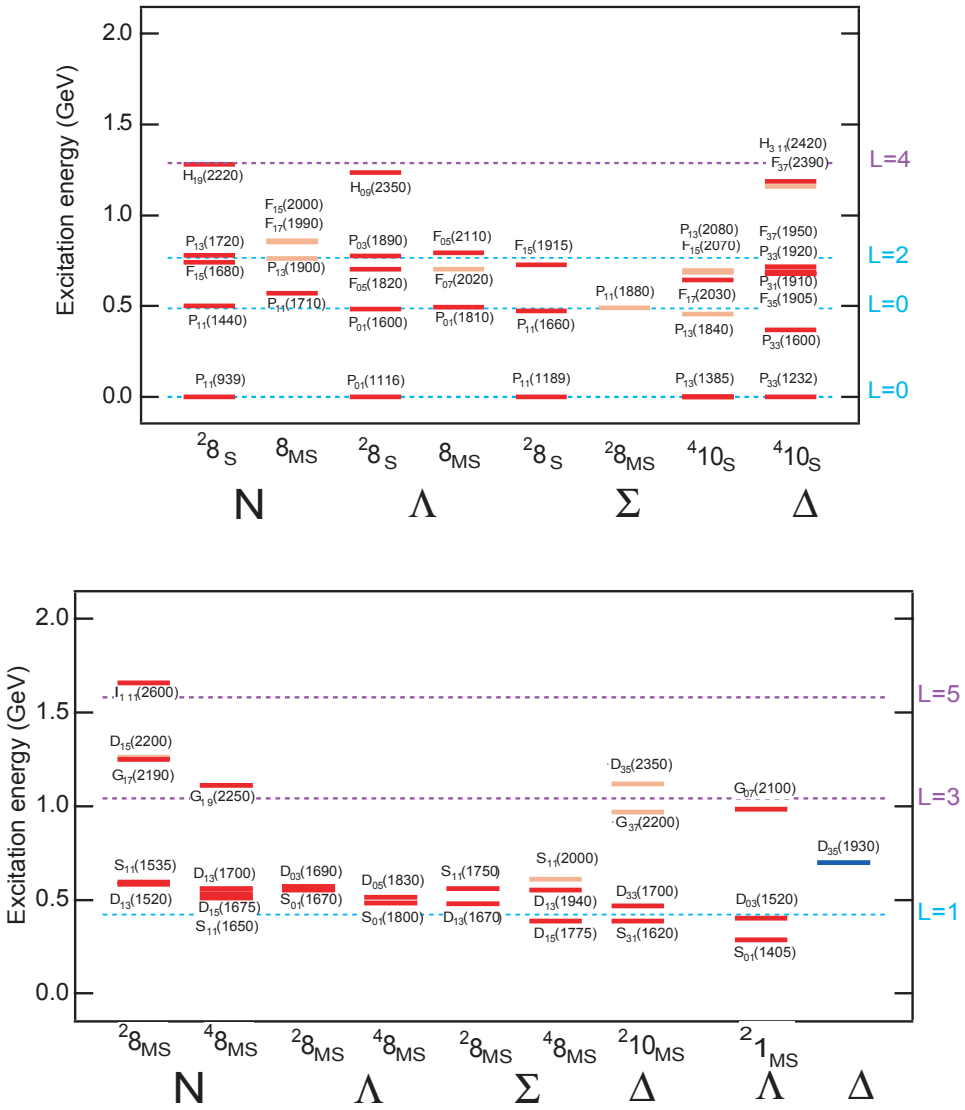

Figure 1.4: The mass spectrum of positive (top figure) and negative (bottom figure) parity baryons, which are three or four stars in PDG database [12]. The DOQ prediction is also superimposed as dashed lines [24]. The labels on the horizontal axis are ${}^{2S+1}D_{\sigma}$ for the representation $SU(2)_{\rm spin} \times SU(3)_{\rm flavor}$, where the superscript $2S+1$ denotes the spin degeneracy, D represents the dimension of the flavor $SU(3)$ representation and σ indicates the symmetry of the spatial wave function.

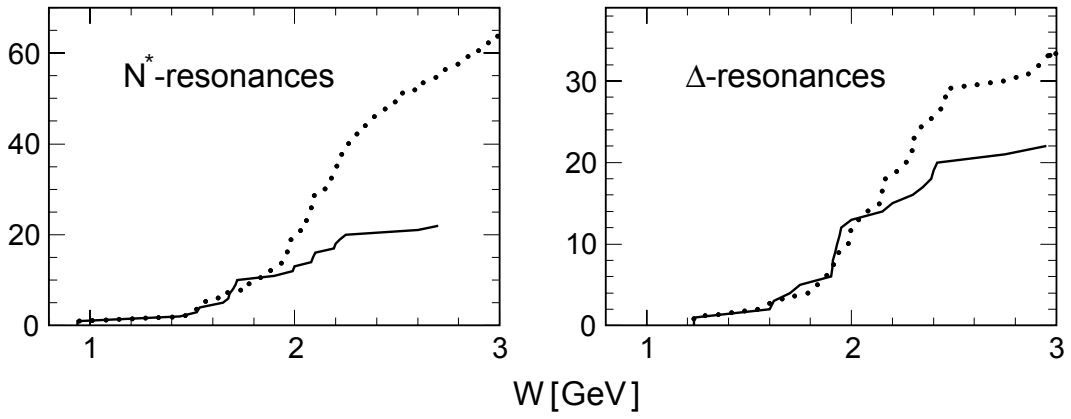

Figure 1.5: The number of nucleon (left figure) and Δ (right figure) resonances as a function of mass [7]. The curves in these figure shows a comparison between CQM prediction [26] (dotted curves) and experimental observation [12] (solid curves).

from ground state baryons for each spin-flavor multiplets. A flavor-independent systematics is clearly seen for all multiplets in this figure, and the DOQ prediction reproduces well this systematics. The transition between excited states with the same parity, so called *intra-band transition*, is allowed with specific spin selection-rules by emitting a pion. On the other hand, the transition between a excited state and the ground state is referred to as *inter-band transition*. The relation between the intra-band and inter-band transitions are illustrated in Fig. 1.3. Such a fresh look is important for deeper understanding of the mechanism.

The CQM predicts a substantial number of *missing* baryons which have not so far been observed. There are two possible explanations for this "missing resonance problem" [15] :

1. The dynamical quark degrees of freedom used in the model are not physically realized. For instance, if two quarks in the three valence quarks are tightly bound each other (see the middle picture in Fig. 1.1), the number of internal degrees of freedom would be reduced; this results in the fewer baryon population.

2. The missing resonances couple weakly to the formation channel. Most of experimental studies for the excited baryons have been performed with partial-wave analysis in the πN channel. Hence, investigating other formation channels should lead to the observation of missing states in this scenario.

By considering these two scenarios, the nearest way to solve the problem would be to study baryon resonances with various formation channels experimentally. An approach of the missing-resonance search with the pion-induced reaction initially has the problem that the resonances could couple weakly to the πN channel. Hence, the photon-induced reaction is a good tool to study the missing baryon states. Experimental work to search for missing resonances in photo-production with various final states like

$\pi\pi N$, ηN, $\pi\Delta$, ρN, ωN, $\eta' N$, $K\Lambda$, $K\Sigma$, is being carried out at many photon-beam facility, such as MAMI/Mainz, ELSA/Bonn, CLAS/JLab, GRAAL/ESRF and LEPS/SPring-8. Figure 1.5 shows the difference of the number of nucleon and Δ resonances between the experiment and a theoretical prediction as a function of mass. Significant differences begin with resonance masses of 2 GeV/c^2. Therefore, studying the photoproduction of the baryon resonances around 2 GeV/c^2 is very important; it would give us a new insight into the non-perturbative QCD, especially the internal structure of the baryons.

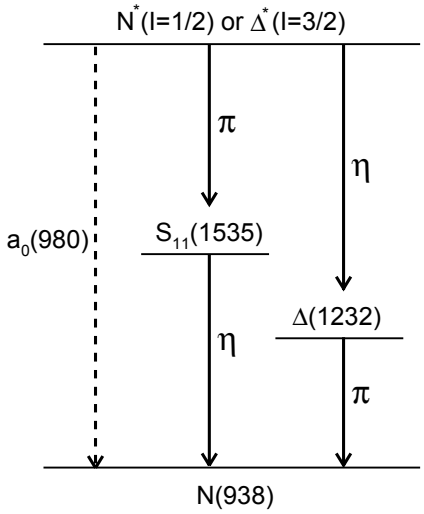

Figure 1.6: Three possible decay-modes of the baryon resonance (N^* or Δ^*) to the ground-state nucleon $N(938)$ in the $\pi^0\eta p$ final state.

1.2 The $\gamma p \to \pi^0\eta p$ reaction

The study of the $\gamma p \to \pi^0\eta p$ reaction has the advantages to understand the s-channel baryon-resonances around $\sqrt{s} = 2$ GeV/c^2.

1. **Lack of the experimental data for the $\gamma p \to \pi^0\eta p$ reaction**
   Since the final state of the reaction includes the two neutral mesons (π^0 and η) with the main decay channel into 2γ, the experimental studies have been completely missing from the old database in which most of the photoproduction data are taken from bubble chamber experiments. In general, study of such unmeasured reactions is important since there is a possibility of finding new baryon resonances.

2. **Distinction among the final-state particles**
   In general, it is very important to identify the decay channel of a baryon resonance for understanding the baryon structure. For instance, recent study of the double-π^0 photoproduction at MAMI/Mainz [27] and GRAAL/ESRF [28] has given useful information on the properties of baryon resonances at the second-resonance region, where a resonance-peak corresponding to the $P_{11}(1440)$ or $D_{13}(1520)$ resonances is clearly observed around $E_\gamma \sim 800$ MeV in the $\gamma p \to \pi^0\pi^0 p$ total cross-section. The dominant contribution to the resonance peak has a model dependence and it has been still under discussion. In any case, the sequential decay via Δ plays an important role of the reaction mechanism ($P_{11}(1440) \to \pi^0\Delta$ or $D_{13}(1520) \to \pi^0\Delta$). However, it is difficult to identify which π^0 belongs to decay from Δ in the case of $\pi^0\pi^0 p$. In contrast to this essential difficulty, the $\pi^0\eta p$ reaction can identify the resonance sequential decay rather easily since both π^0 and η mesons are distinguishable.

3. **Interesting physical topics**
   There are several physical topics related to the baryon resonances around 2 GeV/c^2 in the $\gamma p \to \pi^0 \eta p$ reaction for different decay modes, especially for the $\eta\Delta^+$, $\pi^0 S_{11}(1535)$ and $a_0(980)p$ final states. In latter part of this section, we will discuss interesting physics relating to these three specific decay channels individually.

1.2.1 The $\eta\Delta^+$ decay channel

The important property of the $\eta\Delta^+$ decay channel is isospin selectivity. If a s-channel baryon resonance, which is referred to as B^* in this paper, is formed by η ($I = 0,\ I_3 = 0$) and Δ^+ ($I = 3/2,\ I_3 = +1/2$), the isospin of the B^* resonance is uniquely determined as $I = 3/2,\ I_3 = +1/2$ (a Δ^* resonance). The life time of the baryon resonance decaying with the strong interaction is typically 10^{-23} seconds, which corresponds to the width of a few 100 MeV. Consequently, the baryon resonances around 2 GeV/c^2 are expected to be overlapped among them. Therefore, the isospin selectivity is essentially important to exclude contributions from the N^* ($I = 1/2$) resonances.

Capstick and Robert have calculated both the γN and $\eta\Delta$ amplitudes [29] for various predicted Δ^* resonances with a relativistic CQM [11]. The predictions from the calculation are summarized below:

- A sizeable photo-coupling and a large $\eta\Delta$ strength are predicted for the $F_{35}(1990)$ resonance, which corresponds to $F_{35}(2000)$ with two-star rating in the PDG database [12].
- The missing second $D_{35}(2165)$ resonance has a large $\eta\Delta$ decay branch, whereas the first D_{35} resonance couples to the πN channel and has already observed experimentally. The contribution from the $D_{35}(2165)$ would be dominant in the mass region around 2150 MeV/c^2, and hence it is possible to discover a missing $D_{35}(2165)$ resonance.

Therefore, the $\gamma p \to \pi^0 \eta p$ reaction study in the $\eta\Delta$ channel gives us a great chance to observe the missing $D_{35}(2165)$ resonance and the weak $F_{35}(1990)$ resonance. Such an experiment to search for the missing Δ^* resonances in the $\eta\Delta$ photoproduction has already been proposed at CB-ELSA/Bonn [30].

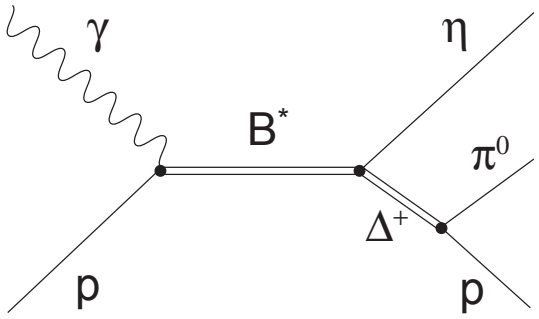

Figure 1.7: Diagram for the $\gamma p \to B^* \to \eta\Delta^+ \to \pi^0 \eta p$ reaction.

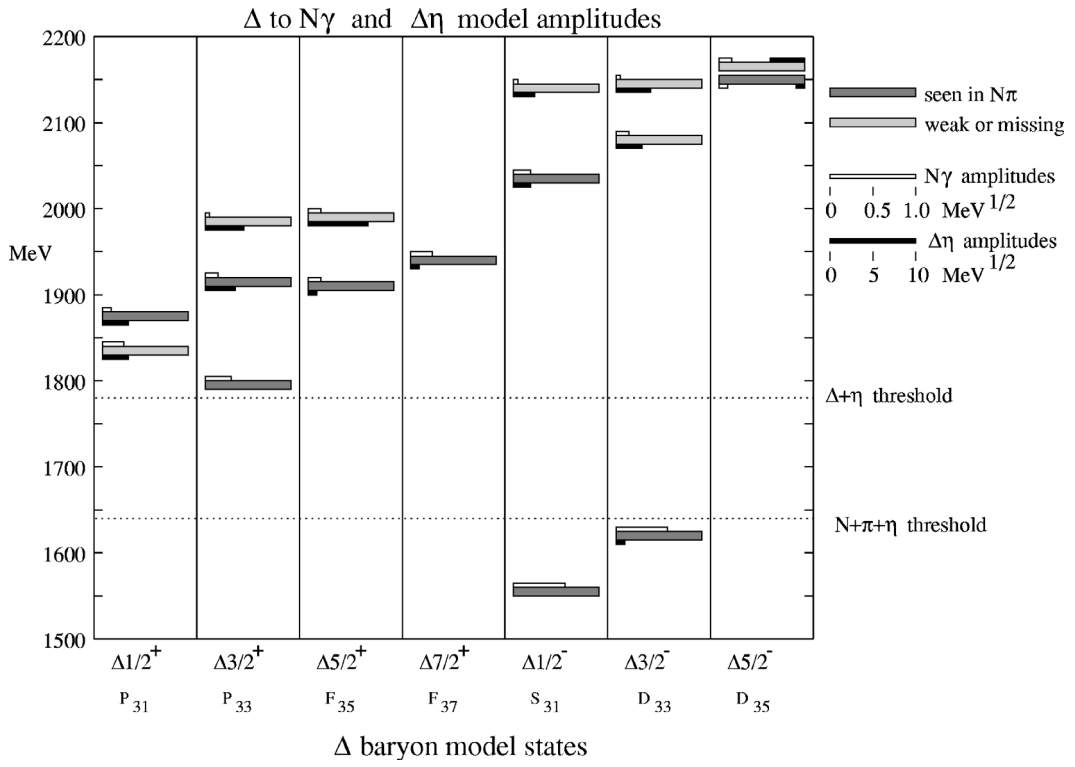

Figure 1.8: Mass predictions, and γN and $\eta\Delta$ decay amplitude predictions for Δ^* baryons up to 2200 MeV in the $\gamma N \to \eta\Delta$ reaction [29].

1.2.2 The $\pi^0 S_{11}(1535)$ decay channel

Since the $S_{11}(1535)$ resonance couples strongly to the ηN system, a sequential decay of the $\gamma p \to B^* \to \pi^0 S_{11}(1535) \to \pi^0\eta p$ can be studied in the $\gamma p \to \pi^0\eta p$ reaction (see Fig. 1.9). In this case, the isospin of the B^* resonances formed by π^0 ($I = 1,\ I_3 = 0$) and $S_{11}(1535)$ ($I = 1/2,\ I_3 = +1/2$) is either $I = 1/2$ or $I = 3/2$, and hence the B^* can be a N^* resonance or a Δ^* resonance.

The $\pi^0 S_{11}(1535)$ channel is an interesting decay-mode from a DOQ model point of view. As discussed above, the transition by emitting a pion between the two excited-states with the same parity (intra-band transition) is only allowed with a specific spin selection-rule. Figure 1.10 shows a schematic diagram of the selection rule among the negative-parity baryon-resonances. Four possible intra-band transitions from $L = 3$ state to $L = 1$ state are

$$\begin{aligned} J^P &= 7/2^- \to 3/2^-,\ \ 7/2^- \to 1/2^-, \\ &\quad\ 5/2^- \to 3/2^-,\ \ 5/2^- \to 1/2^-. \end{aligned}$$

where J^P denotes the total spin and parity of an excited baryon. These spin-parity states can be assigned to the well established baryon-resonances [24], which are found in the PDG database with (four- or

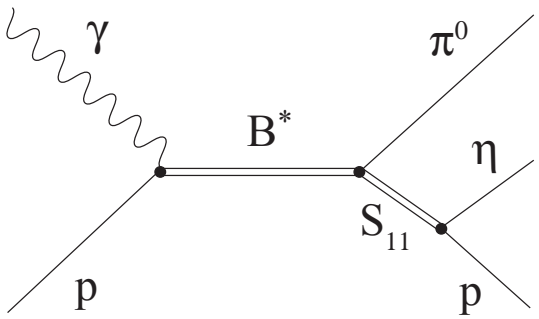

Figure 1.9: Diagram for the $\gamma p \to B^* \to \pi^0 S_{11}(1535) \to \pi^0 \eta p$ reaction.

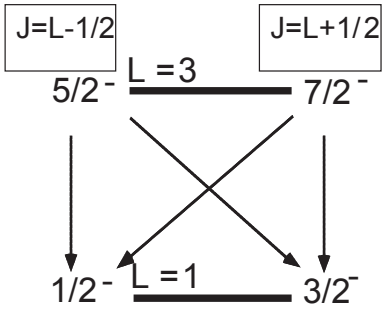

Figure 1.10: Diagram for the $\gamma p \to B^* \to \pi^0 S_{11}(1535) \to \pi^0 \eta p$ reaction.

three-star rating) [12]:

$$\begin{aligned} J^P \;=\; & G_{17}(2190) \to D_{13}(1520), \;\; G_{17}(2190) \to S_{11}(1535), \\ & D_{15}(2200) \to D_{13}(1520), \;\; D_{15}(2200) \to S_{11}(1535). \end{aligned}$$

Therefore, both the intra-band transitions, $G_{17}(2190) \to S_{11}(1535)$ and $D_{15}(2200) \to S_{11}(1535)$, is expected to be observed in the sequential decay $\gamma p \to B^* \to \pi^0 S_{11}(1535) \to \pi^0 \eta p$, where the B^* state is $G_{17}(2190)$ or $D_{15}(2200)$ in this case.

Koma et al. have evaluated the decay widths for each transitions [25]. The result is shown in Table 1.1. The decay widths of the $7/2^- \to 1/2^-$ and $5/2^- \to 1/2^-$ transitions are rather small. It is worth trying to observe the intra-band transitions experimentally in the $\gamma p \to \pi^0 \eta p$ reaction since there is no experimental evidence so far.

$7/2^- \to 3/2^-$	$7/2^- \to 1/2^-$	$5/2^- \to 3/2^-$	$5/2^- \to 1/2^-$
7.9 MeV	9.9 MeV	39.3 MeV	0.7 MeV

Table 1.1: Decay widths for each intra-band transition between $L = 3$ and $L = 1$ states with negative parity [25].

1.2.3 The $a_0(980)p$ decay channel

The decay channels discussed so far ($\eta\Delta^+$ and $\pi^0 S_{11}(1535)$) are classified as a sequential decay, where a s-channel baryon-resonance decays into a ground-state proton via an intermediate baryon (see Fig. 1.6). On the other hand, it is also possible that a B^* resonance decays directly into the ground state by meson emission of $\pi^0\eta$. The lowest-lying candidate is the $a_0(980)$ resonance. The spin-parity of the $a_0(980)$ is $J^P = 0^+$ and its isospin is $I = 1$: the $a_0(980)$ is a scalar-isovector meson.

Despite the $a_0(980)$ resonance is a well-established state experimentally (the first observation of the a_0 resonance was reported by Ammar et al. in 1968 [31]), its property is not well-known. Experimental

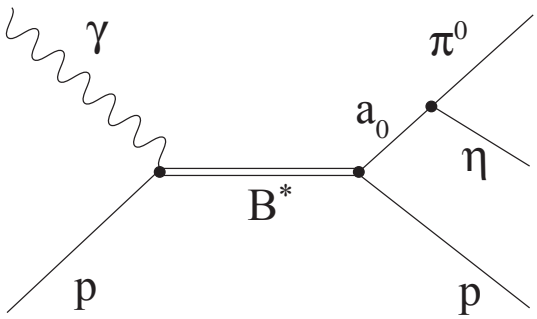

Figure 1.11: Diagram for the $\gamma p \to B^* \to a_0(980)p \to \pi^0\eta p$ reaction.

observables, such as the relatively narrow width (Γ = 50-100 MeV/c^2) [12], the small two-photon decay width [32, 33] and the large branching ratio of the $\phi \to \gamma a_0$ decay [34, 35, 36], seem to be inconsistent with theoretical predictions from a conventional $q\bar{q}$ picture [37, 38, 39]. For this reason, there are many interpretations for the nature of the a_0 resonance: 1) $K\bar{K}$ molecule [40], 2) four quark state ($qq\bar{q}\bar{q}$) [41], 3) compact $qq\bar{q}\bar{q}$ state with a long $K\bar{K}$ tail, 4) dynamically generated meson-meson resonance [42]. However, there is no crucial experimental evidence to identify these candidates so far.

Concerning the baryon resonance, there is no experimental evidence for the existence of the baryons that decay into the $a_0(980)N$ channel. Furthermore, there is also no theoretical argument about such baryons[1]. Discovery of such a baryon resonance would shed light on the hadron internal structure in terms of not only baryon excitations but also the property of the $a_0(980)$ resonance. The nominal $a_0(980)p$ production-threshold is 1920 MeV/c^2. Hence, the study of the baryon resonance with the $a_0(980)p$ final state around 2 GeV/c^2 (near the production threshold) is quite promising to find new resonances because in general decay amplitudes tend to decrease rapidly as the three momentum available to the final particles increases and the wave function overlaps diminish [29].

[1]There are some papers that discuss the a_0 photoproduction near the $K\bar{K}$ threshold [42, 43]. However, s-channel baryon resonances are not taken into account.

1.3 The aim of this thesis

Objective and method

The main objective of this study is **to search for baryon resonances via the $\gamma p \to \pi^0 \eta p$ reaction around 2 GeV/c^2 and to investigate the reaction mechanism**. The experimental method for investigating the $\gamma p \to \pi^0 \eta p$ reaction is summarized as follows: (1) as an incident photon beam, the high-energy photons ($E_{\rm beam}$: 1.62-2.40 GeV) which are generated by the backward Compton-scattering (BCS) process at the LEPS/SPring-8 facility are used. (2) A 50 mm thick polyethylene (CH_2) and a 40 mm thick carbon targets are utilized. (3) In order to identify the reaction process, 4-photons from π^0 and η decay ($\pi^0 \to \gamma\gamma$ and $\eta \to \gamma\gamma$) are detected and analyzed.

An outline of this thesis

In Chapter 2, we will discuss the experimental setup in detail. At first, an overview of the Laser-Electron-Photon facility at SPring-8 (LEPS) is given. Various experimental devices, such as an electro-magnetic (EM) calorimeter and plastic scintillators, are discussed.

The LEPS backward calorimeter was utilized for the first time in this experiment. We will evaluate the performance of the calorimeter in Chapter 3. Photon-reconstruction efficiency and detector resolutions are very important in the photon calorimetry. They are evaluated using both Monte-Carlo simulation and experimental data. An clustering algorithm for obtaining correct photon-hits is also examined.

In Chapter 4, procedure of data analysis will be discussed. The final goal of the data analysis is to extract clean $\gamma p \to \pi^0 \eta p$ event samples originating from the protons in the CH_2 target. To reach this goal we will first select 4γ-event samples from all triggered events. A kinematical analysis is performed for all 4γ-event samples to select correct photon combinations. Events with large statistical significance are selected as $\pi^0\eta$-event samples. Finally, in order to limit the samples to the events originating from the exclusive $\gamma p \to \pi^0 \eta p$ reaction, a missing-mass cut will be applied. Physical meanings of all cuts applied in the data analysis are described.

The experimental result and its interpretation will be discussed in Chapter 5. Finally, we will summarize this study in Chapter 6.

Chapter 2

Experiment

2.1 The photon beam

2.1.1 The SPring-8 facility

The experiment was performed at the Laser-Electron-Photon beam line at SPring-8 (LEPS). SPring-8 is a synchrotron-radiation facility located in the West-Harima region in Japan (see Fig. 2.1). Three main accelerators of the facility (1 GeV linear accelerator, 8 GeV syncroton, and 8 GeV storage ring) are shown in Fig. 2.2. Thermal electrons generated at an electron gun are accelerated up to 1 GeV by the linear accelerator having a length of 140 m. Then, the electrons are transported to the electron synchrotron whose circumference is 396 m. The electron beam is accelerated up to 8 GeV in the synchrotron accelerator and injected to the storage ring. The circumference of the storage ring is 1436 m. Storage electrons having an energy of 8 GeV circulate in the storage ring with a repetition period of 4.79 μsec. During the

Figure 2.1: A Bird's eye view of SPring-8 in August 2001

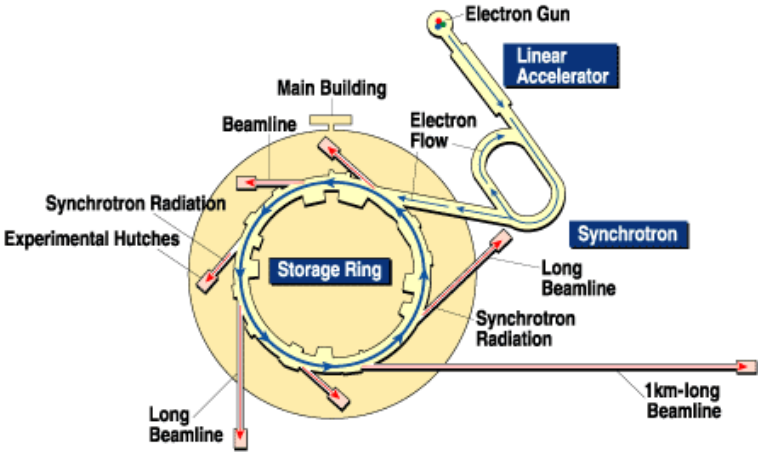

Figure 2.2: The accelerator configuration of SPring-8. The linear accelerator, the synchrotron and the storage ring are main component of the configuration.

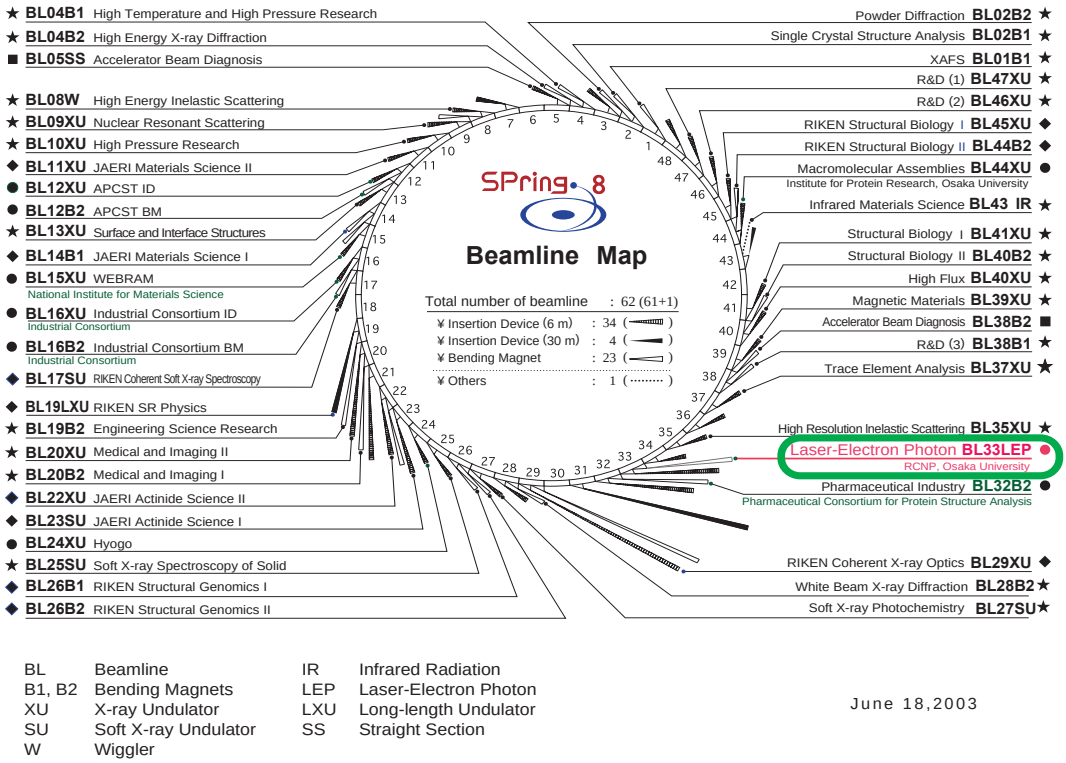

Figure 2.3: Beam line map of SPring-8.

Table 2.1: The performance of the storage ring of the SPring-8 [44].

Energy	8 GeV	Energy spread (σ_E/E)	1.01×10^{-3}
Circumference	1435.948 m	Storage current	100 mA
Radio Frequency	508.6 MHz	Number of beam lines	62
Number of bunch	23	Bunch interval	1.966 nsec
Bunch length (FWHM)	40 psec	Emittance	$\sim$7 nm·rad
Beam size (vertical)	10.1 μm	Beam size (horizontal)	378 μm
Beam divergence (V)	1.75 μrad	Beam divergence (H)	15.5 μrad

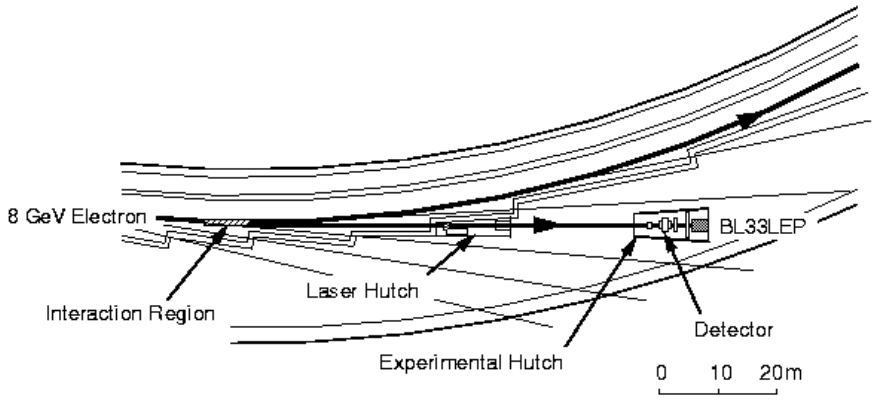

Figure 2.4: An outline of the LEPS beam line.

circulation in the storage ring, the electrons emit synchrotron radiation at bending magnets or insertion devices, such as undulator and wiggler placed at the storage ring. The synchrotron radiation is then transported to each beam lines and utilized for research on material science, life science and so on. Figure 2.3 shows a beam line map of the SPring-8. Totally 62 beam lines can be constructed at this facility and 44 beam lines are working from May 7, 2003.

The energy loss through emitting synchrotron radiation is compensated by acceleration equipment installed in four RF stations along the ring. The radio frequency (RF) of the storage ring is 508.6 MHz and the bunch interval of the storage electrons is 1.966 nsec. The structure of the beam filling (filling pattern) is decided depending on the user requirement. The maximum storage current is 100 mA and typical lifetime of the storage electrons is 20-60 hours. The beam performance of the storage ring is summarized in Table 2.1.

2.1.2 Laser-Electron-Photon beam line

The LEPS facility is a beam line for quark-nuclear physics at SPring-8. An illustration of the facility is shown in Fig. 2.4. A high-energy photon-beam produced by backward Compton scattering of laser photons off electrons in the storage ring was utilized for this experiment.

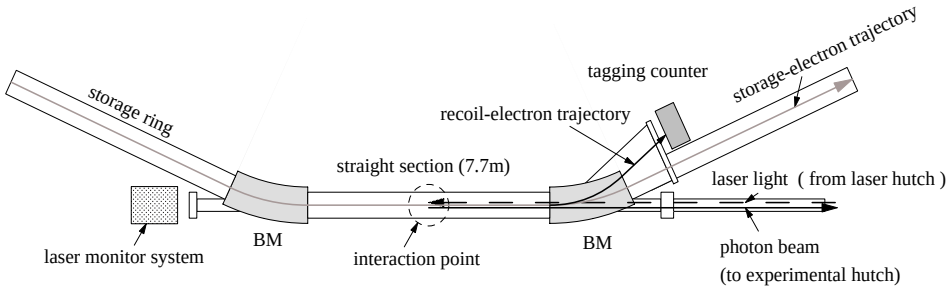

Figure 2.5: An illustration around the interaction region of the LEPS beam line.

Overview of the LEPS beam line

Figure 2.5 shows an outline of the LEPS beam-line. An ultraviolet laser ($\lambda = 333 \sim 363$ nm) generated from Ar-ion laser placed in the laser hatch is injected to the storage ring. When the laser photon collides with an storage electron circulating in the ring, the laser photon is scattered via the process of the backward Compton scattering (BCS). Since the energy difference between the laser photon ($E_L \sim 3.5$ eV) and the storage electron ($E_e = 8$ GeV) is quite large, the scattered photon gains an energy of about 5×10^7 times higher than that of the laser photon. The scattered angle of the photon beam is limited within a narrow cone ($1/\gamma_e \approx 64$ μrad) due to the Lorentz boost.

When the collision occurs, the storage electron as well as the laser photon is also scattered. The recoil electron looses its energy but the scattering angle in the laboratory frame is negligibly small. The trajectory of the recoil electron deviates from nominal trajectory the bending magnet because the momentum of the recoil electrons is relatively low comparing to the storage electrons. Therefore, the bending magnet works as a momentum analyzing magnet for recoil electrons.

Kinematics of the backward Compton Scattering

In this section we discuss the kinematics of the backward-Compton-scattering process. Figure 2.6 shows the kinematical variables in the BCS process. When a laser photon with an energy k_1 collides an electron with a high energy E_e with a relative angle $\theta_1 \simeq 180°$, the photon is scattered with a scattering angle of θ_2. If $E_e \gg k_1$, the scattered photon is directed strongly in the backward direction because of the Lorentz boost. As the result, the energy of the scattered photon (BCS photon) gains due to the Fitzgerald-Lorentz effect in the recoil process. The energy of a BCS photon E_γ is expressed as

$$E_\gamma = k_1 \frac{1 - \beta \cos\theta_1}{1 - \beta \cos\theta_2 + \frac{k_1(1-\cos\theta)}{E_e}} \tag{2.1}$$

where β is an incident electron velocity in unit of the speed of light and $\theta = \theta_2 - \theta_1$. Assuming $\gamma = E_e/m_e \gg 1$, $\beta \simeq 1$, $\theta_1 \simeq 180°$ and $\theta_2 \ll 1$, Eq. (2.1) can be rewritten as

$$E_\gamma = \frac{4E_e^2 k_1}{m_e^2 + 4E_e k_1 + \theta_2^2 \gamma^2 m_e^2}, \tag{2.2}$$

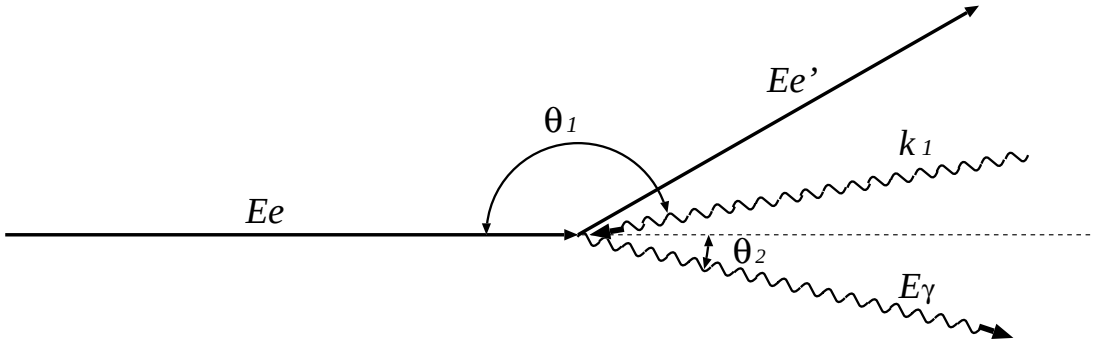

Figure 2.6: Kinematical variables in the BCS process.

where m_e is the electron mass of 0.511 MeV and $\gamma \sim 16000$ at $E_e = 8$ GeV. The maximum energy of a BCS photon (Compton edge) is obtained at $\theta_2 = 0°$:

$$E_\gamma^{\max} = \frac{4E_e^2 k_1}{m_e^2 + 4E_e k_1}. \tag{2.3}$$

The differential cross section of the BCS process can be calculated as a function of the BCS photon energy [45]:

$$\frac{d\sigma}{dE_\gamma} = \frac{2\pi r_e^2 a}{E_\gamma^{\max}}(\chi + 1 + \cos^2\alpha) \tag{2.4a}$$

$$a = \frac{m_e^2}{m_e^2 + 4E_e k_1} \tag{2.4b}$$

$$\chi = \frac{\rho^2(1-a)^2}{1-\rho(1-a)} \tag{2.4c}$$

$$\cos\alpha = \frac{1-\rho(1+a)}{1-\rho(1-a)} \tag{2.4d}$$

$$\rho = \frac{E_\gamma}{E_\gamma^{\max}} \tag{2.4e}$$

where $\gamma_e = 2.818$ fm is the classical electron radius. Figure 2.7 shows the differential cross sections for the BCS process between 8 GeV incident electrons and laser photons with different wave lengths (275, 351 and 488 nm). As one can see from the figure, photons with the sub-GeV energy can be efficiently obtained by the BCS process.

Laser system

The laser system is one of the main apparatus of the LEPS beam-line. The Ar-ion laser having dual Brewster-window produced by Coherent company is utilized as a incident laser at LEPS beam-line. By using a half mirror having a specific curvature radius, called output coupler, one can select the wave length of the laser light to the UV region (333.6 - 363.8 nm). Figure 2.8 shows typical wave-length distribution. The diameter of the laser beam is 1.7 mm at output window and its divergence is 0.31 mrad.

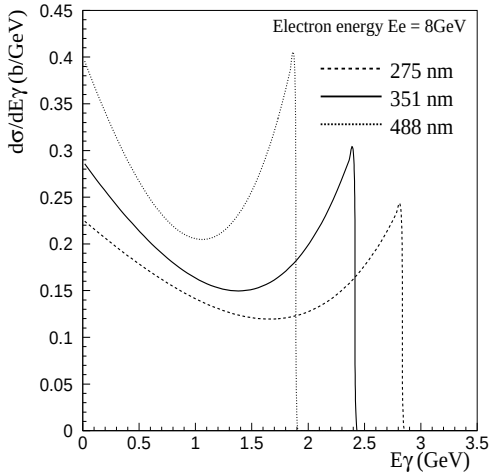

Figure 2.7: Differential cross section of the BCS.

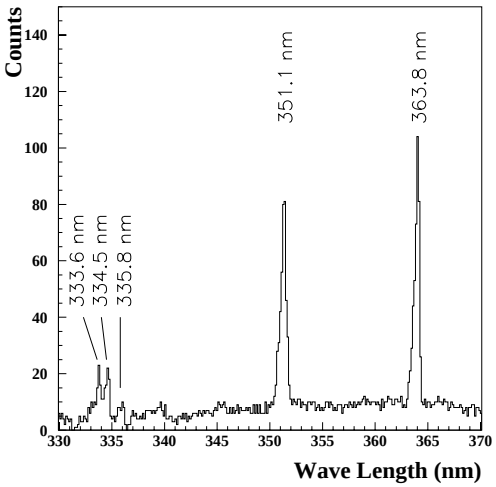

Figure 2.8: Typical laser intensity.

Tagging system

The energy E_γ of the BCS photon beam is determined by the recoil electron energy $E_{e'}$ as

$$E_\gamma = E_e - E_{e'}. \tag{2.5}$$

The energy of the 8-GeV circuiting electron E_e was determined as 7.975 $\pm$ 0.003 GeV. The energy $E_{e'}$ is measured by a tagging system located in the storage ring. Since the scattered electrons due to the BCS process loose its energy, it is relatively strongly bent and deviates from the central orbit in the 8-GeV ring when it passes through the bending magnet placed at the end of the straight section. In order to detect the recoil electrons, the tagging system installed at the exit of the bending magnet was utilized.

Figure 2.11 shows the structure of the tagging system. The tagging system is placed at the outside of a beam vacuum pipe for the 8 GeV electron beam. The tagging system covers a region 4.5 - 6.5 GeV in the energy of recoil electrons. This energy region corresponds to the energy of the BCS photons 1.5 - 3.5 GeV. The lower limit of 1.5 GeV is due to the fact that the tagging system can't be positioned closer to the central orbit of the 8 GeV electrons. The tagging system consists of plastic scintillator (PL) hodoscopes and silicon strip detectors (SSD's) as shown in Fig. 2.11. There are two layers of the combination of the PL hodoscope and the SSD. Each PL hodoscope layer consists of 10 plastic scintillation counters. The size of the plastic scintillator is 10.0 mm high, 8.6 mm wide, and 5.0 mm thick. The plastic scintillators are stacked with an overlap of 2.2 mm as illustrated in Fig. 2.11. The PMT (HAMAMATSU R1635P) with a 3/8 inch diameter is coupled to the plastic scintillator through a light guide. The size of the SSD is 10.0 mm high, 51.2 mm wide, and 0.5 mm thick. The strip pitch is 0.1 mm. There are 512 strips in total.

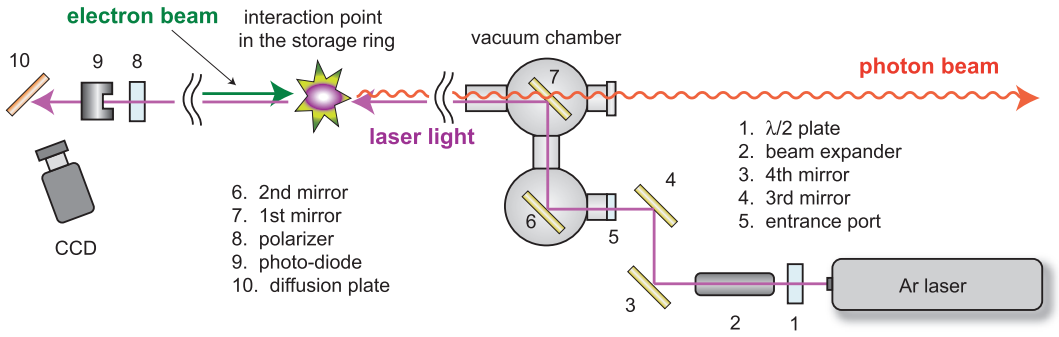

Figure 2.9: An outline of the laser optics at the LEPS beam-line.

Table 2.2: Specifications of elements used in the LEPS laser system.

	Manufacture name (company)	Material	Size (mm)
Ar laser	Coherent Innova Sabre (Coherent)	-	-
$\lambda/2$ plate	for 351 nm (SURUGA)	Quartz	17×17×2t
Beam expander	(SURUGA)		
entrance port	(MDC)	(SUPRASIL1)	ICF114
4th mirror	optical mirror (OPTO·LINE)	Quartz	$80\phi \times 12$t
3rd mirror	optical mirror (OPTO·LINE)	Quartz	$80\phi \times 12$t
2nd mirror	optical mirror (FUJITOKU)	Si (Aluminum)	$100\phi \times 19$t
1st mirror	optical mirror (FUJITOKU)	Si (Aluminum)	$100\phi \times 6$t
Glan-laser prism	PGL8310 (OptMax)	α-BBO	$10\phi \times 26$t
Photo diode	S1406-05(HAMAMATSU)	-	-

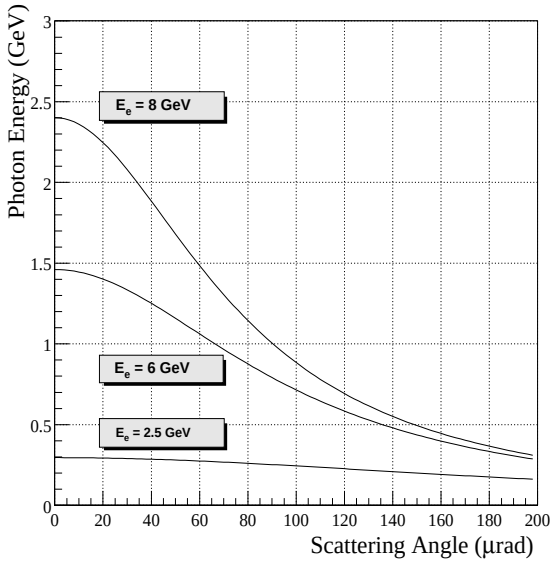

Figure 2.10: Photon energy as a function of scattering angle.

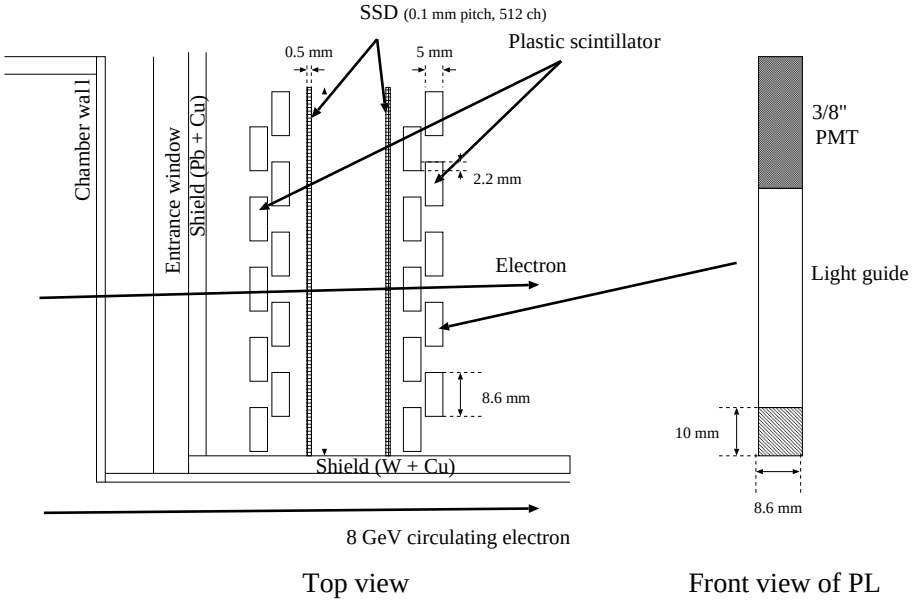

Figure 2.11: Electron tagging system.

2.2 Experimental devices

2.2.1 Lead scintillating fiber calorimeter (Lead/SCIFI)

Lead/SCIFI detectors have been used as electro-magnetic calorimeters at many high-energy physics facilities in the world [46, 47]. In comparison with other homogeneous devices, this sampling-type device has some advantages and disadvantages. An advantage is that the signal is generally fast because the active material is plastic scintillator. It can be designed for a relatively low price. A disadvantage is the worse energy resolution due to sampling fluctuations.

Our backward calorimeter consists of 252 modules of Lead/SCIFI, covering angular region from 30° to 100° for polar angle, and from 0° to 360° for azimuthal angle. It corresponds to solid angle of 2.08π(sr). A matrix of scintillating fibers (Pol.Hi.Tech.0042) is embedded in a lead alloy (Pb:94%, Sb:6%) that serves as a radiator. The diameter of the scintillating fibers is 1 mm and are aligned parallel to each other. The refractive index of core (clad) region of the fiber is 1.590 (1.492). Figure 2.12 shows one such Lead/SCIFI block. The construction parameters for the Lead/SCIFI modules are summarized in the Table 2.3. An acrylic light guide is used to collect the scintillation light and guide it to the photo-cathode. The optimal shape and length of the light guide ($L_{\text{guide}} = 27$ cm) were determined using a ray-tracing simulation[48]. Light-transmission coefficient from the entrance of the light guide to the photo-tube window (T_{guide}) is also described in Table 2.3. The T_{guide} is determined by the ratio of between the area of entrance surface of the light guide and the area of the PMT face. The length of one module is 220 mm which corresponds to 13.7 radiation lengths. A 2-inch photo-multiplier tube (H7195) produced by HAMAMATSU is attached

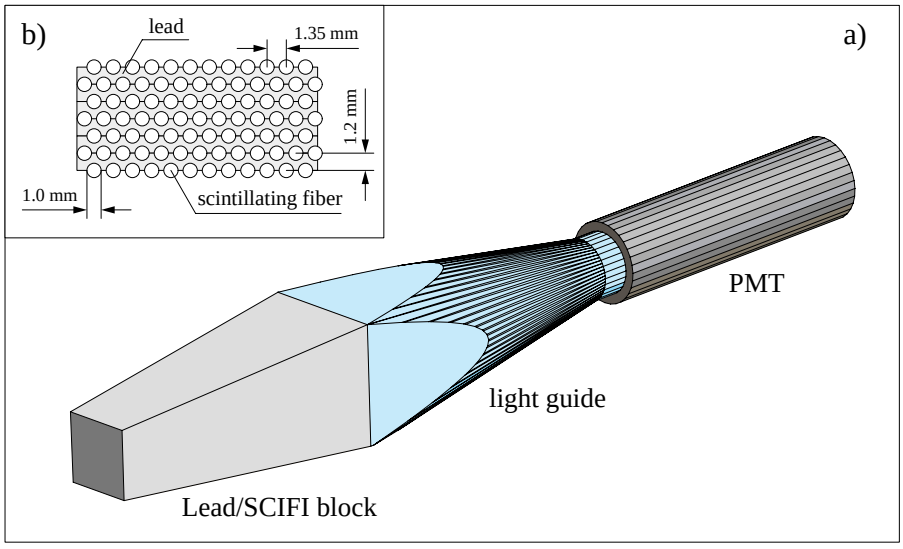

Figure 2.12: (a) A Lead/SCIFI module, consisting of three parts: a Lead/SCIFI block, a conically shaped acrylic light guide, and photo-multiplier tube, with lengths of 220 mm, 270 mm, and 215 mm, respectively. (b) An enlarged illustration of the front face of a Lead/SCIFI module.

Table 2.3: Lead/SCIFI construction parameters

TYPE	B-3	B-4	B-5	B-6
θ coverage	30°∼40°	40°∼50°	50°∼60°	60°∼70°
$N_{\rm modules}$	36	36	36	36
Volume(cm^3)	704.47	870.17	1010.01	1119.39
Weight(kg)	3.23	3.99	4.63	5.13
PMT Type	H3178-61	H7195	H7195	H7195
PMT Size(inch)	$1\frac{1}{2}$	2	2	2
$T_{\rm guide}$	0.578	0.749	0.702	0.665

TYPE	B-7	B-8	B-9
θ coverage	70°∼80°	80°∼90°	90°∼100°
$N_{\rm modules}$	36	36	36
Volume(cm^3)	1194.56	1232.82	1232.82
Weight(kg)	5.47	5.65	5.65
PMT Type	H7195	H7195	H7195
PMT Size(inch)	2	2	2
$T_{\rm guide}$	0.640	0.628	0.628

to one end of the light guide with Bicron BC600 optical cement. For the most forward 36 modules, 1.5-inch H3178 photo-tubes were used because of a geometrical reason. The angular interval between 2 adjacent modules is 10° in both the azimuthal and the polar direction.

2.2.2 Charged-particle veto-counter (CV)

To identify the charged particles originated from the target, 12 sets of 5 mm thick plastic scintillators which are made of polyvinyltoluene base BC-408 produced by Saint-Gobain was used (CV). The CV counters are depicted schematically in Fig. 2.14. The scintillators were wrapped with 15 μm-thick aluminum foil. An acrylic light guide having a length of 136 mm was attached to the one end of the scintillator. The HAMAMATSU photo-tube H7195 was used to count scintillation photons proportional to the deposited energy of charged particles. Each counters were placed around the beam axis. By using CV counters charged particles, emitted in the angular region from 24° to 108° for polar angle and from 0° to 360° for azimuthal angle, are identified.

2.2.3 Forward lead-glass counter (LG)

For forward photon rejection, a detector assembly consists of 8 lead-glass (SF-6) blocks of a 3 × 3 matrix was utilized (see Fig. 2.15). These blocks had been originally used by the E135 collaboration at KEK [49, 50, 51]. Each block having a cross section of 75 × 75 mm^2 and a length of 235 mm ($13.1X_0$) was placed downstream the target.

Prior to the experiment, an measurement for energy calibration of the LG was performed. Each blocks was placed on the beam axis one by one. The LEP beam was injected onto the center of the front

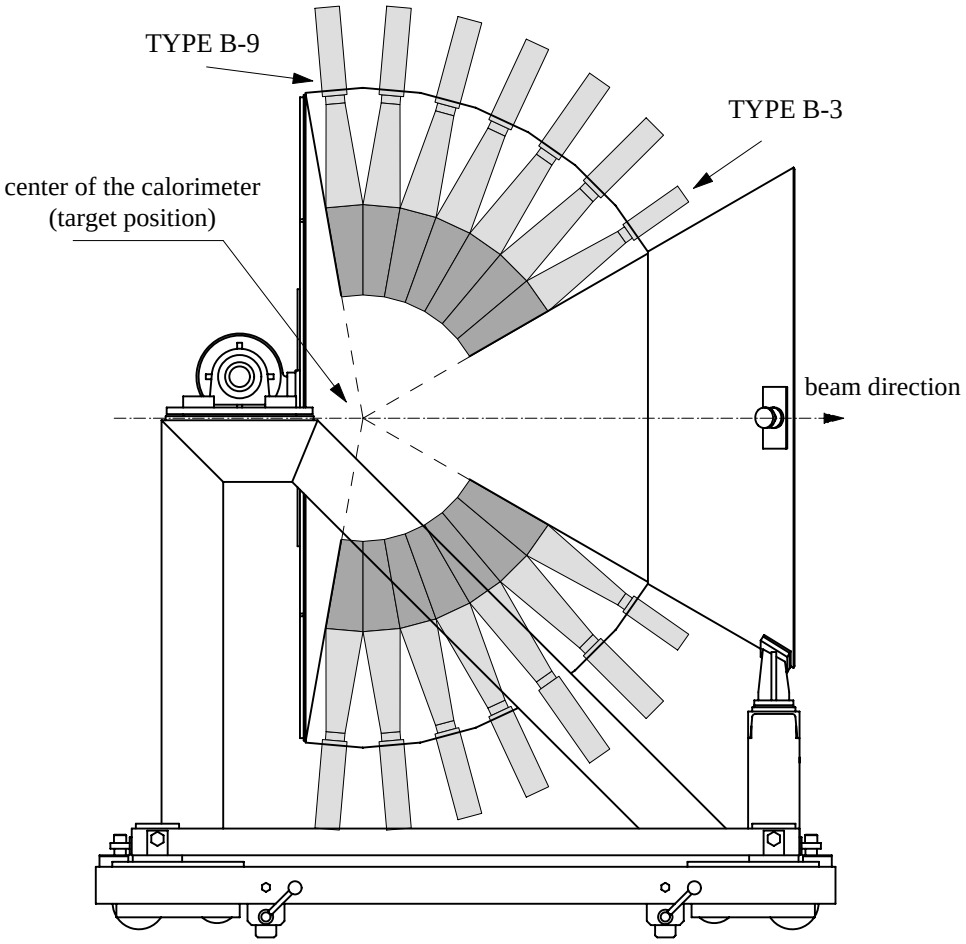

Figure 2.13: Side view of the backward calorimeter.

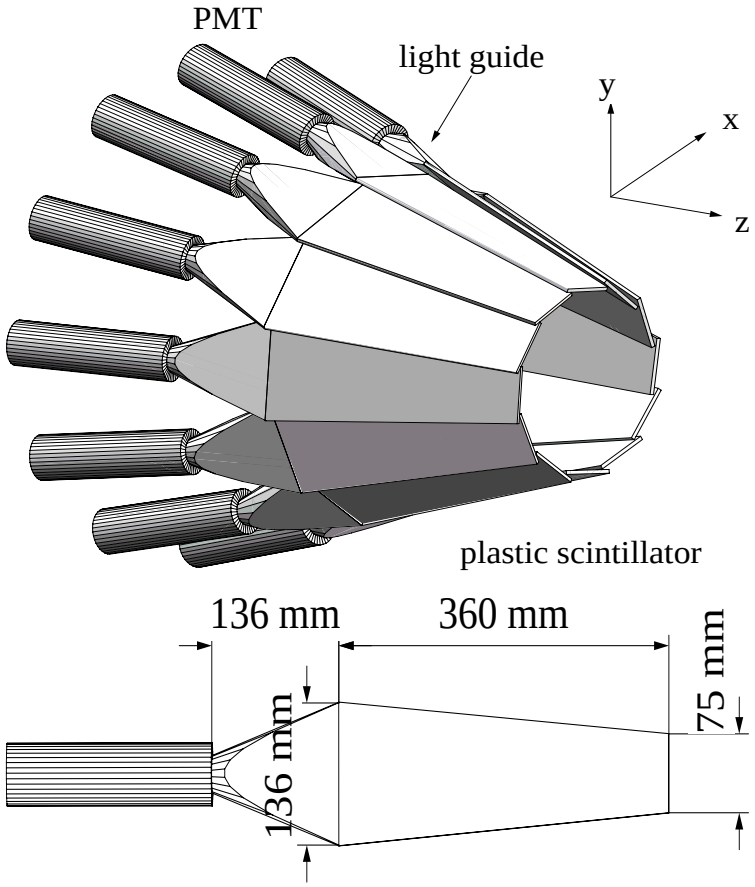

Figure 2.14: Schematic view of the Charged-particle veto-counter (CV). Polar angles between 24° to 108°, and azimuthal angles from 0° to 360° are covered.

surface. Signals from the TAG#6 scintillator was required as a trigger. Figure 2.16 shows the photon-energy distribution for LG#0 block after the calibration. Since the TAG#6 covers energy region of 2.34 GeV$< E_\gamma <$2.40 GeV, the energy spread was convoluted in the width of the observed distribution ($\sigma_{\rm obs}$). The beam-energy spread ($\sigma_{\rm beam}$) was estimated as 34.6 MeV by assuming that the energy distributes was flat in the above energy region. Therefore the energy resolution of a LG block ($\sigma_{\rm LG}$) was obtained as

$$\sigma_{\rm LG} \quad = \quad \sqrt{\sigma^2_{\rm obs} - \sigma^2_{\rm beam}}. \tag{2.6}$$

The result is summarized in the Table 2.4.

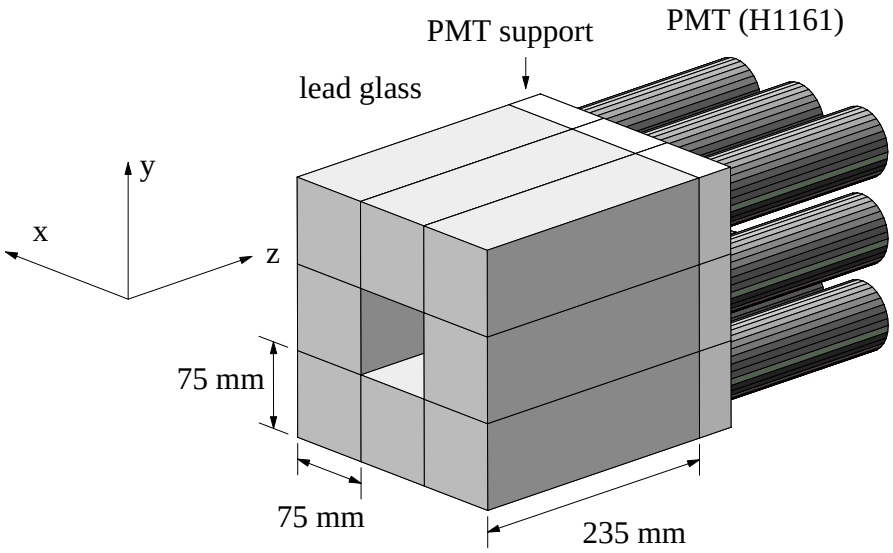

Figure 2.15: Schematic view of the forward lead-glass counter.

Table 2.4: $\sigma_{\rm obs}$: observed width for the energy distribution. $\sigma_{\rm LG}$: energy resolution of the LG block for the photon energy of 2.37 GeV.

LG	$\sigma_{\rm obs}$ (MeV)	$\sigma_{\rm LG}$ (MeV)
#0	161.6	157.8
#1	162.2	158.5
#2	136.7	132.2
#3	142.6	138.3
#4	142.6	138.3
#5	159.5	155.7
#6	150.8	146.8
#7	136.2	131.7

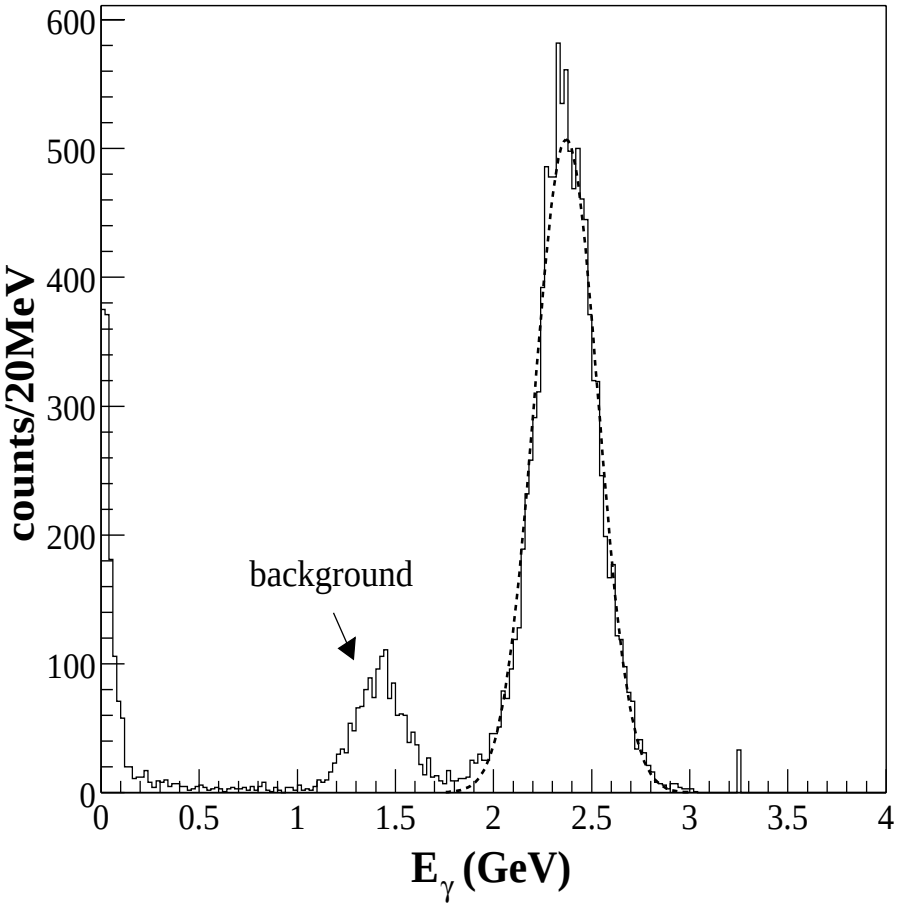

Figure 2.16: Energy spectrum of the photons tagged by TAG#6 (2.34 GeV $< E_\gamma <$ 2.40 GeV), measuring by LG#0.

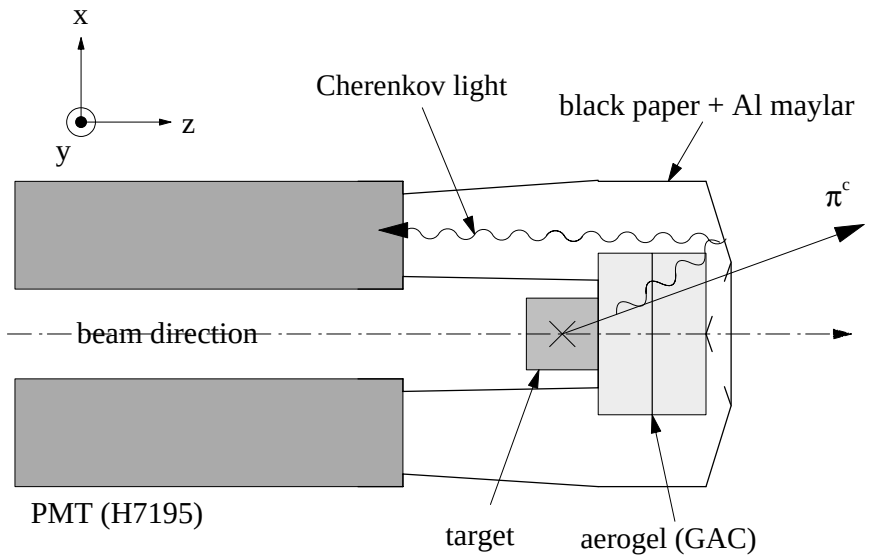

Figure 2.17: An illustration of the AC counter.

2.2.4 Aerogel Cherenkov counter (AC)

An aerogel counter (AC) were prepared for identification of the protons from electrons and charged pions. As a Cherenkov radiator, two layer of silica aerogel with refractive index of 1.05 were used. The total length of the aerogels were about 60 mm (see Table 2.5). Figure 2.17 shows an illustration of the AC counter. Four PMTs (HAMAMATSU H7195) were utilized for detecting Cherenkov light (two of them are not shown in Fig. 2.17). The relation between Cherenkov angle and particle momentum for the AC counter is drawn in Fig. 2.18.

Table 2.5: Properties of silica aerogel.

Aerogel	diameter (mm)	thickness (mm)	index
#0	90.00	28.45	1.0500
#1	90.00	28.95	1.0493

2.3 Experimental setup

The experimental setup is shown in Fig. 2.19. A nuclear target was placed at the center of the calorimeter. For charged-particle rejection, 5-mm thick plastic scintillators (UVeto) were placed upstream of the target. Furthermore, an active collimator (ATC) which consists of 8 lead-glass blocks were placed in order to reject low energy photons which come from upstream of the target. To identify the charged particles

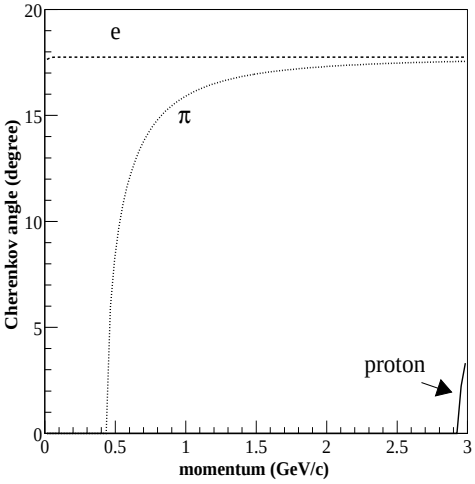

Figure 2.18: Cherenkov angle for different charged particles. The refractive index of AC is 1.05.

originated from the target, 12 sets of 5-mm thick plastic scintillators were used.

An aerogel Cherenkov counter (AC) with a refractive index of 1.05 and forward plastic scintillators (PC) were installed for $\pi^{\pm}$ and recoil-proton identification. A detector assembly of 8 lead-glass blocks forming a 3×3 matrix (LG) was placed downstream of the calorimeter. The AC, PC and LG counters were used only for checking properties of background processes.

2.3.1 Targets

CH_2(50 mm), C(40 mm) and Cu(3 mm) were used as targets. In this study, Carbon and CH_2 targets were analyzed for extracting proton target contribution. The size of these targets are listed in Table 2.6.

Table 2.6: The nuclear targets used for the experiment.

Target	diameter	thickness	density
CH_2	40.0 mmϕ	50.0 mm (0.330 mol/cm^2)	0.923 g/cm^3
C	40.0 mmϕ	40.0 mm (0.577 mol/cm^2)	1.73 g/cm^3
Cu	40.0 mmϕ	0.5 mm × 6 (0.042 mol/cm^2)	8.96 g/cm^3

2.4 Trigger condition

As a trigger for the LEPS data acquisition system [52], an OR signals from the Lead/SCIFI modules was required in coincidence with a signal from the tagging scintillators. To reject events initiated by contaminant particles in the incoming beam, the UVeto counter and an OR signals from the ATC detectors

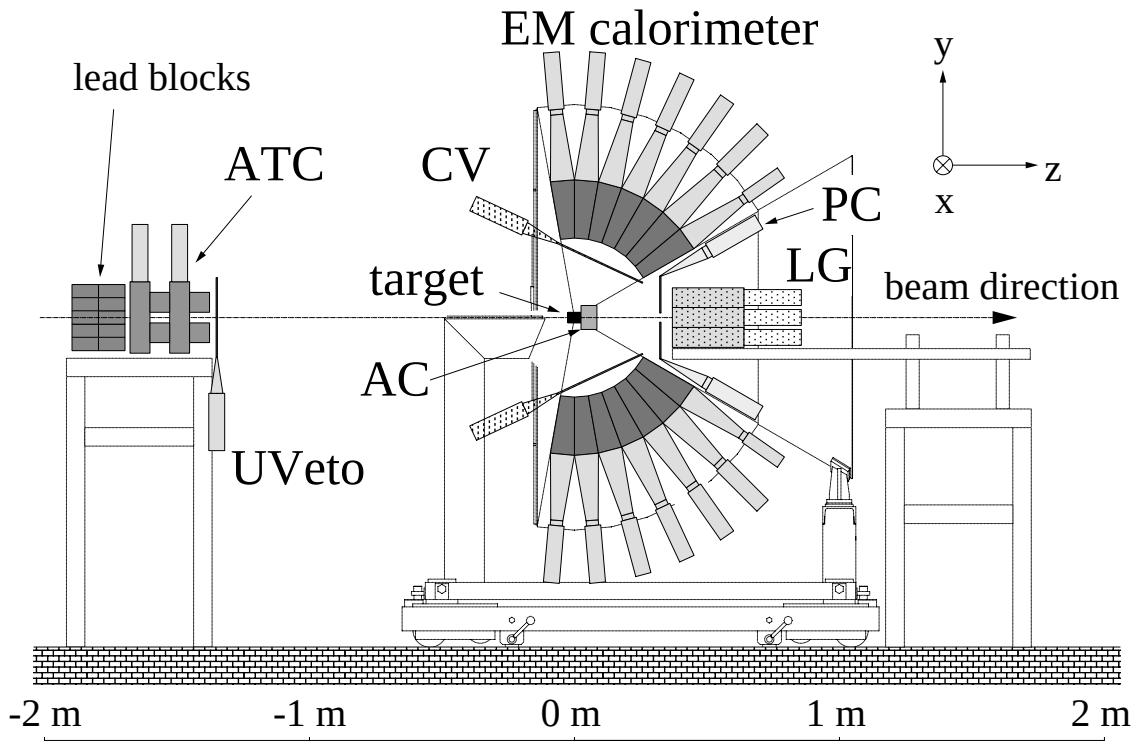

Figure 2.19: Setup for the present experiment. A tagged photon beam generated at 70 m upstream from the target is injected on to a nuclear target. A veto counter upstream from the target suppresses the triggers due to charged particle contamination in the incoming beam.

were employed as a veto.

- TAG : an AND signals of an OR signals from upstream tagging scintillators and an OR signals from downstream tagging scintillators.
- GAMMA : an OR signals from the backward calorimeter (except for TYPE B-3 and TYPE B-9 modules).
- UVeto : signals from the upstream veto scintillator.
- ATC : an OR signals from active collimator (8-blocks of lead glass counters).

By using these expressions, the trigger condition for the experiment was defined as

$$\text{TAG} \otimes \text{GAMMA} \otimes (\overline{\text{UVeto} \oplus \text{ATC}}).$$

The average trigger rate was 180 Hz for CH_2, 240 Hz for C, 160 Hz for Cu, and 120 Hz for W. The average dead time for each target was less than 18%.

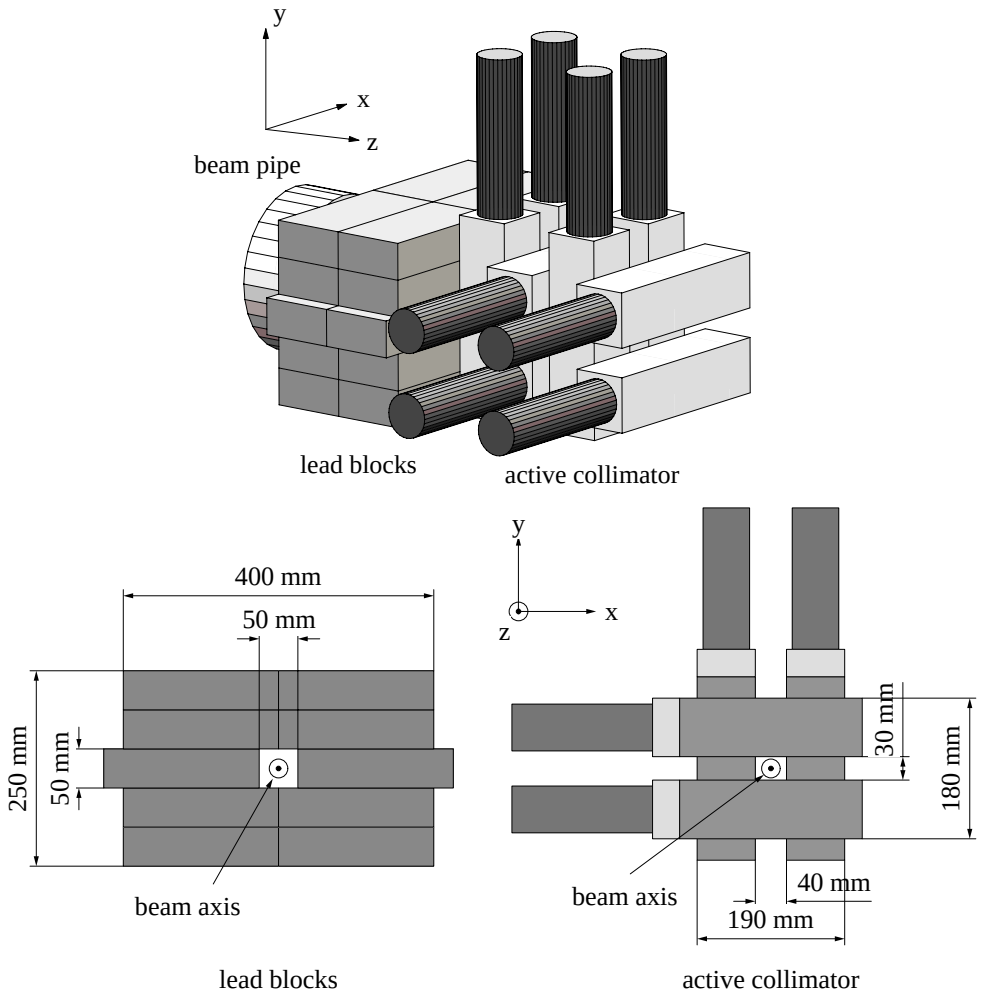

Figure 2.20: Schematic drawing of the ATC counters.

2.5 Energy calibration

Prior to the experiment, we measured the cosmic rays. Cosmic muon peaks measured by some typical Lead/SCIFI modules were utilized to optimize the high voltage value applied for the photomultipliers. (see Fig. 2.21). According to the GEANT3 Monte-Carlo simulation, the average energy deposit caused by passing cosmic muon is about 12 MeV and this energy deposit corresponds to the case of 200 MeV incident photon. High voltage values were set so that the dynamic range of ADC corresponds to 2 GeV incident photons.

A relative calibration of modules was performed assuming azimuthal symmetry around the beam axis. Exponential functions were fitted to all raw ADC spectra (see Fig. 2.22). This results in a relative calibration for all modules with same θ. Afterwards, the relative calibration with respect to the θ direction

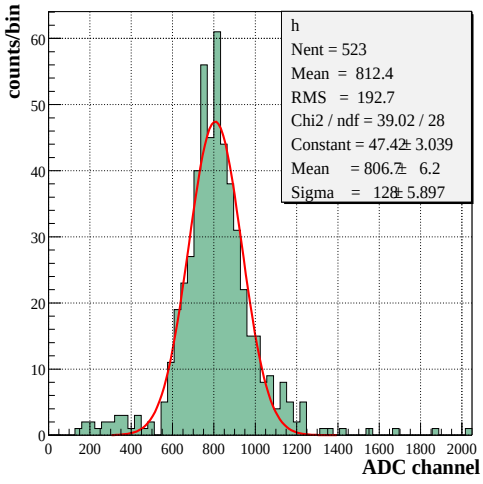

Figure 2.21: The cosmic muon signal detected by a Lead/SCIFI module. The average energy deposit of penetrating cosmic muon is about 12MeV.

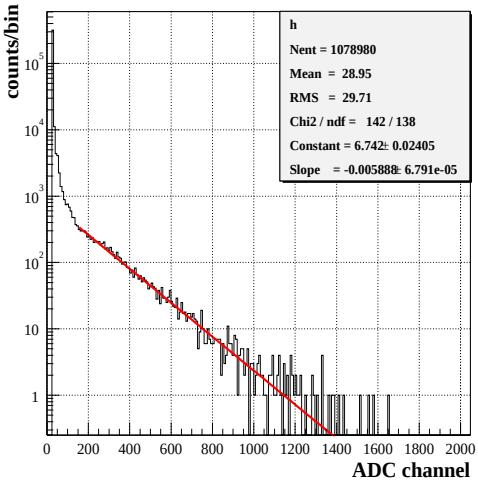

Figure 2.22: Typical raw ADC distribution with CH_2 target. The slope values of the exponential functions are used for relative energy calibration.

was done using the π^0 peak reconstructed from 2- cluster events in the same θ row, where the clustering algorithm will be discussed in Section 3.3 in detail. The reconstructed peak for different rows were then scaled to each other. The energy of the cluster is taken to be the energy deposited in the central module of the cluster.

For absolute energy calibration, the same procedure was repeated, but in this case with summed energy of the clusters. Absolute energy calibration was performed to the well-known π^0 mass in the reconstructed 2γ spectrum.

Figure 2.23 shows the reconstructed 2γ invariant mass distribution after the energy calibration. To obtain this plot, a center of gravity method was introduced to obtain better localization of the γ clusters (see Section 3.5.2). In Fig. 2.23, one can see a calibrated π^0 peak and a pronounced η bump around 0.55 GeV. The reconstructed π^0 mass resolution was 19 MeV and the corresponding relative resolution was 14%. The reconstructed η mass was within error-bars equal to the value listed in the PDG database. This shows that the energy calibration, performed using the π^0 events, works well for higher invariant masses. Therefore, we concluded that the energy calibration method was successful.

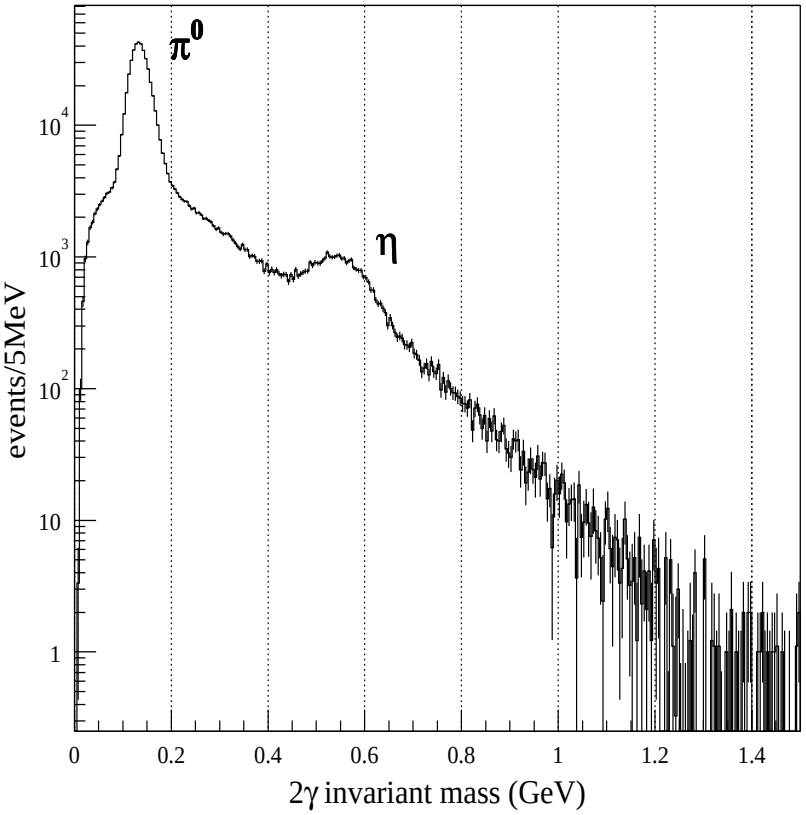

Figure 2.23: Reconstructed invariant 2γ mass distribution with a CH_2 target after the energy calibration. The subtraction of the empty-target contribution, which affects mainly the low mass region bellow π^0 mass, are already performed.

2.6 Data summary

The experiment was performed from November, 2001 to January, 2002. The experimental run was about 20 days in total. Filling patterns of the storage ring was changed three times during the beam time. This condition is summarized in Table 2.7.

Table 2.7: The term of the beam time and filling patterns

Beam time	Run number	Filling pattern
2001/11/29 ∼ 2001/12/ 5	23012 ∼ 23147	11 bunch train × 29
2001/12/ 6 ∼ 2001/12/ 8	23148 ∼ 23195	11 bunch train × 29
2001/12/ 8 ∼ 2001/12/11	23196 ∼ 23277	1 bunch(1.5 mA) + multi bunch
2002/ 1/20 ∼ 2002/ 1/28	23315 ∼ 23496	203 bunches - 4bunches × 7

The scaler information was recorded during the data taking. It includes, for example, the number of signals from trigger, tagging scintillator, clock pulse and so on. The summary of the total counts of these signals for all the analyzed data is listed in Table 2.8.

Table 2.8: Data summary for each targets. These values are calculated with scaler data. $T_{\rm real}$ and $T_{\rm live}$: real and accutual counting time, $\overline{R_{\rm trig}}$ and $\overline{R_{\rm tag}}$: averaged trigger and tagger rate, $\Sigma_{\rm trig}$ and $\Sigma_{\rm tag}$: accumulated trigger and tagger counts, $\Sigma_{\rm n\gamma}$: the number of photon beam estimated from $\Sigma_{\rm tag}$ (see LEPS technical note No.15 in detail).

Target	Carbon			CH_2		
polarization	Vert.	Hori.	total	Vert.	Hori.	total
$T_{\rm real}$ (h)	36.6	46.5	83.1	30.5	34.7	65.2
$T_{\rm live}$ (h)	29.4	38.8	68.1	25.2	29.8	55.0
live time	80.3%	83.4%	81.9%	82.9%	85.8%	84.3%
$\overline{R_{\rm trig}}$ (cps)	283	226	251	234	190	210
$\overline{R_{\rm tag}}$ (kcps)	582	476	522	613	512	559
$\Sigma_{\rm trig}$	2.99×10^7	3.16×10^7	6.16×10^7	2.13×10^7	2.03×10^7	4.16×10^7
$\Sigma_{\rm tag}$	7.68×10^{10}	7.96×10^{10}	1.56×10^{11}	6.73×10^{10}	6.39×10^{10}	1.31×10^{11}
$\Sigma_{\rm n\gamma}$	6.33×10^{10}	6.75×10^{10}	1.31×10^{11}	5.84×10^{10}	5.65×10^{10}	1.15×10^{11}

Target	Copper			Empty		
polarization	Vert.	Hori.	total	Vert.	Hori.	total
$T_{\rm real}$ (h)	49.4	68.3	117.8	36.1	44.7	80.7
$T_{\rm live}$ (h)	42.8	60.8	103.4	33.8	42.4	76.1
live time	86.6%	89.0%	87.8%	93.7%	94.9%	94.3%
$\overline{R_{\rm trig}}$ (cps)	179	142	157	72.0	56.5	63.4
$\overline{R_{\rm tag}}$ (kcps)	554	450	493	576	462	513
$\Sigma_{\rm trig}$	2.75×10^7	3.10×10^7	5.86×10^7	8.76×10^6	8.63×10^6	1.74×10^7
$\Sigma_{\rm tag}$	9.85×10^{10}	1.11×10^{11}	2.09×10^{11}	7.48×10^{10}	7.44×10^{10}	1.49×10^{11}
$\Sigma_{\rm n\gamma}$	8.83×10^{10}	1.01×10^{11}	1.89×10^{11}	7.30×10^{10}	7.24×10^{10}	1.45×10^{11}

Chapter 3

Performance of the backward calorimeter

The backward calorimeter of the LEPS facility was utilized for the first time in this experiment. Therefore, detailed studies of its performance were carried out. This will be discussed in this chapter.

3.1 Development of the Monte-Carlo simulation code

To evaluate the response of the calorimeter, a simulation code which took into account all the details of the experimental setup was developed using the Geant4 package [53, 54]. The geometry described in the code is shown in Fig. 3.1. It contains the backward calorimeter (BG) and its support structure, the charged-particle veto-counters (CV) and proton counters (PC).

As discussed in Section 2.2.1, the Lead/SCIFI module has a fine structure consisting of scintillating fibers (SCIFI), lead-alloy radiator (PB) and optical cement (GLUE). Therefore, shower particles generated in a module cross the borders of various materials many times. In Geant4, the tracking of particles is done in finite step size. Each step has to be set sufficiently small, compared to the distance between various boundaries to ensure proper energy-loss calculation. As a consequence, much computing time is needed in order to obtain the correct energy loss in the Lead/SCIFI modules. To save the computing time, two independent codes are employed, depending on the purpose of a particular calculation.

- CODE 1: A most realistic code. The geometry of Lead/SCIFI modules is defined in full detail including scintillating fibers, lead alloy and optical cement. The maximum step length and the cut-off range is set to 0.01 mm and 0.05 mm respectively. The calculation time is quite long[1] due to short step lengths. This code is employed to estimate efficiencies and resolutions which require an accurate simulation.

- CODE 2: An approximate code. The Lead/SCIFI material is regarded as a homogeneous material consisting of a mixture of the relevant materials. The calculation time is 12 times faster than that

[1]The calculation time for 10^4 events for a 1 GeV photon is about 2 days.

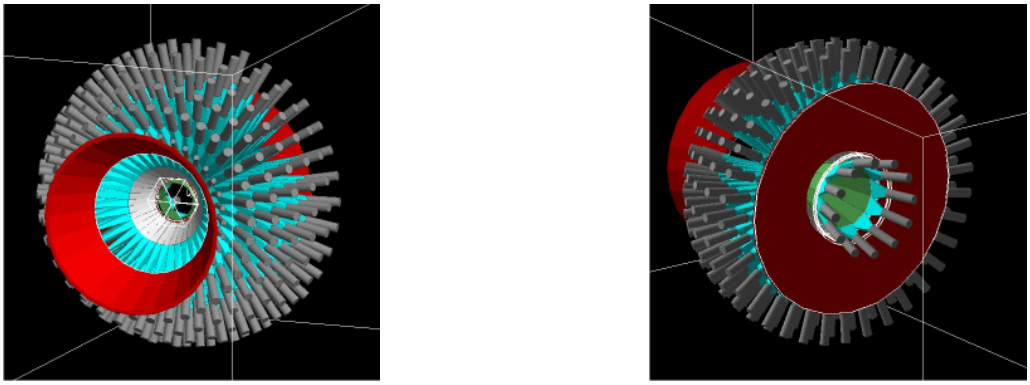

Figure 3.1: Detector components described in the simulation code.

of CODE 1. This code is used for the acceptance calculations for which many events have to be generated.

The validity of CODE 2 was evaluated by comparing its response with one obtained from CODE 1. It will be discussed in Appendix B. In the remaining part of this chapter, the results of all the Monte-Carlo calculations performed using CODE 1 are discussed.

3.2 Detector response

The detector response of a single module to an isolated photon will be discussed in this section.

A Lead/SCIFI module consists of fibers, radiator material and optical cement but scintillation photons are emitted only from the fiber region. The number of scintillation photons is proportional to the energy deposit in this active region. Therefore, the energy deposit in the fiber region is a measure for the readout from the ADCs in the real setup. Figure 3.2(a) and 3.2(b) show the energy deposit in the active region of the fibers and the full module, respectively. The peak shape in Fig, 3.2(a) has a nearly Gaussian distribution; The shape in Fig. 3.2(b) has a low-energy tail. This tail is due to the leakage of electromagnetic shower to the out side of the module. Figure 3.3 shows the plot of the deposited energy in the fiber region versus the incident-photon energy (E_γ). The deposited energy has a good linearity with E_γ. The ratio between the peak of the energy deposit in the fiber region and E_γ is 10.6 $\pm$ 0.1%.

Figure 3.2(c) shows the sampling ratio, defined as the ratio of the deposited energy in the active region to the total energy deposit in a module. The width of the sampling ratio depends on E_γ. It falls off with $1/\sqrt{E_\gamma}$ (see Fig. 3.4 and Fig. 3.5). This dependence is due to the fact that the sampling fluctuation (the variation of the number of shower particles in the active region) is governed by Poisson statistics. The average sampling ratio is about 12% and it is independent of the photon energy.

Figure 3.6 shows the energy deposit in the fiber region for different angle of incidence of photons ($\theta_\gamma = 55^o, 56^o, 57^o$) for $E_\gamma = 500$ MeV. The angle of $\theta_\gamma = 55^o$ corresponds to parallel incidence to the fiber axis of TYPE B-5 modules (see Fig. 3.7). As shown in Fig. 3.6, in the case of $\theta_\gamma = 55^o$, a broader

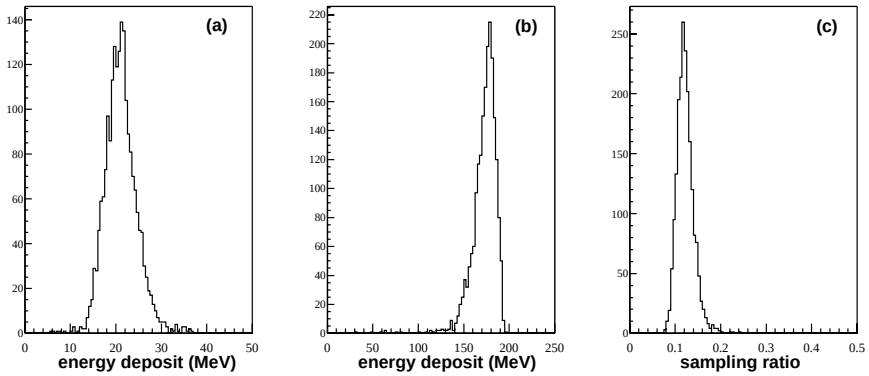

Figure 3.2: Responses of a TYPE B-5 module where the photons (E_γ = 200 MeV) are injected to near the center of the detector face ($\theta_\gamma = 56^o$). (a) The distribution of energy deposit in fiber region. (b) The distribution of energy deposit in a module (c) The distribution of the sampling ratio.

distribution is obtained compared to the case where the incidence angle of photons is slightly off the fiber axis. Furthermore, for parallel incidence, some photons escape from the detector (no energy deposit) as indicated by "undetected events" in Fig. 3.6. This means that both the energy resolution and the detection efficiency are worse for photons injected directly on a fiber along the fiber axis. The reason is that the shower development is incomplete in this case since the probability of shower generation in the fiber region is reduced. As a consequence, the energy leakage to the rear of the module increases. The effect is seen only if the incident angle is within 0.5^o with respect to the fiber axis.

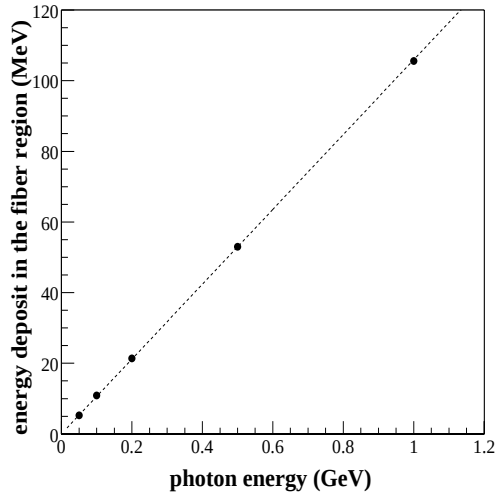

Figure 3.3: Deposited energy in the fiber region as a function of the photon energy. The dotted line corresponds to the first-order polynomial-function fitted to the plot.

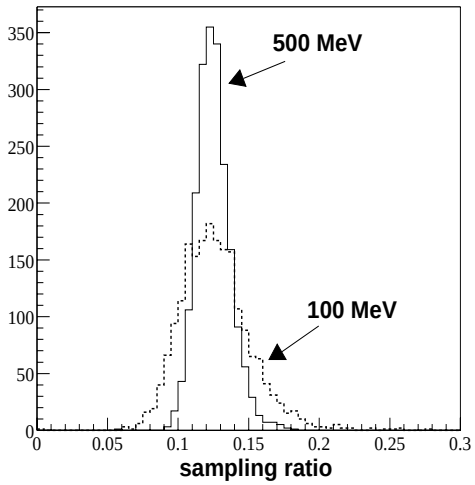

Figure 3.4: Distributions of sampling ratio for 100 MeV photons (dashed line) and for 500 MeV photons (solid line).

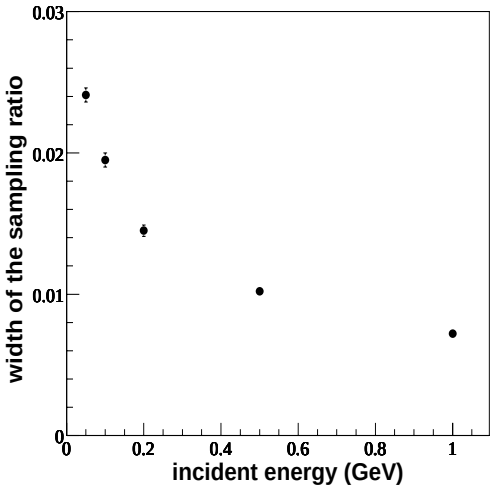

Figure 3.5: Energy dependence of the width of the sampling ratio.

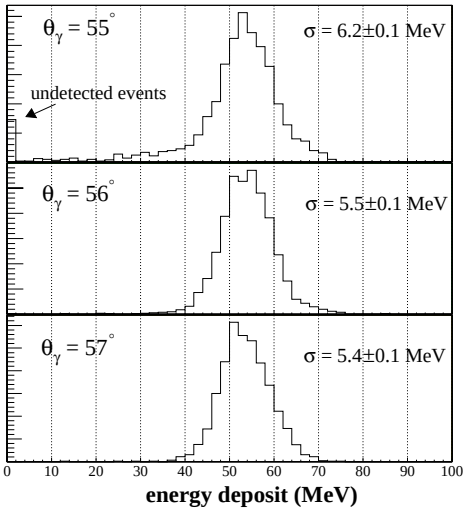

Figure 3.6: Distributions of energy deposit in fiber region of a TYPE B-5 module for each incident angle ($\theta_\gamma = 55^o, 56^o, 57^o$)

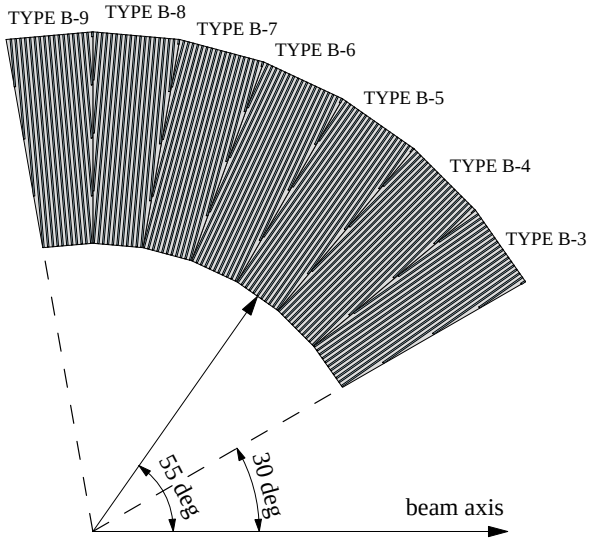

Figure 3.7: Schematic geometry of the Lead/SCIFI modules and scintillating fibers. The line corresponding to the incident angle of $\theta_\gamma = 55^o$ is drawn. Note that the size of the scintillating fibers is not correctly scaled.

3.3 Performance of the photon reconstruction

3.3.1 Clustering algorithm

To obtain the correct hit patterns, a special clustering algorithm has been developed on the basis of strategy described below.

1. At first, the modules whose signals exceed a certain threshold (E_{th}) are selected. The sensitivity of the clustering algorithm varies with this E_{th}. Reducing the threshold makes it more sensitive, but it also increases the probability of making false clusters (cluster splitting).

2. Then the algorithm combines all modules with $E < E_{th}$ adjacent to the ones selected in (I). Each set is then regarded as one cluster. If there are shared modules in the peripheral region of a cluster, the deposited energy of such modules simply divided by the number of the clusters which share the deposited energy.

3. Finally, the hit position, the second moment (the extent of energy-deposition spread from the mean value) and the total deposited energy of each cluster are calculated.

The choice of E_{th} in (I) influences the probability of cluster splitting. Cluster splitting is caused by events in which non-adjacent modules have the signal of $E > E_{th}$, but are actually due to a single photon. Figure 3.9 shows the probability of cluster splitting for different photon energies as a function of E_{th}. The probability increases with decreasing the photon energy.

The sensitivity of finding photon hits is reduced when higher E_{th} is selected. The reconstruction efficiency for $\gamma N \rightarrow \pi^0\pi^0 N$ reaction as a function of E_{th} is shown in Fig. 3.10. Here the events are generated on the basis of phase-space distribution. At higher E_{th}, the algorithm loses low energy photons

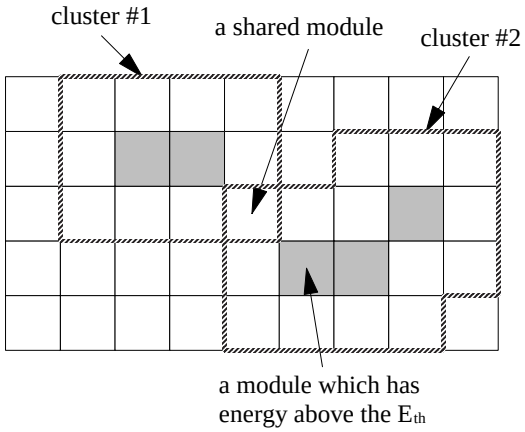

Figure 3.8: An illustration of a typical 2- cluster event. Hatched modules have energy deposit above E_{th}. Energy deposit of a shared module (center of this figure) are divided into two.

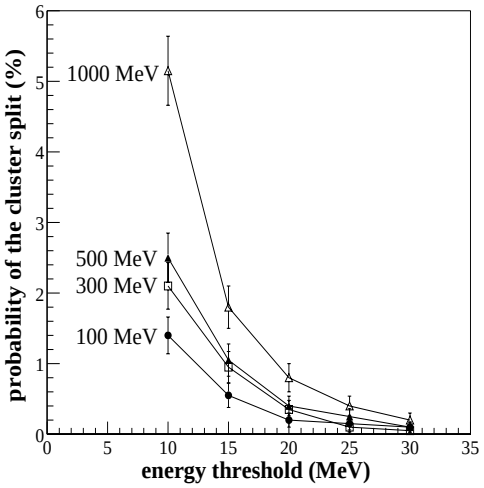

Figure 3.9: Probabilities of cluster splitting for each photon energies as a function of the E_{th}. Isolated photons are generated isotropically in the region of $45^{o} \leq \theta_{\gamma} \leq 85^{o}$

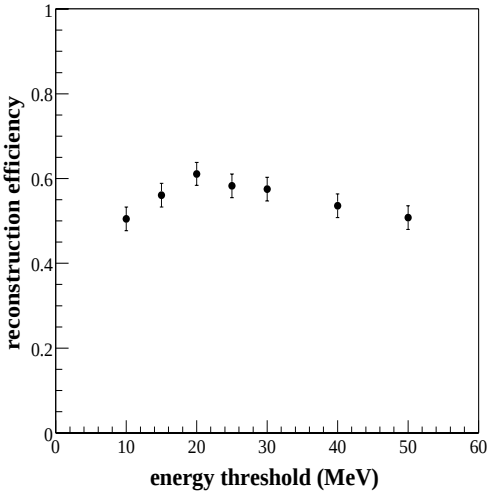

Figure 3.10: The reconstruction efficiency for the $\gamma N \rightarrow \pi^0\pi^0 N$ reaction as a function of the E_{th}.

and thus the efficiency is reduced. On the other hand, for lower E_{th} the efficiency is lower since the probability of the cluster-splitting increases.

Finally the threshold was set to $E_{th} = 20$ MeV. The probability of cluster splitting was less than 1% for photons below 1 GeV. The reconstruction efficiency for the reaction $\gamma N \rightarrow \pi^0\pi^0 N$ was maximized ($\sim 60\%$) in this case.

3.3.2 Detection efficiency

The detection efficiency with $E_{th} = 20$ MeV is shown in Fig. 3.11 as a function of the incident angle of photons with respect to the central module axis (θ'). The efficiency drops near the central module axis ($\theta' \leq 0.5^{o}$) because of the low interaction probability between shower particles and the fiber material as described in Section 3.2. The solid angle for the region of $\theta' \leq 0.5^{o}$ is only 0.9% to the full solid-angle coverage. This drop does not depend on E_{γ}. For low-energy photons, the efficiency decreases as θ' increases since the deposited energy is shared with neighboring modules. As a result, each of the modules has an energy below E_{th}. For photons with $E_{\gamma} > 100$ MeV, the efficiency is almost 100%, independent of θ', except for the drop near the central module axis.

3.3.3 Separation efficiency

The ability to separate two photons that hit close to each other is one of the important parameters of the calorimeter. It is mainly determined by the size of the detector segmentation. The backward calorimeter is segmented in 10 degree intervals for both the polar and azimuthal angles.

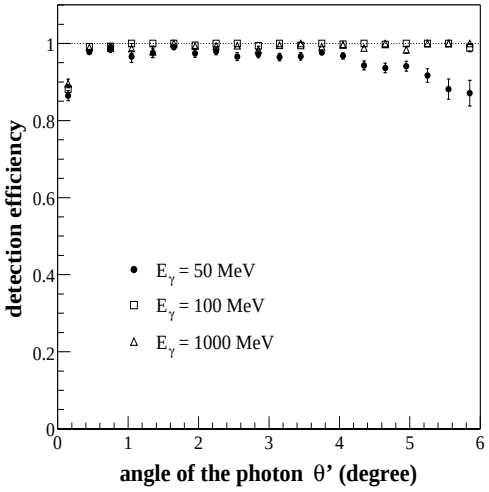

Figure 3.11: Detection efficiencies for each photon energies as a function of the incident angle with respect to the central module axis (θ=55°, ϕ=0°). The both symbols which are the square and the triangle are almost overlapped each other.

The probability of finding a single cluster for two nearby photons (γ_1 and γ_2) is shown in Fig. 3.12. In this figure various combinations of photon energies for the two hits are examined. The summed energy of the two photons is 400 MeV ($E_{\rm sum} = E_{\gamma_1} + E_{\gamma_2}$). The probability of finding a single cluster (and thus missing one hit) is almost 100% for $\theta_{\gamma\gamma} < 10^{\rm o}$ and it gradually reduces to 0% with opening angle. The separation efficiency for the case where $E_{\gamma_1} = 50$ MeV and $E_{\gamma_2} = 350$ MeV is lower than for other combinations because of the low detection efficiency of γ_1 (see Fig. 3.11). Except for this effect, the separation efficiency is almost independent of the energies of γ_1 and γ_2.

To further reduce the probability of cluster merging, the second moment (D) was taken into account. For both the polar and azimuthal angles, it is calculated by

$$D_\theta = \frac{\sum_i \theta_i^2 E_i^{\alpha_\theta}}{\sum_i E_i^{\alpha_\theta}} - \left(\frac{\sum_i \theta_i E_i^{\alpha_\theta}}{\sum_i E_i^{\alpha_\theta}} \right)^2 \tag{3.1}$$

$$D_\phi = \frac{\sum_i \phi_i^2 E_i^{\alpha_\phi}}{\sum_i E_i^{\alpha_\phi}} - \left(\frac{\sum_i \phi_i E_i^{\alpha_\phi}}{\sum_i E_i^{\alpha_\phi}} \right)^2 , \tag{3.2}$$

where θ_i and ϕ_i are the angle of central module axis for the i-th module in a cluster, $E_i^{\alpha_\theta}$ and $E_i^{\alpha_\phi}$ are energy deposit in i-th module. The α_θ and α_ϕ are weight parameters for both polar and azimuthal angles which will be discussed in Section 3.5.2; They are 0.45 and 0.50 respectively. A separation function was

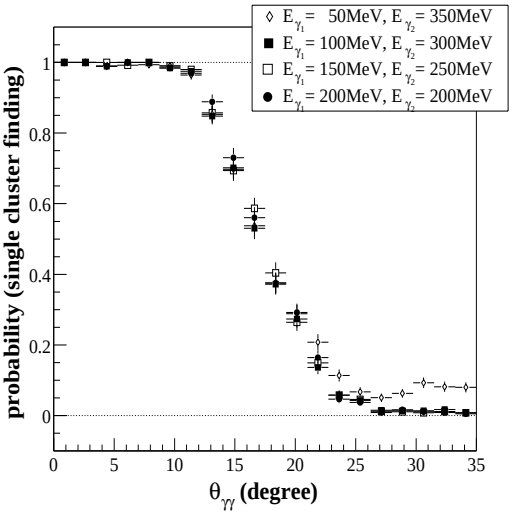

Figure 3.12: Probability of single cluster finding for two nearby hits for various combinations of photon energies ($E_{\rm sum}$ = 400 MeV).

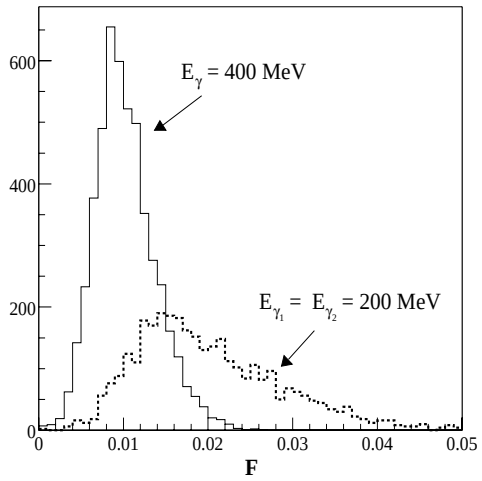

Figure 3.13: Distribution of the separation function F for single photon and double photon events which are realized as a single hit by the algorithm due to the cluster merging.

introduced, given by:

$$F = \sqrt{D_\theta^2 + D_\phi^2}. \tag{3.3}$$

Figure 3.13 shows the distribution of the separation function for single-photon events and double photon-hit events which are reconstructed as a single hit by the algorithm (cluster merging). For the single-photon case, the distribution is much narrower and located at relatively small F region comparing to the double photon-hit case. About 99% of the events are included within $F \leq 0.02$. For the double photon-hit case the events with $F > 0.02$ can be safely rejected since 99% of these events are due to cluster merging. Figure 3.14 shows the probability of cluster merging with and without cut on the F. The probability is drastically reduced when employing the cut, especially for $10^o < \theta_{\gamma\gamma} < 25^o$. However double-hit events with an opening angle less than 8^o cannot be rejected using the $F > 0.02$ cut.

As a consequence, the algorithm separates hits correctly in the case of the nearby double-hit events if $\theta_{\gamma\gamma} > 25^o$. However, for $\theta_{\gamma\gamma} < 8^o$ most of these hits (∼95% in the case of $E_{\rm sum}$ = 400 MeV) are incorrectly reconstructed.

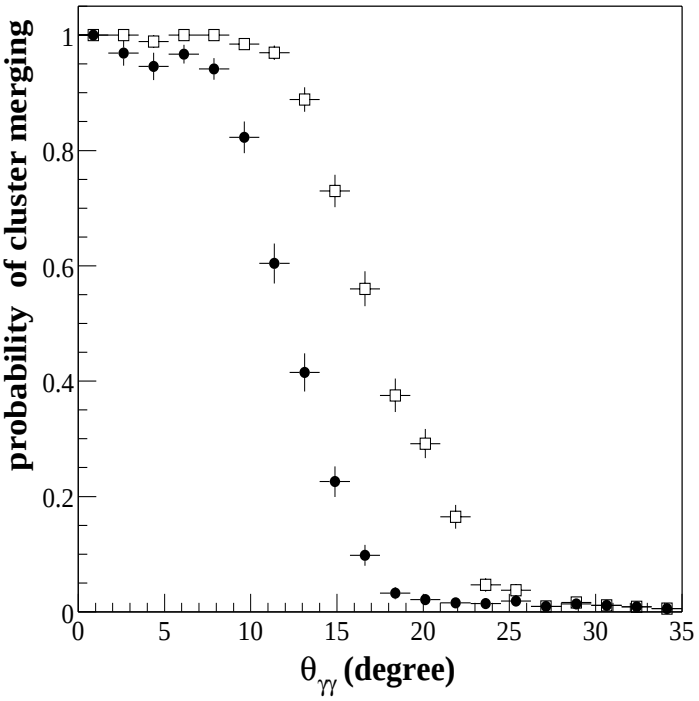

Figure 3.14: Probability of cluster merging for 2-photon hits with $F > 0.02$ cut (filled circles) and without the cut (open squares). The both photon energies are 200 MeV. The probability was reduced especially in the range of $10^{\circ} < \theta_{\gamma\gamma} < 25^{\circ}$ with the cut.

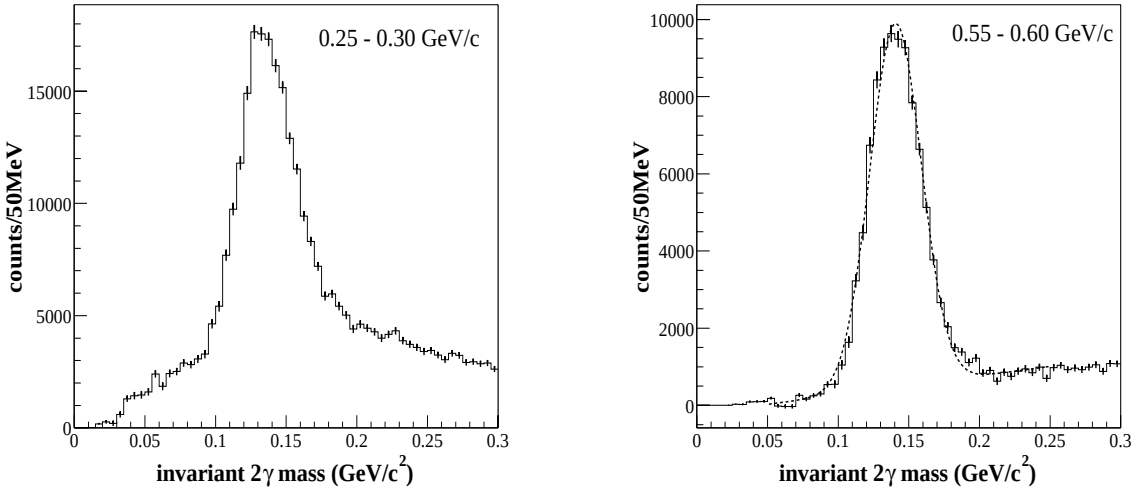

Figure 3.15: Reconstructed 2γ-mass distribution with a CH_2 target. This plot is obtained after subtraction of the empty-target contribution. (left) $0.25< p_{\gamma\gamma} <0.30$ GeV/c. (right) $0.55< p_{\gamma\gamma} <0.60$ GeV/c. The dotted line corresponds to a Gaussian function with a linear background.

3.4 Estimation of the fluctuation of photo-electron statistics

The resolution of the calorimeter obtained from the Monte-Carlo simulation is determined by the fluctuation of the number of shower-particles in the active region. However, in the real measurement other factors contribute to the resolution. One of the important factors is the fluctuation of photo-electron (p.e.) statistics. The number of photo-electons ($N_{\rm p.e.}$) for fixed deposited energy is affected by the scintillation efficiency, light-transmission to the photo-cathode and the quantum efficiency of the phototubes. In order to estimate the resolution due to the fluctuation of the $N_{\rm p.e.}$, the mass resolution of the π^0 meson (σ_{π^0}) obtained by the experimental data was compared with the resolution obtained from the Monte-Carlo simulation. Figure 3.15 shows the reconstructed 2γ invariant-mass distribution obtained with a CH_2 target after subtraction of the empty-target contribution. The clustering algorithm (see Section 3.3.1) was used to obtain these data. A π^0-meson peak was clearly identified in these plots (m_{π^0} =135 MeV/c^2). Background from uncorrelated $\gamma\gamma$-pairs was reduced for higher reconstructed momentum ($p_{\gamma\gamma}$). The comparison between mass resolution (σ_{π^0}/m_{π^0}) in the data and in the Monte-Carlo simulation is shown in Fig. 3.16. Because of unreliability for estimating the background shape at the low momentum side, only the π^0 resolution is plotted in the momentum region of $0.45 < p_{\gamma\gamma} < 1.10$. The shape of the background distribution was assumed to be a linear function (see Fig. 3.15). The resolutions found in both the data and Monte-Carlo simulation were almost independent of π^0 momentum and deviate slightly from each other in the medium-momentum range (0.4 GeV/c to 0.7 GeV/c). The reason is that the resolution obtained from Monte-Carlo simulation does not include the contribution from the fluctuation of the number of photo-electrons.

The avarage number of photo-electrons ($\overline{N_{\rm p.e.}}$) for a 1 GeV photon is estimated as

$$\overline{N_{\rm p.e.}} \quad = \quad \overline{dE_{\rm active}} \cdot Y_{\rm scinti} \cdot T \cdot Q \tag{3.4}$$

where $\overline{dE_{\rm active}}$ denotes the average energy-deposit in the active region, $Y_{\rm scinti}$ is the light yield of the scintillation fiber, T is the light-transmission coefficient from the fiber to the phototube and Q is the quantum efficiency. The $\overline{dE_{\rm active}}$ was calculated by using the Monte-Carlo simulation to be 116.2±0.2 MeV for 1 GeV photons. The scintillation efficiency of the SCIFI (Pol.Hi.Tech 0042) is 2.8% and it is same as those for the scintillation fibers produced by Bicron (BCF series). Therefore, we adopted $Y_{\rm scinti}$=8000 photons/MeV as given in the Bicron catalog. From the ray-tracing simulation, we estimated the light-transmission coefficient as T=0.024. The quantum efficiency for scintillation light having a wave length of 420 nm is 0.21 where the light output is maximum. Thus, the estimated $\overline{N_{\rm p.e.}}$ is 4700 (p.e.) and the relative fluctuation of number of photo-electrons is 1.5% ($=\sqrt{4700}/4700$) for 1 GeV photons. Since the fluctuation of the $N_{\rm p.e.}$ is governed by Poisson statistics, the resolution due to the fluctuation of the number of photo-electron ($\sigma_{\rm p.e.}$) can be represented as

$$\frac{\sigma_{\rm p.e.}}{E} \quad = \quad \frac{1.5\%}{\sqrt{E}} \tag{3.5}$$

where E is the photon energy in GeV. Figure 3.17 shows the same plot as Fig. 3.16 but the photon energy obtained in the Monte-Carlo simulation is smeared with $\sigma_{\rm p.e.}$. The agreement between experimental data and Monte-Carlo simulation has been improved. Therefore, the Equation 3.5 is confirmed to be utilized for reproducing the real detector resolution.

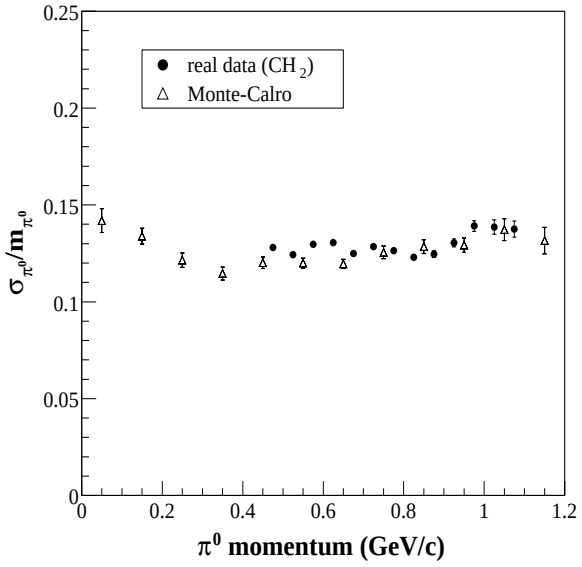

Figure 3.16: Mass resolution for π^0-mesons as a function of the momentum for real data (filled circles) and Monte-Carlo result (open triangles).

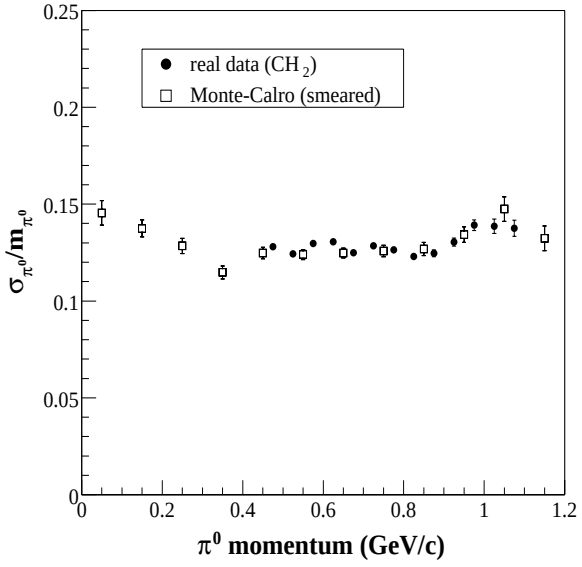

Figure 3.17: Mass resolution for π^0-mesons resolution as a function of the momentum for real data (filled circles) and Monte-Carlo result with the smearing (open squares).

3.5 Estimation of the energy and angular resolution

The energy and angular resolutions of the calorimeter were estimated using the Monte-Carlo simulation. The resolution due to the photo-electron statistics was taken into account. The obtained energy and angular resolutions are employed in the physics analysis for example when using the kinematical fitting to pick up the correct photon pairs from all 2-photon combinations. To include the resolution information, the resolutions are parameterized.

3.5.1 Energy resolution

The energy resolution of the calorimeter is parameterized as

$$\frac{\sigma_E}{E} = \sqrt{\left(\frac{a}{\sqrt{E}}\right)^2 + b^2}, \tag{3.6}$$

where E is the photon energy in GeV. The constant a corresponds to the fluctuations governed by Poisson statistics such as the number of shower-particles fluctuation and photo-electron fluctuation. The b term represents the resolution due to the shower leakage. This term is mainly determined by detector shape.

Figure 3.18 shows the energy resolution of the calorimeter as a function of the photon energy. For comparison, the energy resolution obtained without smearing of the resolution due to photo-electron statistics is also plotted in this figure. The difference is small. This is due to the fact that the energy resolution of the calorimeter is dominated by the fluctuation of the number of shower-particles.

Equation 3.6 was applied to fit the data. The parameters obtained are

$$\begin{aligned} a &= 0.052 \pm 0.001 \ \ \mathrm{GeV}^{1/2} \\ b &= 0.044 \pm 0.002 \end{aligned}$$

The parameters were used in the physics analysis.

3.5.2 Angular resolution

The photon-hit position was determined using the center-of-gravity method with weight parameters [55]. In this method, the polar and azimuthal angles are calculated from

$$\theta^* = \frac{\sum_i \theta_i E_i^{\alpha_\theta}}{\sum_i E_i^{\alpha_\theta}} \quad , \quad \phi^* = \frac{\sum_i \phi_i E_i^{\alpha_\phi}}{\sum_i E_i^{\alpha_\phi}}, \tag{3.7}$$

where θ^* and ϕ^* are the calculated angles, θ_i and ϕ_i are the angle of central module axis for the ith module, $E_i^{\alpha_\theta}$ and $E_i^{\alpha_\phi}$ are the energy deposit in the ith module, α_θ and α_ϕ represent weight parameters for polar and azimuthal angles, respectively. The weight parameters determine the importance of contributions from modules with different energy deposition. If α is set to unity, the method corresponds to the 'simple' center-of-gravity method [56]. If α were 0, the obtained angle would just be the average angle

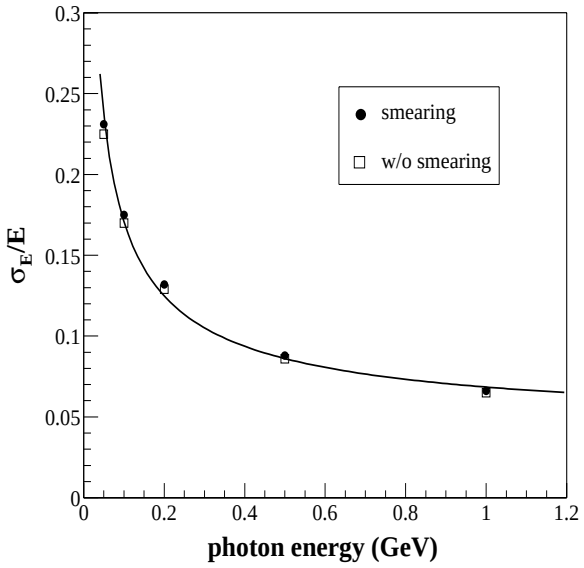

Figure 3.18: The energy resolution (σ_E/E) as a function of the photon energy. For comparison, the resolution obtained without the smearing is also plotted (open square). The solid curve represents the result of fitting the smeared plot with Equation 3.6.

of the modules. Figure 3.19 shows the dependence of the angular resolution on the weight parameter. The angular resolution was obtained from the width of the residual distribution ($\theta - \theta^*$). Reduced χ^2 values of the residual distributions are also plotted in this figure. Minima were found at $\alpha_\theta = 0.45$ and $\alpha_\phi = 0.50$, respectively. This can be explained as following: if α is chosen too small, the energy weighting is not sufficient. On the other hand, if α is chosen too large, the residual distribution deviates significantly from a Gaussian distribution since the systematic shift between the true angle and the determined one becomes large.

The dependence of the angular resolution on polar angle (θ_γ) is plotted in Fig. 3.20, using above values for α_θ and α_ϕ. The resolutions for both polar and azimuthal angles do not show a strong dependence on θ_γ. The difference was less than 5% for the polar angular resolution and 8% for azimuthal angular resolution. Therefore, both resolutions were considered to be independent of the θ_γ in the further analysis of the data.

Figure 3.21 shows the angular resolutions as a function of the photon energy. The resolutions become better with increasing photon energy. However, the dependence does not follow the $1/\sqrt{E}$ dependence which is expected from the shower-particle statistics. The reason is that at the lowest energies the calculated angle from the center-of-gravity method is often simply the angle of the central module axis since most of energy is deposited in one module only. The RMS value of the residual distribution which becomes rectangular in this case is about 2.9 degree [2]. In order to parameterize the energy dependence of

[2]The angular interval of between two modules is 10^o for both polar and azimuthal angle. The RMS value of the

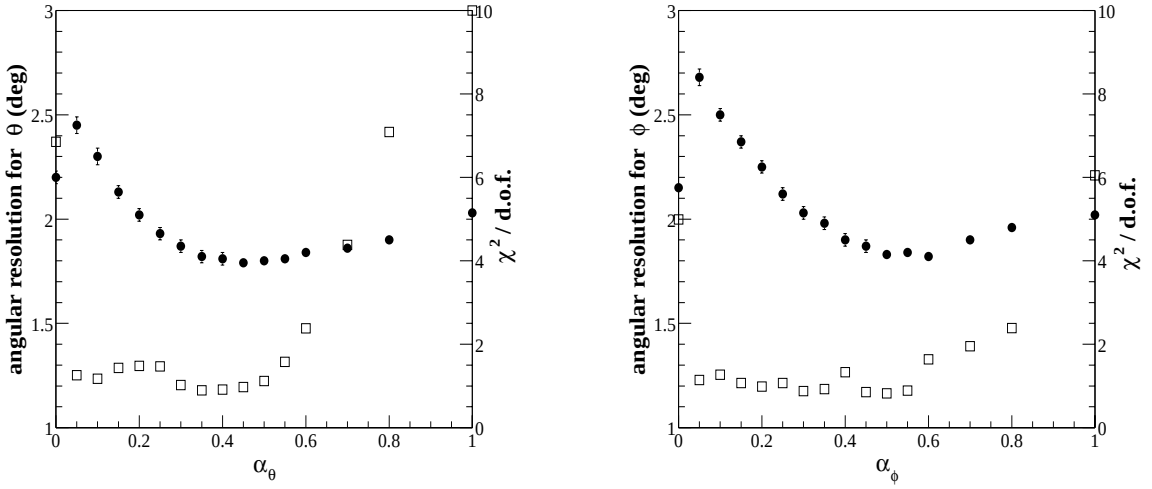

Figure 3.19: The α_θ and α_ϕ dependence of the polar-angle resolution for the photon energy of 200 MeV (filled circles). Right scale shows reduced χ^2 values of the residual distributions (open squares).

the angular resolutions as a function of E_γ, an exponential term was introduced by taking this additional constraint into account.

$$\sigma \quad = \quad p_0 \exp(p_1 E) + \frac{p_2}{\sqrt{E}} + p_3, \tag{3.8}$$

where p_0, p_1, p_2 and p_3 are free parameters and E is the photon energy in GeV. This function reproduced the energy dependence well. The coefficients were obtained to be $p_0 = (1.01 \pm 0.06)$, $p_1 = (0.128 \pm 0.042)$, $p_2 = (0.79 \pm 0.16)$ and $p_3 = (-3.07 \pm 0.62)$ for polar-angle resolution. In the case of azimuthal-angle resolution, those were given as $p_0 = (1.09 \pm 0.06)$, $p_1 = (0.075 \pm 0.046)$, $p_2 = (1.09 \pm 0.18)$ and $p_3 = (-3.20 \pm 0.45)$.

rectangular distribution in the range of [-5°,5°] is $5°/\sqrt{3} \sim 2.9°$

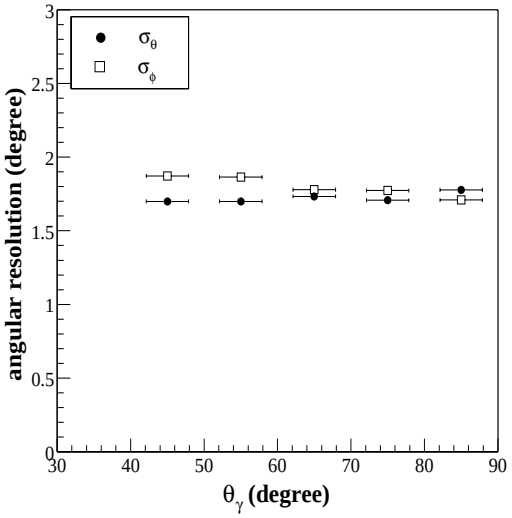

Figure 3.20: Polar-angle dependence of the angular resolutions for the photon energy of 200 MeV.

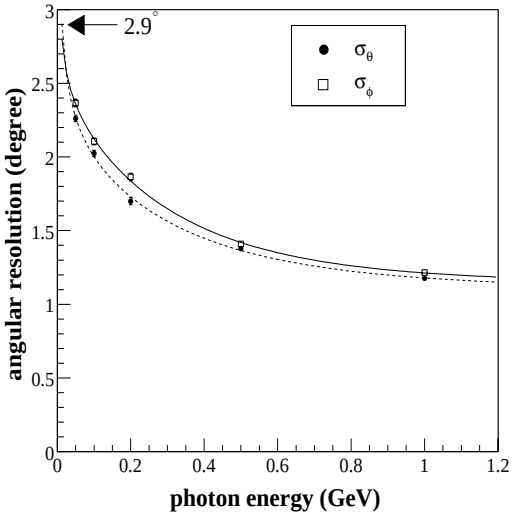

Figure 3.21: Angular resolutions for the polar and azimuthal angle at around $\theta_\gamma = 55^o$ as a function of photon energy. The solid and dashed lines correspond to the fitting result with the equation 3.8 for the polar and azimuthal angles respectively. The resolution of 2.9 degree corresponds to the RMS value of the rectangular distribution in the range of [-5^o, 5^o] (see text).

Chapter 4

Data analysis

The final objective of the data analysis is to obtain clean $\gamma p \to \pi^0 \eta p$ event samples from the triggered events. In this chapter we will discuss how to extract the final $\gamma p \to \pi^0 \eta p$ samples. At first, 4γ-event samples are selected from the triggered event for each target (carbon, CH_2 and empty) by introducing several selection cuts. This process will be discussed in Section 4.1. Then, a kinematical analysis is performed in order to select the correct $\gamma\gamma$-pairs from the 4γ-event samples. Events with small χ^2 values are then regarded as $\pi^0\eta$ samples. The procedure is described in Section 4.2. Finally, $\pi^0\eta p$ event samples are obtained by selecting the events whose missing mass of the $p(\gamma, \pi^0\eta)X$ reaction is within proton-mass region. It is discussed in Section 4.4.

4.1 Selection for 4γ-event samples

4.1.1 Cluster recognition

The clustering algorithm, which is discussed in detail in Section 3.3, is applied to the experimental data with an energy threshold of $E_{\rm th} = 20$ MeV. The energy threshold was determined to maximize the reconstruction efficiency for the $\gamma p \to \pi^0\pi^0 p$ reaction, and the acceptance loss for the $\gamma p \to \pi^0 \eta p$ reaction is minimized at the same time. This aspect will be discussed later in Section 4.3.

Figure 4.1 shows the distributions of the number of reconstructed cluster ($N_{\rm clst}$) for each target. Note that the data includes clusters produced by both neutral and charged particle hits since signals from the CV counters are not required at this moment. Events reconstructing no cluster are caused when signals from calorimeter modules exceeds the discriminator threshold ($V_{th} = -20$ mV corresponding to the energy deposit ∼10-15 MeV) but smaller than E_{th}. The shapes of the distributions are similar as shown in Fig. 4.1 for the carbon and CH_2 targets. However for the empty target, the ratio of $N_{\rm clst} = 1$ is high compared with those in other targets. The reason is that noise signals are involved in the events with $N_{\rm clst} = 1$ for empty target. About half of events with $N_{\rm clst} = 1$ was originating from noise signals. The origin of the noise signal has not been confirmed yet, but it would be due to an electric discharge between photo-cathode and aluminum foil, which is used for a light-guide reflector [1] . Since the noise

[1]The noise signals were generated even at the beam off condition. The 2 modules (B5-28 and B8-22) of totally 252

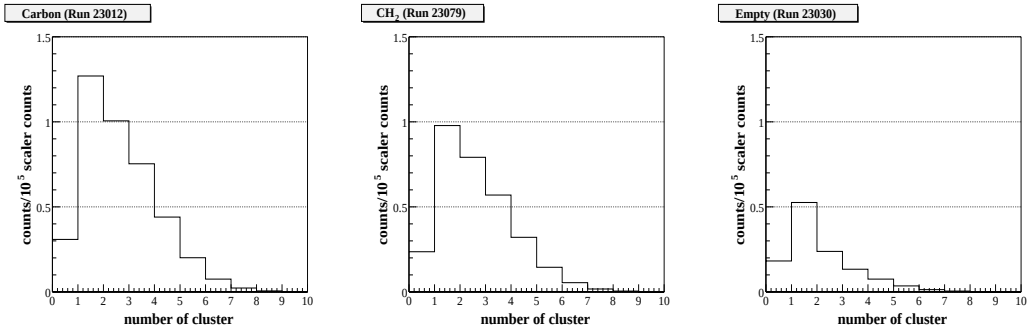

Figure 4.1: Distributions of the number of reconstructed cluster with the energy threshold $E_{\rm th} = 20$ MeV for different targets. The histograms are normalized by the accumulated scaler counts of the tagging counter.

signals were generated randomly (and thus not coincident with beam), these events can be rejected by applying a TDC cut.

Next, these clusters were classified into three categories by taking account of signals from CV counters and TDC values of the calorimeter modules. We defined a cluster produced by neutral particle as a *neutral cluster*, and that produced by charged particle as a *charged cluster*. In addition, a cluster whose TDC timing did not coincide with beam was defined as a *off-timing cluster*. The discrimination was achieved as follows

1. At first, the TDC value of the central module ($\mathrm{TDC_{center}}$) of a cluster was checked. A typical TDC distribution of a Lead/SCIFI module is shown as the left plot in Fig. 4.2. If the $\mathrm{TDC_{center}}$ of the cluster was within ± 30 channels (± 15 ns) around the true timing, the signal was regarded as on-timing. Otherwise, the cluster was regarded as a *off-timing* cluster and then it was discarded. The off-timing cluster was mainly caused by three reasons: (1) noise signals from photo-multiplier of Lead/SCIFI module, (2) cosmic-rays passing through the calorimeter, and (3) signals coming from different beam bunches. The accidental signals due to (1) and (2) yielded sharp peak in the TDC spectrum because trigger timing was not determined by the tagging counter, but the Lead/SCIFI module itself.

2. Then the TDC value of the CV counter, which covered the central module of the on-timing cluster, was investigated. The right plot in Fig. 4.2 shows a typical TDC distribution measured with a CV counter. If the TDC value of the CV counter was within ± 30 channels (± 15 ns) around the true timing, the cluster was regarded as a charged cluster. Other on-timing cluster was considered to be a neutral cluster.

The distributions of the number of neutral clusters and charged clusters are shown in Fig. 4.3 and Fig. 4.4, respectively. The distributions for carbon and CH_2 targets are almost the same again. The neutral clusters

modules were noisy.

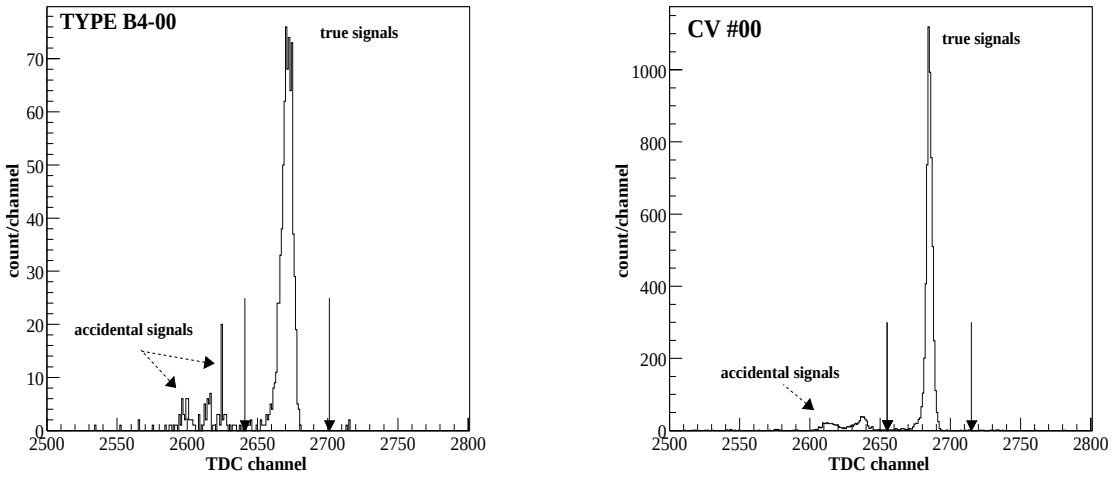

Figure 4.2: TDC distributions for a typical Lead/SCIFI module (left) and a CV counter (right). The two arrows beside the true peak are corresponding to the TDC cut positions. These plots are obtained from run23315 (filling pattern: 203 bunches - 4 bunches $\times$ 7).

in the plot of the empty target mainly comes from low-energy shower-particles produced at upstream of the target. This background event was yielded in coincidence with the beam bunch, and hence it was not rejected by the TDC cut. The ratio of the number of events with 4-neutral clusters to the triggered events was 2.1% (1.3%) for the carbon (empty) target.

4.1.2 Cuts to extract 4γ-event samples

Neutral cluster selection and edge-module cut

Although the calorimeter covered an angular region from 30° to 100° for polar angle θ, events with 4 neutral-clusters in the region of $40° < \theta < 90°$ were required for 4γ-event samples selection. The reason was that neutral clusters located in the region of $30° < \theta < 40°$ and $90° < \theta < 100°$, where the corresponding modules were TYPE B-3 and TYPE B-9 (see Fig. 2.13 on page 29), had the following problems:

- Large amount of energy can be leaking out to the outside of the calorimeter because of lack of peripheral modules. It gives wrong energy information.
- The estimation of the energy and angular resolutions was difficult since the resolutions strongly depended on hit position of the incident photons.
- Signals from TYPE B-3 and TYPE B-9 modules (we refer to these modules as “edge modules”) were not included in OR circuit of the calorimeter. Therefore, the signals did not provide event triggers.

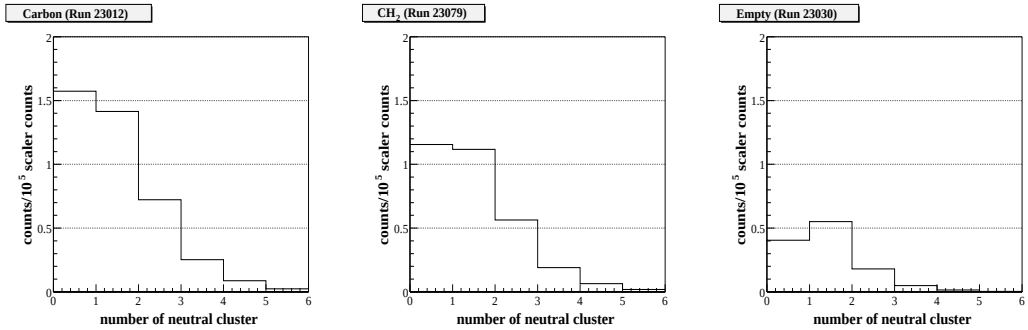

Figure 4.3: Distributions of the number of reconstructed neutral cluster with $E_{th} = 20$ MeV for different targets. The histograms are normalized by the accumulated scaler counts of the tagging counter.

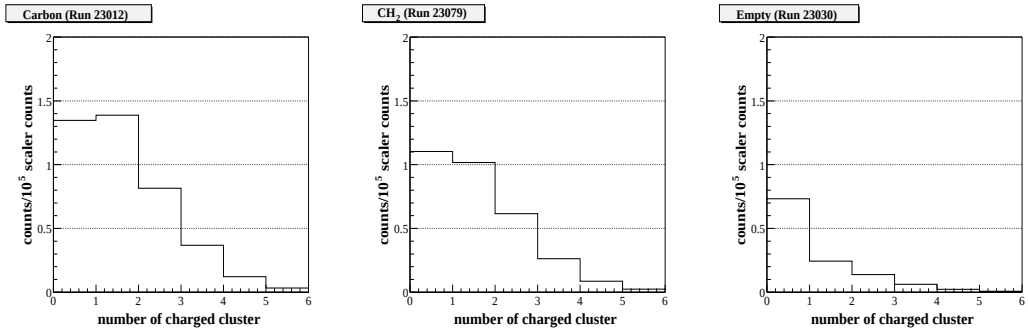

Figure 4.4: Distributions of the number of reconstructed charged cluster with $E_{\rm th} = 20$ MeV for different targets. The histograms are normalized by the number of triggered events.

The probability of finding the event which was $N_{\gamma(40^\circ-90^\circ)}$=4 to the triggered events was 0.61% for carbon target, 0.58% for CH_2 target, and 0.30% for empty target respectively. To reject the events of neutral clusters in the edge modules, the following cut was required:

No neutral cluster in the region of $30^\circ < \theta_\gamma < 40^\circ$ and $90^\circ < \theta_\gamma < 100^\circ$.

Therefore, the TYPE B-3 and TYPE B-9 modules were utilized as veto counters. The cut statistics of the edge-module cut for a typical carbon-target run is summarized in Table 4.1.

Cluster merging cut

When 2-photons hit close to each other, the clustering algorithm would not separate out the two hits, and only single cluster was found as described in Section 3.3.3, This effect was important when the opening angle of 2-photons was less than 25 degree. Therefore, events with $N_{\gamma(40^\circ-90^\circ)} = 4$, which were selected as 4γ-event candidates previously, may include events with 5 or more photon hits. In order to suppress

Table 4.1: Cut statistics of the edge-module cut for typical carbon-target run.

	Carbon (run23012)	rejection
Triggered events	503165	
No neutral clusters on TYPE B-3 modules	411691	1.222±0.001
No neutral clusters on TYPE B-9 modules	466738	1.078±0.001
No neutral clusters on both TYPE B-3 and B-9 modules	383009	1.314±0.001

the events with cluster merging, the separation function F defined in Section 3.3.3 was employed.

$$F = \sqrt{D_\theta^2 + D_\phi^2}$$

where D_θ and D_ϕ are the second moment for both the polar and azimuthal angles. Figure 4.5 shows the distributions of maximum separation function ($F_{\max}$) among all neutral clusters for different number of neutral clusters. The most of events concentrates below $F_{\max} = 0.02$ for all plots. According to the Monte-Carlo simulation, about 99% of the events for single-photon hit the give $F_{\max}$ value with less than 0.02 (see Fig. 3.13). Therefore, events with $F_{\max} > 0.02$ can be regarded as events coming from double-photon hits, and hence rejected from events with $N_{\gamma(40^\circ-90^\circ)} = 4$. This cut was referred as "cluster-merging cut". The rejection factors due to the cluster-merging cut were estimated for different $N_{\gamma(40^\circ-90^\circ)}$ events for a typical carbon-target run. The result is listed in Table 4.2.

Table 4.2: Cut statistics for the cluster-merging cut

	examined	passed	rejection
$N_{\gamma(40^\circ-90^\circ)} = 1$	155498	142115	1.094±0.001
$N_{\gamma(40^\circ-90^\circ)} = 2$	53901	46775	1.152±0.002
$N_{\gamma(40^\circ-90^\circ)} = 3$	13637	11291	1.208±0.005
$N_{\gamma(40^\circ-90^\circ)} = 4$	3231	2590	1.247±0.011
$N_{\gamma(40^\circ-90^\circ)} = 5$	577	444	1.300±0.030
$N_{\gamma(40^\circ-90^\circ)} = 6$	94	74	1.270±0.068

$n_{\rm tag}$=1 selection

For a baryon-resonance search, the energy value of the incident beam is inevitable since the most interesting observable is the $\sqrt{s}$ distribution (the total energy of the center of mass system for incident photon and target proton). The energy of the photon beam ($E_{\rm beam}$) is obtained from the hit positions of the recoil electrons, which is accompanied with the photon beam, at the tagging counter. Therefore, at least a single track reconstructed with tagging counter was required for further analysis. Ideally, the number of tracks reconstructed with the tagging counter ($n_{\rm tag}$) is 1 for a certain trigger event. However, the $n_{\rm tag}$ was not always equal to 1 because of background processes such as (i) accidental signals due to the slow response of the SSD, (ii) shower particles produced at the support structure of the tagging counter, (iii)

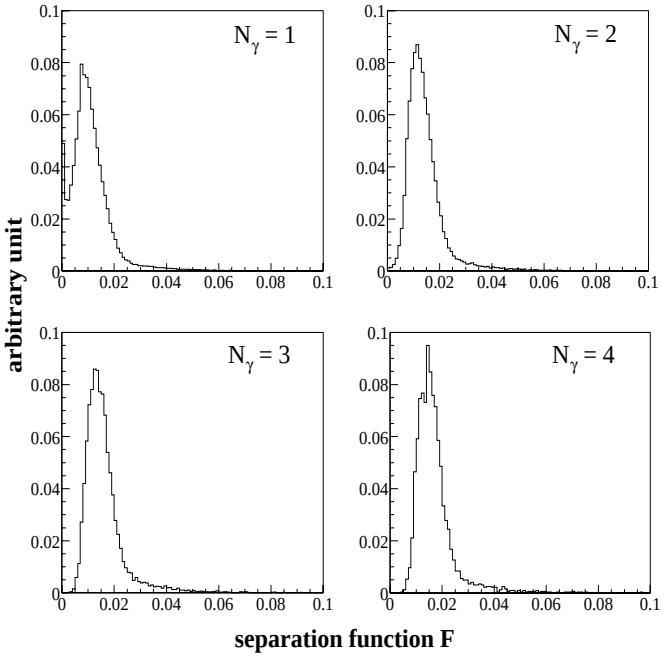

Figure 4.5: Distributions of the separation function $F_{\max}$ for different N_γ events obtained in the carbon-target run. The events with $F_{\max} < 0.02$ are selected in order to reject cluster merging events.

accidental signals generated by X-ray hits. Events in the processes (i) and (ii) result in $n_{\rm tag}$>1. On the other hands, events in the process (iii) results in $n_{\rm tag}$=0.

The $n_{\rm tag}$ distribution for a typical carbon-target run (Run 23012) is shown in Fig. 4.6. The ratio of events with $n_{\rm tag}$=1 to the triggered events was about 64% in this case. The run dependence of this ratio is plotted in Fig. 4.7. The ratio fluctuates for each target, particularly it reduces in the case of empty target. Moreover, the ratio strongly depends on the filling pattern of the storage electrons. A qualitative explanation is that the trigger condition of the experiment is not so tight against low-energy shower-particles produced upstream of the target, and hence the shower particles gives trigger signals accidentally. The situation improved when events including the 2-neutral clusters reconstructing a π^0 were required (see Fig. 4.8) because these events were originated from the target. For further analysis, events with $n_{\rm tag}$=1 were selected in order to obtain better energy information.

Beam energy cut

The designed energy range of the tagged photon-beam was between 1.5 GeV and 2.4 GeV at the LEPS beamline. However, the lower limit of the energy range for the first term of the experiment was about 1.6 GeV because of mis-alignment of the upstream tagging counter. Figure 4.9 shows the distribution of the beam energy ($E_{\rm beam}$) with $n_{\rm tag}$= 1 events in this term. The situation was recovered by reinstalling the

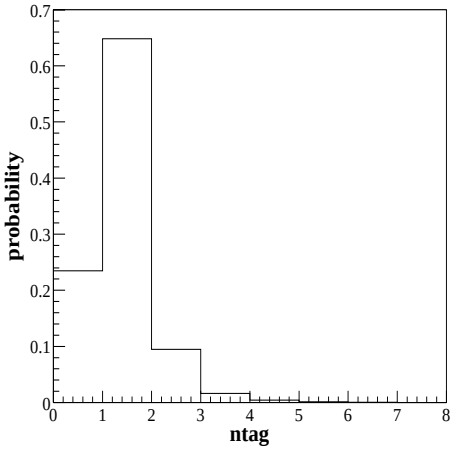

Figure 4.6: Ratios of the number of events reconstructed with the tagging system to the trigger events as a function of the $n_{\rm tag}$. The histogram is plotted for a typical carbon data (Run 23012).

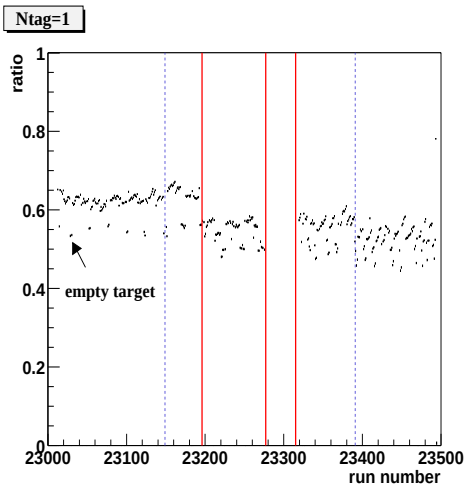

Figure 4.7: Ratios between the number of $n_{\rm tag}$=1 events and the number of triggered events as a function of the run number. The solid lines show the border lines of the different filling patterns of the SPring-8 operation and the dashed lines correspond to the time of changing the laser focus for the backward Compton scattering.

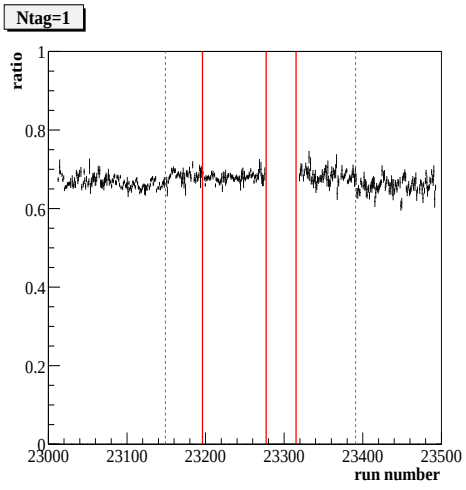

Figure 4.8: Ratios with $n_{\rm tag}$=1 in the $\gamma A \rightarrow \pi^0 X$ events as a function of the run number. The meanings of the solid and dashed lines are the same as in Fig. 4.7.

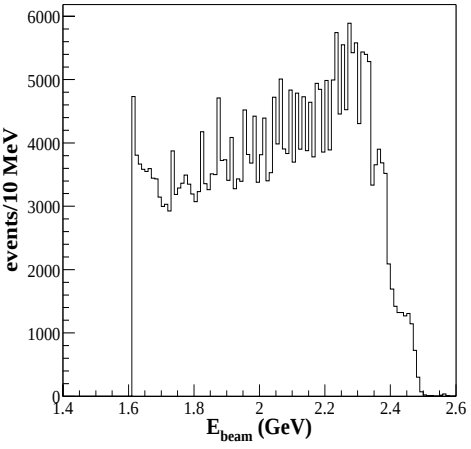

Figure 4.9: Energy distribution of the photon beam after selecting $n_{\rm tag}$=1 events. The plot is obtained from the analyses of a typical carbon data (Run 23012).

tagging counter after the Run 23315. In order to keep consistency between both the data sets [2], following cut was applied to data.

$$1.62 \text{ GeV} < E_{\text{beam}} < 2.40 \text{ GeV}$$

With this beam energy, we searched for the s-channel resonances in the region of

$$1.98 \text{ GeV}/c^2 < \sqrt{s} < 2.32 \text{ GeV}/c^2.$$

Cut summary for the 4γ-event samples

After applying all cuts discussed above, the number of events for each target was reduced as follows.

Target	triggered event	after applying the cuts	rejection
Carbon	61555462	126828	485.3±1.4
CH_2	41603385	82156	506.4±1.8
Copper	58581486	65540	893.8±3.5
Empty	17388120	15813	1099.6±8.7

The run statistics and the conditions of each cut are summarized in Table 4.3. The survived samples involve of four good neutral clusters and a good tagger track. Therefore, we referred these sample as "4γ-event samples" and they were used for further analysis. Note that the 4γ-event samples may include events with charged clusters produced by $\pi^{\pm}$ in addition to 4γ clusters. These events were rejected by a missing-mass cut as discussed later.

The invariant 4γ-mass (M_{4_γ}) is calculated as

$$M_{4\gamma} = \sqrt{(p_{\gamma_1} + p_{\gamma_2} + p_{\gamma_3} + p_{\gamma_4})^2}, \tag{4.1}$$

where p_{γ_i} is the observed four momentum vector for the ith photon. Figure 4.10 shows the invariant 4γ mass distribution of the 4γ-event samples for different targets. All the distributions show a peak at around 0.3 GeV/c^2. The main contribution to this low mass peak is 3 or more π^0 production events (and thus some photons escape from the detector coverage). The lines corresponding to the $\pi^0\eta$ threshold ($M_{\pi^0} + M_\eta = 0.68$ GeV/c^2) are shown in Fig. 4.10 . In the next section, we will discuss the kinematical analysis to obtain the $\pi^0\eta$ events by using the 4γ-event samples.

[2] All CH_2 data were taken before Run 23315 while about 20% of the carbon data were obtained after run 23315.

Table 4.3: Cut statistics for selecting the 4γ-event samples for each target

Carbon target

cut	examined	passed	rejection
(Triggered events)		(61555462)	
$N_{\gamma(40^\circ-90^\circ)} = 4$	61555462	378233	162.7±0.3
Edge-module cut	378233	235676	1.605±0.002
Cluster merging cut	235676	191097	1.233±0.001
$n_{\mathrm{tag}} = 1$	191097	133640	1.430±0.002
$1.62 < E_{\mathrm{beam}} < 2.40$ GeV	133640	126828	1.053±0.001

CH_2 target

cut	examined	passed	rejection
(Triggered events)		(41603385)	
$N_{\gamma(40^\circ-90^\circ)} = 4$	41603385	240261	173.2±0.4
Edge-module cut	240261	148043	1.623±0.003
Cluster merging cut	148043	120898	1.224±0.002
$n_{\mathrm{tag}} = 1$	120898	85793	1.409±0.002
$1.62 < E_{\mathrm{beam}} < 2.40$ GeV	85793	82156	1.044±0.001

Copper target

cut	examined	passed	rejection
(Triggered events)		(58581486)	
$N_{\gamma(40^\circ-90^\circ)} = 4$	58581486	196378	298.3±0.7
Edge-module cut	196378	126164	1.556±0.003
Cluster merging cut	126164	102171	1.235±0.002
$n_{\mathrm{tag}} = 1$	102171	72247	1.414±0.003
$1.62 < E_{\mathrm{beam}} < 2.40$ GeV	72247	65540	1.102±0.001

Empty target

cut	examined	passed	rejection
(Triggered events)		(17388120)	
$N_{\gamma(40^\circ-90^\circ)} = 4$	17388120	52347	332.2±1.5
Edge-module cut	52347	31224	1.676±0.006
Cluster merging cut	31224	24579	1.270±0.004
$n_{\mathrm{tag}} = 1$	24579	17184	1.430±0.006
$1.62 < E_{\mathrm{beam}} < 2.40$ GeV	17184	15813	1.087±0.002

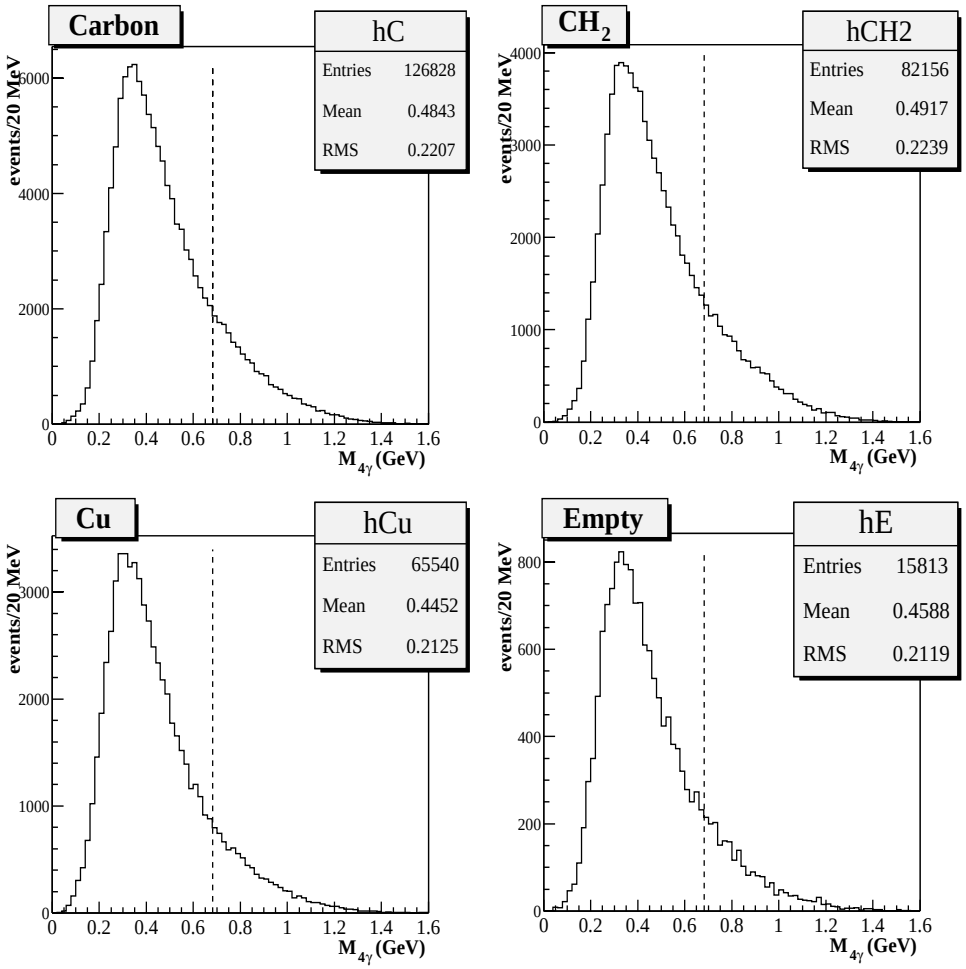

Figure 4.10: Invariant 4γ-mass distributions of the 4γ-event samples for different targets. The dashed lines in each plot correspond to the $\pi^0\eta$ production threshold of $M_{4\gamma}$ =0.68 GeV/c^2.

4.2 Kinematical analysis for $\pi^0\eta$ event selection

In the previous section the 4γ-event samples were extracted from the triggered events. The obtained 4γs in the samples include photons coming from such as $\pi^0\pi^0$ decay other than $\pi^0\eta$ decay. To select $\pi^0\eta$ events from the samples a kinematical analysis will be performed. In this section we will discuss, first, a procedure of the kinematical fitting in detail (Section 4.2.1). Then a rough estimate of the number of $\pi^0\eta$ events will be given (Section 4.2.2). Finally, we will discuss how to select the $\pi^0\eta$ samples for each target with hypothesis testing (Section 4.2.3).

4.2.1 Kinematical fitting

The kinematical fitting is a least-square fitting under the constraints which are required from the physical law. The constraints are chosen depending on physics objective to be investigated, and hence one need to assume at least one hypothesis for the kinematical fitting. Experimental observables, such as energy, momentum and angle of emission, are modified during the fitting process. If the difference between the fitted values and observed ones for a certain event were quite large comparing to the known detector resolutions, one would expect that the hypothesis was wrong for that event. Conversely, if the difference is reasonable, one can conclude that the event would be satisfied the hypothesis. By using the kinematical fitting the statistical significance for a certain hypothesis can be evaluated quantitatively. Here, we will discuss how to calculate the statistical significance with the kinematical fitting. In most part of the discussion we referred to a text book written by Frodesen *et al* [57].

Kinematical variables

Now we define *measured variables* (x_i) as the experimental observables that are 4-momentum components of the 4-photons measured with the calorimeter. Since the photon is massless, the magnitude of the momentum is same as the total energy. Therefore, totally 12 set of the measured variables is used in the fitting algorithm:

$$\text{measured variables} \ : \ E_{\gamma_1},\ \theta_{\gamma_1},\ \phi_{\gamma_1},\ E_{\gamma_2},\ \theta_{\gamma_2},\ \phi_{\gamma_2},\ E_{\gamma_3},\ \theta_{\gamma_3},\ \phi_{\gamma_3},\ E_{\gamma_4},\ \theta_{\gamma_4},\ \phi_{\gamma_4}$$

where E_{γ_i}, θ_{γ_i} and ϕ_{γ_i} denote the energy, the polar angle and the azimuthal angle of i-th photon respectively. In addition to that, *fitted variables* (x_i^*) are defined as modified values of the observables after the kinematical fitting. Similar to the measured variables, the 12 set of the fitted variables are denoted as listed below:

$$\text{fitted variables} \ : \ E^*_{\gamma_1},\ \theta^*_{\gamma_1},\ \phi^*_{\gamma_1},\ E^*_{\gamma_2},\ \theta^*_{\gamma_2},\ \phi^*_{\gamma_2},\ E^*_{\gamma_3},\ \theta^*_{\gamma_3},\ \phi^*_{\gamma_3},\ E^*_{\gamma_4},\ \theta^*_{\gamma_4},\ \phi^*_{\gamma_4}.$$

For further convenience, two (12×1)-dimensional column vectors, which consist of the measured variables and the fitted variables, are introduced.

$$\boldsymbol{x} \equiv \begin{pmatrix} E_{\gamma_1} \\ \theta_{\gamma_1} \\ \vdots \\ \phi_{\gamma_4} \end{pmatrix}, \quad \boldsymbol{\eta} \equiv \begin{pmatrix} E^*_{\gamma_1} \\ \theta^*_{\gamma_1} \\ \vdots \\ \phi^*_{\gamma_4} \end{pmatrix} \tag{4.2}$$

These column vectors are employed in the fitting algorithm as described later.

Hypothesis and constraints of the kinematical fitting

The purpose of the kinematical fitting in this study is to select correct $\gamma\gamma$-pairs from 4γ-event samples. Therefore, a statistical test for all 4γ-event samples, where the photons are labeled as γ_1, γ_2, γ_3 and γ_4, will be performed under the following hypothesis:

- Hypothesis : All 4γ-event samples come from $\pi^0\eta$ decay and these mesons decay into photons as $\pi^0 \to \gamma_1\gamma_2,\ \eta \to \gamma_3\gamma_4$.

This assumption gives us following constraints derived from 4-momentum conservation law,

$$f_1 = m^2_{\gamma_1\gamma_2} - m^2_{\pi^0} = 0 \tag{4.3}$$

$$f_2 = m^2_{\gamma_3\gamma_4} - m^2_{\eta} = 0, \tag{4.4}$$

where m_{π^0} and m_η are the masses of π^0 (135 MeV/c^2) and η (547 MeV/c^2) mesons, $m_{\gamma_i\gamma_j}$ denotes the invariant mass of i-th and j-th photons. In the fitting algorithm the invariant mass of 2-photons is calculated with the kinematical variables

$$\begin{aligned} m^2_{\gamma_i\gamma_j} &= 2E_{\gamma_i}E_{\gamma_j}(1-\cos\theta_{\gamma_i\gamma_j}) \\ &= 2E_{\gamma_i}E_{\gamma_j}\{1-\sin\theta_{\gamma_i}\sin\theta_{\gamma_j}\cos(\phi_{\gamma_i}-\phi_{\gamma_j})-\cos\theta_{\gamma_i}\cos\theta_{\gamma_j}\}, \end{aligned} \tag{4.5}$$

where the $\theta_{\gamma_i\gamma_j}$ is the opening angle between i-th and j-th photon. The matrix notation of these constraints (2×1 dimension) is defined as

$$\boldsymbol{f} \equiv \begin{pmatrix} f_1 \\ f_2 \end{pmatrix} = \boldsymbol{0}. \tag{4.6}$$

Minimization

The quantitative estimate of the deference between fitted variables and the measured variables is performed by the χ^2 test:

$$\chi^2 = \sum_{i=1}^{12} \frac{(x_i - x_i^*)^2}{\sigma_i^2}. \tag{4.7}$$

Here the σ_i is the detector resolution for the i-th component of the measured variable. Using the matrix notation for x_i and x_i^* which have been defined in Eq.(4.2), one can rewrite Eq.(4.7) as

$$\chi^2 = (\boldsymbol{x}-\boldsymbol{\eta})^T G(\boldsymbol{x}-\boldsymbol{\eta}), \tag{4.8}$$

where G^{-1} is 12-dimensional covariant matrix, which is described with the detector resolutions. If the resolutions are independent each other, the inverse matrix of G is a diagonal matrix and it is represented as

$$G^{-1} = \begin{pmatrix} \sigma^2_{E_{\gamma_1}} & 0 & \dots & 0 \\ 0 & \sigma^2_{\theta_{\gamma_1}} & \dots & 0 \\ \vdots & \vdots & \ddots & \vdots \\ 0 & 0 & \dots & \sigma^2_{\phi_{\gamma_4}} \end{pmatrix} \tag{4.9}$$

According to the Least-Squares principle the best estimate of the fitted variables $\boldsymbol{\eta}$ is achieved when following equations are satisfied simultaneously.

$$\chi^2 = (\boldsymbol{x}-\boldsymbol{\eta})^T G(\boldsymbol{x}-\boldsymbol{\eta}) \;=\; (\text{minimum}), \tag{4.10}$$

$$\boldsymbol{f} \;=\; \boldsymbol{0} \tag{4.11}$$

An approach to solve this problem is the method of Lagrangian multipliers, which introduces undefined Lagrange coefficients for each constraints. This method reformulates the constrained χ^2 minimization (Eq.(4.10) and Eq.(4.11)) to an unconstrained minimization

$$\chi^2 \;= (\boldsymbol{x}-\boldsymbol{\eta})^T G(\boldsymbol{x}-\boldsymbol{\eta}) + 2\boldsymbol{\lambda}^T\boldsymbol{f} \;=\; (\text{minimum}) \tag{4.12}$$

where the $\boldsymbol{\lambda}$ is (2×1)-dimensional Lagrangian multiplier. The minimized condition is achieved when derivatives of χ^2 with respect to all unknowns ($\boldsymbol{\eta}$ and $\boldsymbol{\lambda}$ in this case) are zero:

$$\frac{\partial\chi^2}{\partial\eta} \;=\; -2G(\boldsymbol{x}-\boldsymbol{\eta}) + 2F^T\boldsymbol{\lambda} \;=\; 0 \tag{4.13}$$

$$\frac{\partial\chi^2}{\partial\lambda} \;=\; 2\boldsymbol{f} \;=\; 0 \tag{4.14}$$

where the matrix F (of dimension 2×12) is defined by

$$F \equiv \begin{pmatrix} \frac{\partial f_1}{\partial E^*_{\gamma_1}} & \frac{\partial f_1}{\partial \theta^*_{\gamma_1}} & \cdots & \frac{\partial f_1}{\partial \phi^*_{\gamma_4}} \\ \frac{\partial f_2}{\partial E^*_{\gamma_1}} & \frac{\partial f_2}{\partial \theta^*_{\gamma_1}} & \cdots & \frac{\partial f_2}{\partial \phi^*_{\gamma_4}} \end{pmatrix} \tag{4.15}$$

Thus, from (4.13) and (4.14), we have

$$G(\boldsymbol{\eta}-\boldsymbol{x}) + F^T\boldsymbol{\lambda} = 0 \tag{4.16}$$

$$\boldsymbol{f} = 0 \tag{4.17}$$

The solution of the set of equations (4.16) and (4.17) will be found by an iteration procedure.

Here we introduce the iteration number ν which is the number of iteration to be performed. The equations (4.16) and (4.17) are rewritten with the iteration number ν as follows:

$$G(\boldsymbol{\eta}^{\nu+1}-\boldsymbol{x}) + (F^T)^\nu\boldsymbol{\lambda}^{\nu+1} = 0 \tag{4.18}$$

$$\boldsymbol{f}^\nu = 0, \tag{4.19}$$

where the $\boldsymbol{\eta}^{\nu+1}$ and $\boldsymbol{\lambda}^{\nu+1}$ denote the fitted variables and Lagrange multipliers for the next iteration. A Taylor expansion of the constraint equations (4.19) around the point $\boldsymbol{\eta}^{\nu}$ is

$$\boldsymbol{f}^{\nu} + F^{\nu}(\boldsymbol{\eta}^{\nu+1} - \boldsymbol{\eta}^{\nu}) \quad = \quad 0. \tag{4.20}$$

Here the first-order term was only considered. The Eq.(4.20) is reformulated by eliminating $\boldsymbol{\eta}^{\nu+1}$ with Eq.(4.18). It is then

$$\boldsymbol{f}^{\nu} + F^{\nu}\left[\boldsymbol{x} - G^{-1}(F^{T})^{\nu}\boldsymbol{\lambda}^{\nu+1} - \boldsymbol{\eta}^{\nu}\right] \quad = \quad 0. \tag{4.21}$$

Then, one can obtain new vector $\boldsymbol{\lambda}^{\nu+1}$ of Lagrangian multipliers

$$\boldsymbol{\lambda}^{\nu+1} \quad = \quad F^{\nu}G^{-1}(F^{T})^{\nu}\left[f^{\nu} + F^{\nu}(\boldsymbol{x} - \boldsymbol{\eta}^{\nu})\right]. \tag{4.22}$$

Finally, the fitted variables for $(\nu+1)$-th iteration are now determined from Eq.(4.18).

$$\boldsymbol{\eta}^{\nu+1} \quad = \quad \boldsymbol{x} - G^{-1}(F^{T})^{\nu}\boldsymbol{\lambda}^{\nu+1} \tag{4.23}$$

The measured variables $\boldsymbol{x}$ is good approximation for the initial fitted variables $\boldsymbol{\eta}^{0}$. Therefore, all unknown values for the second iteration ($\boldsymbol{\lambda}^{1}$ and $\boldsymbol{\eta}^{1}$) is obtained from Eq.(4.22) and Eq.(4.23). The iteration is terminated when the constraint equations (4.19) is sufficiently small ($< 10^{-5}$ GeV^2), otherwise the minimization procedure is performed again from Eq.(4.22) with the new fitted variables $\boldsymbol{\eta}^{1}$. After the convergence, the χ^2 value is calculated from Eq.(4.8) using $\boldsymbol{\eta}$ at the final iteration.

The minimized χ^2 for the $\gamma\gamma$-pairs ($\gamma_1\gamma_2$ and $\gamma_3\gamma_4$) under the hypothesis ($\pi^0 \rightarrow \gamma_1\gamma_2,\ \eta \rightarrow \gamma_3\gamma_4$) can be obtained in this way. Since the fitting include two constraints, which require that invariant masses of two $\gamma\gamma$ pairs satisfy known masses of π^0 and η, it is called a **2C-kinematical fitting**. The number of degree of freedom is 2 in this case.

Summary of the iteration procedure

1. Input the measured variables $\boldsymbol{x}$ to the $\boldsymbol{\eta}^{0}$ as initial values.
2. Find the Lagrangian multipliers for the next iteration $\boldsymbol{\lambda}^{\nu+1}$ from Eq.(4.22).
3. Determine the new vector of fitted variables $\boldsymbol{\eta}^{\nu+1}$ from Eq.(4.23).
4. Calculate the constraint values f_1 and f_2 from (4.19). If both f_1 and f_2 are smaller than the threshold 10^{-5} GeV^2, these constraints are regarded as converged, and hence the iteration procedure is stopped, otherwise the process will return back to the (2) and further iteration will be proceeded.
5. The χ^2 value is calculated from Eq.(4.8) with final $\boldsymbol{\eta}$.

4.2.2 Evaluation of the background contaminating to the $\pi^0\eta$ events

The 2C-kinematical fitting discussed previously enables us to extract "$\pi^0\eta$-like samples" from the 4γ-event samples. There is some possibility of contaminating the extracted samples with background events in which the kinematical condition of the 4-photons is similar to that of the $\pi^0\eta$ production events. For this reason, evaluating the background properties is very important before applying the kinematical fitting to the real-data samples. Here, we will identify the origin of the background process and then evaluate how much the background events contribute to the extracted $\pi^0\eta$-like events, which will be referred as "$\pi^0\eta$ samples", after the kinematical fitting.

There was a useful distribution in order to check the background properties. It was the invariant 2γ-mass distribution for the specific $\gamma\gamma$-combination which is selected from 4-photons in the 4γ-event samples as follows:

1. At first, a 1C-kinematical fitting was applied to the all possible $\gamma\gamma$-combinations in the 4γ-event samples. The hypothesis assumed in the kinematical fitting was that a $\gamma\gamma$-pair belongs to decay from π^0 meson. Therefore, the constraint in the fitting algorithm is $m^2_{\gamma_1\gamma_2} - m^2_{\pi^0} = 0$. The number of possible combinations is 6 ($=_4 C_2$) in this case.

2. Afterwards, the $\gamma\gamma$-pair with the minimum χ^2 combination among the all combinations was picked out. The invariant-mass distribution of this $\gamma\gamma$-pair ($M_{2\gamma(1)}$) is expected to localize around the π^0 mass in the case of both $\pi^0\eta$- and $\pi^0\pi^0$-production events. Figure 4.11 shows the $M_{2\gamma(1)}$ distributions for different $M_{4\gamma}$ mass regions with carbon target. For the most of 4γ-events samples the distributions concentrate around π^0 mass. This means that the samples include at least a $\gamma\gamma$-pair originating from π^0 decay.

3. Finally, the remaining $\gamma\gamma$-pair, which was the specific combination described above, was obtained. For $\pi^0\eta$ events the remaining $\gamma\gamma$-pair originates from η decay. Hence, the invariant-mass of the remaining $\gamma\gamma$-pair ($M_{2\gamma(2)}$) distributes around η mass ($M_\eta = 547$ MeV/c^2). Similarly, in the case of $\pi^0\pi^0$ events, the distribution shows a peak at π^0 mass. In contrast, for background events the mass distribution shows a continuum distribution. Therefore, the $M_{2\gamma(2)}$ distribution is useful for checking background properties.

Figure 4.12 shows the $M_{2\gamma(2)}$ distributions for different $M_{4\gamma}$ mass regions with carbon target. Two prominant peaks at π^0 and η mass regions were observed in these plots. Therefore, it is evident that there are the $\pi^0\pi^0$- and $\pi^0\eta$-production events in the 4γ-event samples. A continuum distribution under the η peak was then identified as the background contaminating to the $\pi^0\eta$ samples.

The number of $\pi^0\eta$ signals in the 4γ-event samples was estimated from $M_{2\gamma(2)}$ distributions for both CH_2 and carbon target. A polynomial+Gaussian function were fitted to the distributions in the region of 0.30 GeV/c^2 $< M_{2\gamma(2)} <$ 0.85 GeV/c^2 (see the solid curves in Fig. 4.12). the results for each $M_{4\gamma}$ mass regions are shown in Table 4.4. Note that the number of events for 0.7 GeV/c^2 $< M_{4\gamma} <$ 0.9 GeV/c^2 is underestimated. The reason is that the $M_{2\gamma(2)}$ distribution for $\pi^0\eta$ signals near the production

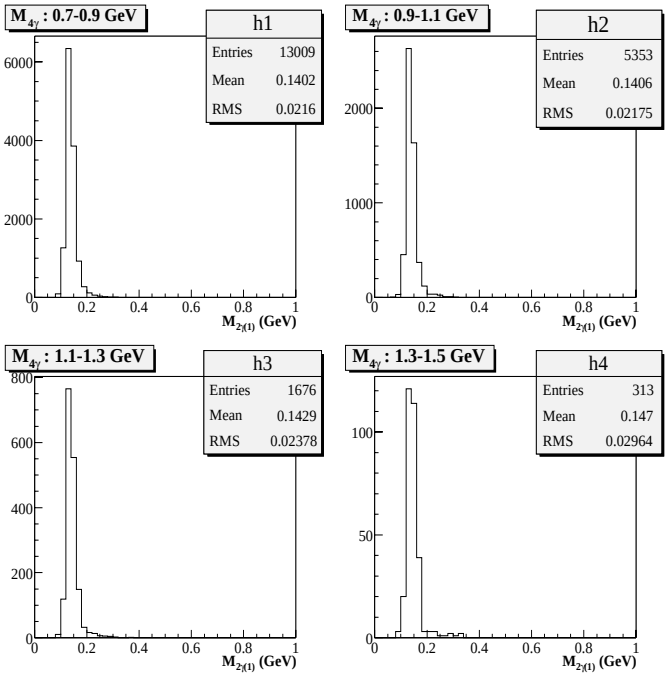

Figure 4.11: $M_{2\gamma(1)}$ distributions for different $M_{4\gamma}$ regions. These plots are obtained from the 4γ-event samples for the carbon target.

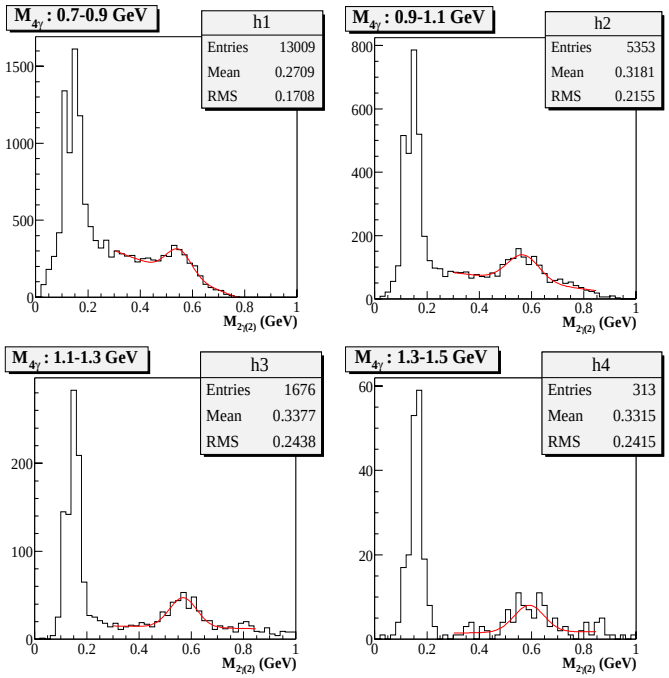

Figure 4.12: $M_{2\gamma(2)}$ distributions of the remaining $\gamma\gamma$-pair for different $M_{4\gamma}$ regions. These plots are obtained from the 4γ-event samples for the carbon target. The solid curve is a fit to data around the η-mass region with Gaussian peak corresponding to η-mass above an straight-line background.

threshold has low-mass tail due to the wrong combination for the 1C-kinematical fitting. This effect will be discussed in Section 4.3.

	0.7-0.9 GeV	0.9-1.1 GeV	1.1-1.3 GeV	1.3-1.5 GeV	0.7 GeV $<M_{4\gamma}$
Carbon (events)	1019±88	640±70	220±33	46±13	1818± 112
CH_2 (events)	723±74	417±55	161±29	—	1256± 94

Table 4.4: The number of $\pi^0\eta$ signals in the 4γ samples for different $M_{4\gamma}$ regions. The result is obtained with polynomial+Gaussian fitting in Fig. 4.12.

The origin of the continuum background in the $M_{2\gamma(2)}$ mass distribution was interpreted qualitatively as the $\gamma N \to \pi^0\pi^0\pi^0 N$ reaction for following reasons:

- Since the polar-angle coverage of the calorimetor was limited in $30^\circ < \theta < 100^\circ$, some photons produced by multi-π^0 (more than $3\pi^0$) production events were emitted to the out of the detector coverage, especially to the forward direction. Therefore, such background reactions cause the continuum background in the $M_{2\gamma(2)}$ mass distribution when only 4-photons are accepted with the calorimeter, and other photons are escaped from detector covarage.

- Following reactions are also allowed kinematically with photon beam ($1.62 < E_{\rm beam} < 2.40$ GeV).

$$\begin{aligned} \gamma N \to \eta N \to \pi^0\pi^0\pi^0 N \quad &: \quad \pi^0 + (\text{uncorreted})\gamma\gamma \text{ detection} \\ \gamma N \to \pi^0\eta N \to \pi^0\pi^0\pi^0\pi^0 N \quad &: \quad \pi^0 + (\text{uncorreted})\gamma\gamma \text{ detection} \end{aligned}$$

  However, the $\gamma N \to \eta N \to \pi^0\pi^0\pi^0 N$ reaction did not contribute to the continuum background at above the $\pi^0\eta$ production threshold because the phase-space factor of the $\eta \to 3\pi^0$ decay was small, and hence the reconstructed 4γ mass was restricted in the lower $M_{4\gamma}$ region (less than $M_{4\gamma} \sim 0.4$ GeV/c^2).

  For the same reason, the background contribution from the $\gamma N \to \pi^0\eta N \to \pi^0\pi^0\pi^0\pi^0 N$ reaction is expected to be small above the $\pi^0\eta$ production threshold since three of π^0 mesons are decay products from η meson.

Therefore, the main background process is likely to be the $\gamma N \to 3\pi^0 N$ reaction which is not via η meson.

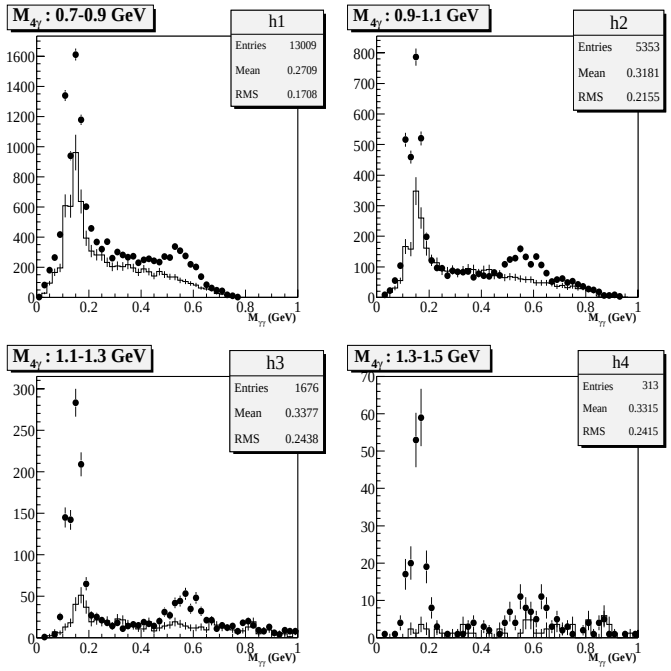

Figure 4.13: $M_{2\gamma(2)}$ distributions of the remaining $\gamma\gamma$-pair for different $M_{4\gamma}$ regions. Filled circles is the same plot as Fig. 4.12 (carbon data). The histograms represent Monte-Carlo samples ($\gamma N \to 3\pi^0 N$)

Here, we demonstrate how the $\gamma N \to 3\pi^0 N$ reaction contributes to the invariant 2γ-mass distribution. Since reaction mechanism for the $3\pi^0$-production reaction was unknown[3], the Monte-Carlo (MC) samples based on the 4-body phase space of $3\pi^0 N$ events, which take Fermi motion of the target nucleon into account, were compared with experimental data. Figure 4.13 shows the same plots as Fig. 4.12, but with the MC samples. The normalization between MC samples and experimental data was achieved by scaling each plots in the region of $0.2 < M_{2\gamma(2)} < 0.4$ GeV/c^2 with plots for $1.1 < M_{4\gamma} < 1.3$ GeV/c^2 mass region. Using one scaling parameter, one can reproduce the continuum background in the $M_{2\gamma(2)}$ distribution for higher $M_{4\gamma}$ mass region ($0.9 < M_{4\gamma} < 1.5$ GeV/c^2). The discrepancy for lower mass region would be caused by low-mass tail of $\pi^0\eta$ signals due to the wrong $\gamma\gamma$ combination (see Fig. 4.35 in Section 4.3).

[3]The preliminary result reported by CB-ELSA collaboration indicates that the reaction mechanism of the $\gamma p \to \pi^0\pi^0 p$ reaction is dominantly sequential processes via $\pi^0\Delta^+$ and $\pi^0 N^*(1520)$ [58]. Thus $\gamma p \to \pi^0 N^*(1520) \to \pi^0\pi^0\pi^0 p$ is one of the possible background processes since the $N^*(1520)$ resonance can decay into the $\pi^0\Delta^+ \to \pi^0\pi^0 p$ final state. In addition to that, the $\gamma p \to K_s\Sigma^+$ reaction is also a candidate of the background when the K_s and Σ^+ are decay into $\pi^0\pi^0$ and $\pi^0 p$, respectively.

4.2.3 Hypothesis testing for $\pi^0\eta$-event selection

Here, we will discuss how to apply the 2C-kinematical fitting, which has been introduced in Section 4.2.1, to the experimental data.

Hypotheses and constraints

The 4γ-event samples above the $\pi^0\eta$ production threshold ($M_{4\gamma} = 0.68$ GeV/c^2) dominantly came from the $\pi^0\pi^0$ and $\pi^0\eta$ production events. Therefore, two hypotheses were tested for each event:

- Hypothesis $H_{\rm I}$: the 4γs belong to decay from $\pi^0\eta$
- Hypothesis $H_{\rm II}$: the 4γs belong to decay from $\pi^0\pi^0$

These hypotheses introduce following constraints for the kinematical fitting:

$$\left.\begin{array}{rcl} M^2_{\gamma_i\gamma_j} - M^2_{\pi^0} &=& 0 \\ M^2_{\gamma_k\gamma_l} - M^2_{\eta} &=& 0 \end{array}\right\} \quad (i \neq j \neq k \neq l) \quad \text{for } H_{\rm I} \tag{4.24}$$

$$\left.\begin{array}{rcl} M^2_{\gamma_i\gamma_j} - M^2_{\pi^0} &=& 0 \\ M^2_{\gamma_k\gamma_l} - M^2_{\pi^0} &=& 0 \end{array}\right\} \quad (i \neq j \neq k \neq l) \quad \text{for } H_{\rm II}, \tag{4.25}$$

where $M_{\gamma_i\gamma_j}$ is invariant mass of i-th and j-th photons, M_{π^0} and M_η are known masses for π^0 (135 MeV/c^2) and η (547 MeV/c^2), respectively.

Possible combinations of $\gamma\gamma$ pairs

Since it is unknown which photons in a pair belong to decay from π^0 and η, it is necessary to investigate all possible $\gamma\gamma$ combinations for each event. The number of possible combinations was counted as follows: (1) a $\gamma\gamma$ pair was picked up from the 4-photons ($_4C_2$), (2) a second $\gamma\gamma$ pair was picked up from the remaining photons ($_2C_2$). Thus, the number of possible combinations for the hypothesis $H_{\rm I}$ is 6:

$$_4C_2 \times_2 C_2 \quad = \quad 6$$

Similarly the number of possible combinations for the hypothesis $H_{\rm II}$ can be obtained in the same way. However it is reduced to be 3 in this case since each π^0 is not distinguishable:

$$\frac{_4C_2 \times_2 C_2}{2!} \quad = \quad 3$$

More plainly, all the two $\gamma\gamma$-combinations which will be investigated for each event are listed as

$$\begin{array}{lll} (\gamma_1\gamma_2, \gamma_3\gamma_4), & (\gamma_1\gamma_3, \gamma_2\gamma_4), & (\gamma_1\gamma_4, \gamma_2\gamma_3) \\ (\gamma_3\gamma_4, \gamma_1\gamma_2), & (\gamma_2\gamma_4, \gamma_1\gamma_3), & (\gamma_2\gamma_3, \gamma_1\gamma_4) \end{array} \quad \text{for } H_{\rm I},$$

and

$$(\gamma_1\gamma_2, \gamma_3\gamma_4), \quad (\gamma_1\gamma_3, \gamma_2\gamma_4), \quad (\gamma_1\gamma_4, \gamma_2\gamma_3) \quad \text{for } H_{\rm II},$$

where the γ_i (i =1, 2, 3 and 4) denotes ith photon. Therefore, the 2C-kinematical fitting was performed totally 9 times for each 4γ-event samples.

Resolutions for the kinematical variables

The information of resolutions for the 12-kinematical variables (E_{γ_1}, θ_{γ_1}, ϕ_{γ_1}, E_{γ_2}, ..., ϕ_{γ_4}) was necessary for the χ^2 estimate in the kinematical fitting. The energy resolution for the i-th photon ($\sigma_{E_{\gamma_i}}$) is obtained from Eq. (3.6):

$$\frac{\sigma_{E_{\gamma_i}}}{E_{\gamma_i}} = \sqrt{\left(\frac{a}{\sqrt{E_{\gamma_i}}}\right)^2 + b^2},$$

where the parameter a and b have been estimated in Section 3.5.1 as

$$a = 0.052, \quad b = 0.044.$$

The angular resolutions for the i-th photon ($\sigma_{\theta_{\gamma_i}}$ and $\sigma_{\phi_{\gamma_i}}$) have been parameterized as Eq. (3.8):

$$\sigma_{\theta(\phi)_{\gamma_i}} = p_0 \exp(p_1 E_{\gamma_i}) + \frac{p_2}{\sqrt{E_{\gamma_i}}} + p_3,$$

where the 4 parameters have been estimated in Section 3.5.2 as

$p_0 = 1.01$, $p_1 = 0.128$, $p_2 = 0.79$ and $p_3 = -3.07$ for polar angle resolution

$p_0 = 1.09$, $p_1 = 0.075$, $p_2 = 1.09$ and $p_3 = -3.20$ for azimuthal angle resolution

In the case of a 100 MeV (1 GeV) incident photon, for example, the resolutions were calculated with above parameterization and they are $\sigma_{E_\gamma} = 17$ MeV (68 MeV), $\sigma_{\theta_\gamma} = 2.0^o$ (1.2^o) and $\sigma_{\phi_\gamma} = 2.1^o$ (1.2^o), respectively. These values were set to the covariant matrix G^{-1} in Eq. (4.9).

χ^2 probability distribution for the minimum χ^2 combination

As mentioned, it is unknown which is the correct $\gamma\gamma$ combination in the 4γ-event samples. Therefore, one need to assume a certain condition in which a combination is most likely to be correct one. Here, the best combinations for each hypothesis were assumed to be the minimum χ^2 combinations among the all possible $\gamma\gamma$-pairs. We defined the χ^2 value for the minimum χ^2 combination under the $H_{\rm I}$ as $\chi^2_{\rm I}$, and that under the $H_{\rm II}$ as $\chi^2_{\rm II}$. A useful quantity for evaluating the goodness of fit, so called χ^2 probability ($\Pr(\chi^2)$), was introduced

$$\Pr(\chi^2) = \int_{\chi^2}^{\infty} f(z,n)dz \tag{4.26}$$

where the $f(z,n)$ denotes the χ^2 probability-density function for n-degree of freedom. The χ^2 probability is a function depending on the χ^2 and is one by one correspondence for each χ^2 value. For pure $\pi^0\eta$ samples, the χ^2 probability distribution with $n = 2$ is expected to show a flat distribution with the 2C-kinematical fitting under the $H_{\rm I}$ [4]. On the other hand, for events coming from background processes, the

[4]There is some possibility for obtaining wrong $\gamma\gamma$-pairs by selecting the minimum χ^2 combination. In this case, the χ^2-probability distribution is shifted toward higher probability side. However the probability of selecting wrong combination is small (at most 7%). Therefore, the $\Pr(\chi^2)$ distribution makes a flat distribution.

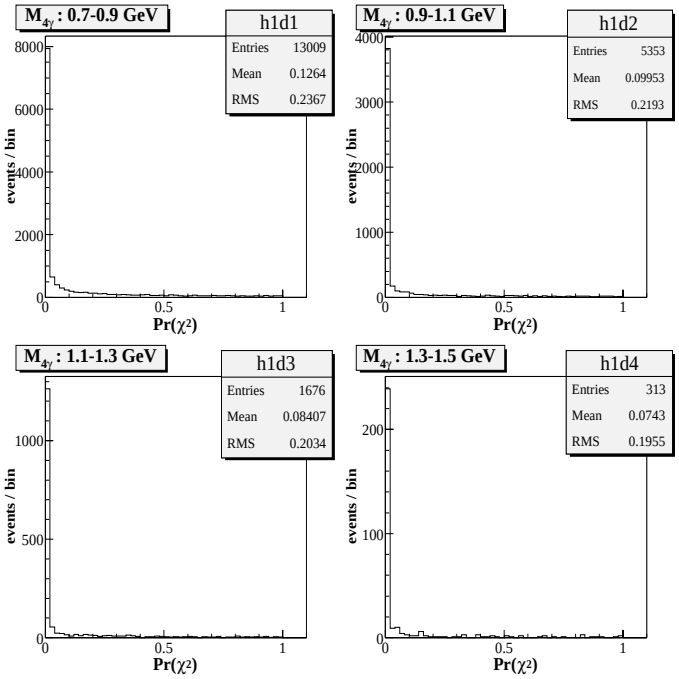

Figure 4.14: $\Pr(\chi^2)$ distributions for the best $\pi^0\eta$ combination for different $M_{4\gamma}$ mass regions. The plots are for all 4γ-event samples with the carbon target.

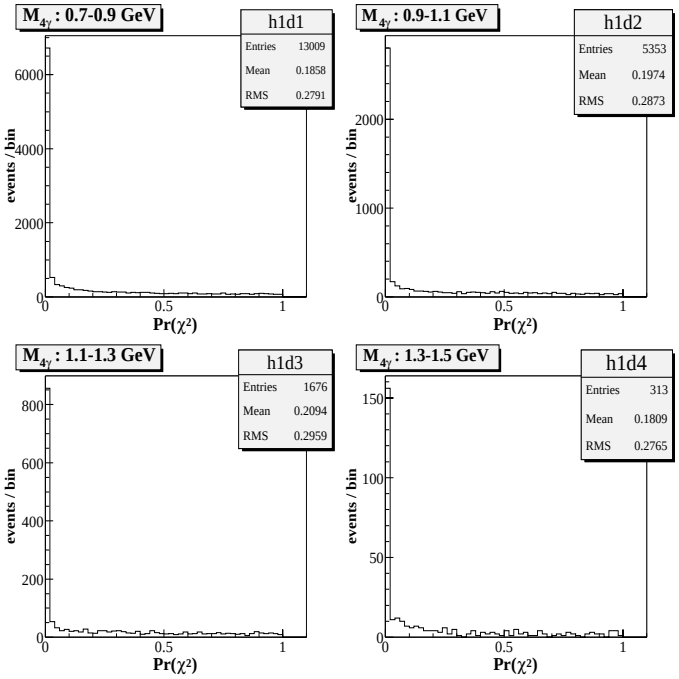

Figure 4.15: $\Pr(\chi^2)$ distributions for the best $\pi^0\pi^0$ combination for different $M_{4\gamma}$ mass regions. The plots are for all 4γ-event samples with the carbon target.

χ^2 values obtained from the fitting are relatively large, and hence the distribution concentrates around $\Pr(\chi^2) = 0$.

Figure 4.14 shows the χ^2 probability distributions for minimum χ^2 combination under the hypothesis $H_{\rm I}$ (we refer to this combination as the best $\pi^0\eta$ combination) for different $M_{4\gamma}$ mass regions. The plots were obtained from all 4γ-event samples with the carbon target. The most of events concentrate at $\Pr(\chi^2) = 0$ for all $M_{4\gamma}$ mass regions. For higher $\Pr(\chi^2)$, the distributions are flat, and hence these events are originated from $\pi^0\eta$ production. The non-flat distribution at lower $\Pr(\chi^2)$ were observed. This aspect becomes more prominent as $M_{4\gamma}$ mass decreases. This is attributed to the contamination from background events, such as $\pi^0\pi^0$ and π^0+ uncorrelated $\gamma\gamma$ events. The χ^2 probability distributions for minimum χ^2 combination under the hypothesis $H_{\rm II}$ (the best $\pi^0\pi^0$ combination) are plotted in Fig. 4.15. Similar discussion is also adopted in this case.

Two-dimensional $\gamma\gamma$-mass plot and χ^2 probability cut

Let us check the 2-dimensional plots of the invariant masses of two $\gamma\gamma$-pairs for both the best $\pi^0\eta$ combination (Fig. 4.16) and the best $\pi^0\pi^0$ combination (Fig. 4.17). The data in these plots are all 4γ-event samples with the carbon target. By comparing both figures, one notice following remarks:

- The prominent bands along the x- and y-axis in Fig. 4.17 come from the π^0+uncorrelated $\gamma\gamma$ background due to multi-π^0 production, which has been discussed in Section 4.2.2.
- The $\pi^0\eta$ spots are clearly visible for $M_{4\gamma} > 0.9$ GeV/c^2 in Fig. 4.16. However for the plot with 0.7 GeV$< M_{4\gamma} < 0.9$ GeV/c^2, the spot corresponding to the $\pi^0\eta$ events are overlapped with the strong diagonal band and is not clearly seen.
- The diagonal bands along the physical boundary ($M_{\gamma\gamma}|_x + M_{\gamma\gamma}|_y = M_{4\gamma}$) in the plots for the best $\pi^0\eta$ combinations are originating from the $\pi^0\pi^0$ and π^0+uncorrelated $\gamma\gamma$ events.
- The 4γ-event samples above the $\pi^0\eta$ production threshold dominantly come from $\pi^0\pi^0$, $\pi^0\eta$ and π^0+uncorrelated $\gamma\gamma$ events.

In order to select $\pi^0\eta$-event candidates, a $\Pr(\chi^2_I) > 0.1$ cut was applied for all 4γ-event samples. This cut was corresponding to the 1.64σ cut for 2C-kinematical fitting under the hypothesis $H_{\rm I}$. Figure 4.18 and Figure 4.19 show the 2-dimensional plots of the invariant $\gamma\gamma$ masses for both the best $\pi^0\eta$ and the best $\pi^0\pi^0$ combinations with the $\Pr(\chi^2_I) > 0.1$ cut. The ellipsoidal spots in Fig. 4.18 are corresponding to the region of the 1.64σ mass resolution of the calorimeter for $\pi^0\eta$. For lower $M_{4\gamma}$ mass ($M_{4\gamma} < 0.9$ GeV/c^2), it is clear that the events coming from $\pi^0\pi^0$ and π^0+ uncorrelated $\gamma\gamma$ are contaminating to the $\pi^0\eta$ candidates. On the other hand, for higher $M_{4\gamma}$ mass, the contribution from these background events is suppressed; for example, the bands along the x- and y-axis, which come from the π^0+ uncorrelated $\gamma\gamma$ background, and $\pi^0\pi^0$ spot in Fig. 4.17 are strongly suppressed in Fig. 4.19.

One can obtain the $\pi^0\pi^0$ candidates in the same way. We applied a $\Pr(\chi^2_{\rm II}) > 0.1$ cut for 4γ-event samples, and the result is shown in Fig. 4.20 and Fig. 4.21. The spots in Fig. 4.21 are corresponding to the

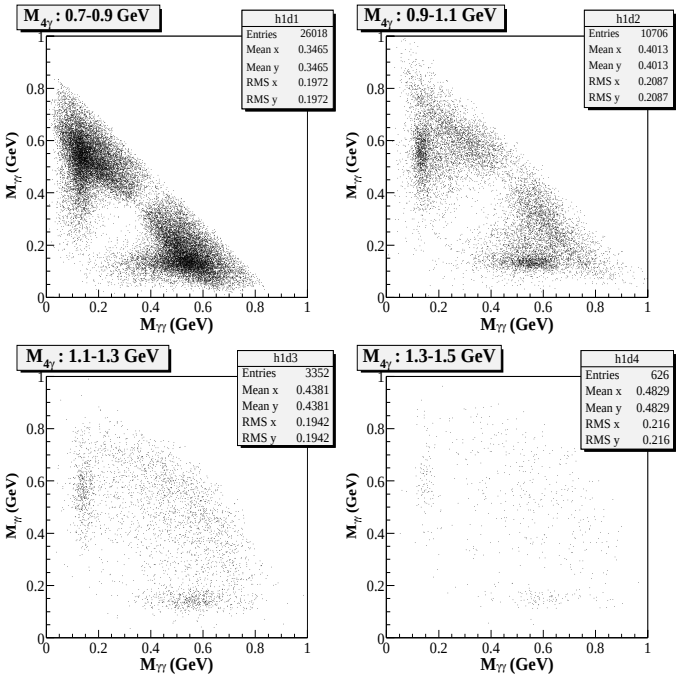

Figure 4.16: Two-dimensional plots of the invariant masses of two $\gamma\gamma$-pairs with the best $\pi^0\eta$ combination for different $M_{4\gamma}$ mass regions. All 4γ-event samples with the carbon target are plotted. These plots include 2 entries/event so that the plots are symmetric.

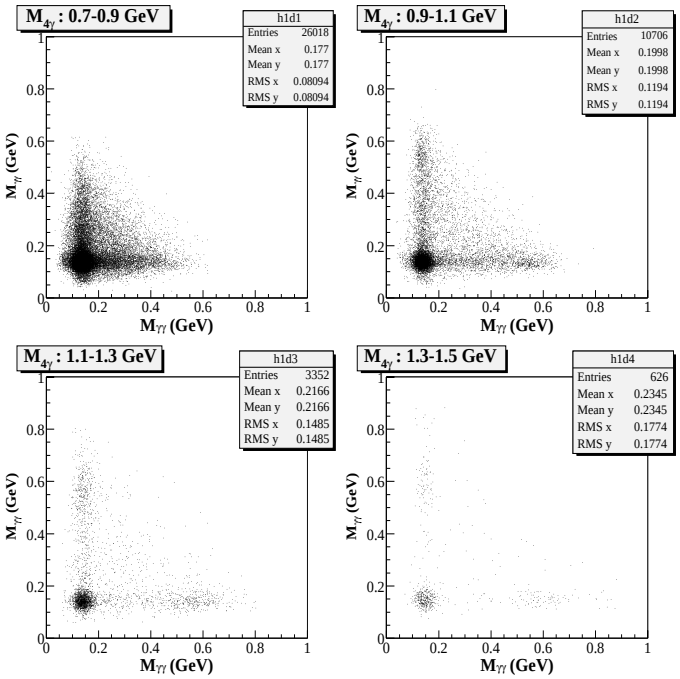

Figure 4.17: Two-dimensional plots of the invariant masses of two $\gamma\gamma$-pairs with the best $\pi^0\pi^0$ combination for different $M_{4\gamma}$ mass regions. All 4γ-event samples with the carbon target are plotted. These plots include 2 entries/event so that the plots are symmetric.

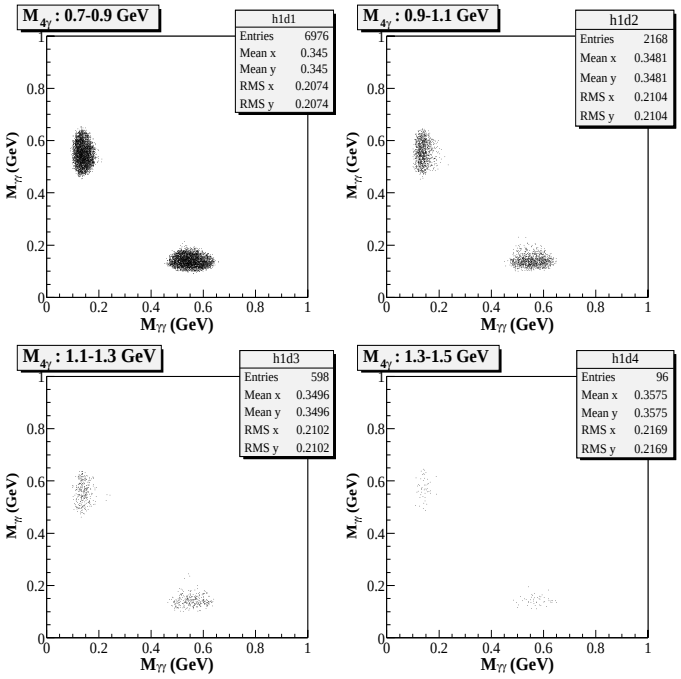

Figure 4.18: Two-dimensional plots of the invariant masses of two $\gamma\gamma$-pairs with the best $\pi^0\eta$ combination for different $M_{4\gamma}$ mass regions. A $\Pr(\chi^2_{\rm I}) > 0.1$ cut is required. Other conditions are same as Fig. 4.16.

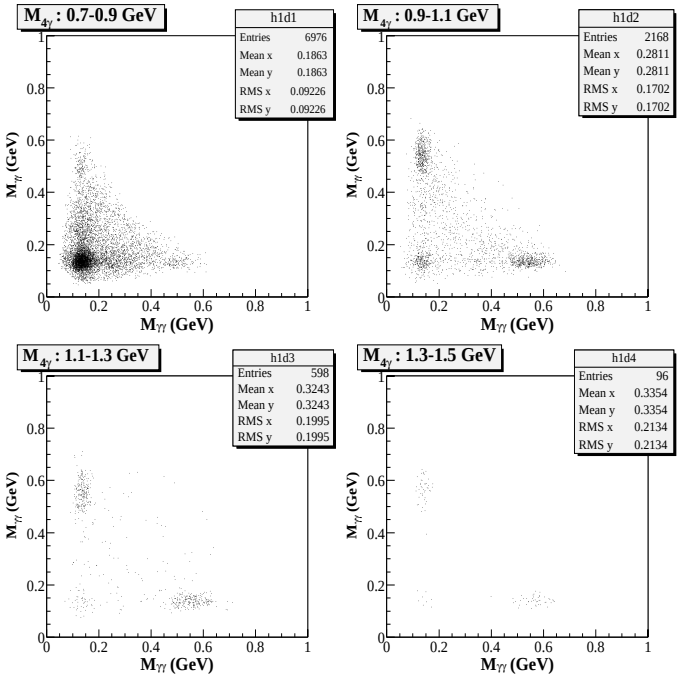

Figure 4.19: Two-dimensional plots of the invariant masses of two $\gamma\gamma$-pairs with the best $\pi^0\pi^0$ combination for different $M_{4\gamma}$ mass regions. A $\Pr(\chi^2_{\rm I}) > 0.1$ cut is required. Other conditions are same as Fig. 4.17.

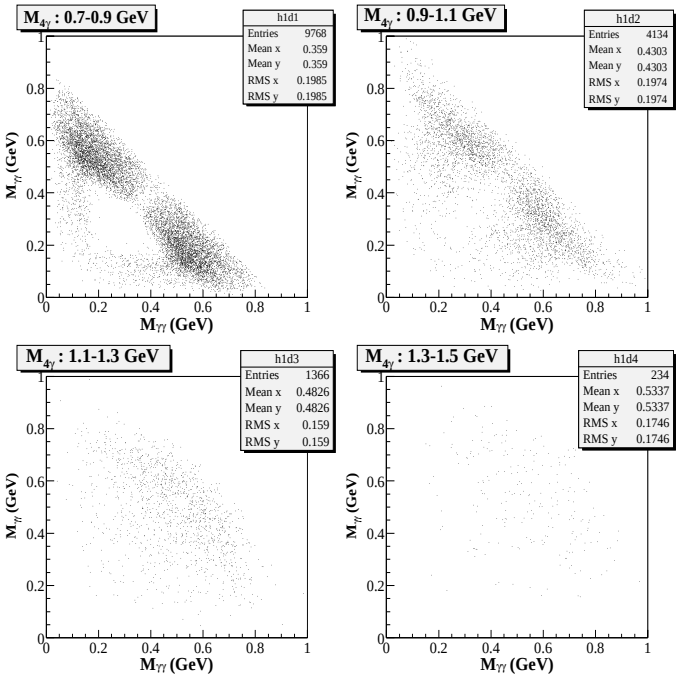

Figure 4.20: Two-dimensional plots of the invariant masses of two $\gamma\gamma$-pairs with the best $\pi^0\eta$ combination for different $M_{4\gamma}$ mass regions. A $\Pr(\chi^2_{\rm II}) > 0.1$ cut is required. Other conditions are same as Fig. 4.16.

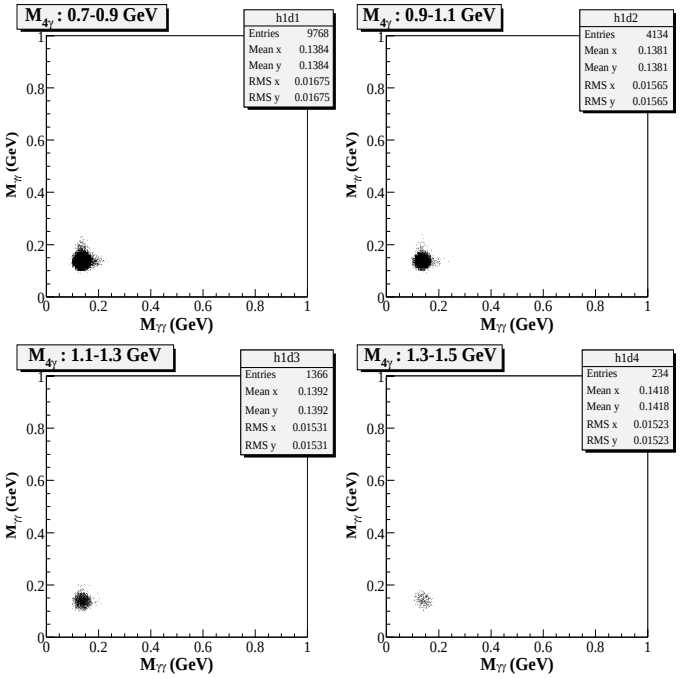

Figure 4.21: Two-dimensional plots of the invariant masses of two $\gamma\gamma$-pairs with the best $\pi^0\pi^0$ combination for different $M_{4\gamma}$ mass regions. A $\Pr(\chi^2_{\rm II}) > 0.1$ cut is required. Other conditions are same as Fig. 4.17.

region of the 1.64σ mass resolution of the calorimeter for $\pi^0\pi^0$. It is obvious that the $\pi^0\pi^0$ events make the diagonal band along the physical boundary in the plots of the best $\pi^0\eta$ combination. For this reason, the $\pi^0\pi^0$ events were expected to be contaminating to the $\pi^0\eta$ candidates at lower $M_{4\gamma}$-mass region by picking up a wrong combination. The cut statistics for both the $\Pr(\chi^2_I) > 0.1$ cut and the $\Pr(\chi^2_{II}) > 0.1$ cut are summarized in Table 4.5 and Table 4.6, respectively.

Target	4γ-event samples	with $\Pr(\chi^2_I) > 0.1$ cut	rejection factor
Carbon	126828	6042	21.00±0.26
CH_2	82156	4288	19.16±0.28
Copper	65540	2496	26.26±0.52
Empty	15813	643	24.59±0.95

Table 4.5: Cut statistics for the $\Pr(\chi^2_I) > 0.1$ cut ($\pi^0\eta$ candidates)

Target	4γ-event samples	with $\Pr(\chi^2_{II}) > 0.1$ cut	rejection factor
Carbon	126828	51562	2.460±0.008
CH_2	82156	34602	2.374±0.010
Copper	65540	23612	2.776±0.014
Empty	15813	6330	2.498±0.024

Table 4.6: Cut statistics for the $\Pr(\chi^2_{II}) > 0.1$ cut ($\pi^0\pi^0$ candidates)

Rejection the $\pi^0\pi^0$ contamination in the $\pi^0\eta$ candidates

The $\pi^0\eta$ candidates, obtained by applying the $\Pr(\chi^2_I) > 0.1$ cut, involved the $\pi^0\pi^0$ background at lower $M_{4\gamma}$ region. For further clean up, we introduced an additional cut in order to suppress the $\pi^0\pi^0$ contamination in the $\pi^0\eta$ candidates. Figure 4.22 shows the $\Pr(\chi^2_{II})$ versus $\Pr(\chi^2_I)$ plots for 4γ-event samples with the carbon target. The most of events are localized at $\Pr(\chi^2_I) = 0$ or $\Pr(\chi^2_{II}) = 0$; However, some of events are scattered whole region of the plot. This means that these events satisfy both $\pi^0\eta$- and $\pi^0\pi^0$-event conditions at the same time. Figure 4.23 shows the probability of satisfying this condition as a function of the $M_{4\gamma}$ mass. It is clear that these events dominantly come from the 4γ-event samples near the $\pi^0\eta$ production threshold.

A $\Pr(\chi^2_I) > \Pr(\chi^2_{II})$ cut (equivalently $\chi^2_I < \chi^2_{II}$ cut) rejects selectively $\pi^0\pi^0$-like events from the $\pi^0\eta$ candidates. Two dimensional plots for the $\pi^0\eta$ candidates with $\Pr(\chi^2_{II}) > \Pr(\chi^2_I)$ are shown in Fig. 4.24 and Fig. 4.25. The events are localized inside both $\pi^0\eta$ and $\pi^0\pi^0$ spots. These events were rejected with the $\Pr(\chi^2_I) > \Pr(\chi^2_{II})$ cut. Figure 4.26 and Figure 4.27 show the same plots but with $\Pr(\chi^2_I) > \Pr(\chi^2_{II})$ cut. In comparison with these plots and Fig. 4.20 and Fig. 4.21, the $\pi^0\pi^0$ spots for the best $\pi^0\pi^0$ combinations is suppressed by applying the cut. The cut statistics of the $\Pr(\chi^2_I) > \Pr(\chi^2_{II})$ cut is summarized in Table 4.7. Although it seems that in the lower $M_{4\gamma}$ region the background events from $\pi^0\pi^0$ are still remained, we refer to these samples as "**$\pi^0\eta$-event samples**" for further analysis, which are 4γ-event samples satisfying $\Pr(\chi^2_I) > 0.1$ and $\Pr(\chi^2_I) > \Pr(\chi^2_{II})$.

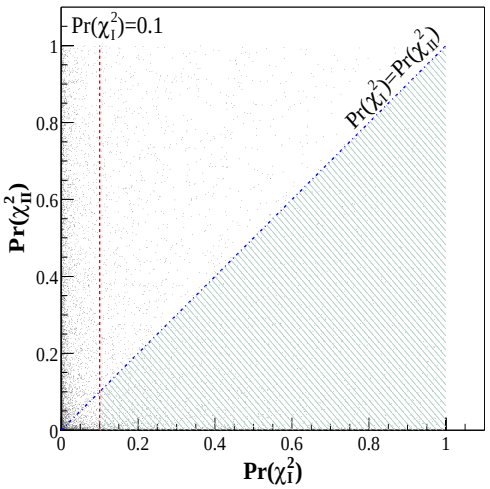

Figure 4.22: Plot of the $\Pr(\chi^2_{\rm II})$ versus $\Pr(\chi^2_I)$ for 4γ-event samples with the carbon target. The most of events concentrate along the x- and y-axis. The dotted line corresponds to the cut position for $\pi^0\eta$-candidate selection.

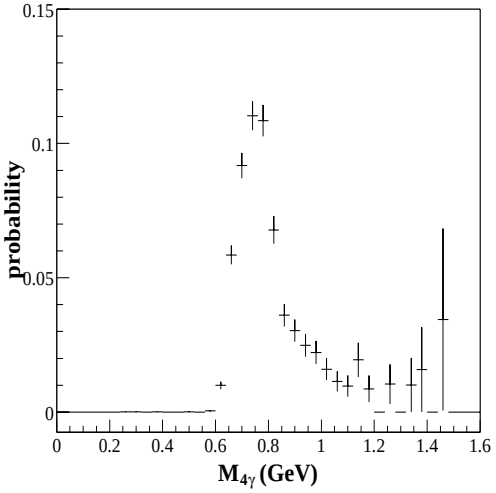

Figure 4.23: Probability of finding events with $\Pr(\chi^2_I) > 0.1$ and $\Pr(\chi^2_{\rm II}) > 0.1$ in the 4γ-event samples as a function of the $M_{4\gamma}$.

Target	$\pi^0\eta$ candidates	with $\Pr(\chi^2_I)$ >$\Pr(\chi^2_{\rm II})$ cut	rejection factor
Carbon	6042	5011	1.20±0.01
CH_2	4288	3547	1.21±0.01
Copper	2496	2143	1.16±0.01
Empty	643	529	1.22±0.02

Table 4.7: Cut statistics for the $\Pr(\chi^2_I)$ >$\Pr(\chi^2_{\rm II})$ cut ($\pi^0\eta$-event samples)

Here, the estimate of the signal to noise (S/N) ratio for the $\pi^0\eta$-event samples is discussed. The signal (S) was defined as the number of $\pi^0\eta$ signals in the $\pi^0\eta$-event samples. The noise (N) was defined as the number of background events, such as $\pi^0\pi^0$ production, in the $\pi^0\eta$-event samples. Table 4.8 shows a breakdown of the $\pi^0\eta$-event samples in each $M_{4\gamma}$ region. The $\pi^0\eta$-event samples involve both the signal and noise events, and hence the number of $\pi^0\eta$-event samples is equal to $S+N$. The number S was regarded as 90% of $\pi^0\eta$ signals which were estimated in Section 4.2.2 (see Table 4.4). Here, the "90%" is attributed to the 10% acceptance loss due to the $\Pr(\chi^2_I) > 0.1$ cut. Therefore, we have

$$\frac{S}{N} = \left(\frac{S+N}{S} - 1\right)^{-1} = \left(\frac{(\text{number of } \pi^0\eta \text{ event samples})}{(\text{number of } \pi^0\eta \text{ signals})} - 1\right)^{-1}.$$

The result is listed in Table 4.9. Note that the number of $\pi^0\eta$ signals for $M_{4\gamma} = 0.7$-0.9 GeV/c^2 in Table 4.4 is underestimated as mentioned previously. Thus, the S/N ratio for this $M_{4\gamma}$ mass region is expected to be slightly higher than the listed value in Table 4.9. Consequently, the S/N ratio for $M_{4\gamma} > 0.7$

	0.7-0.9 GeV	0.9-1.1 GeV	1.1-1.3 GeV	1.3-1.5 GeV	0.7 GeV<$M_{4\gamma}$
Carbon (events)	2865	1015	286	45	4213
CH_2 (events)	1953	779	189	33	2958

Table 4.8: The number of $\pi^0\eta$-event samples for each $M_{4\gamma}$ mass region.

	0.7-0.9 GeV	0.9-1.1 GeV	1.1-1.3 GeV	1.3-1.5 GeV	0.7 GeV<$M_{4\gamma}$
Carbon (events)	0.47±0.06	1.3±0.3	2.2±1.2	12±50	0.63±0.06
CH_2 (events)	0.50±0.08	0.9±0.2	3.3±2.7	—	0.62±0.07

Table 4.9: S/N ratio of the $\pi^0\eta$-event samples for each $M_{4\gamma}$ mass region.

GeV/c^2 in the Table is also somewhat better. Nevertheless, it should be pointed out that the S/N ratio for lower $M_{4\gamma}$ mass region is not good. Probably stronger cut is needed. Such a cut will be introduced in Section 4.4 later.

Summary

In Section 4.2, we have discussed the hypothesis testing for obtaining the $\pi^0\eta$-event samples from the 4γ-event samples which have been selected in Section 4.1. After the introduction of the kinematical-fitting method, a conceivable background contaminating to the $\pi^0\eta$-event samples was studied: π^0 and uncorrelated $\gamma\gamma$ events coming from the $\gamma N \rightarrow 3\pi^0 N$ reaction was dominant. The $\pi^0\eta$-event samples have been obtained by applying following 2 cuts:

$$\Pr(\chi^2_I) > 0.1 \quad \text{and} \quad \Pr(\chi^2_I) > \Pr(\chi^2_{\rm II}).$$

The S/N ratio of the $\pi^0\eta$-event samples was not good, particularly near the $\pi^0\eta$ production threshold ($M_{4\gamma} = 0.68$ GeV/c^2) because of background from $\pi^0\pi^0$ production events. Therefore, further strong cut was necessary in order to improve the S/N ratio. This cut will be introduced in Section 4.4.

In the next section, we will study the response of the $\pi^0\eta p$ signals with Monte-Carlo samples.

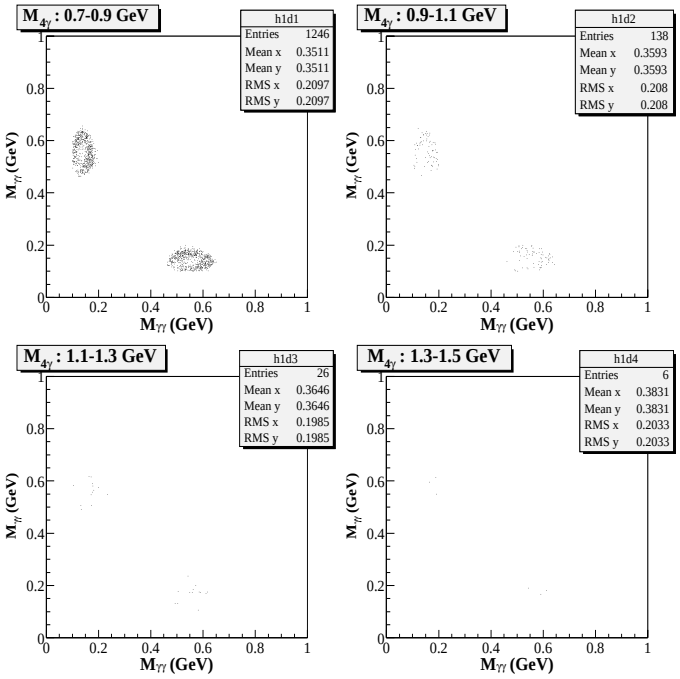

Figure 4.24: Two-dimensional plots of the invariant masses of two $\gamma\gamma$-pairs with the best $\pi^0\eta$ combination for different $M_{4\gamma}$ mass regions. A $\Pr(\chi^2_{\rm II}) > 0.1$ cut is required. Other conditions are same as Fig. 4.16.

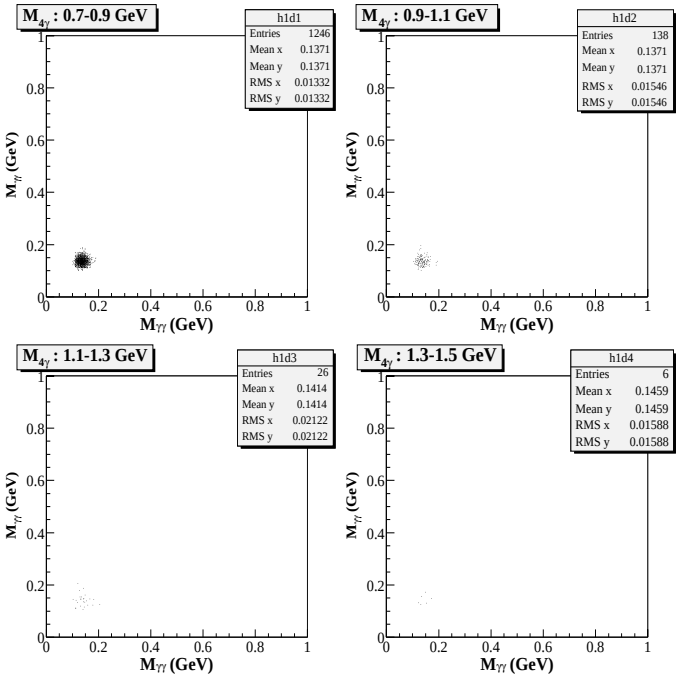

Figure 4.25: Two-dimensional plots of the invariant masses of two $\gamma\gamma$-pairs with the best $\pi^0\pi^0$ combination for different $M_{4\gamma}$ mass regions. A $\Pr(\chi^2_{\rm II}) > 0.1$ cut is required. Other conditions are same as Fig. 4.17.

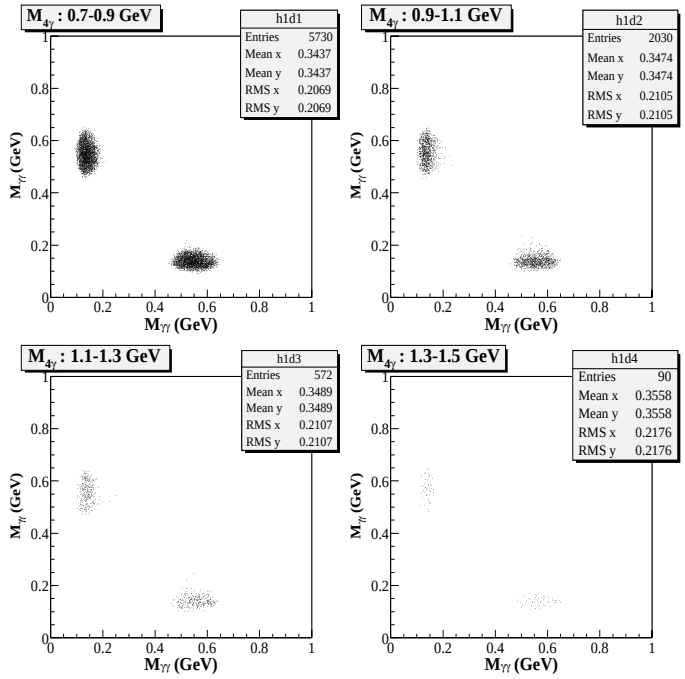

Figure 4.26: Two-dimensional plots of the invariant masses of two $\gamma\gamma$-pairs with the best $\pi^0\eta$ combination for $\pi^0\eta$-event samples. Other conditions are same as Fig. 4.16.

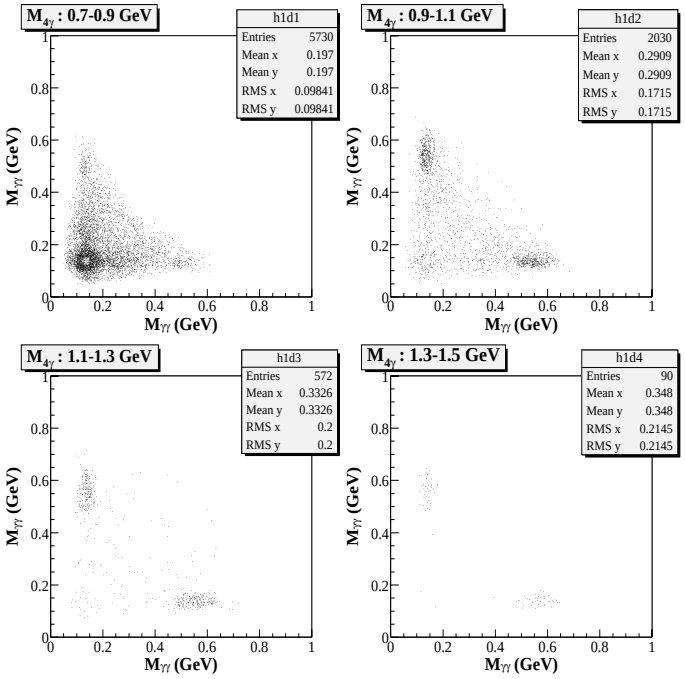

Figure 4.27: Two-dimensional plots of the invariant masses of two $\gamma\gamma$-pairs with the best $\pi^0\pi^0$ combination for $\pi^0\eta$-event samples. Other conditions are same as Fig. 4.17.

4.3 Monte-Carlo study for the $\gamma p \to \pi^0 \eta p$ reaction

In this section, the signals from the $\gamma p \to \pi^0 \eta p$ reaction with actual experimental setup will be evaluated by using Monte-Carlo (MC) event samples. The MC samples were generated under the assumption that the reaction follows 3-body phase space distribution. The possible final states of the $\gamma p \to \pi^0 \eta p$ reaction are mainly 4-channels as listed below.

$$\begin{aligned}
\pi^0 + \eta + p &\to 4\gamma + p \ (39.4\%) \\
\pi^0 + \eta + p &\to \pi^0 + 3\pi^0 + p \to 8\gamma + p \ (32.5\%) \\
\pi^0 + \eta + p &\to \pi^0 + \pi^+\pi^-\pi^0 + p \to \pi^+ + \pi^- + 4\gamma + p \ (22.6\%) \\
\pi^0 + \eta + p &\to \pi^0 + \pi^+\pi^-\gamma + p \to \pi^+ + \pi^- + 3\gamma + p \ (4.7\%)
\end{aligned}$$

In this section, we assumed that the generated π^0 and η mesons decayed into only 2γ-channels (thus only the $4\gamma p$ final state was considered). The z-position distribution of the production vertex was assumed to be a flat distribution in the region of $z = [-25$ mm, $+25$ mm], which was the same size of the CH_2 target. For x and y directions, Gaussian distributions of $\sigma_x = 6.2$ mm and $\sigma_y = 2.0$ mm within $r < 20$ mm region were assumed by taking the size of the target and the beam spread into account. A simulation code based on the Geant4 package was utilized for this purpose. The lead/SCIFI detector was defined as an approximate geometry with homogeneous materials to reduce computing time. This simulation code (CODE 2) is discussed in detail in appendix B.

4.3.1 Photon reconstruction

Since the detector coverage of the backward calorimeter was limited, the probability of accepting all 4γs coming from $\pi^0\eta$ decay was small. Figure 4.28 shows the probability distribution of the number of accepted photon with the backward calorimeter ($N_{\rm accept}$) for generated 4γs. Note that the histogram was obtained by just counting the number of photon emitted into the angular region from 40^o to 90^o. Therefore, low energy photons ($E_\gamma < 20$ MeV) and photons with small opening angle ($\theta_{\gamma\gamma} < 10^o$) were also counted, where those photons would be lost in the clustering process. The probability of $N_{\rm accept} = 4$ was only 2.8% because of small detector coverage. The most probable value of $N_{\rm accept}$ was about 1.5 (see Fig. 4.28).

Now we concentrate on event samples with $N_{\rm accept} = 4$. At first, the photon reconstruction with $E_{th} = 20$ MeV was performed for the event samples. The distribution of number of reconstructed neutral cluster $N_{\gamma(40^\circ-90^\circ)}$, defined in Section 4.1.2, is shown in Fig. 4.29 as a solid histogram. The result shows that the reconstructing 4-neutral cluster is most probable (about 67%). However, events with the $N_{\gamma(40^\circ-90^\circ)} < 4$ are also seen. There are two reasons: (1) photons with energy less than 20 MeV were included, which were insensitive for the clustering algorithm (2) some photons hit near each other, and hence the clustering algorithm did not identify both of them (cluster merging). For the $\gamma p \to \pi^0 \eta p$ reaction, events with $N_{\gamma(40^\circ-90^\circ)} < 4$ was dominantly caused by the latter reason. The hatched histogram in Fig. 4.29 shows the distribution of the number of reconstructed cluster with the

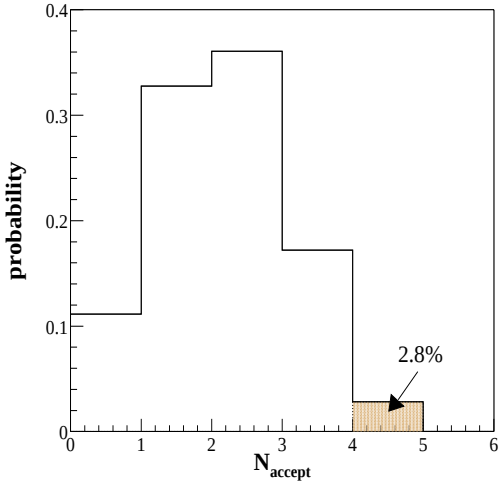

Figure 4.28: Probability distribution of the number of photons emitted into the angular region of $40^{\circ} < \theta_{\gamma} < 90^{\circ}$ for the $\gamma p \to \pi^0 \eta p \to 4\gamma p$ reaction.

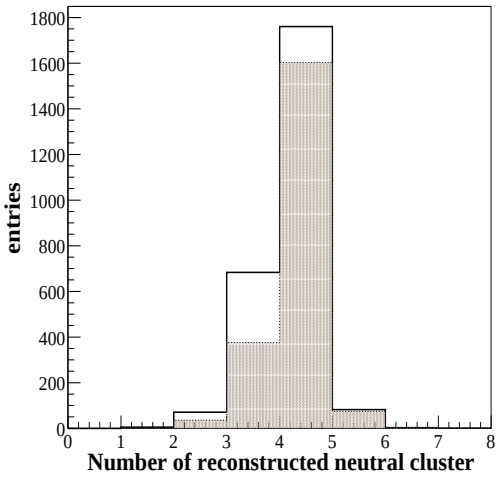

Figure 4.29: The number of reconstructed neutral clusters for 4γ-detection events for events with $N_{\rm accept} = 4$. The edge module cut has already applied in the plots. The hatched histogram represents the result with the cluster-merging cut.

cluster-merging cut ($F < 0.02$). Applying the cluster-merging cut, one can reject about half of events with $N_{\gamma(40^{\circ}-90^{\circ})} = 3$.

As for the events with $N_{\gamma(40^{\circ}-90^{\circ})} = 5$, these events were due to the contribution of the cluster splitting. The cluster splitting is caused by backward-scattering process, which makes energy spoils irrespective of the photon-hit position as discussed in Section 3.3.1.

4.3.2 The effect of the cluster splitting

So far, we have discussed the event samples with $N_{\rm accept} = 4$. However, since $N_{\rm accept}$ is unknown in the real data analysis, the number of reconstructed cluster $N_{\gamma(40^{\circ}-90^{\circ})}$ becomes an index to obtain 4γ-event samples. Actually, we required $N_{\gamma(40^{\circ}-90^{\circ})} = 4$ in order to select the 4γ-event samples in the analysis (see Section 4.1.2). In this case, it is difficult to know the influence from the background due to cluster splitting events. Therefore, it is worth investigating the effect from the background due to cluster splitting with MC event samples.

Contribution to the 4γ-event samples

Figure 4.30 shows $N_{\rm accept}$ distribution with same cuts as introduced to obtain the 4γ-event samples in the data analysis (see Section 4.1.2). As one can see, selected 4γ-event samples mainly come from the $N_{\rm accept} = 4$ events. However, events with $N_{\rm accept} < 4$ also contribute in the samples. This shows that

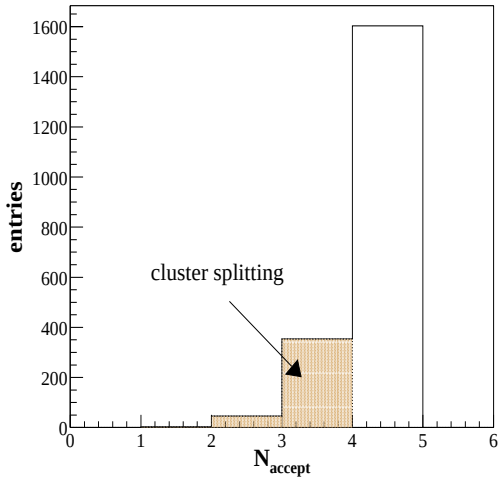

Figure 4.30: Distribution of the number of accepted photons ($N_{\rm accept}$) with same cuts as the cuts to obtain 4γ-event samples in the real data analysis (see section 4.1.2). The hatched region represents contribution from cluster splitting events.

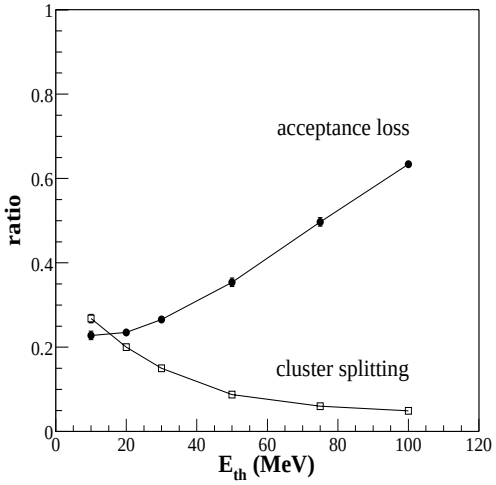

Figure 4.31: E_{th} dependence of the contribution from the cluster-splitting events (open squares) and acceptance loss (filled circles).

the number of photon emitted into the detector region is only three photons (or sometime two photons), but observed number of cluster is 4. Therefore, the origin of these events is cluster-splitting events.

The contribution from cluster-splitting events depends on the energy threshold E_{th} defined in the clustering algorithm. This dependence is plotted in Fig. 4.31 as a function of the E_{th}. In case of $E_{\rm th} = 20$ MeV, the ratio of the number of cluster-splitting events to the total 4γ-event samples was about 20%. The effect of cluster splitting is suppressed by increasing the energy threshold $E_{\rm th}$ as described in Section 3.3. For instance, by increasing the threshold from 20 MeV to 50 MeV, the contamination of the cluster-splitting events was reduced from 20% to 10%. On the other hands, increasing the $E_{\rm th}$ causes acceptance loss because the sensitivity for low-energy photons decreases in this case. It might be better to choose $E_{th} = 50$ MeV in comparison with $E_{\rm th} = 20$ MeV since the background events due to the cluster-splitting would be reduced. However, we kept the E_{th} to be 20 MeV because (1) the statistics of the final $\pi^0\eta p$ samples in the experimental data was not enough (see Section 4.4), and hence it was better to keep $E_{\rm th}$ to be small value in order to gain the signal acceptance, (2) most of the background events could be rejected by applying the χ^2 probability cut under the $\pi^0\eta$ hypothesis ($H_{\rm I}$).

Contribution to the invariant 4γ-mass distribution

Figure 4.32 shows a 2-dimensional plot of the invariant 4γ-mass ($M_{4\gamma}$) reconstructed from the 4γ-event samples versus invariant 4γ-mass calculated from MC event-generator. For the most of events, the

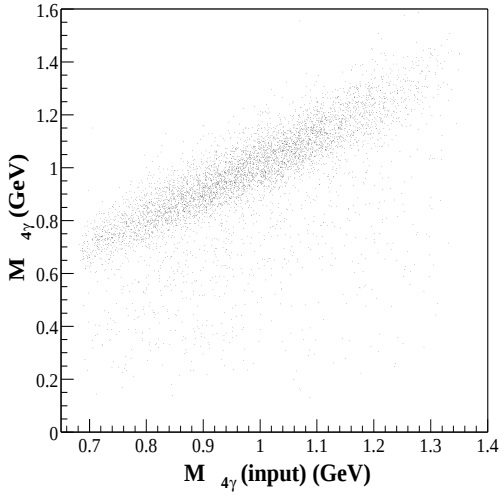

Figure 4.32: Two dimensional plot of the observed invariant 4γ-mass ($M_{4\gamma}$) versus invariant 4γ-mass for generated by Monte-Carlo simulation $M_{4\gamma}$(input) for the 4γ-event samples.

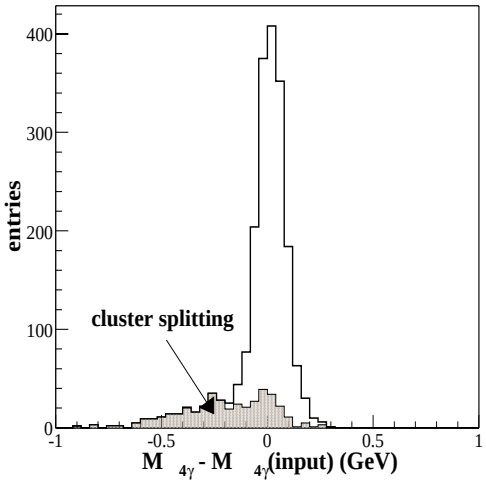

Figure 4.33: Residual distribution of the invariant 4γ-mass for the 4γ event samples. The hatched region is contribution from the cluster-splitting events.

distribution of the reconstructed $M_{4\gamma}$ was localized at correct mass with an extent due to the finite detector resolution. For some events, the distribution deviated from correct mass; it was scattered at lower $M_{4\gamma}$ region. The residual distribution ($M_{4\gamma} - M_{4\gamma}$(input)) for the same samples is shown in Fig. 4.33. One can see a low-energy tail in the distribution. The residual distribution of the cluster-splitting events (events with $N_{\rm accept} < 4$) is also superimposed as a hatched histogram in Fig. 4.33. From this plot, it is obvious that the low energy tail is originated from the cluster-splitting events. After all, we understood the cluster-splitting events resulted in a lower-mass tail in invariant 4γ-mass distribution; For other events the invariant 4γ-mass was correctly reconstructed.

4.3.3 $\pi^0\eta$-event analysis with MC samples

Here, we will discuss $\pi^0\eta$-event analysis with MC samples. In Section 4.2.2, the $M_{2\gamma(1)}$ and $M_{2\gamma(2)}$ distributions were introduced in order to check the background properties and to estimate $\pi^0\eta$-signals for experimental data. Let us check these distributions for clean $\pi^0\eta p$ samples generated by Monte-Carlo simulation. Figure 4.34 and 4.35 show the $M_{2\gamma(1)}$ and $M_{2\gamma(2)}$ distributions for 4γ-event samples obtained from MC samples. These plots can be compared with those from experimental data (see Fig. 4.11 and Fig. 4.12). The π^0 peaks for each $M_{4\gamma}$ mass regions were correctly reconstructed in Fig. 4.34. Furthermore, the η peaks were also observed in Fig. 4.35 correctly. The low-mass tail in the $M_{2\gamma(2)}$ distribution in the region of $0.7 < M_{4\gamma} < 0.9$ GeV was caused by background events due to the cluster-splitting and misidentification of the best π^0 combination. This means that the estimate of the number

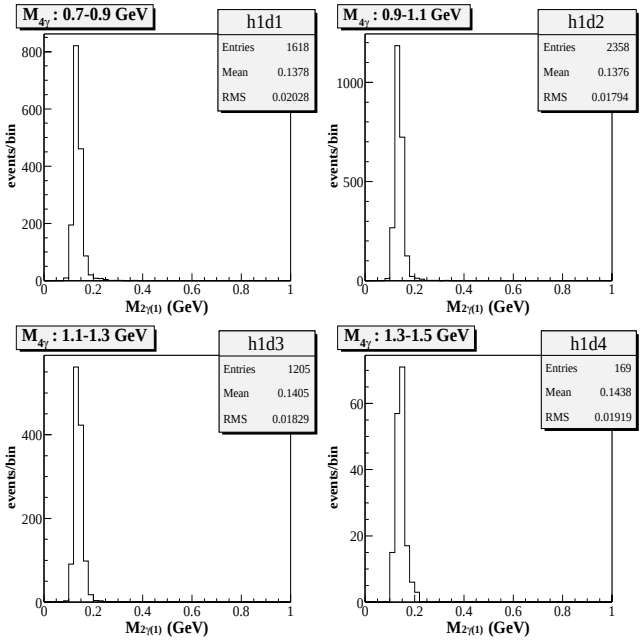

Figure 4.34: $M_{2\gamma(1)}$ distributions of the 4γ-event samples [MC samples (the $\gamma p \to \pi^0 \eta p \to 4\gamma p$ reaction)].

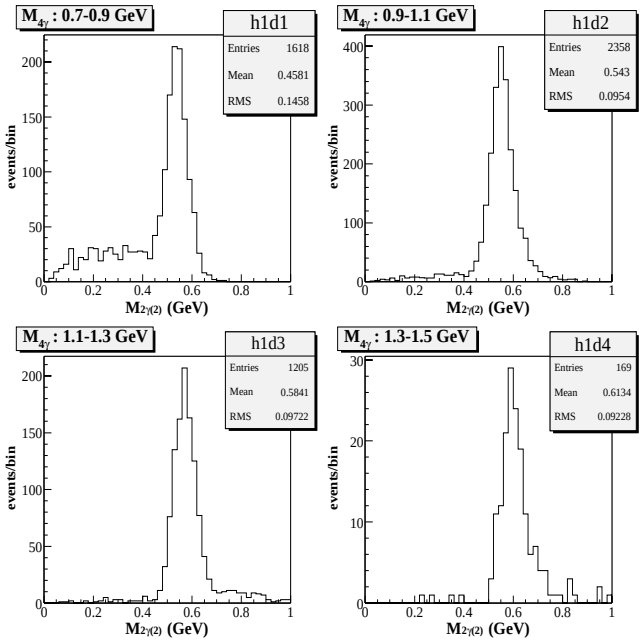

Figure 4.35: $M_{2\gamma(2)}$ distributions of the 4γ-event samples [MC samples (the $\gamma p \to \pi^0 \eta p \to 4\gamma p$ reaction)].

of $\pi^0\eta$ signals with Gaussian+polynomial functions, which have been performed in Section 4.2.2, has resulted in underestimate in this $M_{4\gamma}$-mass regions.

In Section 4.2.3, we have discussed background contaminations in the $\pi^0\eta$-event samples by using the two-dimensional plots of the invariant $\gamma\gamma$ masses for both the best $\pi^0\eta$ and best $\pi^0\pi^0$ combination with the carbon-target data. It is worth checking these plots for pure $\pi^0\eta p$ events with Monte-Carlo samples here. The two-dimensional plots for 4γ-event samples obtained from MC samples are shown in Fig. 4.36 and Fig. 4.37, respectively. These figures can be compared with plots for the carbon data, which have been shown in Fig. 4.16 and Fig. 4.17. The $\pi^0\eta$ spots are clearly observed in Fig. 4.36. In contrast, the $\pi^0\eta$ spots are not so clearly seen in the carbon data, especially at lower $M_{4\gamma}$ mass regions, because of strong background originating from $\pi^0\pi^0$ events (see Fig. 4.16). As for the best $\pi^0\pi^0$ combination, there is no strong locus around $\pi^0\pi^0$ and no bands along the x- and y-axis in the MC plots as seen in the carbon plots. Therefore, it is evident that the experimental data includes the events coming from $\pi^0\pi^0$ events and π^0+uncorrelated $\gamma\gamma$ events in the 4γ-event samples.

4.3.4 The effect of the production-vertex position

In the real-data analysis, the information of the production vertex position is unknown because there is no tracking device for recoil protons. Thus, it is important to investigate the effect of production position using the MC event samples.

Acceptance

At first, the z position dependence of the acceptance for the $\pi^0\eta$-event was investigated. Figure 4.38 shows the acceptance of the $\pi^0\eta$-event samples as a function of the production-vertex position along the z-axis. The acceptance clearly depends on the production-vertex position. The result indicates that the acceptance at $z = -25$ mm, where this position is the same as the upstream edge of the CH_2 target, is 20% larger than that at the center of the target. On the other hands, at downstream edge of the target ($z = +25$ mm) the acceptance is lower about 20% relative to the center of the target. The reason is that in the case of the production at the upstream edge the calorimeter covers relatively forward angular region comparing to the case of central production, and hence much photons can be detected with the calorimeter.

Invariant 4γ mass distribution

The invariant 4γ mass is also affected by the production-vertex position. In the real-data analysis, we have assumed that all photons were produced at the center of the target since actual production position was unknown. Therefore, observed photon angles will be slightly shifted from actual ones if the production position is not the center of the target.

Before the investigation of the z position dependence, we introduce the invariant $\pi^0\eta$ mass ($M_{\pi^0\eta}$) using the fitted variables obtained from the kinematical fitting under the $\pi^0\eta$ hypothesis ($H_{\rm I}$) instead

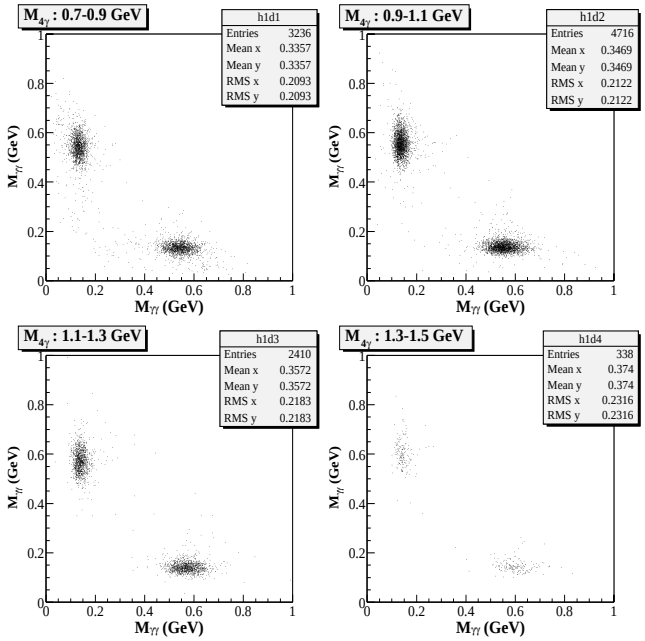

Figure 4.36: Two-dimensional plots of the invariant masses of two $\gamma\gamma$-pairs with the best $\pi^0\eta$ combination for different $M_{4\gamma}$ mass regions [MC samples]. These plots include 2 entries/event so that the plots are symmetric.

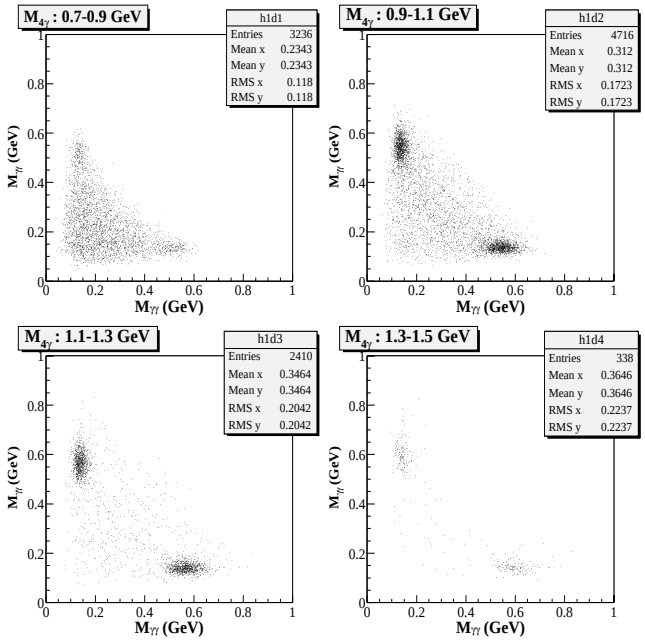

Figure 4.37: Two-dimensional plots of the invariant masses of two $\gamma\gamma$-pairs with the best $\pi^0\pi^0$ combination for different $M_{4\gamma}$ mass regions [MC samples]. These plots include 2 entries/event so that the plots are symmetric.

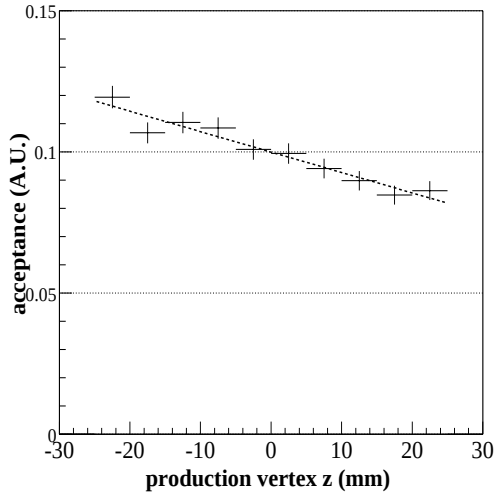

Figure 4.38: Production position dependence (along the z-axis) of the $\pi^0\eta$-event acceptance.

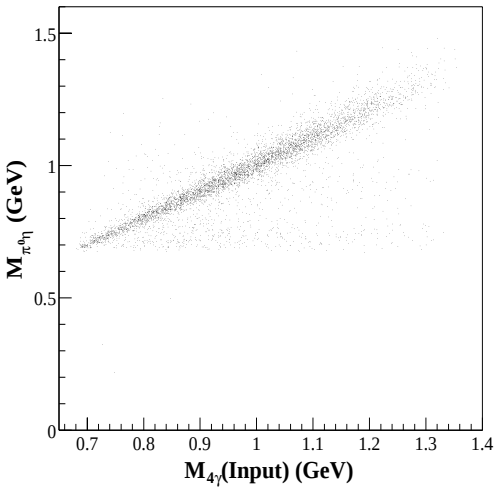

Figure 4.39: Two dimensional plot of the invariant $\pi^0\eta$-mass ($M_{\pi^0\eta}$) versus invariant 4γ-mass for generated by Monte-Carlo simulation $M_{4\gamma}$(input) for the 4γ-event samples.

of the observed variables. As described in Section 4.1, the invariant 4γ mass ($M_{4\gamma}$) can be calculated as

$$M_{4\gamma} \quad = \quad \sqrt{(p_{\gamma_1} + p_{\gamma_2} + p_{\gamma_3} + p_{\gamma_4})^2},$$

where p_{γ_i} is the observed four momentum vector for the ith photon. In the case of the invariant $\pi^0\eta$ mass, four-momentum vectors of the 4-photons is calculated with fitted variables, and hence we have

$$M_{\pi^0\eta} \quad \equiv \quad \sqrt{(p^*_{\gamma_1} + p^*_{\gamma_2} + p^*_{\gamma_3} + p^*_{\gamma_4})^2}, \tag{4.27}$$

where $p^*_{\gamma_i}$ is the fitted four momentum vector for the ith photon. Figure 4.39 shows a 2-dimensional plot of the invariant $\pi^0\eta$ mass versus invariant 4γ-mass calculated from MC event-generator. Compared with Fig. 4.39 and Fig. 4.32, we recognize that the mass resolution is drastically improved for the $M_{\pi^0\eta}$ case. The improvement is prominent at near the $\pi^0\eta$ production threshold.

Now let us check the z position dependence of the invariant mass distribution. In Fig. 4.40 the residual distributions ($\Delta M_{4\gamma}$=$M_{4\gamma}$−$M_{4\gamma}$(input) and $\Delta M_{\pi^0\eta}$=$M_{\pi^0\eta}$−$M_{4\gamma}$(input)) and its z-position dependence are plotted. Because of wrong angle estimate, the $M_{4\gamma}$ at the upstream edge of the CH_2 target is somehow ($\sim$ 20 MeV) large compared with the value of the central production. Similarly, the z-position dependence is also seen in the $M_{\pi^0\eta}$ plot; However, the effect is small in this case. As a consequence, the average resolutions of the $M_{4\gamma}$ and $M_{\pi^0\eta}$ in the $\gamma p \to \pi^0\eta p$ reaction are estimated to be $\sigma = 56 \pm 2$ MeV and $\sigma = 26 \pm 1$ MeV, respectively.

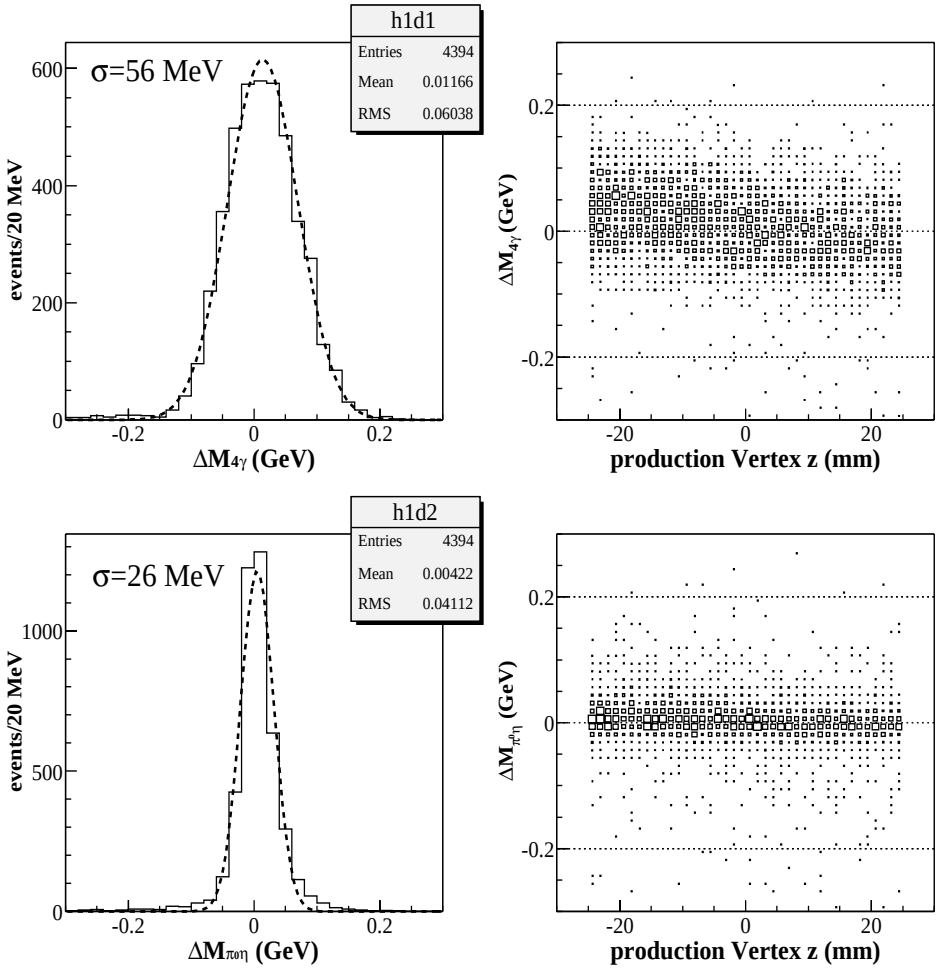

Figure 4.40: Residual distributions of invariant masses for the $\pi^0\eta$-event samples [MC samples]. (left upper) The $\Delta M_{4\gamma}$ ($=M_{4\gamma}-M_{4\gamma}$ (input)) distribution with Gaussian fitting function. (right upper) 2D-plot of $\Delta M_{4\gamma}$ versus z vertex position. (left lower) The $\Delta M_{\pi^0\eta}(=M_{\pi^0\eta}-M_{4\gamma}$ (input)) distribution with Gaussian fitting function. (right lower) 2D-plot of $\Delta M_{\pi^0\eta}$ versus z vertex position.

Missing mass distribution

The missing mass of the $p(\gamma, 4\gamma)X$ reaction ($MM_{\gamma 4\gamma}$) was obtained from

$$MM_{\gamma\,4\gamma} \quad = \quad \sqrt{(p_{\rm beam} + p_p - p_{\gamma_1} - p_{\gamma_2} - p_{\gamma_3} - p_{\gamma_4})^2}, \tag{4.28}$$

where $p_{\rm beam}$ denotes the four momentum vector of the incident beam $p_{\rm beam} = (0, 0, E_{\rm beam}, E_{\rm beam})$, and p_p is the four momentum vector of target proton $p_p = (\ 0,\ 0,\ 0,\ M_p = 938$ MeV), respectively. For the $\gamma p \to \pi^0 \eta p$ reaction, the missing particle X is proton, and hence the $MM_{\gamma 4\gamma}$ distribution shows a peak at the proton mass. The left-upper plot in Fig. 4.41 shows $MM_{\gamma 4\gamma}$ distribution of the $\pi^0\eta$-event samples; The right-upper plot shows $MM_{\gamma 4\gamma}$ versus production position along z-axis. As one can see, the missing mass also depends on the production position due to the same reason for the case of the invariant mass. However, the dependence is opposite: at the upstream edge of the target, the missing mass is small compared with the central production. This aspect results in the asymmetric missing-mass distribution since the detector acceptance is favorable for the upstream production.

Using the fitted variables, one can improve the missing-mass resolution similar to the invariant mass calculation. We defined the missing mass of the $p(\gamma, \pi^0\eta)X$ reaction as

$$MM_{\gamma\,\pi^0\eta} \quad = \quad \sqrt{(p_{\rm beam} + p_p - p^*_{\gamma_1} - p^*_{\gamma_2} - p^*_{\gamma_3} - p^*_{\gamma_4})^2}. \tag{4.29}$$

The $MM_{\gamma\pi^0\eta}$ distribution and its z-position dependence are shown in bottom plots in Fig. 4.41. The average resolution of the missing mass was improved from 107 ± 1 MeV (for $M_{4\gamma}$am) to 72 ± 1 MeV (for $M_{\pi^0\eta}$).

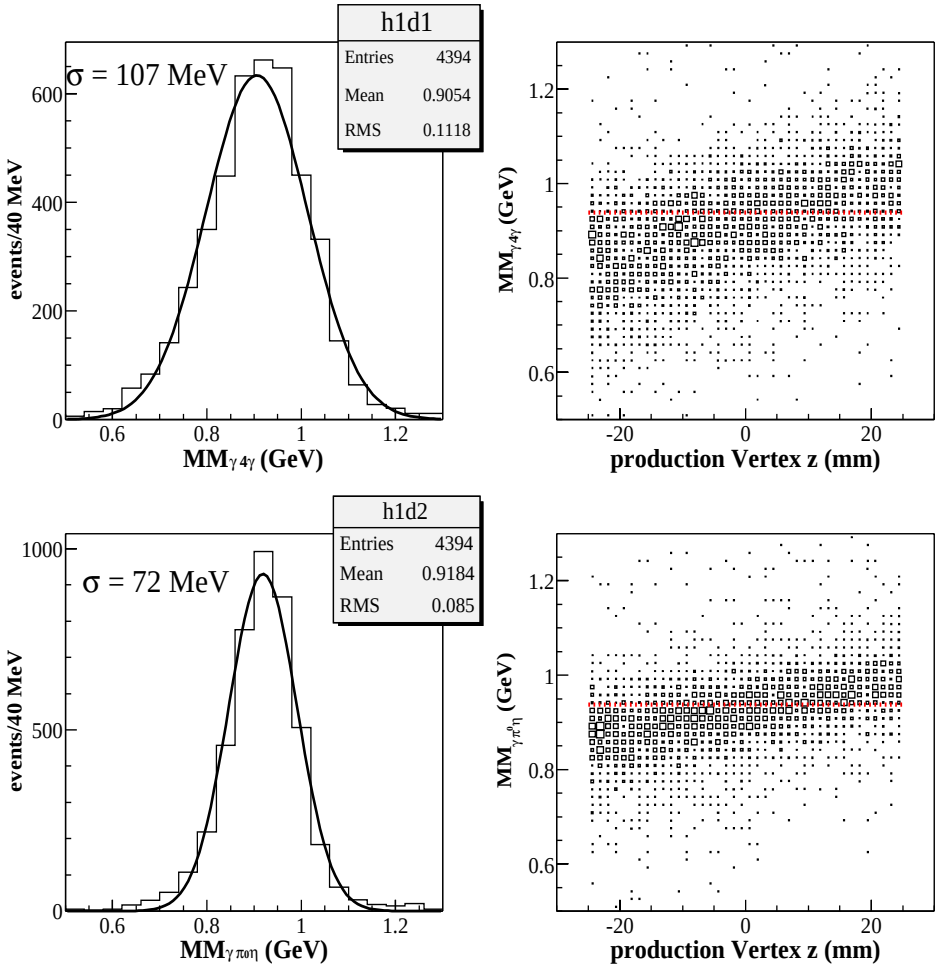

Figure 4.41: Missing mass distributions of the $\pi^0\eta$-event samples [MC samples]. (left upper) The $MM_{\gamma 4\gamma}$ distribution with Gaussian fitting function. (right upper) 2D-plot of $MM_{\gamma 4\gamma}$ versus z vertex position. The dotted line in the plot shows nominal proton mass ($M = 938$ MeV). (left lower) The $MM_{\gamma\pi^0\eta}$ distribution with Gaussian fitting function. (right lower) 2D-plot of $MM_{\gamma\pi^0\eta}$ versus z vertex position. The dotted line in the plot shows nominal proton mass ($M = 938$ MeV).

4.4 Selection for the $\pi^0\eta p$ samples

In Section 4.2, we have obtained $\pi^0\eta$ samples by selecting events satisfying 10% significance level for the $\pi^0\eta$ hypothesis. These samples, however, included background events which stem from $\pi^0\pi^0$ decay at lower $M_{4\gamma}$ region (see Table 4.9). In order to suppress this background, we will first introduce a strong cut, so called ε cut, in Section 4.4.1. Afterward, a beam-flux normalization between the CH_2 and carbon data will be performed to obtain the proton target data; This method will be described in Section 4.4.2. As discussed in the introduction, the aim of this study is to find new baryon resonance with $\gamma p \to \pi^0\eta p$ reaction. Although we have no hydrogen target for the γ-counter experiment, proton-target data can be extracted from CH_2 data by subtracting carbon contribution. Finally, in Section 4.4.3, we will discuss the missing-mass cut that selects the events originating from the exclusive $\gamma p \to \pi^0\eta p$ reaction. After applying the missing-mass cut, we obtain the clean $\gamma p \to \pi^0\eta p$ samples, which is the final goal of the analysis part.

4.4.1 The ε cut

We introduced a powerful cut to reject $\pi^0\pi^0$ contamination in the $\pi^0\eta$-event samples. This cut was based on the fact that the opening-angle distribution was quite different between two photons from π^0 decay and those from uncorrelated $\gamma\gamma$ background. The following quantity is defined for this purpose with $\gamma_1\gamma_2$ pair belonging to decay from π^0 for the best $\pi^0\eta$ combination

$$\varepsilon \equiv E_{\gamma_1} E_{\gamma_2}, \tag{4.30}$$

where the E_{γ_i} is the energy of the ith photon. We will first discuss physical meaning of the cut. Then the rejection and acceptance loss due to the ε cut will be evaluated.

Physical meaning of the ε cut

In general, when a neutral meson M^0 decays into two photons ($M^0 \to \gamma_1 + \gamma_2$), the opening angle between γ_1 and γ_2 has a minimum value:

$$\theta_{12}|_{\min} = \cos^{-1}(2\beta^2 - 1), \tag{4.31}$$

where the β is a velocity of the decaying particle M^0. According to 2-body kinematics, if the angular distribution of γ_1 (or γ_2) is isotropic in the M^0 rest frame, the probability distribution as a function of θ_{12} is described as

$$w(\theta_{12}) = \frac{\sin\theta_{12}}{4\gamma^2\beta\sin^3(\theta_{12}/2)\sqrt{\beta^2 - \cos^2(\theta_{12}/2)}} \tag{4.32}$$

where the $\gamma = (1-\beta^2)^{-1/2}$. Figure 4.42 shows the probability distributions of the 2γ-opening angle originating from π^0 decay for different π^0 momenta. The distribution concentrates around minimum opening angle. The minimum opening angle $\theta_{12}|_{\min}$ varies depending on the π^0 momentum; the $\theta_{12}|_{\min}$ decreases as the momentum increases. The probability distribution is localized in the relatively small θ_{12}

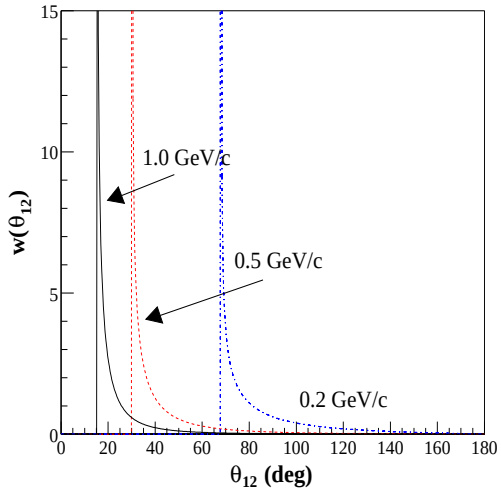

Figure 4.42: Opening angle distributions of 2γs coming from π^0 decay for different π^0 momenta.

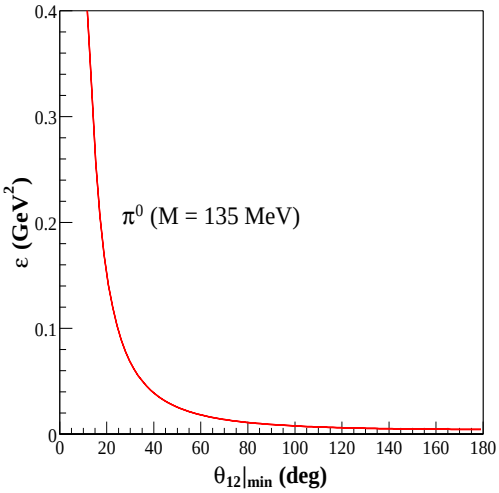

Figure 4.43: $\theta_{12}|_{\rm min}$ dependence of the ε.

region. It is attributed to the small mass of the π^0 meson. This property is very useful when one try to distinguish 2γs coming from π^0 decay from uncorrelated $\gamma\gamma$, since there is no such physical constraint for the uncorrelated $\gamma\gamma$.

For the $\pi^0 \to \gamma\gamma$ decay, the relation between the opening angle θ_{12} and the energies of the photons is simple; It is represented as

$$M^2_{\pi^0} \;=\; 2E_{\gamma_1}E_{\gamma_2}(1-\cos\theta_{12}) \;=\; 2\varepsilon(1-\cos\theta_{12}). \tag{4.33}$$

Therefore, the ε corresponds one-to-one with the opening angle, where the ε increases as opening angle decreases (see Fig. 4.43). As a consequence, the ε for uncorrelated $\gamma\gamma$ is relatively small comparing to that of $\gamma\gamma$ coming from π^0 decay.

A good example of this aspect is seen in invariant $\gamma\gamma$ mass distribution in the 2γ-event samples, where the samples are selected with $N_{\gamma(40^\circ-90^\circ)} = 2$ cut, instead of the $N_{\gamma(40^\circ-90^\circ)} = 4$ cut, and other cuts are same as the 4γ-event samples. The mass distribution for the carbon target is shown in Fig. 4.44 (only 5% of the 2γ-event samples are plotted). The π^0 and η peaks are observed above the uncorrelated $\gamma\gamma$ background, where the background mainly comes from $2\pi^0$ and $3\pi^0$ production events. Figure 4.45 shows the 2-dimensional plot of ε versus invariant $\gamma\gamma$ mass with the same samples. From this plot one notices that the uncorrelated $\gamma\gamma$ background is localized along the $\theta_{12} = 180^o$ line. Moreover, the π^0 locus is extended to higher ε region comparing to the background locus at around $M_{\gamma\gamma} \sim 0.135$ GeV/c^2. This is attributed to the small opening angle of the $\pi^0 \to \gamma\gamma$ decay. Therefore, selecting higher ε region enable us to separate π^0 signals from background events. Note that events with low-momentum π^0 are also rejected with the ε cut at the same time. This effect will be evaluated later with MC-event samples.

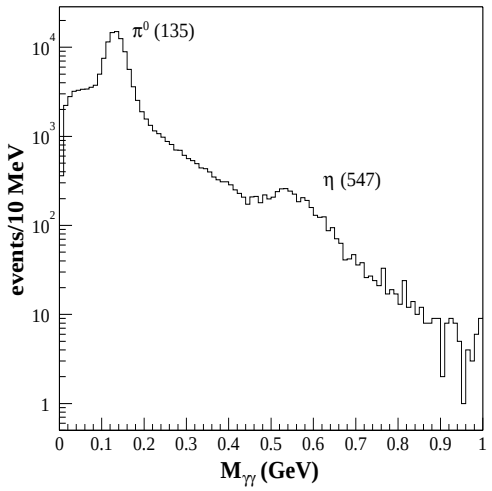

Figure 4.44: Invariant $\gamma\gamma$-mass distribution of the 2γ-event samples for the carbon data (only 5% samples are plotted).

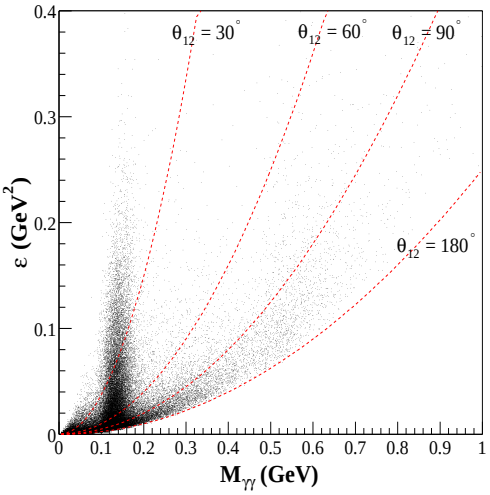

Figure 4.45: 2-dimensional plot of ε versus invariant $\gamma\gamma$ mass with the same samples in Fig. 4.44.

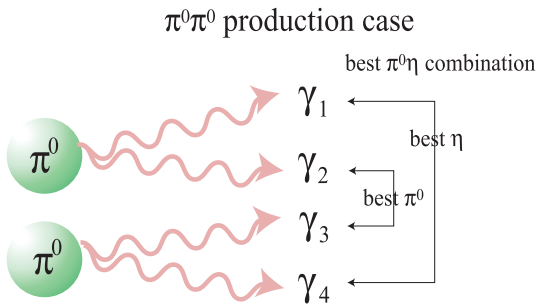

Figure 4.46: Two $\pi^0 s$ are produced and decay into $\pi^0_1 \to \gamma_1\gamma_2$ and $\pi^0_2 \to \gamma_3\gamma_4$. Using the 2C kinematical fitting under hypothesis $H_{\rm I}$, one obtained the best $\pi^0\eta$ combination as $\eta \to \gamma_1\gamma_4$ and $\pi^0 \to \gamma_2\gamma_3$.

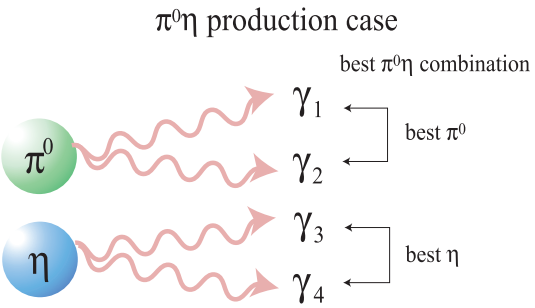

Figure 4.47: A π^0 and an η are produced and decay into $\pi^0 \to \gamma_1\gamma_2$ and $\eta \to \gamma_3\gamma_4$. Using the 2C kinematical fitting under hypothesis $H_{\rm I}$, one obtained the best $\pi^0\eta$ combination as $\eta \to \gamma_3\gamma_4$ and $\pi^0 \to \gamma_1\gamma_2$ correctly.

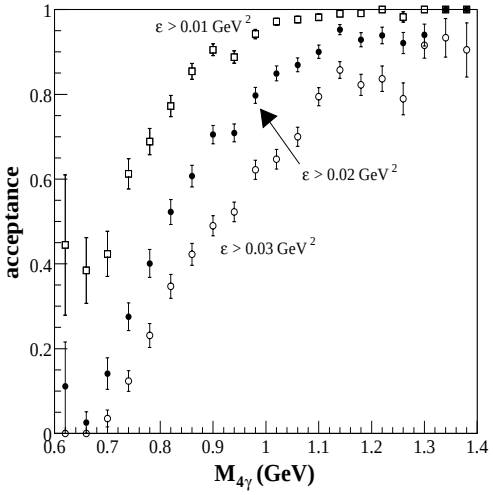

Figure 4.48: $M_{4\gamma}$ dependence of the $\gamma p \to \pi^0\eta p$ signal-acceptance for different ε-cut values [MC samples].

Next, we will explain why the ε cut is effective for the $\pi^0\pi^0$-event rejection from the $\pi^0\eta$-event samples. Suppose an event in which two π^0s are produced and those decay into $\pi^0_1 \to \gamma_1\gamma_2$ and $\pi^0_2 \to \gamma_3\gamma_4$ (see Fig. 4.46); Using the 2C-kinematical fitting under the hypothesis $H_{\rm I}$, one may obtain the best $\pi^0\eta$ combination as $\eta \to \gamma_1\gamma_4$ and $\pi^0 \to \gamma_2\gamma_3$. When the invariant 4γ mass ($M_{4\gamma}$) of the event is near the $\pi^0\eta$ threshold ($\sim$0.68 GeV/c^2), the event would satisfy both $\Pr(\chi^2_I) > 0.1$ and $\Pr(\chi^2_I) > \Pr(\chi^2_{\rm II})$ conditions. In this case the event is selected as a $\pi^0\eta$-event sample. This kind of events are removed by the ε cut because the $\gamma\gamma$-pair of the best π^0 combination is inevitably incorrect in this case[5]. In contrast, in the case of the $\pi^0\eta$ production (see Fig. 4.47), photon combinations are correctly identified for most of events ($\sim$ 95%) by the kinematical fitting. Therefore, those events are not strongly suppressed.

Acceptance loss and background rejection due to the ε cut

Applying the ε cut, one can reject the $\pi^0\pi^0$ background from the $\pi^0\eta$-event samples. However, true $\pi^0\eta$ events which include a low momentum π^0 are also removed from the samples as described previously. This effect was evaluated using MC event samples. The acceptance of the $\gamma p \to \pi^0\eta p$ reaction is shown in Fig. 4.48 as a function of the $M_{4\gamma}$ for various ε cuts. For lower $M_{4\gamma}$ mass, the samples were strongly suppressed because the phase space for the $\pi^0\eta$ decay was small at near the $\pi^0\eta$ threshold (thus π^0 momentum was also small). The suppression became more prominent as the ε value increases.

The ε distribution for the $\pi^0\eta$-event samples of the carbon target is shown in Fig. 4.49. The events concentrated strongly at low ε edge. The minimum ε value is determined by the energy threshold of the clustering algorithm ($E_{th} = 20$ MeV). Event reduction, which was defined as the number of survived events after the cut divided by the number of total $\pi^0\eta$-event samples, is plotted in Fig. 4.50. The

[5]In Fig. 4.46 the $\gamma_2\gamma_3$ pair is a uncorrelated $\gamma\gamma$ combination, and hence this event would be rejected by the ε cut.

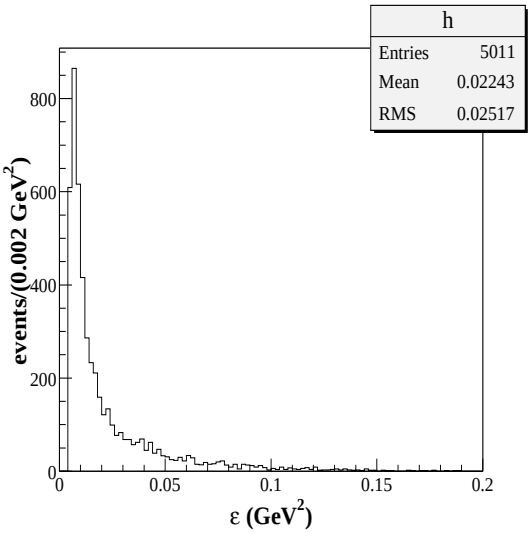

Figure 4.49: ε distribution of the $\pi^0\eta$-event samples for the carbon target.

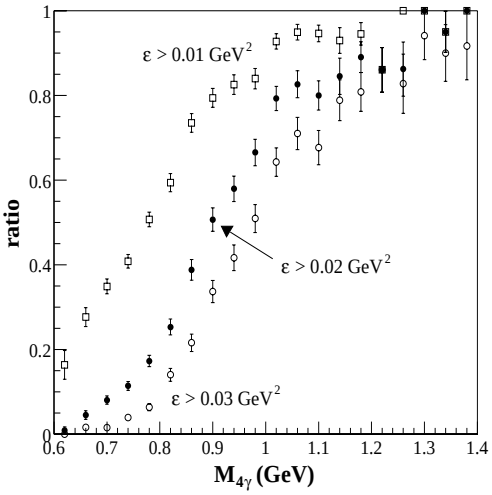

Figure 4.50: $M_{4\gamma}$ dependence of the ratio (= survived events/total events) for different ε-cut values. The plots are obtained from $\pi^0\eta$-event samples for the carbon target.

$M_{4\gamma}$ dependence seems to be similar to that of the acceptance loss for the $\gamma p \to \pi^0\eta p$ signal samples estimated from MC samples (Fig. 4.48). However, note that the $\pi^0\eta$-event samples of experimental data were contaminated with $\pi^0\pi^0$ background, on the other hand, the those of MC samples come from pure $\gamma p \to \pi^0\eta p$ reaction.

Figure 4.51 shows the same plots as Fig. 4.27 but for different ε cuts in the region of 0.7 GeV/c^2 $< M_{4\gamma} <$ 0.9 GeV/c^2. The $\pi^0\pi^0$ locus in these plots was much reduced as compared with the $\pi^0\eta$ loci (cf. the left-top plot in Fig. 4.37) when the ε cut becomes tighter. This means that although the $\pi^0\eta$-signal loss is not negligible, the $\pi^0\pi^0$ background can be strongly rejected with the ε cut. As a result, the S/N ratio of the $\pi^0\eta$ signals to the background $\pi^0\pi^0$ events is expected to be improved at lower $M_{4\gamma}$ mass region.

The ε cut and the proton-target data

Whereas the ε cut is useful to suppress the $\pi^0\pi^0$ background, one may think that the cut is too strong and results in biased data especially at the lower $M_{4\gamma}$ region. For instance, if the $\gamma p \to \pi^0\eta p$ reaction mainly proceeds via the $\eta\Delta^+$ intermediate state, the data would be biased due to the cut since the available phase space for Δ^+ decaying into a π^0 and a proton is expected to be small. However, by checking the proton-target data, one notices that the $\pi^0\eta$ events coming from the proton target dominate in the region of 0.9 GeV/c^2 $< M_{4\gamma} <$ 1.1 GeV/c^2. Figure 4.52 shows $M_{2\gamma(2)}$ distributions for the CH_2, carbon

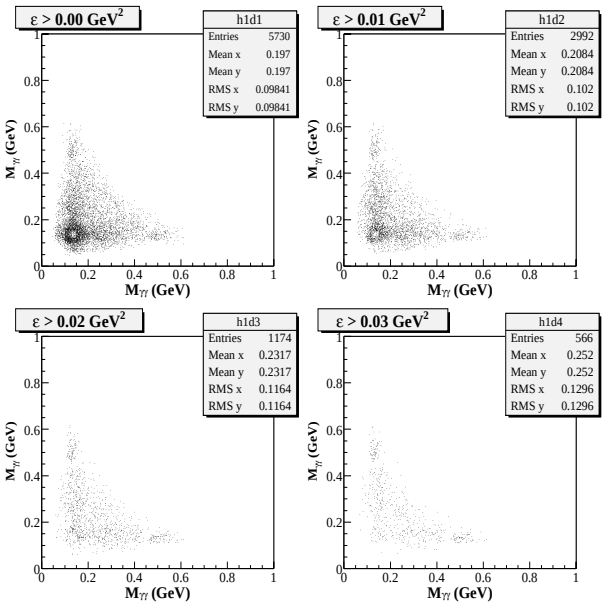

Figure 4.51: Two-dimensional plots of the invariant masses of two $\gamma\gamma$-pairs with the best $\pi^0\pi^0$ combination for different ε-cut values. The carbon-target data selected as 4γ-event samples in the region of 0.7 GeV/c^2 $< M_{4\gamma} <$ 0.9 GeV/c^2 are plotted. These plots include 2 entries/event so that the plots are symmetric.

and proton targets [6] for different $M_{4\gamma}$ mass regions, where the $M_{2\gamma(2)}$ was defined in Section 4.2.2. The remarkable aspects from these plots were following:

- The $\pi^0\eta$ signals was clearly seen in the plot for the proton target in the region of 0.9 GeV/c^2 $< M_{4\gamma} <$ 1.1 GeV/c^2. However, at lower $M_{4\gamma}$ the dominant contribution seems to be the background from the $3\pi^0$ production events (cf. Fig. 4.13).

- There was no structure in the plot for the proton target in the region of 1.3 GeV/c^2 $< M_{4\gamma} <$ 1.5 GeV/c^2. This arises from the fact that the phase space for either $\pi^0\pi^0$ or $\pi^0\eta$ production is small although for the nucleon target inside nuclei the phase space is large enough to produce them with help from Fermi momentum. This result supports the validity of the normalization factor.

From the former aspect, one can expect that the ε cut does not affect the final $\gamma p \to \pi^0\eta p$ samples. It will be discussed later (see Section 4.5.2).

In order to evaluate the effect of the ε cut on the $\pi^0\eta$-event samples, the missing mass $MM_{\gamma\pi^0\eta}$ distributions for the proton target was checked. Figure 4.53 shows the $MM_{\gamma\pi^0\eta}$ distributions for the CH_2, carbon and proton targets with various ε-cut values. There were two peaks in the plots for the proton target: (i) a peak at around nucleon mass ($MM_{\gamma\pi^0\eta}\sim$ 0.94 GeV/c^2), (ii) a peak at $MM_{\gamma\pi^0\eta}\sim$1.2 GeV/c^2. The first peak was originated from the exclusive $\gamma p \to \pi^0\eta p$ reaction. On the other hand, the

[6] The proton-target data were extracted from the CH_2 distributions by subtracting the carbon spectra with optimal scale factor; this method will be discussed in the next section.

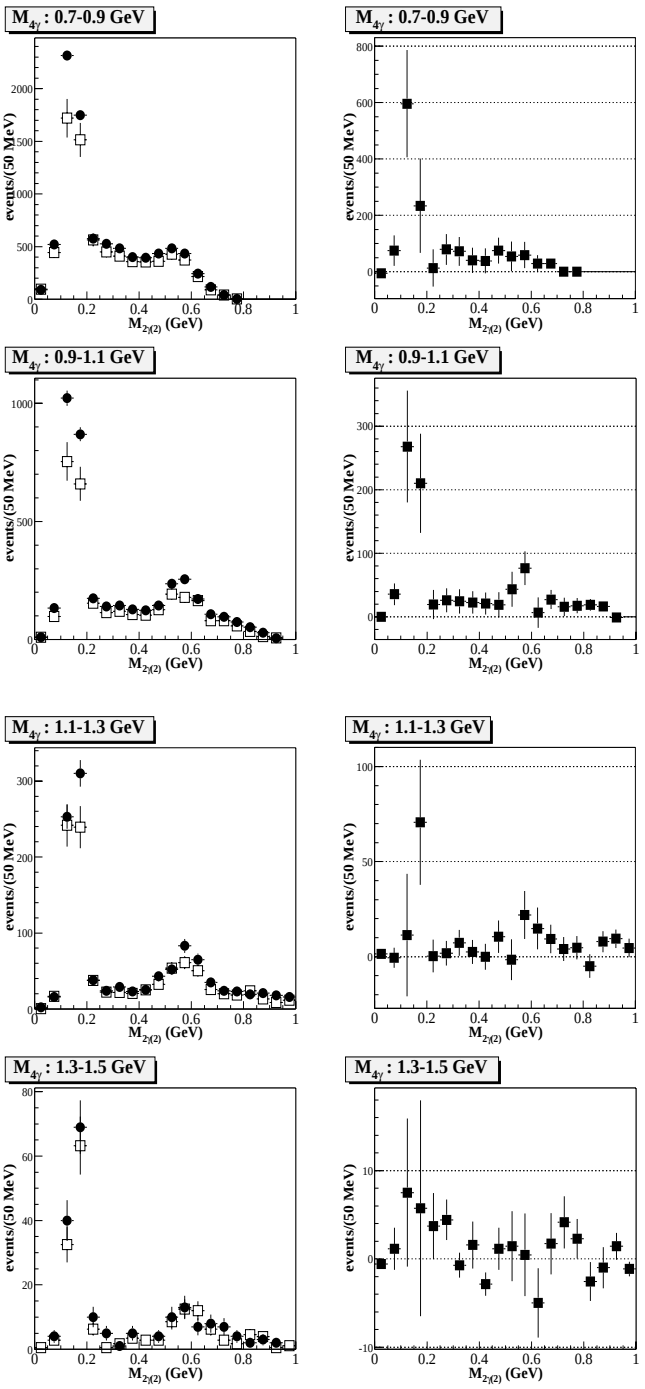

Figure 4.52: $M_{2\gamma(2)}$ distributions of the remaining $\gamma\gamma$-pair for different $M_{4\gamma}$ regions. These plots were obtained from the 4γ-event samples for each target: (filled circles) CH_2, (open squares) carbon, (filled squares) proton target contribution.

second peak stemmed from background contamination of the $\pi^0\pi^0$ production events. Relative strength of the background peak against the nucleon peak reduced as the ε cut became tight. Better separation between nucleon and background peaks were achieved when the ε value was 0.02 GeV^2. Therefore, we applied the $\varepsilon > 0.02$ GeV^2 cut to the $\pi^0\eta$-event samples in order to suppress the $\pi^0\pi^0$ background. By using the 3-body phase space of $\pi^0\eta p$ events generated by MC simulation, the average acceptance-loss was estimated to be 50% for $M_{4\gamma}$ =0.7-0.9 GeV/c^2, 20% for $M_{4\gamma}$ =0.9-1.1 GeV/c^2 and 7% for $M_{4\gamma}$ =1.1-1.3 GeV/c^2, respectively. The cut statistics for the ε cut is summarized in Table 4.10.

Table 4.10: Cut statistics for the ε cut

Target	$\pi^0\eta$-event samples	$\varepsilon > 0.02$ GeV^2 cut	rejection factor
Carbon	5011	1616	3.10±0.06
CH_2	3547	1121	3.16±0.08
Copper	2143	618	3.47±0.12
Empty	529	148	3.57±0.25

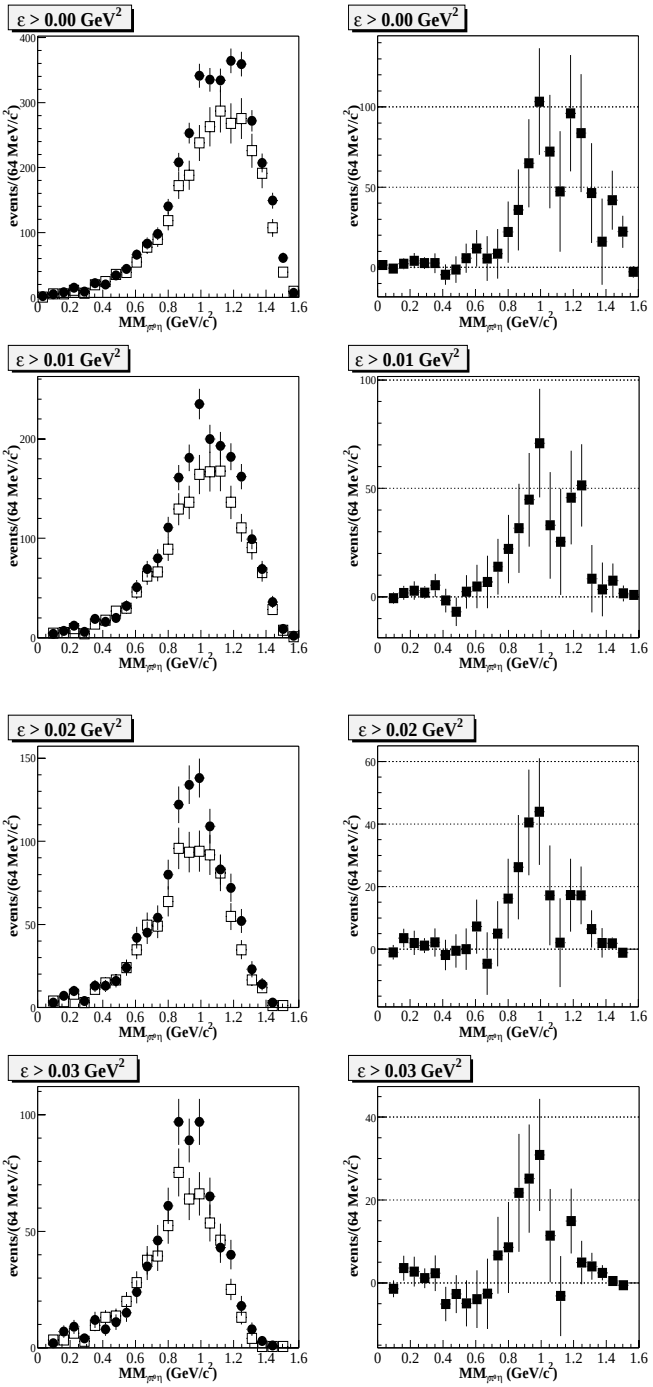

Figure 4.53: $MM_{\gamma\pi^0\eta}$ distributions for different ε-cut values. These plots were obtained from the $\pi^0\eta$-samples for each target: (filled circles) CH_2, (open squares) carbon, (filled squares) proton target contribution.

4.4.2 Beam-flux normalization among the different targets

In order to extract the proton-target contribution from the CH_2 data, one have to evaluate the carbon contribution in the CH_2 data. In the experiment, the number of photons irradiated on to the each CH_2 and carbon target was different; Furthermore, the number of carbon nuclei per unit area inside both targets were also different. Therefore, proper normalization of the distributions between the CH_2 and carbon targets was necessary. The missing-mass ($MM_{\gamma\pi^0\eta}$) distribution is one of the good tools for this purpose because the data for each target was dominately originated from the carbon-target contribution in the lower $MM_{\gamma\pi^0\eta}$ region. This arises from the fact that the $MM_{\gamma\pi^0\eta}$ distribution concentrates around nucleon mass for the proton target; on the other hands, for carbon target the distribution is smeared due to Fermi motion.

The normalization between CH_2 and carbon targets

A scale factor, which normalizes the difference of the beam flux between the carbon and CH_2 data, was estimated by comparing the $MM_{\gamma\pi^0\eta}$ histogram for the carbon target with that for the CH_2 target in the region of $MM_{\gamma\pi^0\eta} < 0.7$ GeV/c^2 (see Fig. 4.54). The $MM_{\gamma\pi^0\eta}$ resolution for the proton target was $\sigma = 72$ MeV, which has been estimated from MC simulation (the missing-mass distribution for the MC samples has been shown in Fig. 4.41). Thus, the data for both targets are expected to be dominated from the carbon-target contribution in this missing-mass region; According to the MC result, the contribution from nucleon peak in the proton-target data was estimated to be 1-2% in the $MM_{\gamma\pi^0\eta} < 0.7$ GeV/c^2

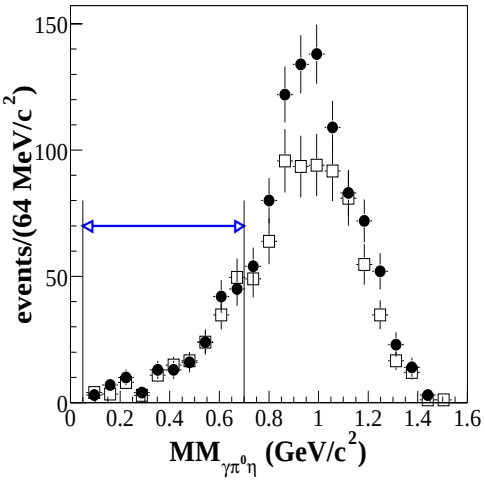

Figure 4.54: $MM_{\gamma\pi^0\eta}$ distributions for the $\pi^0\eta$-event samples with the $\varepsilon > 0.02$ cut. (Filled circles) CH_2 data, (open squares) carbon data which was normalized with the scale factor $k_{\rm scale} = 0.57 \pm 0.06$.

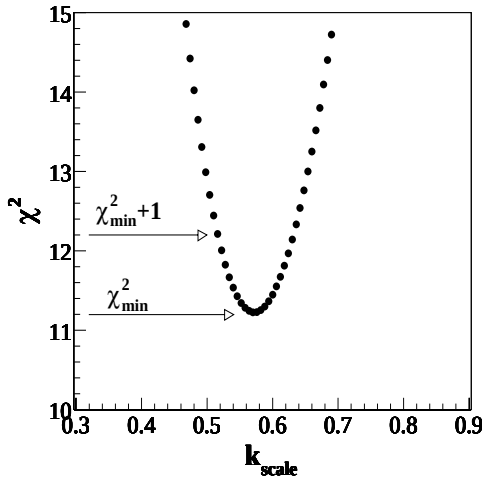

Figure 4.55: χ^2 values as a function of the scale factor $k_{\rm scale}$. The χ^2 minimum ($\chi^2_{\rm min}$) was observed at $k_{\rm scale} = 0.57$.

region. We defined the χ^2 as following equation:

$$\chi^2 = \sum_i \frac{N_{CH_2}(i) - k_{scale} \cdot N_C(i)}{\sigma(i)} \quad (4.34)$$

where k_{scale} is the scale factor to be estimated, $N_{CH_2}(i)$ and $N_C(i)$ are the i-th bin content of the histograms for the CH_2 and the carbon target, respectively. Here, $\sigma(i)$ denotes the error of the subtraction for i-th bin as described as

$$\sigma(i) = \sqrt{N_{CH_2}(i) + k^2_{scale} \cdot N_C(i)}. \quad (4.35)$$

It is obvious that the best estimate for the k_{scale} is achieved when the χ^2 in Eq.(4.34) is minimized. Figure 4.55 shows χ^2 value as a function of k_{scale}. The χ^2 minimum (χ^2_{min}) was obtained at $k_{scale} = 0.57$. The uncertainty of the scale factor k_{scale} was estimated by checking two points where the parabolic function k_{scale} dependence intersect the $\chi^2 = \chi^2_{min} + 1$ line in Fig. 4.55. As a result, we obtained the scale factor k_{scale} as

$$k_{scale} = 0.57 \pm 0.06 \quad (4.36)$$

The validity of the scale factor k_{scale} was checked in an alternative way: checking a scale factor estimated from with the target thickness and number of irradiated photons on the target (k'_{scale}). From the scaler data, which has been discussed in Section 2.6, the effective number of photons for each target was estimated as

$$\Sigma_{n\gamma}(CH_2) = 1.15 \times 10^{11} \quad (4.37a)$$

$$\Sigma_{n\gamma}(carbon) = 1.31 \times 10^{11} \quad (4.37b)$$

where $\Sigma_{n\gamma}$ denotes the effective number of photons for each target (see Table 2.8). The target thicknesses (d) for both the CH_2 and carbon targets are listed below. Here the X_0 denotes radiation length, d_{rad}

Target	d [mm]	X_0 [g/cm^2]	ρ [g/cm^3]	d_{rad}	d_{mol} [mol/cm^2]
CH_2	50.0	42.7	0.923	$0.108X_0$	0.330
C	40.0	44.6	1.73	$0.155X_0$	0.577

is target thickness in terms of radiation-length unit and d_{mol} is the thickness in terms of the amount of substance. The photon beam is expected to be partly absorbed inside the targets; and hence, the correction for the the photon attenuation was also taken into account. The avarage photon attenuation (η_{att}) can be calculated with the target thickness in terms of the radiation length; it is represented as

$$\eta_{att} \equiv \frac{1}{d_{rad}} \int_0^{d_{rad}} e^{-\frac{7}{9X_0}x} dx = \frac{9}{7}\frac{X_0}{d_{rad}}(1 - e^{-\frac{7}{9X_0}d_{rad}}). \quad (4.38)$$

Thus, the η_{att} for each target was obtained as

$$\eta_{att}(CH_2) = 0.959 \quad (4.39)$$

$$\eta_{att}(carbon) = 0.942 \quad (4.40)$$

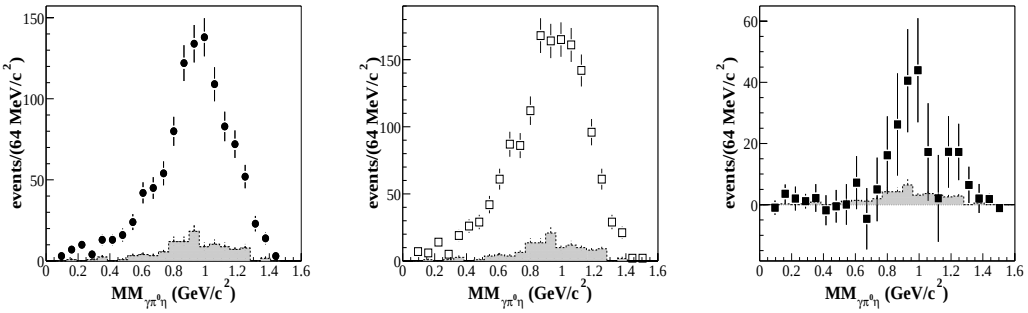

Figure 4.56: $MM_{\gamma\pi^0\eta}$ distribution for CH_2 (filled circles), carbon (open squares) and the proton contribution (filled squares) for the $\pi^0\eta$ samples with the $\varepsilon > 0.02$ GeV^2 cut. The hatched histogram shows empty-target contribution scaled by factor a for the CH_2 target, b for the carbon target and $k_{\rm empty}$ for the proton target.

By using these values, the scale factor $k'_{\rm scale}$ was estimated as

$$k'_{\rm scale} = \frac{\Sigma_{\rm n\gamma}({\rm CH_2})\cdot\eta_{\rm att}({\rm CH_2})}{\Sigma_{\rm n\gamma}({\rm carbon})\cdot\eta_{\rm att}({\rm carbon})}\cdot\frac{d_{\rm mol}({\rm CH_2})}{d_{\rm mol}({\rm carbon})} \tag{4.41}$$

Therefore, we have

$$k'_{\rm scale} = 0.511 \tag{4.42}$$

The $k'_{\rm scale}$ was consistent with the $k_{\rm scale}$ within error. Thus, in the remaining part of this thesis, all carbon distributions were normalized using the factor, $k_{\rm scale} = 0.57 \pm 0.06$.

The empty-target contribution in the proton data

Subtracting the carbon contribution normalized by $k_{\rm scale}$ from the CH_2 data, one can obtain the "proton-target data". However, the data was contaminated by background events originated from materials besides the target, such as the AC counter which was placed just after the target. In order to evaluate the background contribution, we used the empty-target data. The effective number of photons for the empty-target run was obtained from Table 2.8,

$$\Sigma_{\rm n\gamma}({\rm empty}) = 1.45\times10^{11} \tag{4.43}$$

The comparison between the distribution of the CH_2 data (or the carbon one) and the empty-target contribution was perfomed using scale factors

$$a = \Sigma_{\rm n\gamma}({\rm CH_2})/\Sigma_{\rm n\gamma}({\rm empty}) = 0.793 \tag{4.44}$$

for the CH_2 target, and

$$b = \Sigma_{\rm n\gamma}({\rm carbon})/\Sigma_{\rm n\gamma}({\rm empty}) = 0.903 \tag{4.45}$$

for the carbon target, respectively. The left and middle plots in Fig. 4.56 shows the missing-mass distributions of the CH_2 and carbon data with the empty-target contributions. For the proton-target data, the factor which normalizes the beam flux between the proton target and the empty target was estimated as

$$k_{\rm empty} \;=\; a - k_{\rm scale}\cdot b \;=\; 0.28 \pm 0.06, \tag{4.46}$$

where the error in $k_{\rm empty}$ comes from uncertainty for the estimate of $k_{\rm scale}$ (see Eq.(4.36)). The right plot in Fig. 4.56 shows the missing-mass distribution for the proton target. This plot was obtained from

$$N_p(i) \;=\; N_{\rm CH_2}(i) - k_{\rm scale}\cdot N_{\rm C}(i), \tag{4.47}$$

and the background contribution is superimposed in the plot, which was estimated as

$$k_{\rm empty}\cdot N_{\rm empty}(i), \tag{4.48}$$

where the $N_{\rm empty}(i)$ is the i-th bin content of the histogram for the empty target. About 20% of the proton-target data was originated from other than the target.

4.4.3 Missing-mass cut

In order to obtain clean $\pi^0\eta p$-event samples, we will introduce a missing-mass cut in this section.

Figure 4.57 shows the missing-mass distributions for the CH_2 target, the carbon target (left figure) and proton-target contribution (right figure) [7]. The empty-target contribution, which was normalized

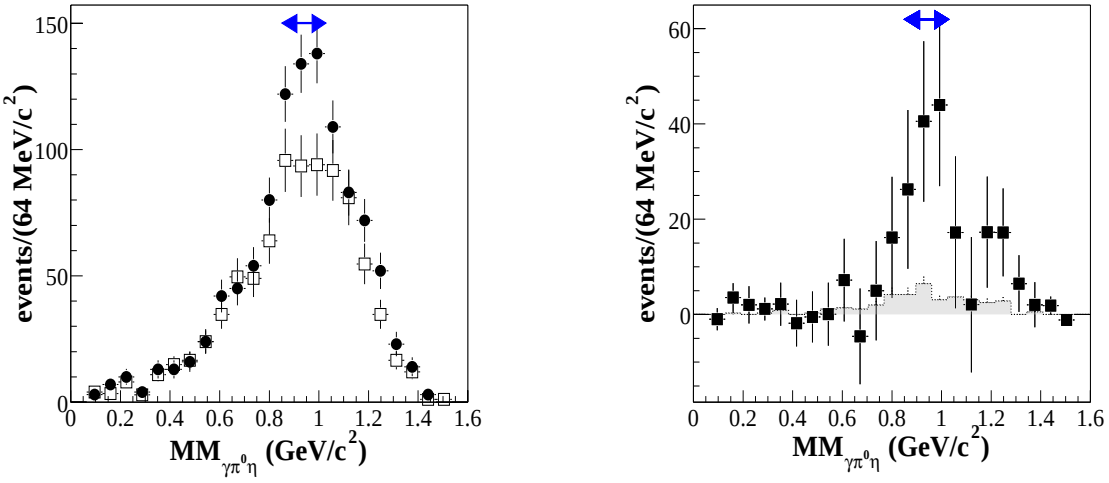

Figure 4.57: $MM_{\gamma\pi^0\eta}$ distribution for CH_2 (filled circles), carbon (open squares) and the proton contribution (filled squares) with the ε cut. The hatched histogram shows empty-target contribution. The arrows in these plots denote the region where samples are selected by missing-mass cut ($MM_{\gamma\pi^0\eta}$:0.85-1.03 GeV/c^2).

[7] These plots are the same as the plots with $\varepsilon > 0.02$ GeV^2 cut in Fig. 4.53.

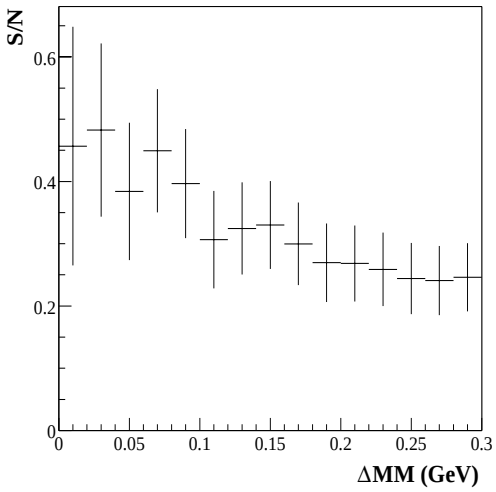

Figure 4.58: S/N ratio as a function of ΔMM.

with the factor $k_{\rm empty}$, is superimposed as a hatched histogram in the proton-target distribution. A clear peak corresponding to the recoil-proton signal was observed in the proton data at around 0.9 GeV/c^2. The mean value and the width of the peak were estimated to be $M = 946 \pm 31$ MeV and $\sigma = 82 \pm 28$ MeV, respectively, after the subtraction of the empty-target contribution. The width of the peak was consistent with the missing-mass resolution expected from the detector resolution ($\sigma = 72$ MeV/c^2, see Fig. 4.41).

The signal to noise ratio (S/N) [8] was estimated from the following equation.

$$\frac{S}{N} \;=\; \frac{S+N}{N} - 1 \;=\; \frac{\sum_i N_{\rm CH_2}(i)}{k_{\rm scale}\cdot\sum_i N_{\rm C}(i)} - 1 \tag{4.49}$$

For the samples applied the ε cut to the $\pi^0\eta$-event samples, the S/N ratio was estimated to be 0.22 ± 0.14, where $k_{\rm scale} = 0.57 \pm 0.06$ and $\sum_i N_{\rm CH_2}(i) = 1121 \pm 34$ counts, $\sum_i N_{\rm C}(i) = 1616 \pm 40$ counts (see Table 4.10). Applying a tight missing-mass cut around the proton peak, one can improve the S/N ratio; it is essentially important in order to reduce the statistical uncertainty of the extracted proton data. Figure 4.58 shows the S/N ratio as a function of the width of the cut region, where the ΔMM denotes the cut window for the missing-mass cut in the region from $0.94 - \Delta MM$ GeV/c^2 to $0.94 + \Delta MM$ GeV/c^2. It is obvious that the S/N ratio increases as the window becomes small, and the ΔMM dependence is almost constant where the ΔMM is less than 100 MeV. We fixed the cut window to be $\Delta MM = 90$ MeV/c^2, which corresponds to the nearly 1σ missing-mass resolution. Thus, the cut range was

$$0.85 \text{ GeV}/c^2 < MM_{\gamma\pi^0\eta} < 1.03 \text{ GeV}/c^2.$$

[8] The S/N ratio was defined as the ratio of the number of $\pi^0\eta$ event coming from the proton target to the number of event from the carbon target.

The arrows in Fig. 4.57 represent the cut region.

The missing-mass cut eliminates the background from $\pi^0\pi^0$-production events, which distribute around $MM_{\gamma\pi^0\eta}$= 1.2 GeV/c^2. The cut statistics of the missing-mass cut is summarized in Table 4.11. The

Table 4.11: Cut statistics for the missing-mass cut ($\pi^0\eta p$-event samples).

Target	without missing mass cut	0.85 GeV$<MM_{\gamma\pi^0\eta}<$ 1.03 GeV	rejection factor
Carbon	1616	469	3.45±0.13
CH_2	1121	380	2.95±0.12
Copper	618	175	3.53±0.23
Empty	148	48	3.08±0.37

$\pi^0\eta$-event samples which satisfy both the ε cut and missing-mass cut were referred to as **"$\pi^0\eta p$-event samples"**. The S/N ratio for the $\pi^0\eta p$-event samples was improved, and it was estimated to be 0.42±0.18 by using Eq.(4.49), where $N_{\mathrm{CH_2}} = 380 \pm 19$ counts, $N_{\mathrm{C}} = 469 \pm 22$ counts and $k_{\mathrm{scale}} = 0.57 \pm 0.06$. From these values, the $\pi^0\eta p$-event samples originated from the proton target was obtained to be 113 ± 36 events, where a statistical significance was 3.2σ. The empty-target contribution in the samples was estimated to be 13.4 ± 5.8 events. Therefore, about 12% of the samples coming from the proton target was contaminated by the background events which stem from other than the target. All cuts applied for obtaining the $\pi^0\eta p$-event samples are summarized in Table 4.12 and Table 4.13.

Table 4.12: Cut summary for all cuts applied for the $\pi^0\eta p$ selection. (the CH_2 and carbon targets)

Carbon target

cut	examined	passed	rejection
(Triggered events)		(61555462)	
$N_{\gamma(40^\circ-90^\circ)} = 4$	61555462	378233	162.7±0.3
Edge-module cut	378233	235676	1.605±0.002
Cluster merging cut	235676	191097	1.233±0.001
$n_{\rm tag} = 1$	191097	133640	1.430±0.002
$1.62 < E_{\rm beam} < 2.40$ GeV	133640	126828	1.053±0.001
$\Pr(\chi^2_I) > 0.1$	126828	6042	21.00±0.26
$\Pr(\chi^2_I) > \Pr(\chi^2_{II})$	6042	5011	1.20±0.01
$\varepsilon > 0.02$ GeV^2 cut	5011	1616	3.10±0.06
0.85 GeV$<MM_{\gamma\pi^0\eta}<$ 1.03 GeV	1616	469	3.45±0.13

CH_2 target

cut	examined	passed	rejection
(Triggered events)		(41603385)	
$N_{\gamma(40^\circ-90^\circ)} = 4$	41603385	240261	173.2±0.4
Edge-module cut	240261	148043	1.623±0.003
Cluster merging cut	148043	120898	1.224±0.002
$n_{\rm tag} = 1$	120898	85793	1.409±0.002
$1.62 < E_{\rm beam} < 2.40$ GeV	85793	82156	1.044±0.001
$\Pr(\chi^2_I) > 0.1$	82156	4288	19.16±0.28
$\Pr(\chi^2_I) > \Pr(\chi^2_{II})$	4288	3547	1.21±0.01
$\varepsilon > 0.02$ GeV^2 cut	3547	1121	3.16±0.08
0.85 GeV$<MM_{\gamma\pi^0\eta}<$ 1.03 GeV	1121	380	2.95±0.12

Table 4.13: Cut summary for all cuts applied for the $\pi^0\eta p$ selection. (the copper and empty targets)

Copper target

cut	examined	passed	rejection
(Triggered events)		(58581486)	
$N_{\gamma(40^\circ-90^\circ)} = 4$	58581486	196378	298.3±0.7
Edge-module cut	196378	126164	1.556±0.003
Cluster merging cut	126164	102171	1.235±0.002
$n_{\rm tag} = 1$	102171	72247	1.414±0.003
$1.62 < E_{\rm beam} < 2.40$ GeV	72247	65540	1.102±0.001
$\Pr(\chi^2_I) > 0.1$	65540	2496	26.26±0.52
$\Pr(\chi^2_I) > \Pr(\chi^2_{II})$	2496	2143	1.16±0.01
$\varepsilon > 0.02$ GeV^2 cut	2143	618	3.47±0.12
0.85 GeV$<MM_{\gamma\pi^0\eta}<$ 1.03 GeV	618	175	3.53±0.23

Empty target

cut	examined	passed	rejection
(Triggered events)		(17388120)	
$N_{\gamma(40^\circ-90^\circ)} = 4$	17388120	52347	332.2±1.5
Edge-module cut	52347	31224	1.676±0.006
Cluster merging cut	31224	24579	1.270±0.004
$n_{\rm tag} = 1$	24579	17184	1.430±0.006
$1.62 < E_{\rm beam} < 2.40$ GeV	17184	15813	1.087±0.002
$\Pr(\chi^2_I) > 0.1$	15813	643	24.59±0.95
$\Pr(\chi^2_I) > \Pr(\chi^2_{II})$	643	529	1.22±0.02
$\varepsilon > 0.02$ GeV^2 cut	529	148	3.57±0.25
0.85 GeV$<MM_{\gamma\pi^0\eta}<$ 1.03 GeV	148	48	3.08±0.37

4.5 Observables

In the previous section, we selected the $\gamma p \to \pi^0\eta p$ samples. In this section, we will discuss experimental observables extracted from the samples. The $\sqrt{s}$ distribution is the most interesting observable since the distribution directly reflects the existence of s-channel baryon resonances; hence we will first mention about the $\sqrt{s}$ distribution for the $\gamma p \to \pi^0\eta p$ samples in Section 4.5.1. Identifying the reaction mechanism is also important as discussed in the introduction. It can be performed by checking the invariant masses, where the conceivable combinations are the $\pi^0\eta$, $\pi^0 p$ and ηp systems in the $\pi^0\eta p$ final state. Therefore, we will discuss the invariant masses for the $\gamma p \to \pi^0\eta p$ samples in Section 4.5.2.

4.5.1 The $\sqrt{s}$ distribution

Now we can obtain the total energy of the center-of-mass system ($\sqrt{s}$) for clean $\gamma p \to \pi^0\eta p$ event samples. The $\sqrt{s}$ was calculated with the four momentum vector of the incident beam ($p_{\rm beam}$) and that of target proton (p_p) as

$$\sqrt{s} \;=\; \sqrt{(p_{\rm beam}+p_p)^2}, \tag{4.50}$$

where these four momentum vectors were obtained from $p_{\rm beam} = (0, 0, E_{\rm beam}, E_{\rm beam})$, and $p_p = (0, 0, 0, M_p = 938$ MeV), respectively. Note that we assumed the target nucleon to be at rest; If the $\sqrt{s}$ distribution originated from nucleons inside the carbon nuclei, then it was smeared due to the Fermi motion. The resolution of the $\sqrt{s}$ ($\sigma_{\sqrt{s}}$) is determined by the energy resolution of the tagging counter ($\sigma = 15$ MeV), and it was estimated to be $\sigma_{\sqrt{s}} \sim 6$ MeV with the Monte-Carlo simulation.

Figure 4.59 shows the $\sqrt{s}$ distributions *without* the missing-mass cut for the CH_2, carbon and the proton target, respectively. The extraction of the proton-target contribution was performed by subtracting the carbon spectrum from the CH_2 distribution. The difference of the shapes between the CH_2 and the carbon distribution was small. It is attributed to the fact that the samples in the CH_2 data is dominately ($\sim 82\%$) stemmed from nucleons in the carbon nuclei in the case of no missing-mass cut. Therefore, the difference of the $\sqrt{s}$ distributions for the the CH_2 and carbon data are expected to be small. This aspect is very important in the sense that the data analysis has been fairly performed for each target.

The situation drastically changed when the missing-mass cut (0.85 GeV $< MM_{\gamma\pi^0\eta} <$ 1.03 GeV) was applied. Figure 4.60 shows the $\sqrt{s}$ distributions for the CH_2, the carbon and the proton target *with* the missing-mass cut. In this case, the S/N ratio increases from 0.22 to 0.42 as discussed in Section 4.4.3. The difference of the shape between CH_2 and carbon distributions was prominent. The proton-target spectrum shows a resonance-like structure at around 2.1 GeV/c^2, indicating the existence of a s-channel baryon-resonance in this mass region.

In order to check the effect of the ε cut, the $\sqrt{s}$ distributions with various ε-cut values are plotted in Fig. 4.61. Although the error-bars were large for looser ε-cut due to the worse S/N ratio, all distributions show a resonance structure around 2.1 GeV/c^2 for the proton target. This tendency was independent of the ε cut.

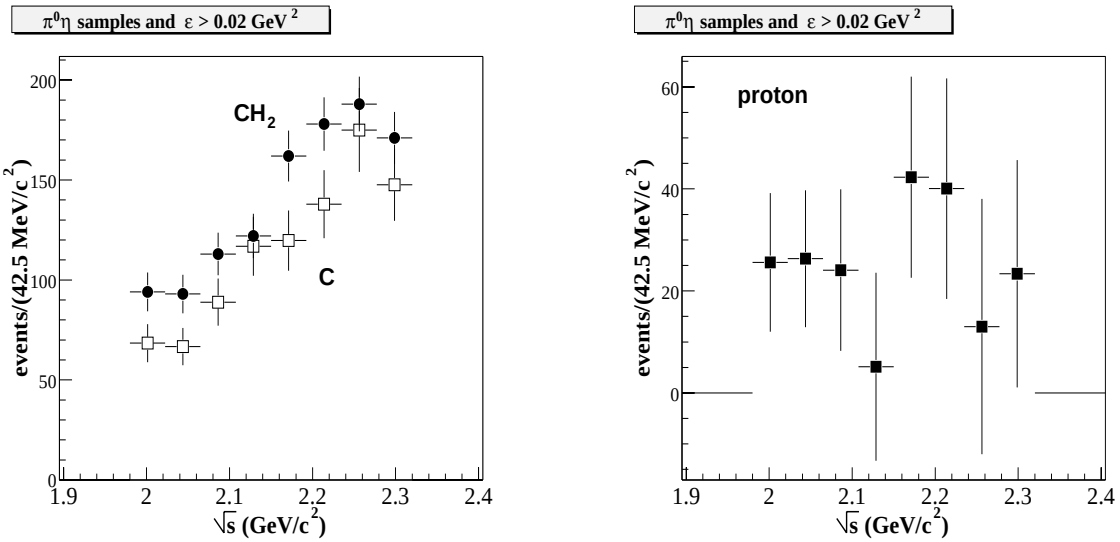

Figure 4.59: $\sqrt{s}$ distributions for the $\pi^0\eta$-event samples with ε cut. (filled circles) the CH_2 data (open squares) the carbon data (filled squares) proton target contribution. The error bars for carbon and proton data include systematic error due to normalization.

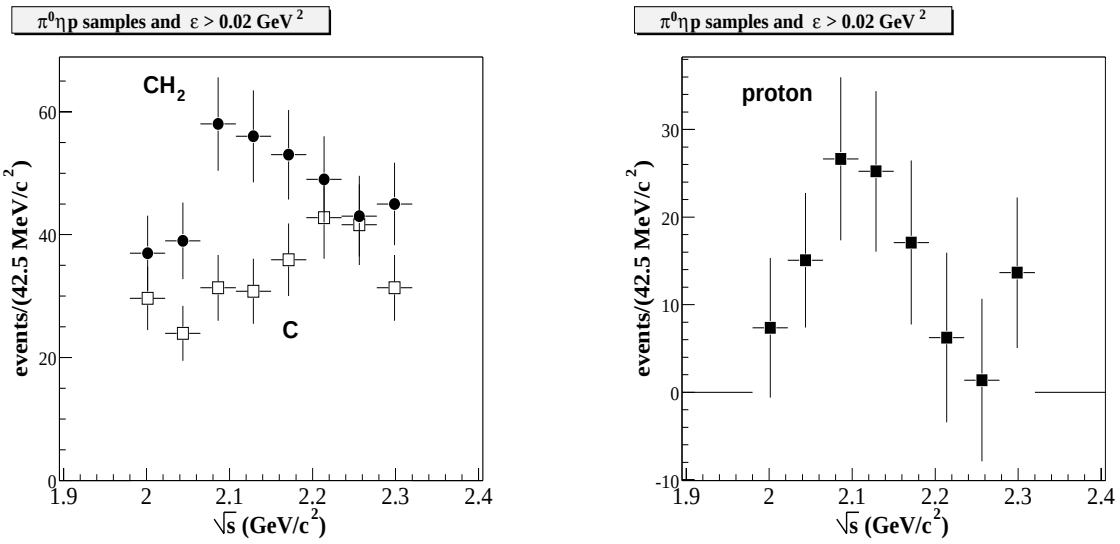

Figure 4.60: $\sqrt{s}$ distributions for the $\pi^0\eta p$-event samples. Those are obtained just applying missing mass cut to Fig. 4.59. (filled circles) the CH_2 data (open squares) the carbon data (filled squares) proton target contribution. The error bars for carbon and proton data include systematic error due to normalization.

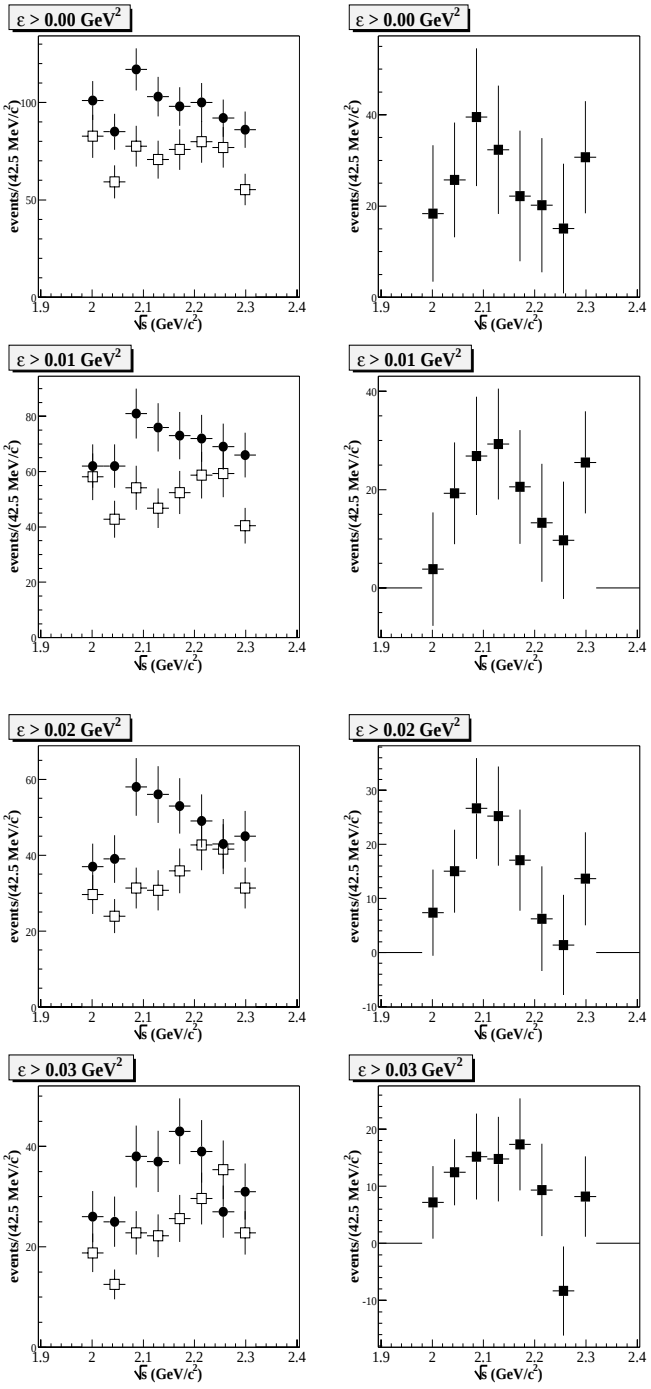

Figure 4.61: $\sqrt{s}$ distributions for the $\pi^0\eta p$ event samples but with various ε-cut values. (filled circles) the CH_2 data (open squares) the carbon data (filled squares) proton target contribution.

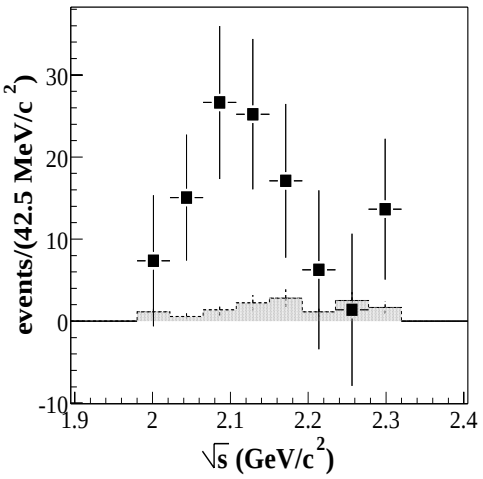

Figure 4.62: $\sqrt{s}$ distribution for the $\pi^0\eta p$-event samples with proton target. The hatched histogram, superimposed in the plot, shows the empty-target contribution normalized by $k_{\rm empty}$.

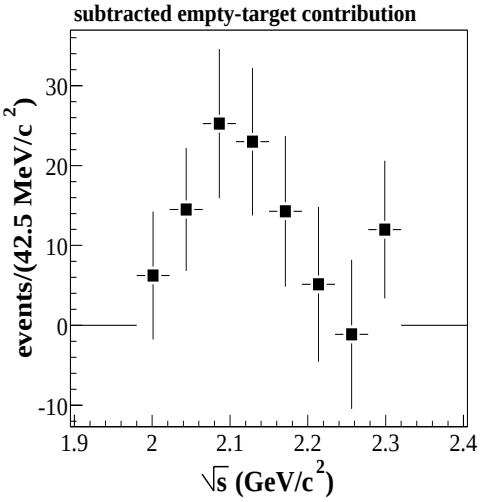

Figure 4.63: $\sqrt{s}$ distribution for the $\pi^0\eta p$-event samples with proton target after the empty-target subtraction.

Correction for the $\sqrt{s}$ distribution

We have seen a resonance-like structure in the $\sqrt{s}$ distribution for the proton target. In order to obtain the mass and the width of the resonance from the distribution, two corrections were necessary: (i) background from the empty-target contribution and (ii) beam-energy dependence. The correction (ii) is attributed to the fact that the relationship between $\sqrt{s}$ and photon-beam energy $E_{\rm beam}$ is one-by-one correspondence, and hence the $\sqrt{s}$ distribution is expected to be correlated to the beam-flux distribution. The estimate of the mass and the width will be discussed later (see Section 5.2). Prior to that, we will perform these corrections to the $\sqrt{s}$ distribution.

Subtraction for the empty-target contribution Figure 4.62 shows the $\sqrt{s}$ distribution for the $\pi^0\eta p$-event samples with proton target, which is the same as the distribution in Fig. 4.60. The empty-target contribution is superimposed in this figure, where it has been normalized by the factor $k_{\rm empty}$ obtained in Section 4.4.2. About 10% of the $\pi^0\eta p$-event samples were originated from outside of the targets in the case of the proton target. This contribution was subtracted from the plots and the result shows in Fig. 4.63.

Beam-flux correction For beam-flux correction, we employed the $\sqrt{s}$ distribution obtained from the triggered events which satisfied both the $n_{\rm tag}$=1 and $1.62 < E_{\rm beam} < 2.40$ GeV conditions. The distribution is shown in Fig. 4.64, where the plot is normalized so that the sum over the region $1.98 < \sqrt{s} < 2.32$

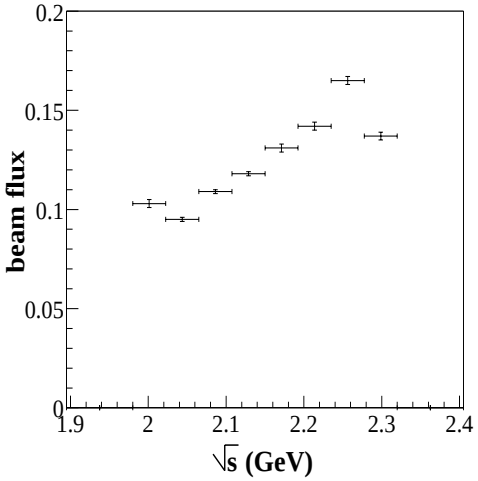

Figure 4.64: $\sqrt{s}$ distribution obtained from the triggered events which satisfy both $n_{\rm tag}$=1 and $1.62 < E_{\rm beam} < 2.40$ GeV conditions.

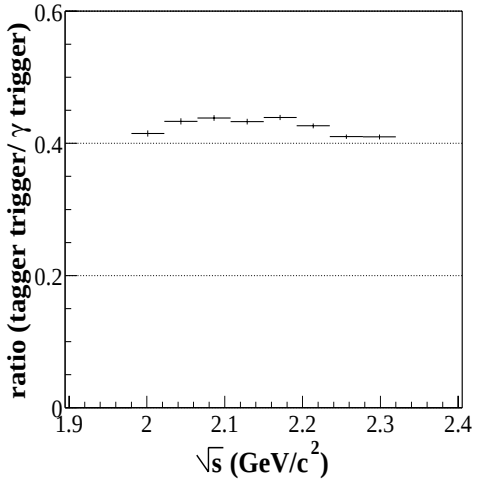

Figure 4.65: Ratio between $\sqrt{s}$ distributions from triggered samples and tagger-trigger data.

GeV/c^2 is to be unity. The error-bars (y-direction) in this plot denote the fluctuation among each run, mainly caused by the fluctuation of the tagging-scintillator efficiency. The systematic error due to the fluctuation was small ($< 7\%$) comparing to the statistical error of the distribution for the proton target. The ratio of between this plot and the $\sqrt{s}$ distributions obtained from tagger-trigger data was checked (see Fig. 4.65) since the $\sqrt{s}$ distribution in Fig. 4.63 might strongly depend on beam energy due to some specific reactions; However, the difference was small. The histogram in Fig. 4.63 was divided by the histogram in Fig. 4.64, and the result is shown in Fig. 4.66. The peak position was somewhat changed toward low-mass side after the beam-flux correction. This plot will be utilized for the estimation of the mass and the width of the resonance in Chapter 5.

4.5.2 The invariant mass distributions

The $\pi^0 p$ system

If the $\gamma p \to \pi^0 \eta p$ reaction dominately proceeds via the $\eta\Delta^+$ intermediate state, the distribution of the invariant $\pi^0 p$ mass ($M_{\pi^0 p}$) would show the Δ peak at around 1.232 GeV/c^2. it is also possible to form other resonance states in the $\pi^0 p$ system, such as $N^*(1520)$, $\Delta^*(1620)$. The $M_{\pi^0 p}$ can be obtained from

$$M_{\pi^0 p} \quad = \quad \sqrt{(p_{\rm beam} + p_p - p^*_{\gamma_3} - p^*_{\gamma_4})^2}, \tag{4.51}$$

where the γ_3 and γ_4 are photons forming the best η combination, and $p_p = (0, 0, 0, M_p)$ is the four-momentum vector of the proton at rest. Figure 4.67 shows the $M_{\pi^0 p}$ distributions for the CH_2, carbon and proton targets for different ε cuts, where the plots with the $\varepsilon > 0.02$ GeV^2 cut are corresponding to those for the $\gamma p \to \pi^0 \eta p$ event samples. As discussed previously, tighter ε cut results in the acceptance

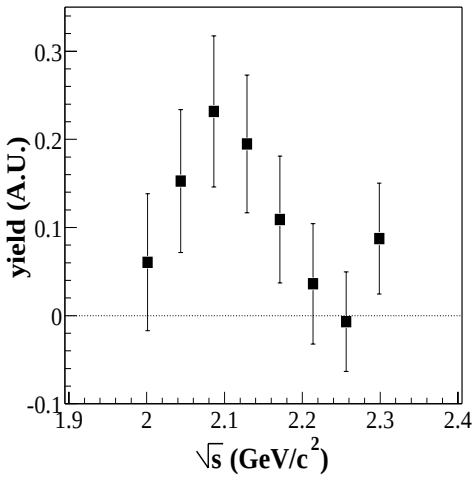

Figure 4.66: $\sqrt{s}$ distribution for the $\pi^0\eta p$-event samples with proton target after the empty-target subtraction and the beam-flux correction.

loss for the low momentum π^0, and hence events with low $M_{\pi^0 p}$ region is strongly suppressed. Neither the Δ peak nor the other resonance peak was observed in Fig. 4.67 even in the case of no ε cut. This means that the contribution from the sequential $\eta\Delta^+$ decay is small in the reaction mechanism of the $\gamma p \to \pi^0\eta p$ reaction at $\cos(\theta^{\rm c.m.}_{\pi^0\eta}) < 0$.

The ηp system

Similar to the $\pi^0 p$ system, invariant ηp mass distribution would show a resonance structure if the $\gamma p \to \pi^0\eta p$ reaction dominately proceeds via the sequential $\pi^0 S_{11}(1535)$ decay. The $M_{\eta p}$ can be obtained from

$$M_{\eta p} \quad = \quad \sqrt{(p_{\rm beam} + p_p - p^*_{\gamma_1} - p^*_{\gamma_2})^2}, \tag{4.52}$$

where the γ_1 and γ_2 are photons forming the best π^0 combination. The $M_{\eta p}$ distributions with different ε cut are shown in Fig. 4.68.

The $\pi^0\eta$ system

The invariant $\pi^0\eta$ mass ($M_{\pi^0\eta}$) can be obtained as

$$M_{\pi^0\eta} \quad = \quad \sqrt{(p^*_{\gamma_1} + p^*_{\gamma_2} + p^*_{\gamma_3} + p^*_{\gamma_4})^2},$$

where $p^*_{\gamma_i}$ is the fitted four momentum vector for the ith photon (see Eq. 4.27). Figure 4.69 shows $M_{\pi^0\eta}$ mass distributions for each target with different ε cut values. As discussed in Section 4.4.1, the samples with lower $M_{4\gamma}$ (or equivalently at lower $M_{\pi^0\eta}$) are strongly suppressed due to the ε cut. This effect is clearly seen in the plots for the CH_2 and carbon targets. The $M_{\pi^0\eta}$ spectrum for the proton

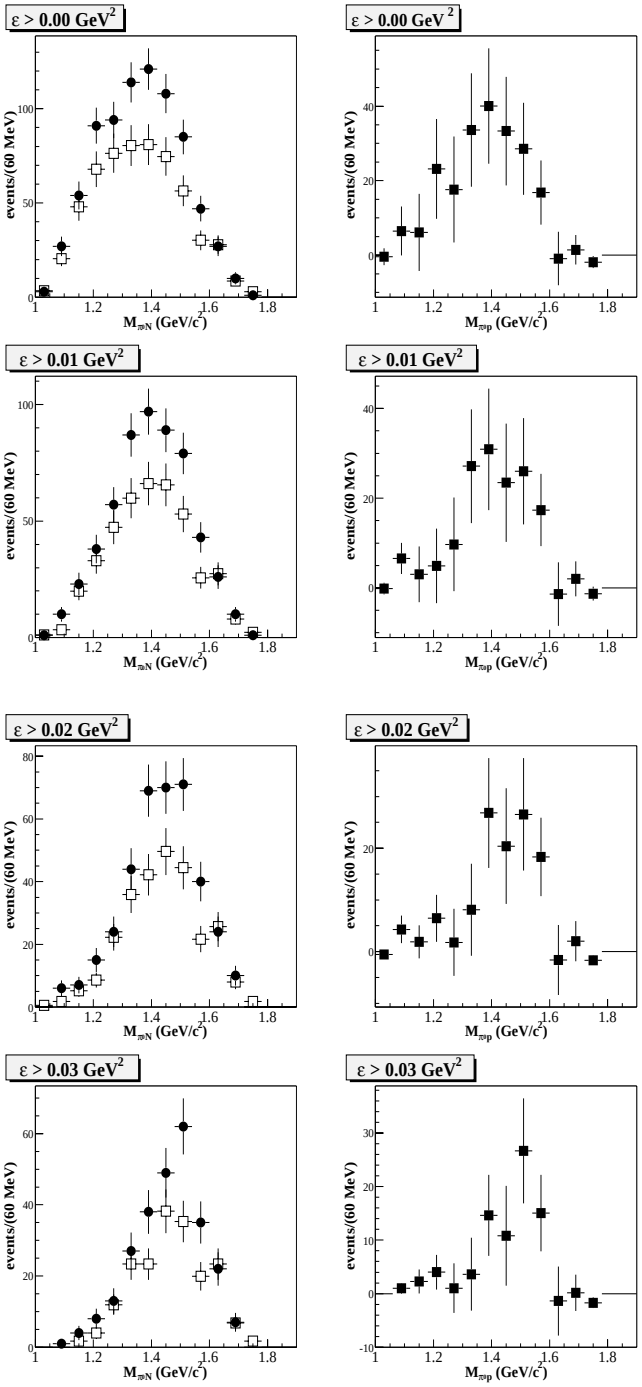

Figure 4.67: $M_{\pi^0 p}$ distributions for the $\pi^0\eta p$ event samples but with various ε-cut values. (filled circles) the CH_2 data (open squares) the carbon data (filled squares) proton target contribution.

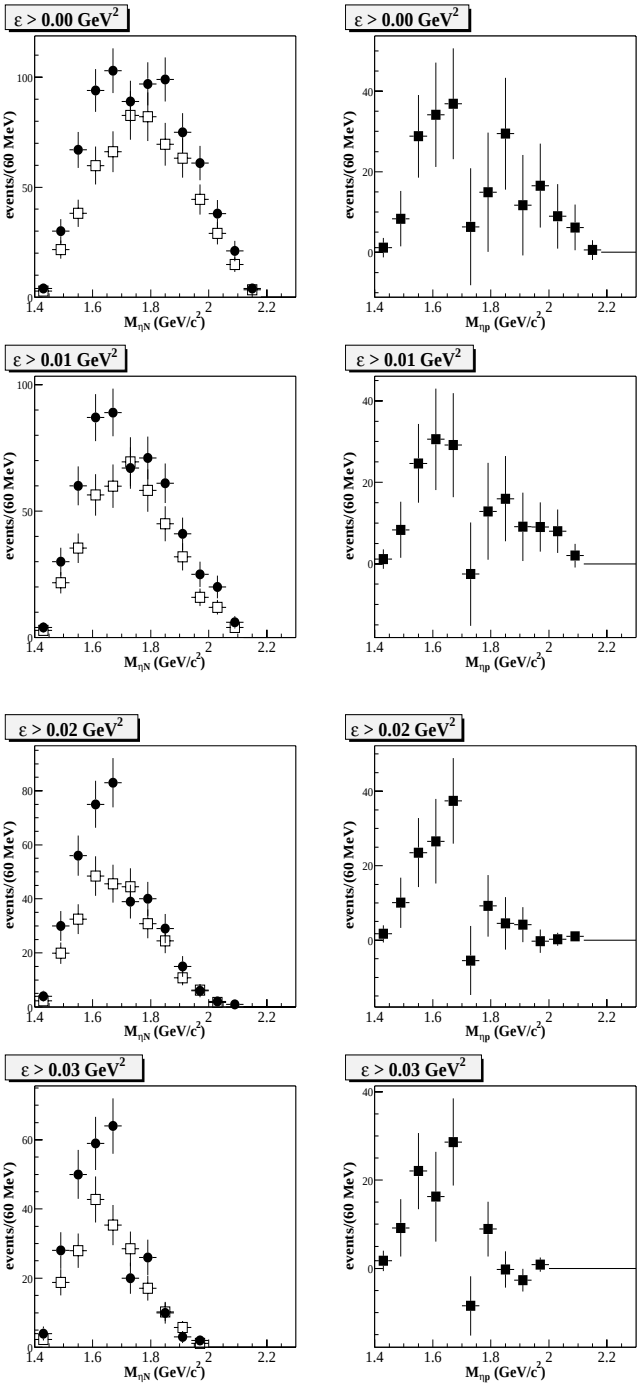

Figure 4.68: $M_{\eta p}$ distributions for the $\pi^0\eta p$ event samples but with various ε-cut values. (filled circles) the CH_2 data (open squares) the carbon data (filled squares) proton target contribution.

target concentrates in the region from 0.9 GeV/c^2 to 1.0 GeV/c^2. This has been expected from the arguments in Section 4.4.1, where the $M_{2\gamma(2)}$ distribution for the proton target has been discussed. The result can be interpreted as the decay of the baryon resonance into the ground state while emitting a scalar-isovector $a_0(980)$ meson, which is the only candidate for coupling with $\pi^0\eta$ system in this mass region [12]. Therefore, the obserbed baryon resonance would couple strongly to the $a_0(980)$ meson.

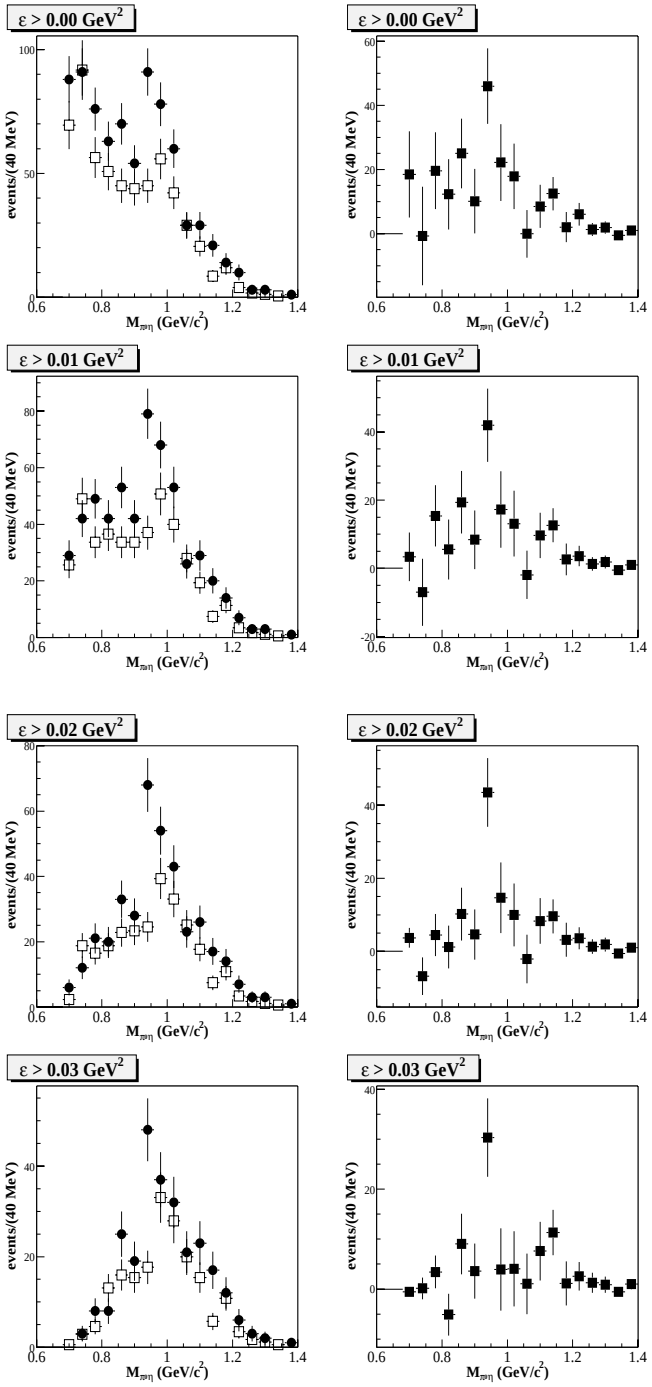

Figure 4.69: $M_{\pi^0\eta}$ distributions for the $\pi^0\eta p$ event samples but with various ε-cut values. (filled circles) the CH_2 data (open squares) the carbon data (filled squares) proton target contribution.

Chapter 5

Result and discussion

5.1 The reaction mechanism of the $\gamma p \to \pi^0 \eta p$ reaction

As discussed in previous chapter, a resonance structure has been observed at around 2.1 GeV/c^2 in the $\sqrt{s}$ distribution for the $\gamma p \to \pi^0 \eta p$ event samples. Furthermore, we found an enhancement at $M_{\pi^0\eta} = 0.9$-1.0 GeV/c^2 in the invariant $\pi^0\eta$ mass spectrum (see Fig. 5.2). This aspect is inferred to come from the fact that the reaction mechanism of the $\gamma p \to \pi^0 \eta p$ reaction at backward angles is dominated by the production of the s-channel baryon resonance that decays into $a_0(980)$ and proton (see Fig. 5.1). In order to confirm whether this interpretation is true, we present systematic arguments in this section.

Acceptance and cut effect

The detector coverage is limited in the region of $\cos\theta^{\mathrm{c.m.}}_{\pi^0\eta} < 0$. Therefore, there is a possibility that the resonance structure might be made due to the acceptance effect, in spite of no existence of baryon resonances. In addition, since we have applied many cuts to obtain the $\pi^0\eta p$-event samples, these cuts might cause a bias with $\sqrt{s}$ dependence. To check both the acceptance and cut effects, MC-event samples were analyzed with the same analysis code and with the same cuts applied to the experimental data. In

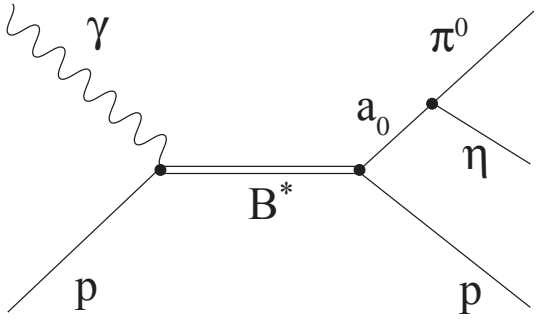

Figure 5.1: Dominant reaction mechanism in the $\gamma p \to \pi^0 \eta p$ reaction at backward angles at around 2.1 GeV/c^2.

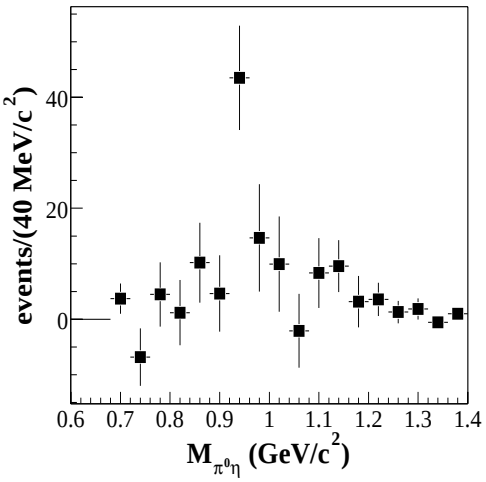

Figure 5.2: $M_{\pi^0\eta}$ mass distribution for the proton target with $\pi^0\eta p$ samples. This plot is the same as the plot in the case of $\varepsilon > 0.02$ GeV^2 in Fig. 4.69.

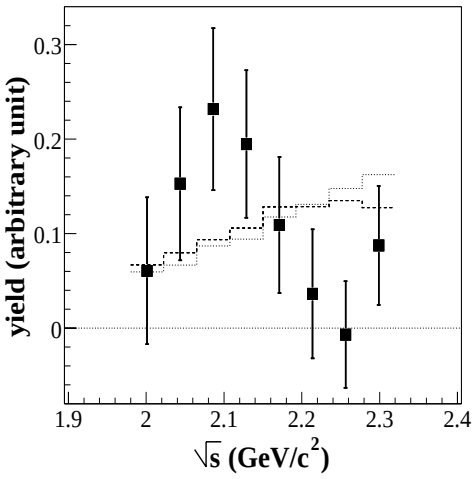

Figure 5.3: $\sqrt{s}$ distribution of the $\pi^0\eta p$-event samples for the proton target (filled squares). This plot is same as that in Fig. 4.66. Two histograms obtained from MC simulation are also superimposed: (Dashed histogram) phase space distribution of the 3-body reaction $\gamma p \to \pi^0\eta p$ (Dotted histogram) phase space distribution of the 2-body $\gamma p \to a_0(980)p$ reaction.

addition, the $\sqrt{s}$ distribution of the MC samples was checked. Two kinds of samples were generated for this purpose:

- (a) 3-body phase space of $\gamma p \to \pi^0\eta p$ events
- (b) 2-body phase space of $\gamma p \to a_0(980)p$ events

where a flat $E_{\rm beam}$ distribution was assumed for both MC samples. The $\sqrt{s}$ distributions obtained from the experimental data, 3-body and 2-body MC samples, are shown in Fig. 5.3, in which the distributions for the MC samples are normalized to the total events of the experimental data. It is evident that both the MC samples do not show any resonance peak. Therefore, we concluded that neither the acceptance effect nor the cut effects make a resonance-like peak in the $\sqrt{s}$ distribution unless the original distribution strongly depends on the $\sqrt{s}$.

Non-resonant backgrounds

In the previous paragraph, we assumed that the original $\sqrt{s}$ distribution has a phase-space distribution. For more practical argument, we will discuss non-resonant background in the a_0 photoproduction near the threshold. Although there is no theoretical calculation for the non-resonant background, some qualitative arguments would be generally considered. Figure 5.4 shows dominant non-resonant diagrams for the

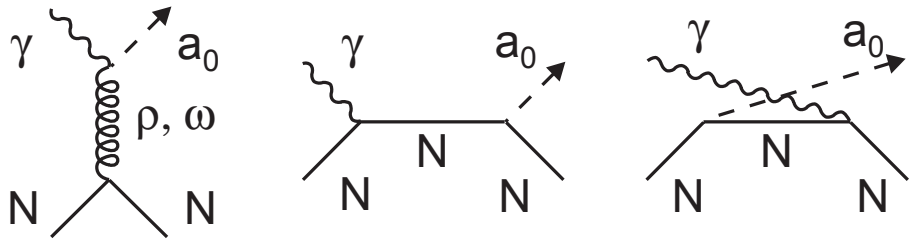

Figure 5.4: Non-resonant background processes near the threshold. (left) t-channel vector-meson exchange, (center) s-channel Born term, and (right) u-channel Born term contributions.

$\gamma N \to a_0 N$ reaction: t-channel vector-meson exchange, s- and u-channel Born term contributions. The t-channel meson-exchange process is important at forward angle; therefore, the contribution is expected to be small since the experimental data is limited in the backward angle region ($\cos\theta^{\rm c.m.}_{\pi^0\eta} < 0$). In general, the energy dependence of the s- and u-channel Born term contributions are expected to increase with increasing energy, or at least remain constant over a large energy range [59]. Thus, it is unlikely to make such the steep rise and fall of the $\sqrt{s}$ distribution due to the Born term contributions. Therefore, one conclude that the resonance-like peak in the $\sqrt{s}$ distribution comes from actually the s-channel resonance production.

The $\sqrt{s}$ distribution with a tight $M_{\pi^0\eta}$ cut

If it is true that the baryon resonance decays into a $a_0(980)$ and a proton, the resonance structure in the $\sqrt{s}$ distribution is expected to remain even after applying a tight $M_{\pi^0\eta}$ cut around $a_0(980)$ region. Figure 5.5 shows the $\sqrt{s}$ distribution for the $\pi^0\eta p$ event sample with $0.9 < M_{\pi^0\eta} < 1.1$ GeV/c^2 cut, which can be compared with the plot without this cut (see Fig. 4.60). The resonance structure still remains as expected. Moreover, the statistical significance of the resonance peak is somewhat improved. The reason is that the S/N ratio (the ratio of the number of $\pi^0\eta$ event coming from the proton target to the number of event from the carbon target) becomes large by selecting the $a_0(980)$ mass region. This result supports that the baryon resonance at around 2.1 GeV/c^2 couples strongly to the $a_0(980)$ resonance. The $\sqrt{s}$ distribution for the samples which excludes the a_0 mass region is also plotted in Fig. 5.6.

On the basis of the arguments mentioned above, the experimental result implies that the $\gamma p \to \pi^0\eta p$ reaction at backward angles ($\cos\theta^{\rm c.m.}_{\pi^0\eta}$ <0) proceeds dominantly via the s-channel baryon-resonance that couples strongly $a_0(980)$ meson and proton. However, since the statistics were not good in the experiment, there is no reason to exclude the hypothesis that no resonance state exists. For instance, a fitting with a constant function to the $\sqrt{s}$ distribution in Fig. 5.3 results in a reasonable fitting (χ^2/d.o.f = 6.7/7). For this reason, higher statistical data is needed for further confirmation of existence of the baryon resonance. Nevertheless, the experimental result is very important because this is the first indication of

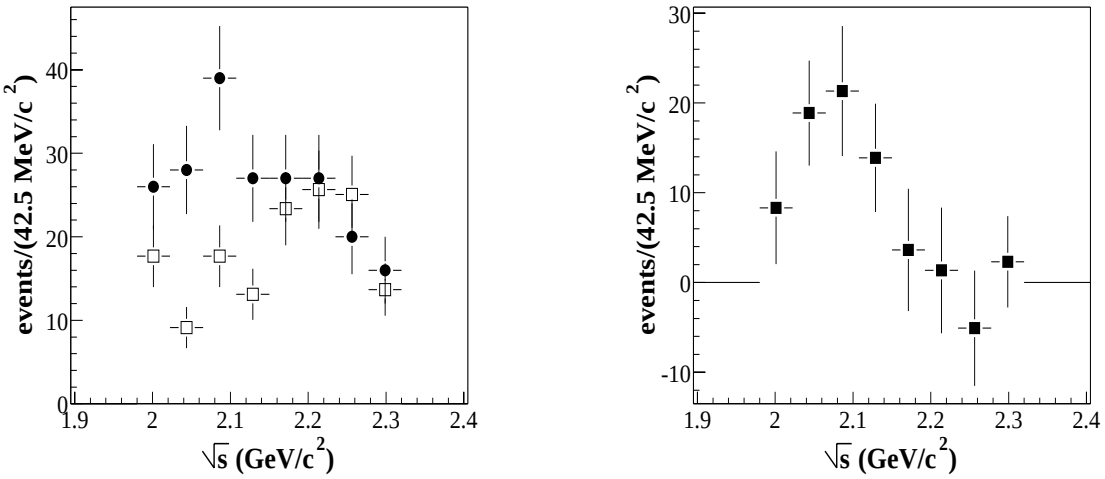

Figure 5.5: The $\sqrt{s}$ distributions for the $\pi^0\eta p$-event samples with $0.9 < M_{\pi^0\eta} < 1.1$ GeV/c^2 cut. (filled circles) the CH_2 data (open squares) the carbon data. Proton target contribution is displayed as the filled squares.

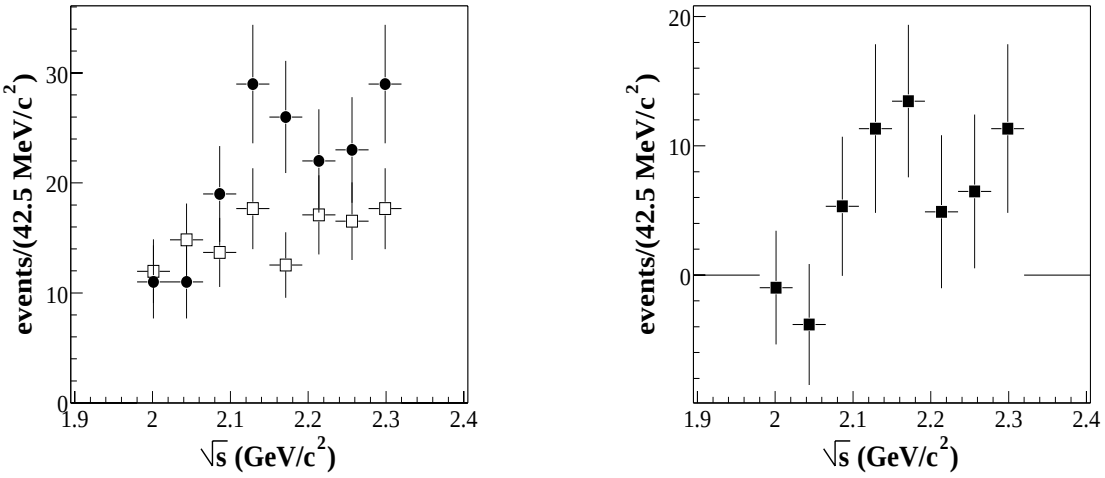

Figure 5.6: The $\sqrt{s}$ distributions for the $\pi^0\eta p$-event samples with cuts $M_{\pi^0\eta} < 0.9$, or $M_{\pi^0\eta} > 1.1$ GeV/c^2 region (thus $a_0(980)$ events are excluded). (filled circles) the CH_2 data (open squares) the carbon data (filled squares) proton target contribution.

the existence of a baryon resonance that decays into the scalar-isovector $a_0(980)$ meson and a proton. Note that there has been no clear evidence for the existence of the baryons that couple to the scalar mesons so far. Therefore, we continue to discuss under the assumption that the baryon resonance exists, in the remaining part.

5.2 Estimate of the mass and width of the baryon resonance

In this section, we will discuss the mass and the width of the resonance state. The mass and the width of the resonance at around 2.1 GeV/c^2 was estimated by comparing the proton spectrum and a distribution obtained from Monte-Carlo simulations assuming a Lorenz function for a resonance distribution with the 2-body phase space of $a_0(980)p$ events. In terms of the mass of the resonance, the χ^2 values as a function of the $\sqrt{s}$ were calculated by assuming different resonance widths ($\Gamma = 90, 120, 150$ MeV/c^2). The result is plotted in Fig. 5.7. The minimum χ^2 is clearly located around $\sqrt{s} = 2080$ MeV/c^2. On the other hands, for the resonance width, the χ^2 values as a function of the width are shown in Fig. 5.8 for the masses of $M = 2060$, 2080 and 2100 MeV/c^2. The χ^2 distribution is asymmetric around minimum value, suggesting that the uncertainty for the width estimation is also asymmetric. From these plots. we recognized that the best fit (minimum χ^2) was achieved when the mass and the width were $M = 2080$ MeV/c^2 and $\Gamma = 100$ MeV/c^2, respectively. The error of these values was obtained from the χ^2 dependence. As a consequence, the mass and the width of the resonance were determined as

$$M \quad = \quad 2080 \pm 20 \ \ \text{MeV}/c^2 \tag{5.1}$$

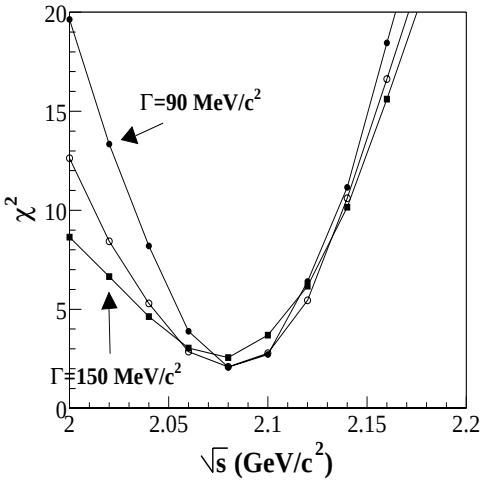

Figure 5.7: χ^2 values as a function of the $\sqrt{s}$ for different resonance width ($\Gamma = 90, 120, 150$ MeV/c^2).

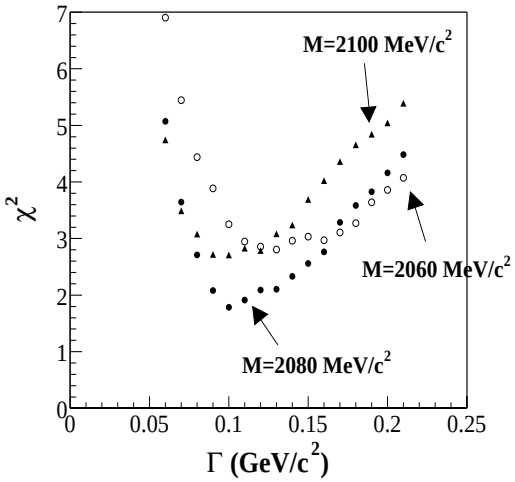

Figure 5.8: χ^2 values as a function of the resonance width for different resonance masses (M =2060, 2080, 2100 MeV/c^2).

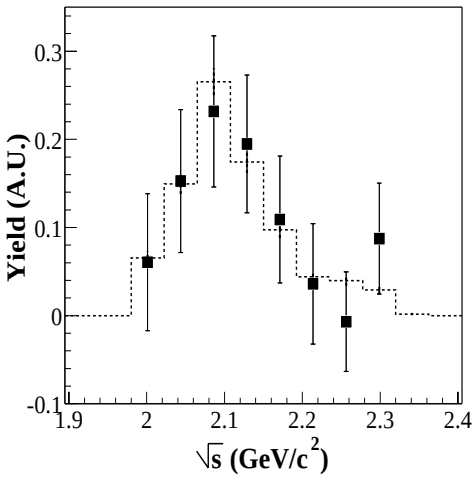

Figure 5.9: $\sqrt{s}$ distributions for both experimental data (filled squares) and MC samples assuming $M =$ 2080 MeV/c^2 and $\Gamma = 100$ MeV/c^2 (histogram).

$$\Gamma \quad = \quad 100^{+60}_{-20} \ \text{MeV}/c^2, \tag{5.2}$$

respectively. Both the experimental data and MC samples with $M = 2080$ MeV/c^2 and $\Gamma = 100$ MeV/c^2 are shown in Fig. 5.9.

5.3 Quantum number of the baryon resonance

The statistics were not good enough to determine the spin-parity of the resonance at $M = 2080$ MeV/c^2. Nevertheless, it is worth to discuss some qualitative nature about the the baryon resonance. Considering the mass of the resonance is approximately 160 MeV/c^2 higher than the $a_0(980)p$ production threshold ($\sim$1920 MeV/c^2). Thus, either s-wave or p-wave could be the main contribution to the reaction. Hence the spin-parity of the resonance would be $J^P = 1/2^+$ for s-wave or $J^P = 1/2^-, 3/2^-$ for p-wave. The third component of the isospin is $I_3 = +1/2$ although the total isospin can be either $I = 1/2$ or $3/2$. The isospin is expected to be determined in the study of the $\pi^+ p \to a_0^+(980)p \to \pi^+\eta p$ reaction.

5.4 Possible candidates for the baryon resonance

5.4.1 From PDG database

Table 5.1 shows all the non-strange baryon resonances listed in PDG database. Considering the mass ($M = 2080 \pm 20$MeV/c^2) and the spin ($J^P = 1/2^+,\ 1/2^-,\ 3/2^-$) of the observed resonance, one can find three possible candidates in the PDG listing: $D_{13}(2080)$, $S_{11}(2090)$ and $P_{11}(2100)$. Here, these labels means the usual notation as $L_{2I2J}(W)$, where W is mass, $L = 0, 1, 2, ...$ the angular momentum

for the decay into the πN-channel given in the spectroscopic notation as $S, P, D, ...$ and I, J are isospin and spin of the resonances, respectively. Therefore, if the observed resonance is regarded as a s-wave resonance, it is uniquely assigned as $P_{11}(2100)$. On the other hand, if the observed resonance is a p-wave resonance, the resonance can be assigned to either $S_{11}(2090)$ for $J^P = 1/2^-$ or $D_{13}(2080)$ for $J^P = 3/2^-$. There is no Δ^* candidate matching the observed resonance in the PDG listing. These three possible N^* resonances have 1-star or 2-star rating in the PDG listing. This means that the observed resonance is not well-established resonance.

Table 5.1: The status of the N and Δ resonances in PDG database [12].

			Status as seen in —						
Particle	$L_{2I\,2J}$	Overall status	$N\pi$	$N\eta$	ΛK	ΣK	$\Delta\pi$	$N\rho$	$N\gamma$
$N(939)$	P_{11}	****							
$N(1440)$	P_{11}	****	****	*			***	*	***
$N(1520)$	D_{13}	****	****	*			****	****	****
$N(1535)$	S_{11}	****	****	****			*	**	***
$N(1650)$	S_{11}	****	****	*	***	**	***	**	***
$N(1675)$	D_{15}	****	****	*	*		****	*	****
$N(1680)$	F_{15}	****	****				****	****	****
$N(1700)$	D_{13}	***	***	*	**	*	**	*	**
$N(1710)$	P_{11}	***	***	**	**	*	**	*	***
$N(1720)$	P_{13}	****	****	*	**	*	*	**	**
$N(1900)$	P_{13}	**	**					*	
$N(1990)$	F_{17}	**	**	*	*	*			*
$N(2000)$	F_{15}	**	**	*	*	*	*	**	
$N(2080)$	D_{13}	**	**	*	*				*
$N(2090)$	S_{11}	*	*						
$N(2100)$	P_{11}	*	*	*					
$N(2190)$	G_{17}	****	****	*	*	*		*	*
$N(2200)$	D_{15}	**	**	*	*				
$N(2220)$	H_{19}	****	****	*					
$N(2250)$	G_{19}	****	****	*					
$N(2600)$	I_{111}	***	***						
$N(2700)$	K_{113}	**	**						
$\Delta(1232)$	P_{33}	****	****	F					****
$\Delta(1600)$	P_{33}	***	***	o			***	*	**
$\Delta(1620)$	S_{31}	****	****	r			****	****	***
$\Delta(1700)$	D_{33}	****	****	b		*	***	**	***
$\Delta(1750)$	P_{31}	*	*	i					
$\Delta(1900)$	S_{31}	**	**	d		*	*	**	*
$\Delta(1905)$	F_{35}	****	****	d		*	**	**	***
$\Delta(1910)$	P_{31}	****	****	e		*	*	*	*
$\Delta(1920)$	P_{33}	***	***	n		*	**		*
$\Delta(1930)$	D_{35}	***	***			*			**
$\Delta(1940)$	D_{33}	*	*	F					
$\Delta(1950)$	F_{37}	****	****	o		*	****	*	****
$\Delta(2000)$	F_{35}	**		r				**	
$\Delta(2150)$	S_{31}	*	*	b					
$\Delta(2200)$	G_{37}	*	*	i					
$\Delta(2300)$	H_{39}	**	**	d					
$\Delta(2350)$	D_{35}	*	*	d					
$\Delta(2390)$	F_{37}	*	*	e					
$\Delta(2400)$	G_{39}	**	**	n					
$\Delta(2420)$	H_{311}	****	****						*
$\Delta(2750)$	I_{313}	**	**						
$\Delta(2950)$	K_{315}	**	**						

**** Existence is certain, and properties are at least fairly well explored.

*** Existence ranges from very likely to certain, but further confirmation is desirable and/or quantum numbers, branching fractions, *etc.* are not well determined.

** Evidence of existence is only fair.

* Evidence of existence is poor.

Chapter 6

Summary

Study of the photoproduction of the baryon resonances is very important since it gives us a new insight into the non-perturbative QCD, especially the internal structure of the baryons. The $\gamma p \to \pi^0 \eta p$ reaction has been studied in order to investigate s-channel baryon resonances around 2 GeV/c^2. This reaction is useful to identify the reaction mechanism since both π^0 and η can be distinguishable, and hence various decay modes such as $\eta\Delta^+$, $\pi^0 S_{11}(1535)$ and $a_0(980)p$ can be studied.

The experiment was performed at the Laser-Electron-Photon facility at SPring-8 (LEPS). A tagged photon-beam of the energy between 1.62 and 2.40 GeV was employed in the experiment. An electromagnetic (EM) calorimeter with the 252 Lead/SCIFI modules was newly constructed and was used for detecting 4-photons coming from the $\pi^0\eta$ decay ($\pi^0 \to \gamma\gamma$, $\eta \to \gamma\gamma$) processes. The calorimeter covered an angular region from 30° to 100° for the polar angle, and from 0° to 360° for the azimuthal angle. The solid angle of the constructed calorimeter covered 2.08π sr. A 50-mm thick polyethylene (CH_2) target and a 40-mm thick carbon target were used in the experiment. To separate photons from any charged particles originating from the target, 12 sets of 5-mm thick plastic scintillators (CV) were placed in front of the calorimeter faces. Totally 6.2×10^7 and 4.2×10^7 triggered events were accumulated in the experiments with the carbon and CH_2 targets, respectively.

In the data analysis, photon reconstruction was the first step. A photon cluster was defined as an event giving the energy deposit larger than an energy threshold $E_{th} = 20$ MeV in any calorimeter module and giving no signal at the same time on the corresponding CV counter. Events with 4 photon-clusters in polar angle θ from 40° to 90° were selected. To suppress the events with a cluster including two photons that hit close to each other, clusters with a large second moment ($F_{\max} > 0.02$) were rejected.

A kinematical analysis was performed for all 4γ-event samples in order to select correct photon combinations. Since the 4γ-event samples above the $\pi^0\eta$ production-threshold ($M_{4\gamma} = 0.68$ GeV/c^2) mainly come from decays of $\pi^0\eta$ and $\pi^0\pi^0$, two hypotheses were tested for each event: $\pi^0\eta$ production ($H_{\rm I}$) and $\pi^0\pi^0$ production ($H_{\rm II}$). A combination with the minimum χ^2 among all the combinations was checked and events above 10% significance level were selected as $\pi^0\eta$ candidates. Furthermore, a cut $\Pr(\chi^2_I) > \Pr(\chi^2_{\rm II})$ was also applied to the $\pi^0\eta$ candidates for $\pi^0\pi^0$ event reduction. After the statistical testing, finally 5011

events in the experiment with the carbon target and 3547 events in the experiment with the CH_2 target remained.

To reduce the background events originating from the $\pi^0\pi^0$ production process, the $\varepsilon > 0.02$ GeV^2 cut was applied. The distribution for the carbon target was normalized to that for the CH_2 target in the region of $MM_{\gamma\pi^0\eta} < 0.7$ GeV/c^2, where the data was dominated by the carbon target contribution. The scale factor for this normalization was determined to be $k_{\rm scale} = 0.57 \pm 0.06$. Events with the missing mass $MM_{\gamma\pi^0\eta}$ from 0.85 GeV/c^2 to 1.03 GeV/c^2 were selected as the $\pi^0\eta p$ event sample. This cut increases the signal to noise ratio (the ratio of the number of $\pi^0\eta$ event coming from the proton target to the number of event from the carbon target) from 0.22 to 0.42 and rejects possible events from the background $\pi^0\pi^0$ production events. As a result, 469 events in the carbon-target measurement and 380 events in the CH_2-target measurement remained.

The $\sqrt{s}$ distribution of the $\pi^0\eta p$ samples clearly shows a resonance structure with $M = 2080 \pm 20$ MeV/c^2 and $\Gamma = 100^{+60}_{-20}$ MeV/c^2. Therefore, we concluded that the $\gamma p \to \pi^0\eta p$ reaction at backward angles dominantly proceeds via the s-channel baryon resonance. The invariant $\pi^0\eta$-mass distribution concentrated in the region from 0.9 GeV/c^2 to 1.0 GeV/c^2. This fact indicates that the resonance couples strongly to the scalar-isovector $a_0(980)$ meson. Considering that the mass of the resonance is approximately 160 MeV/c^2 higher than the $a_0(980)p$ production threshold ($\sim$1920 MeV/c^2), either s-wave or p-wave is expected to be the main contribution to the reaction. Hence, the spin-parity of the resonance is expected to be $J^P = 1/2^+$ for s-wave or $J^P = 1/2^-, 3/2^-$ for p-wave. The third component of the isospin should be $I_3 = +1/2$ although the total isospin is either $I = 1/2$ or $3/2$.

Appendix A

Geometry of the Lead/SCIFI modules

In this appendix, the size of the Lead/SCIFI modules are summarized. The vertices of a polyhedron and angles are defined as illustrated in Fig.A.1.

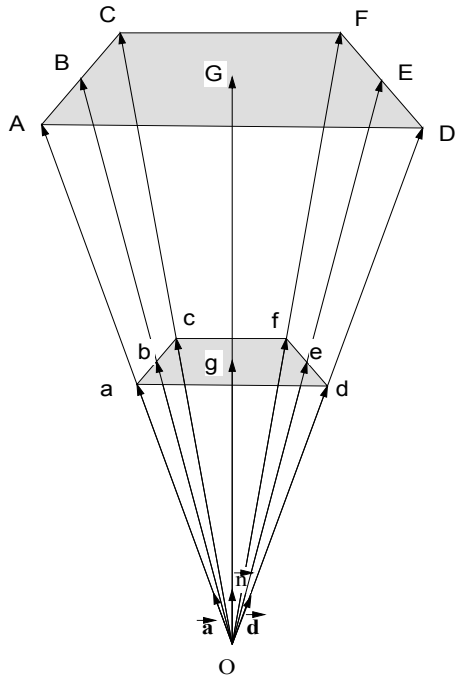

Figure A.1: Definition of the vertices of a Lead/SCIFI polyhedron.

Table A.1: Length of each side and the volume of a TYPE B-3 module.

Polar angle for each unit vector (degree)

θ_a	30.000	θ_b	29.906	θ_c	30.000
θ_d	40.000	θ_e	39.892	θ_f	40.000
ϕ_a	0.000	ϕ_b	5.000	ϕ_c	10.000
ϕ_d	0.000	ϕ_e	5.000	ϕ_f	10.000
θ_g	34.899	ϕ_g	5.000		

Length (mm)

$\overrightarrow{\mathrm{Oa}}$	301.429	$\overrightarrow{\mathrm{Ob}}$	301.143	$\overrightarrow{\mathrm{Oc}}$	301.429
$\overrightarrow{\mathrm{Od}}$	301.617	$\overrightarrow{\mathrm{Oe}}$	301.143	$\overrightarrow{\mathrm{Of}}$	301.617
$\overrightarrow{\mathrm{OA}}$	522.477	$\overrightarrow{\mathrm{OB}}$	521.981	$\overrightarrow{\mathrm{OC}}$	522.477
$\overrightarrow{\mathrm{OD}}$	522.802	$\overrightarrow{\mathrm{OE}}$	521.981	$\overrightarrow{\mathrm{OF}}$	522.802
$\overrightarrow{\mathrm{aA}}$	221.048	$\overrightarrow{\mathrm{bB}}$	220.838	$\overrightarrow{\mathrm{cC}}$	221.048
$\overrightarrow{\mathrm{dD}}$	221.186	$\overrightarrow{\mathrm{eE}}$	220.838	$\overrightarrow{\mathrm{fF}}$	221.186
$\overrightarrow{\mathrm{ac}}$	26.271	$\overrightarrow{\mathrm{cf}}$	52.559	$\overrightarrow{\mathrm{be}}$	52.424
$\overrightarrow{\mathrm{fd}}$	33.795	$\overrightarrow{\mathrm{da}}$	52.559		
$\overrightarrow{\mathrm{AC}}$	45.537	$\overrightarrow{\mathrm{CF}}$	91.103	$\overrightarrow{\mathrm{BE}}$	90.869
$\overrightarrow{\mathrm{FD}}$	58.578	$\overrightarrow{\mathrm{DA}}$	91.103		

Area S(cm^2)

Front face(*acfd*)	15.745	Rear Face(*ACFD*)	47.304

Volume V and Weight W

V	=	704.47(cm^3)
W	=	3.23(kg)

Table A.2: Length of each side and the volume of a TYPE B-4 module.

Polar angle for each unit vector (degree)

θ_a	40.000	θ_b	39.892	θ_c	40.000
θ_d	50.000	θ_e	49.892	θ_f	50.000
ϕ_a	0.000	ϕ_b	5.000	ϕ_c	10.000
ϕ_d	0.000	ϕ_e	5.000	ϕ_f	10.000
θ_g	44.892	ϕ_g	5.000		

Length (mm)

$\overrightarrow{\mathrm{Oa}}$	301.620	$\overrightarrow{\mathrm{Ob}}$	301.146	$\overrightarrow{\mathrm{Oc}}$	301.620
$\overrightarrow{\mathrm{Od}}$	301.819	$\overrightarrow{\mathrm{Oe}}$	301.146	$\overrightarrow{\mathrm{Of}}$	301.819
$\overrightarrow{\mathrm{OA}}$	522.807	$\overrightarrow{\mathrm{OB}}$	521.986	$\overrightarrow{\mathrm{OC}}$	522.807
$\overrightarrow{\mathrm{OD}}$	523.154	$\overrightarrow{\mathrm{OE}}$	521.986	$\overrightarrow{\mathrm{OF}}$	523.154
$\overrightarrow{\mathrm{aA}}$	221.188	$\overrightarrow{\mathrm{bB}}$	220.840	$\overrightarrow{\mathrm{cC}}$	221.188
$\overrightarrow{\mathrm{dD}}$	221.344	$\overrightarrow{\mathrm{eE}}$	220.840	$\overrightarrow{\mathrm{fF}}$	221.334
$\overrightarrow{\mathrm{ac}}$	33.795	$\overrightarrow{\mathrm{cf}}$	52.594	$\overrightarrow{\mathrm{be}}$	52.493
$\overrightarrow{\mathrm{fd}}$	40.302	$\overrightarrow{\mathrm{da}}$	52.594		
$\overrightarrow{\mathrm{AC}}$	58.578	$\overrightarrow{\mathrm{CF}}$	91.162	$\overrightarrow{\mathrm{BE}}$	90.988
$\overrightarrow{\mathrm{FD}}$	69.857	$\overrightarrow{\mathrm{DA}}$	91.162		

Area S(cm^2)

Front face(*acfd*)	19.448	Rear Face(*ACFD*)	58.430

Volume V and Weight W

V	=	870.17(cm^3)
W	=	3.99(kg)

Table A.3: Length of each side and the volume of a TYPE B-5 module.

Polar angle for each unit vector (degree)

θ_a	50.000	θ_b	49.892	θ_c	50.000
θ_d	60.000	θ_e	59.905	θ_f	60.000
ϕ_a	0.000	ϕ_b	5.000	ϕ_c	10.000
ϕ_d	0.000	ϕ_e	5.000	ϕ_f	10.000
θ_g	54.899	ϕ_g	5.000		

Length (mm)

$\overrightarrow{\mathrm{Oa}}$	301.822	$\overrightarrow{\mathrm{Ob}}$	301.149	$\overrightarrow{\mathrm{Oc}}$	301.822
$\overrightarrow{\mathrm{Od}}$	302.010	$\overrightarrow{\mathrm{Oe}}$	301.149	$\overrightarrow{\mathrm{Of}}$	302.010
$\overrightarrow{\mathrm{OA}}$	523.159	$\overrightarrow{\mathrm{OB}}$	521.991	$\overrightarrow{\mathrm{OC}}$	523.159
$\overrightarrow{\mathrm{OD}}$	523.485	$\overrightarrow{\mathrm{OE}}$	521.991	$\overrightarrow{\mathrm{OF}}$	523.485
$\overrightarrow{\mathrm{aA}}$	221.336	$\overrightarrow{\mathrm{bB}}$	220.843	$\overrightarrow{\mathrm{cC}}$	221.336
$\overrightarrow{\mathrm{dD}}$	221.474	$\overrightarrow{\mathrm{eE}}$	220.843	$\overrightarrow{\mathrm{fF}}$	221.474
$\overrightarrow{\mathrm{ac}}$	40.302	$\overrightarrow{\mathrm{cf}}$	52.628	$\overrightarrow{\mathrm{be}}$	52.561
$\overrightarrow{\mathrm{fd}}$	45.591	$\overrightarrow{\mathrm{da}}$	52.628		
$\overrightarrow{\mathrm{AC}}$	69.858	$\overrightarrow{\mathrm{CF}}$	91.222	$\overrightarrow{\mathrm{BE}}$	91.106
$\overrightarrow{\mathrm{FD}}$	79.024	$\overrightarrow{\mathrm{DA}}$	91.222		

Area S(cm^2)

Front face(*acfd*)	22.573	Rear Face(*ACFD*)	67.820

Volume V and Weight W

V	=	1010.01(cm^3)
W	=	4.63(kg)

Table A.4: Length of each side and the volume of a TYPE B-6 module.

Polar angle for each unit vector (degree)

θ_a	60.000	θ_b	59.905	θ_c	60.000
θ_d	70.000	θ_e	69.930	θ_f	70.000
ϕ_a	0.000	ϕ_b	5.000	ϕ_c	10.000
ϕ_d	0.000	ϕ_e	5.000	ϕ_f	10.000
θ_g	64.918	ϕ_g	5.000		

Length (mm)

$\overrightarrow{\mathrm{Oa}}$	302.013	$\overrightarrow{\mathrm{Ob}}$	301.152	$\overrightarrow{\mathrm{Oc}}$	302.013
$\overrightarrow{\mathrm{Od}}$	302.167	$\overrightarrow{\mathrm{Oe}}$	301.152	$\overrightarrow{\mathrm{Of}}$	302.167
$\overrightarrow{\mathrm{OA}}$	523.489	$\overrightarrow{\mathrm{OB}}$	521.996	$\overrightarrow{\mathrm{OC}}$	523.489
$\overrightarrow{\mathrm{OD}}$	523.756	$\overrightarrow{\mathrm{OE}}$	521.996	$\overrightarrow{\mathrm{OF}}$	523.756
$\overrightarrow{\mathrm{aA}}$	221.476	$\overrightarrow{\mathrm{bB}}$	220.844	$\overrightarrow{\mathrm{cC}}$	221.476
$\overrightarrow{\mathrm{dD}}$	221.589	$\overrightarrow{\mathrm{eE}}$	220.844	$\overrightarrow{\mathrm{fF}}$	221.589
$\overrightarrow{\mathrm{ac}}$	45.591	$\overrightarrow{\mathrm{cf}}$	52.658	$\overrightarrow{\mathrm{be}}$	52.622
$\overrightarrow{\mathrm{fd}}$	49.495	$\overrightarrow{\mathrm{da}}$	52.658		
$\overrightarrow{\mathrm{AC}}$	79.025	$\overrightarrow{\mathrm{CF}}$	91.274	$\overrightarrow{\mathrm{BE}}$	91.211
$\overrightarrow{\mathrm{FD}}$	85.791	$\overrightarrow{\mathrm{DA}}$	91.274		

Area S(cm^2)

Front face(*acfd*)	25.018	Rear Face(*ACFD*)	75.165

Volume V and Weight W

V	=	1119.39(cm^3)
W	=	5.13(kg)

Table A.5: Length of each side and the volume of a TYPE B-7 module.

Polar angle for each unit vector (degree)

θ_a	70.000	θ_b	69.930	θ_c	70.000
θ_d	80.000	θ_e	79.963	θ_f	80.000
ϕ_a	0.000	ϕ_b	5.000	ϕ_c	10.000
ϕ_d	0.000	ϕ_e	5.000	ϕ_f	10.000
θ_g	74.946	ϕ_g	5.000		

Length (mm)

$\overrightarrow{\mathrm{Oa}}$	302.169	$\overrightarrow{\mathrm{Ob}}$	301.154	$\overrightarrow{\mathrm{Oc}}$	302.169
$\overrightarrow{\mathrm{Od}}$	302.269	$\overrightarrow{\mathrm{Oe}}$	301.154	$\overrightarrow{\mathrm{Of}}$	302.269
$\overrightarrow{\mathrm{OA}}$	523.759	$\overrightarrow{\mathrm{OB}}$	521.999	$\overrightarrow{\mathrm{OC}}$	523.759
$\overrightarrow{\mathrm{OD}}$	523.933	$\overrightarrow{\mathrm{OE}}$	521.999	$\overrightarrow{\mathrm{OF}}$	523.933
$\overrightarrow{\mathrm{aA}}$	221.590	$\overrightarrow{\mathrm{bB}}$	220.846	$\overrightarrow{\mathrm{cC}}$	221.590
$\overrightarrow{\mathrm{dD}}$	221.664	$\overrightarrow{\mathrm{eE}}$	220.846	$\overrightarrow{\mathrm{fF}}$	221.664
$\overrightarrow{\mathrm{ac}}$	49.495	$\overrightarrow{\mathrm{cf}}$	52.680	$\overrightarrow{\mathrm{be}}$	52.667
$\overrightarrow{\mathrm{fd}}$	51.888	$\overrightarrow{\mathrm{da}}$	52.680		
$\overrightarrow{\mathrm{AC}}$	85.791	$\overrightarrow{\mathrm{CF}}$	91.313	$\overrightarrow{\mathrm{BE}}$	91.289
$\overrightarrow{\mathrm{FD}}$	89.940	$\overrightarrow{\mathrm{DA}}$	91.313		

Area S(cm^2)

Front face(*acfd*)	26.698	Rear Face(*ACFD*)	80.212

Volume V and Weight W

V	=	1194.56(cm^3)
W	=	5.47(kg)

Table A.6: Length of each side and the volume of a TYPE B-8 module.

Polar angle for each unit vector (degree)

θ_a	80.000	θ_b	79.693	θ_c	80.000
θ_d	90.000	θ_e	90.000	θ_f	90.000
ϕ_a	0.000	ϕ_b	5.000	ϕ_c	10.000
ϕ_d	0.000	ϕ_e	5.000	ϕ_f	10.000
θ_g	84.981	ϕ_g	5.000		

Length (mm)

$\overrightarrow{\mathrm{Oa}}$	302.270	$\overrightarrow{\mathrm{Ob}}$	301.155	$\overrightarrow{\mathrm{Oc}}$	302.270
$\overrightarrow{\mathrm{Od}}$	302.305	$\overrightarrow{\mathrm{Oe}}$	301.155	$\overrightarrow{\mathrm{Of}}$	302.305
$\overrightarrow{\mathrm{OA}}$	523.935	$\overrightarrow{\mathrm{OB}}$	522.001	$\overrightarrow{\mathrm{OC}}$	523.935
$\overrightarrow{\mathrm{OD}}$	523.995	$\overrightarrow{\mathrm{OE}}$	522.001	$\overrightarrow{\mathrm{OF}}$	523.995
$\overrightarrow{\mathrm{aA}}$	221.665	$\overrightarrow{\mathrm{bB}}$	220.847	$\overrightarrow{\mathrm{cC}}$	221.665
$\overrightarrow{\mathrm{dD}}$	221.690	$\overrightarrow{\mathrm{eE}}$	220.847	$\overrightarrow{\mathrm{fF}}$	221.690
$\overrightarrow{\mathrm{ac}}$	51.889	$\overrightarrow{\mathrm{cf}}$	52.692	$\overrightarrow{\mathrm{be}}$	52.691
$\overrightarrow{\mathrm{fd}}$	52.695	$\overrightarrow{\mathrm{da}}$	52.691		
$\overrightarrow{\mathrm{AC}}$	89.940	$\overrightarrow{\mathrm{CF}}$	91.333	$\overrightarrow{\mathrm{BE}}$	91.330
$\overrightarrow{\mathrm{FD}}$	91.338	$\overrightarrow{\mathrm{DA}}$	91.333		

Area S(cm^2)

Front face(*acfd*)	27.553	Rear Face(*ACFD*)	82.781

Volume V and Weight W

V	=	1232.82(cm^3)
W	=	5.65(kg)

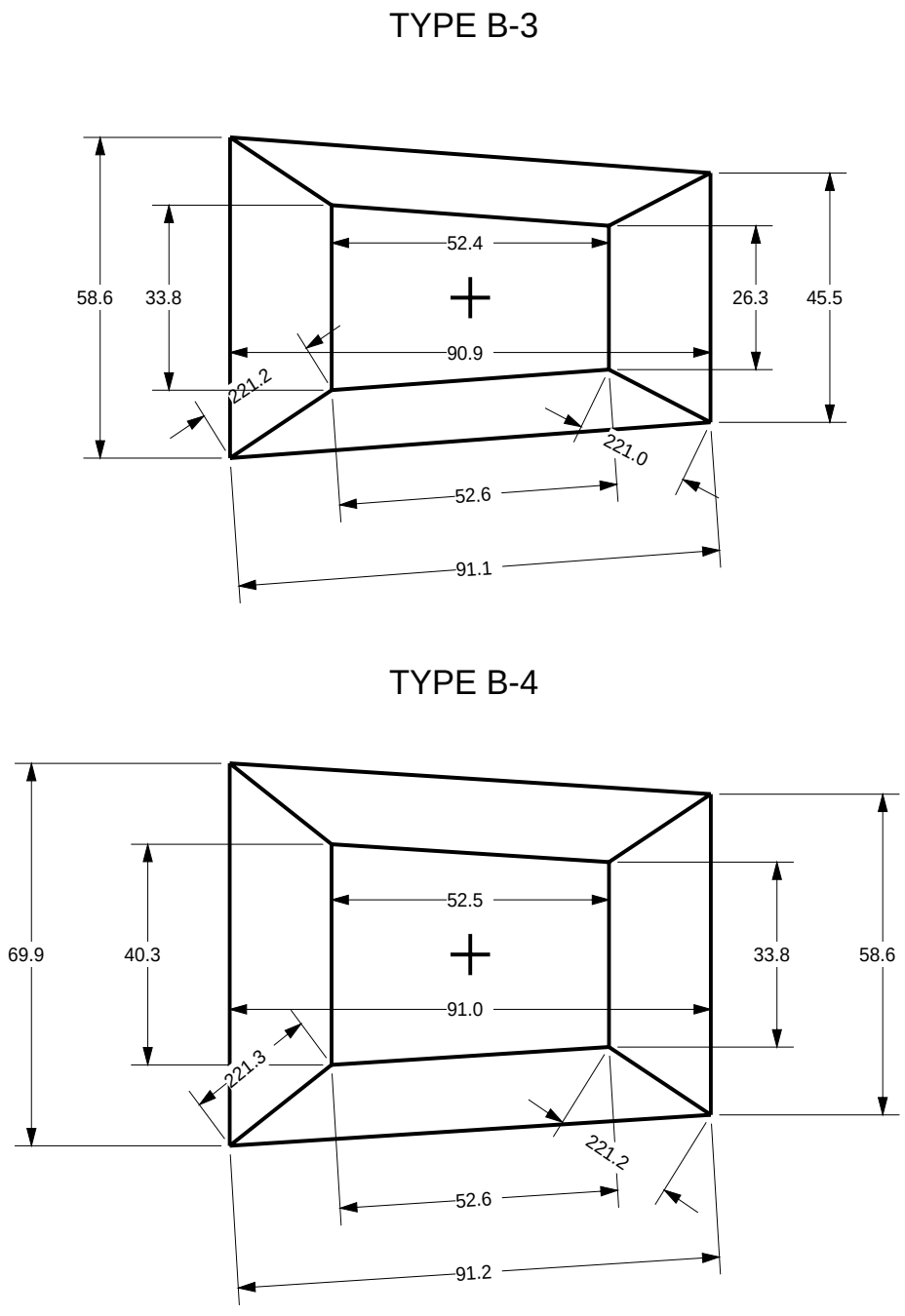

Figure A.2: Geometry of the Lead/SCIFI block (TYPE B-3, TYPE B-4).

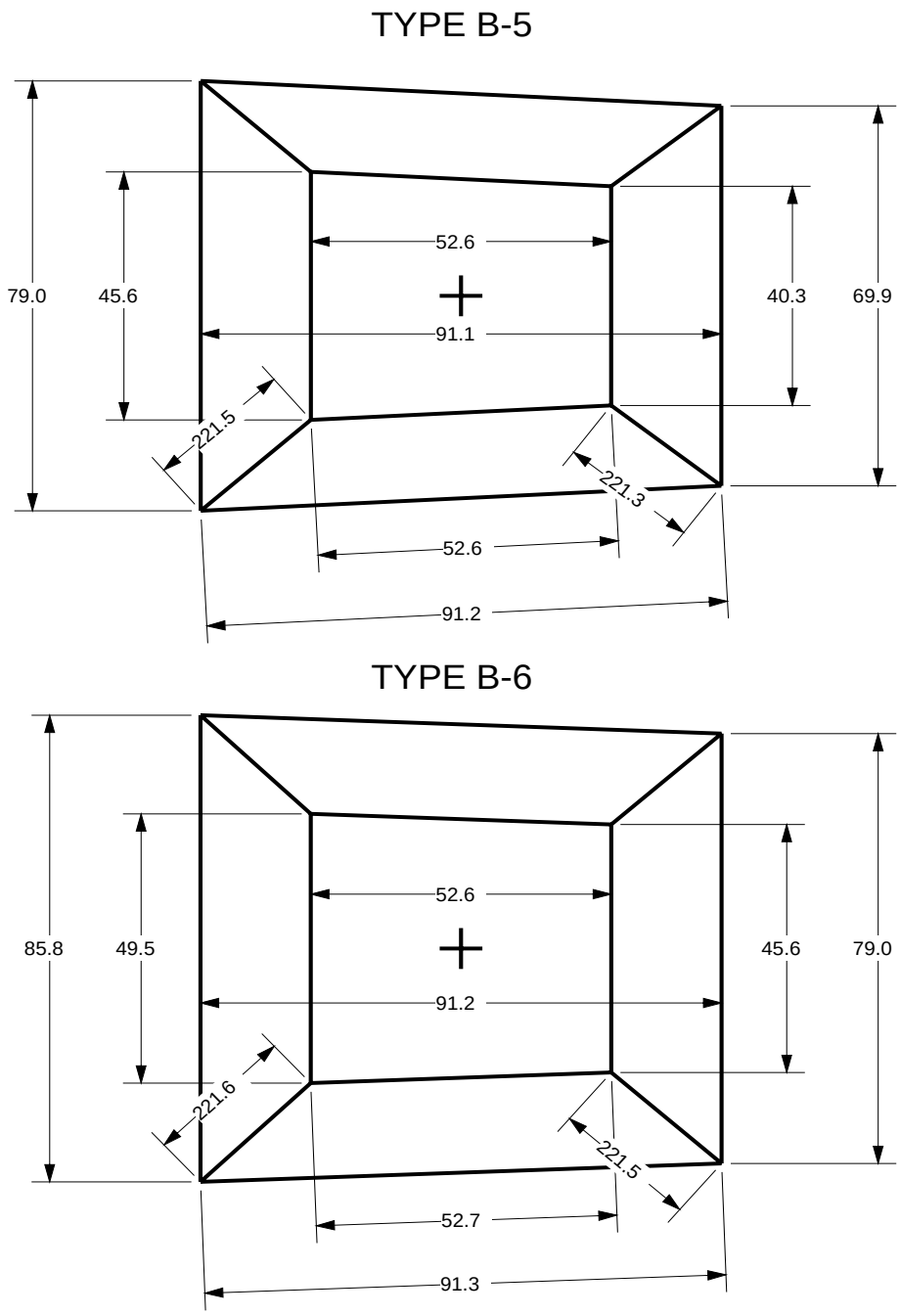

Figure A.3: Geometry of the Lead/SCIFI block (TYPE B-5, TYPE B-6).

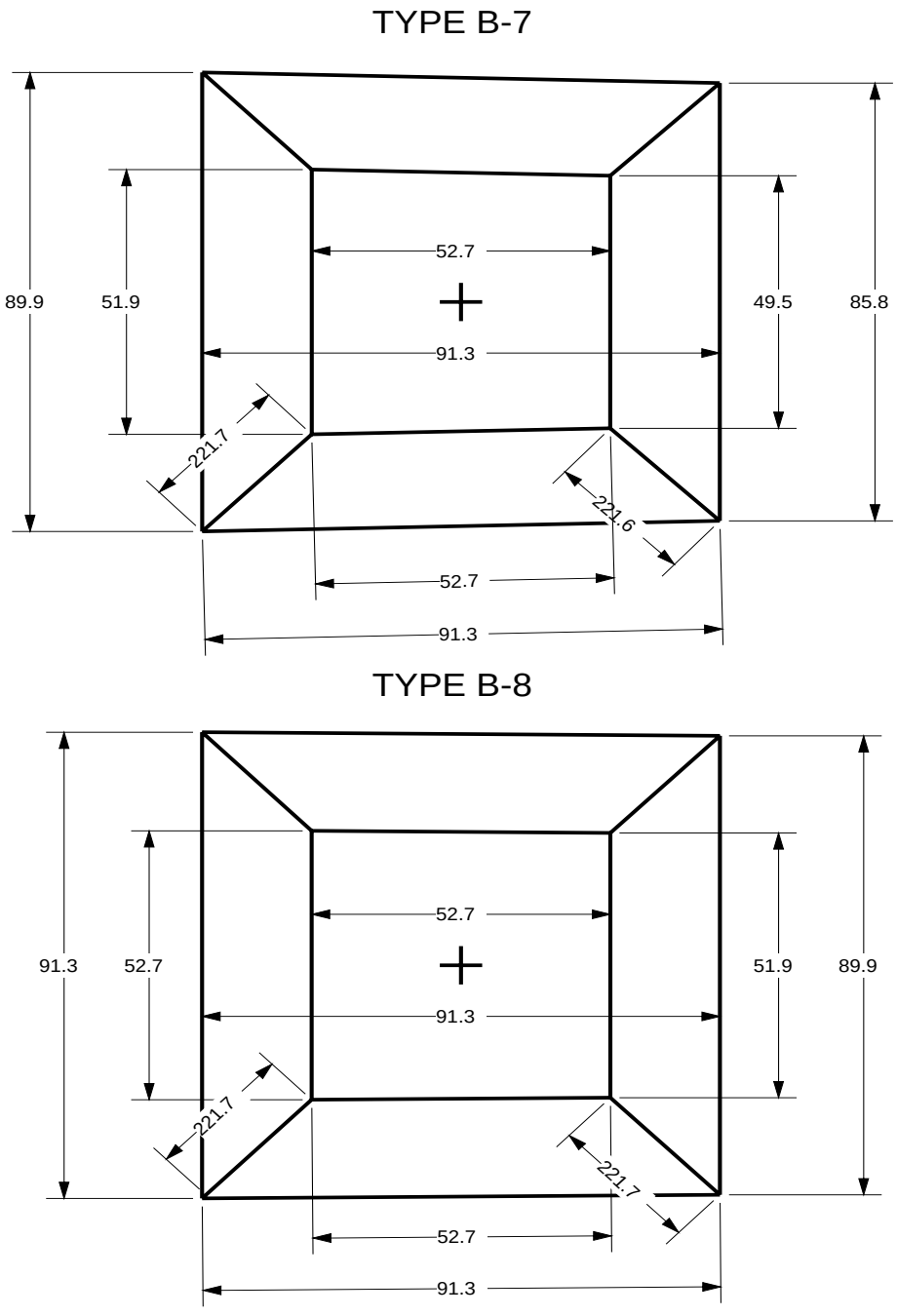

Figure A.4: Geometry of the Lead/SCIFI block (TYPE B-7, TYPE B-8).

Appendix B

Validity of the Monte-Carlo simulation with the simple geometry code

In this Appendix, the validity of the Monte-Carlo simulation code with simple geometry (CODE 2), where the Lead/SCIFI material is regarded as a homogeneous material consisting of a mixture of the scintillating fiber (SCIFI), lead-alloy radiator (PB) and optical cement (GLUE), will be evaluated.

Since the volume ratio among SCIFI and PB and GLUE is 50 : 35 : 15, the density of a mixed material ($\rho_{\rm mixure}$) can be obtained as follows:

$$\rho_{\rm mixure} = 0.50\rho_{\rm SCIFI} + 0.35\rho_{\rm PB} + 0.15\rho_{\rm GLUE}, \tag{B.1}$$

where $\rho_{\rm SCIFI}$, $\rho_{\rm PB}$ and $\rho_{\rm GLUE}$ are 1.05 g/cm^3, 10.9 g/cm^3 and 1.18 g/cm^3, respectively. Since the CODE 2 defines an approximate geometry, the validity of the energy-loss calculation for CODE 2 should be checked. Furthermore the total energy deposit in a Lead/SCIFI module can be calculated using CODE 2, but sampling energy can not be obtained because the module is described as a homogeneous material in this code. Therefore the sampling ratio should be estimated by using the CODE 1.

This situation cannot be reproduced using the CODE 2 since the Lead/SCIFI modules are defined as a homogeneous material. Therefore here the case that the angle of incident photons are tilted 1 degree to the fiber axis will be discussed. The deterioration of the resolution for central incident will be compensated to reproduce real data by smearing the energy deposit overall. This will be discussed in the section 3.4 later.

The comparison between total energy deposit in a TYPE B-5 module for the CODE 1 and for the CODE 2 is shown in figure B.1. The angle of incident photon is $\theta_\gamma = 56^{\rm o}$ and photon energies are 50 MeV, 200 MeV and 1000 MeV respectively. The shape of the distributions are almost consistent between of them but peak positions for the CODE 2 are slightly deviated from the case of CODE 1. This shifts are relatively large for high energy photons. Figure B.2 shows the ratio of the shifts as a function of total energy deposit calculated by the CODE 2. The following function is fitted to the plot

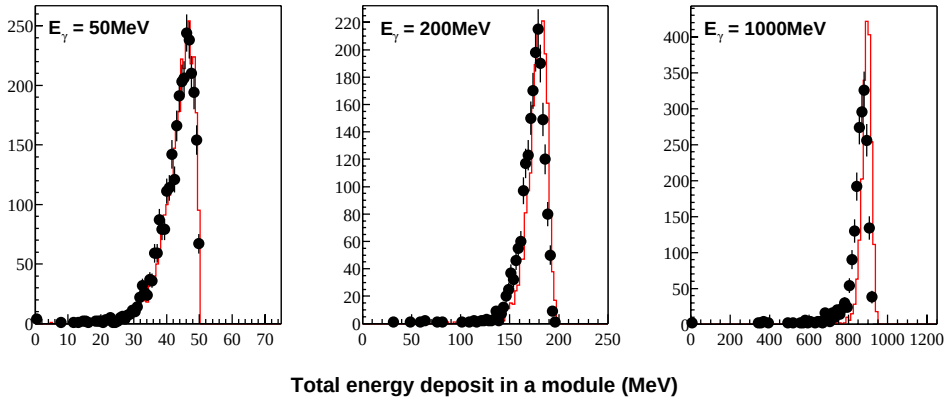

Figure B.1: The distributions of total energy deposit for each photon energy. The histograms in these plot corresponds to the result using the CODE 2 and the filled circles are represented the distribution calculated by the CODE 1.

$$(1 - p_0)\exp(p_1 dE) + p_0, \tag{B.2}$$

where the p_0 and p_1 are free parameters and dE is total energy deposit. This function is constrained to be unity at zero-energy deposit. The shifts are increased as photon energy increases and saturated to 97.5% in the case of $\theta_\gamma = 56°$. This is also caused by same reason of the deterioration of the resolution for central photon incident: the low interaction probability of between shower particles and the radiator material causes shorter effective radiation length. Therefore, shower leakage to behind of a detector increases for the CODE 1 comparing to the CODE 2. The longitudinal shower distribution as a function of detector depth in radiation length is shown in figure B.3. The position of shower maximum can be represented empirically as follows:

$$t_{\max} \quad = \quad 3.9 + \ln E_0, \tag{B.3}$$

where $t_{\max}$ is depth of shower maximum in radiation length and E_0 is photon energy in GeV[60]. The most of shower energy is deposited in a module for 100 MeV. This is the reason why the deviation is relatively small for low energy case. On the other hands, for high energy the position of shower maximum logarithmically increased as the energy increases. Therefore the relative shower leakage would be saturated. The correction for the systematic deviation of total energy deposit between CODE 1 and CODE 2 was made by using the function B.2. The result is shown in figure B.4. Peak positions are almost consistent between each geometries.

Energy deposit in the fiber region (dE_{SCIFI}) for CODE 2 case can be obtained by multiplying total energy deposit by the sampling ratio obtained from CODE 1. The Gaussian function with a right-handed

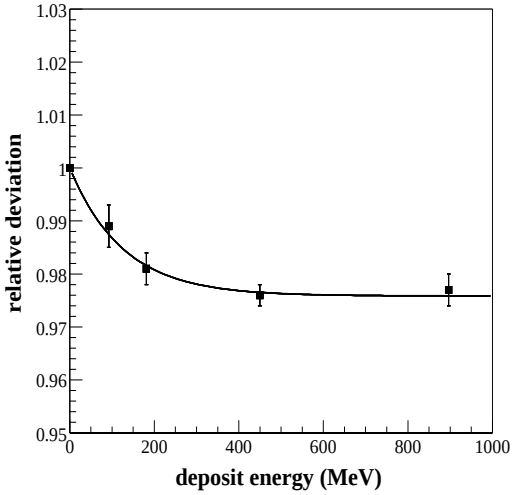

Figure B.2: The ratio of the total energy deposit between CODE 1 and CODE 2 as a function of the energy deposit.

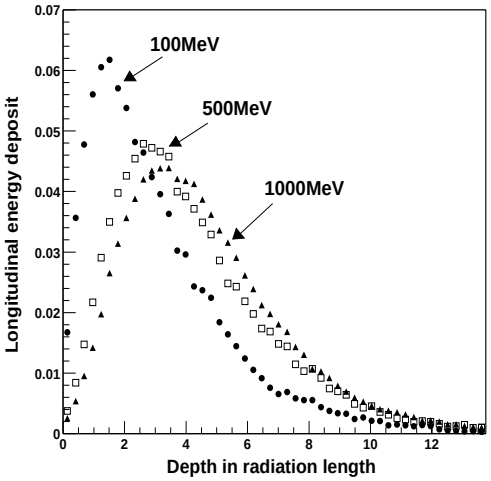

Figure B.3: Longitudinal energy deposit in a module (TYPE B-5) for each photon energies as a function of detector depth. The y-axis scale is normalized by incident energy.

exponential tail is fitted to distributions of the sampling ratio:

$$S(x) = \begin{cases} A \exp -\frac{1}{2}\left(\frac{x-\mu}{\sigma}\right)^2 & x < x_j \\ A \exp -\frac{1}{2}\left(\frac{x_j-\mu}{\sigma}\right)^2 \exp\left(\frac{x_j - x}{b}\right) & x \geq x_j \end{cases} \tag{B.4}$$

where x_j is the joint point of the exponential tail to the Gaussian function[47]. Using this parameterization (dE_{SCIFI}) for CODE 2 is calculated as shown in Figure B.5. In this plot the distribution of (dE_{SCIFI}) for CODE 1 also superimposed for comparison. The dE_{SCIFI} distributions obtained by the CODE 2 are almost consistent with the result of CODE 1.

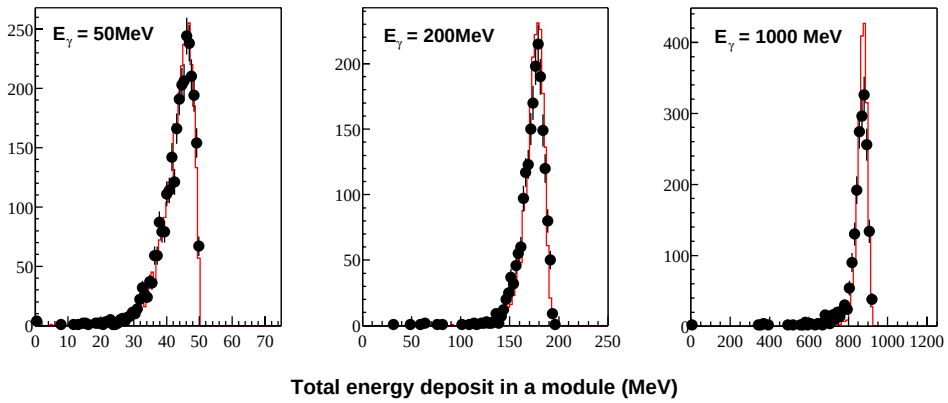

Figure B.4: The distributions of total energy deposit for each photon energy which is made the correction using function B.2. The histograms in these plot corresponds to the result from CODE 2 and the markers are distribution calculated by CODE 1.

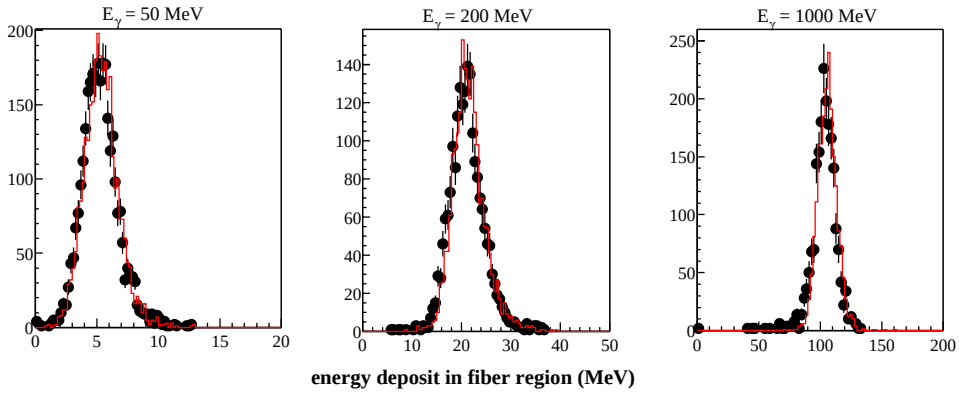

Figure B.5: The dE_{SCIFI} distributions for each photon energies. The histograms corresponds to the result from CODE 2 and the filled circles are distribution calculated by CODE 1.

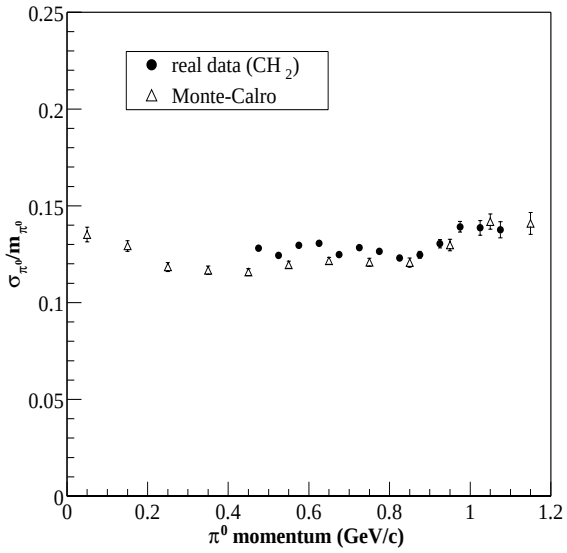

Figure B.6: Mass resolution for π^0-mesons as a function of the momentum for real data (filled circles) and Monte-Carlo result (open triangles). The MC samples were obtained by CODE 2.

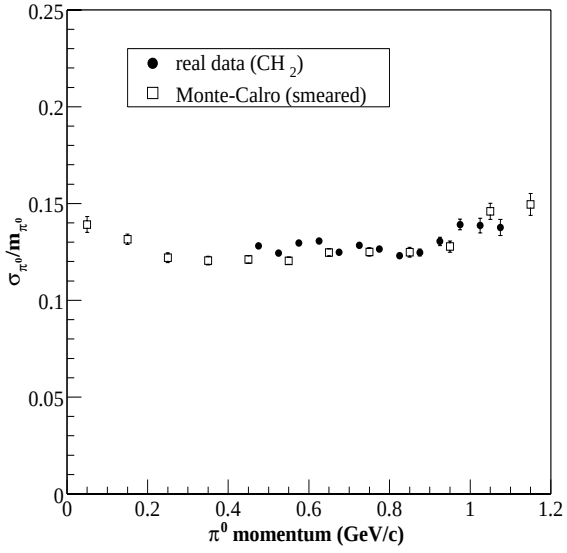

Figure B.7: Mass resolution for π^0-mesons resolution as a function of the momentum for real data (filled circles) and Monte-Carlo result with the smearing (open squares). The MC samples were obtained by CODE 2.

Bibliography

[1] M. Gell-Mann, Phys. Lett. **8**, 214 (1964).

[2] G. Zweig, CERN-TH-412 (1964).

[3] J. E. Augustin *et al.*, Phys. Rev. Lett. **33**, 1406 (1974).

[4] J. J. Aubert *et al.*, Phys. Rev. Lett. **33**, 1404 (1974).

[5] S. W. Herb *et al.*, Phys. Rev. Lett. **39**, 252 (1977).

[6] W. R. Innes *et al.*, Phys. Rev. Lett. **39**, 1240 (1977).

[7] B. Krusche and S. Schadmand, Prog. Part. Nucl. Phys. **51**, 399 (2003), `nucl-ex/0306023`.

[8] T. A. DeGrand, R. L. Jaffe, K. Johnson, and J. E. Kiskis, Phys. Rev. **D12**, 2060 (1975).

[9] T. A. DeGrand and R. L. Jaffe, Ann. Phys. **100**, 425 (1976).

[10] S. Capstick and N. Isgur, Phys. Rev. **D34**, 2809 (1986).

[11] S. Capstick and W. Roberts, Phys. Rev. **D47**, 1994 (1993).

[12] K. Hagiwara *et al.*, Phys. Rev. D **66**, 010001 (2002), URL `http://pdg.lbl.gov`.

[13] N. Isgur and G. Karl, Phys. Lett. **B72**, 109 (1977).

[14] N. Isgur and G. Karl, Phys. Rev. **D18**, 4187 (1978).

[15] S. Capstick and W. Roberts, Prog. Part. Nucl. Phys. **45**, S241 (2000), `nucl-th/0008028`.

[16] M. Koma, Ph.D. thesis, Osaka University (2002).

[17] H. Toki, J. Dey, and M. Dey, Phys. Lett. **B133**, 20 (1983).

[18] R. K. Bhaduri, B. K. Jennings, and J. C. Waddington, Phys. Rev. **D29**, 2051 (1984).

[19] M. V. N. Murthy, M. Dey, J. Dey, and R. K. Bhaduri, Phys. Rev. **D30**, 152 (1984).

[20] M. V. N. Murthy, M. Brack, R. K. Bhaduri, and B. K. Jennings, Z. Phys. **C29**, 385 (1985).

[21] A. Hosaka, H. Toki, and M. Takayama, Mod. Phys. Lett. **A13**, 1699 (1998), hep-ph/9711295.

[22] A. Hosaka, M. Takayama, and H. Toki, Nucl. Phys. **A678**, 147 (2000), hep-ph/9910469.

[23] M. Takayama, H. Toki, and A. Hosaka, Prog. Theor. Phys. **101**, 1271 (1999).

[24] M. Takayama, A. Hosaka, and H. Toki, Nucl. Phys. **A663**, 695 (2000).

[25] M. Koma, A. Hosaka, and H. Toki, Nucl. Phys. **A721**, 617 (2003), nucl-th/0212108.

[26] S. Capstick and W. Roberts, Phys. Rev. **D49**, 4570 (1994), nucl-th/9310030.

[27] A. Braghieri *et al.*, Phys. Lett. **B363**, 46 (1995).

[28] Y. Assafiri *et al.*, Phys. Rev. Lett. **90**, 222001 (2003).

[29] S. Capstick and W. Roberts, Phys. Rev. **D57**, 4301 (1998), nucl-th/9708048.

[30] A. Ehmanns *et al.*, Acta Phys. Pol. **B31**, 2377 (2000).

[31] R. Ammar *et al.*, Phys. Rev. Lett. **21**, 1832 (1968).

[32] D. Antreasyan *et al.* (Crystal Ball collaboration), Phys. Rev. **D33**, 1847 (1986).

[33] T. Oest *et al.* (JADE collaboration), Z. Phys. **C47**, 343 (1990).

[34] M. N. Achasov *et al.*, Phys. Lett. **B438**, 441 (1998), hep-ex/9809010.

[35] R. R. Akhmetshin *et al.* (CMD-2 collaboration), Phys. Lett. **B462**, 380 (1999), hep-ex/9907006.

[36] A. Aloisio *et al.* (KLOE collaboration), Phys. Lett. **B536**, 209 (2002), hep-ex/0204012.

[37] S. Godfrey and N. Isgur, Phys. Rev. **D32**, 189 (1985).

[38] V. M. Budnev and A. E. Kaloshin, Sov. J. Nucl. Phys. **31**, 679 (1980).

[39] T. Barnes, Phys. Lett. **B165**, 434 (1985).

[40] J. D. Weinstein and N. Isgur, Phys. Rev. **D41**, 2236 (1990).

[41] R. L. Jaffe, Phys. Rev. **D15**, 267 (1977).

[42] E. Marco, E. Oset, and H. Toki, Phys. Rev. **C60**, 015202 (1999), nucl-th/9905046.

[43] B. Kerbikov and F. Tabakin, Phys. Rev. **C62**, 064601 (2000), nucl-th/0006017.

[44] T.Kumagai, SPring-8 annual report 2000 p. 16 (2000).

[45] A. D'Angelo *et al.*, Nucl. Instrum. Meth. **A455**, 1 (2000).

[46] D. W. Hertzog *et al.*, Nucl. Instrum. Meth. **A294**, 446 (1990).

[47] D. Babusci *et al.*, Nucl. Instrum. Meth. **A332**, 444 (1993).

[48] T. Matsumura, Master's thesis, Yamagata University (2000).

[49] T. Tsuru *et al.* (E135 and E179 collaboration), Nucl. Phys. Proc. Suppl. **21**, 168 (1991).

[50] K. Takamatsu (E135 collaboration), Nucl. Phys. **A675**, 312c (2000), `hep-ph/9910304`.

[51] K. Takamatsu (E135 collaboration), Prog. Theor. Phys. **102**, E52 (2001), `hep-ph/0012324`.

[52] Y. Sugaya *et al.*, IEEE Trans. Nucl. Sci. **48**, 1282 (2001).

[53] S. Agostinelli *et al.*, SLAC-PUB-9350 (2002).

[54] V. N. Ivanchenko (Geant4 collaboration), Nucl. Instrum. Meth. **A494**, 514 (2002).

[55] R. Carrington *et al.*, Nucl. Instr. and Meth. **163**, 203 (1979).

[56] G. A. Akopdzhanov *et al.*, Nucl. Instr. Meth. **140**, 441 (1977).

[57] A. G. Frodesen, O. Skjeggestad, and H. Tøfte, *Probability and statistics in Particle Physics* (Universitetsforlaget, 1979).

[58] J. Junkersfeld *et al.*, Acta Phys. Polon. **B33**, 941 (2002).

[59] R. Plotzke *et al.* (SAPHIR collaboration), Phys. Lett. **B444**, 555 (1998).

[60] R. G. Fernow, *Introduction to experimental particle physics* (Cambridge University Press, 1989).

Acknowledgments

I would like to sincerely express my gratitude to my supervisors, Prof. T. Nakano, Prof. H. Shimizu and Prof. M. Fujiwara, for their continuous encouragement and helpful suggestions.

I would like to thank my collaborators, Prof. J.K. Ahn, Dr. S. Daté, Prof. K. Hicks, Dr. T. Hotta, Mr. T. Ishikawa, Prof. J. Kasagi, Prof. H. Kawai, Mr. T. Kinoshita, Dr. H. Kohri, Mr. T. Mibe, Mr. K. Miwa, Mr. M. Miyabe, Dr. N. Muramatsu, Mr. T. Nakabayashi, Mr. H. Nakamura, Mr. M. Niiyama, Mr. T. Ooba, Dr. D.S. Oshuev, Prof. C. Rangacharyulu, Dr. P.M. Shagin, Mr. Y. Shiino, Dr. Y. Sugaya, Mrs. M. Sumihama, Mr. Y. Tajima, Dr. H. Yamazaki, Dr. T. Yorita, Mr. H.Y. Yoshida and Prof. R.G.T. Zegers for their supports. I believe the experiment was not successfully finished without their supports.

I would like to acknowledge Advanced Science Research Center of JAERI for the financial support to stay at the SPring-8 site. Thanks to the support, I devoted myself to the present study.

I wish to thank Dr. Y. Asano, Dr. H. Toyokawa, Dr. N. Kumagai, Dr. H. Ookuma and other staffs of SPring-8. The LEPS beam line (BL33LEP) would not be established successfully without their helpful and great supports.

I would like to thank all LEPS collaborators, Mrs. D.S. Ahn, Dr. S. Ajimura, Dr. H. Akimune, Dr. W.C. Chang, Prof. H. Ejiri, Mrs. H. Fujimura, Dr. S. Hasegawa, Prof. K. Imai, Prof. T. Iwata, Mr. Z.Y. Kim, Dr. K. Kino, Prof. S. Makino, Prof. T. Matsuda, Dr. N. Matsuoka, Dr. Y. Miyachi, Mr. M. Morita, Prof. M. Nomachi, Prof. A. Sakaguchi, Mr. T. Sasaki, Mr. Y. Toi, Dr. A. Wakai, Prof. C.W. Wang, Dr. S.C. Wang, Dr. K. Yoyehara, Dr. M. Yoshimira and Dr. M. Yosoi for their construction of the LEPS detectors, and development of the laser system.

I would like to thank Prof. A. Hosaka, Dr. M. Koma and Dr. A. Titov for many helpful comments for this study from theoretical point of view.

I wish to thank M. Kibayashi and S. Ano, technical staffs of Research Center of Nuclear Physics, for their help to construct the backward calorimeter.

Younger students of Research Center of Nuclear Physics support my dairy life. I would like to thank

Mr. A. Shimizu and T. Onuma.

Finally, I would like to thank to my parents and brothers for their continuous encouragement and supports. I would like to express special thanks to my fiancee Mrs. Tomoko Suzuki for her hearty assistance and encouragement with full of love.